Optical Diagnostics of Flows: an Introduction

Emmanuel Rosencher
Scientific Director
of the Physics Branch

Since its founding in 1946 as the major actor in aerospace research in France, Onera has identified the strategic role of optical diagnostics of flows in aerospace development and has achieved recognized expertise in this field. In this first issue of Aerospace Lab, we will describe some recent or on-going developments in the field of optical diagnostics of flows at Onera.

Flows are generated when an object moves in a gaseous environment. It is thus no surprise that we find flow dynamics research in all branches of science and technology: civil and chemical engineering, the automotive industry, energy, etc. Flow dynamics are even more central to aeronautics technology because they provide air lift to planes (non-reacting flow dynamics) as well as moving impetus through combustion (reacting flow dynamics). The great challenges of flow dynamics require the validation of physical models with relevant length ranges spanning dozens of orders of magnitude, from a few Angstroms, at which atoms and molecules collide and bond (particularly in combustion), to a meter range (the size of a combustion chamber or a wing). Optical diagnostics are ideal for addressing this enormous challenge as they can span these different scales, offering both a global view through imaging and a microscopic view through spectroscopy. Moreover, these techniques are non-intrusive, so that they do not disturb the system or bias the measurements as other probing techniques do.

Optical diagnostics of non-reacting flows

In the first part of this Issue, we address the Onera State of the Art in optical diagnostics of non-reacting flows (aerodynamics). Modern problems of Computational Fluid Dynamics (CFD) call for new metrological approaches in terms of spatial and temporal resolutions, measurement precision, etc. which are analyzed in [1]. One aspect of this challenge is to "visualize the invisible": gaseous flows are transparent so we must devise ways to "materialize" their motion (speed), structures (vortices, turbulences, etc.), and basic parameters such as composition, pressure and temperature fields. This materialization of flows may be provided by micro- or nanoparticles, which are either seeded or naturally present (aerosols) and then carried along by the gaseous flow. These particles diffuse light efficiently, which allows for the use of two-dimensional velocity mapping techniques such as Particle Image Velocimetry (PIV in [3] & [4]), Laser Doppler, Doppler Global Velocimetry (LDV and DGV), and Coherent Lidar [6]. Laser plays an essential role in these techniques due to its outstanding properties of directivity, spatial resolution, optical coherence and spectral linewidth. When no such particles are present in the flow, the intrinsic properties of the gas are used: optical index contrast (Schlieren, shadowgraph, etc.) which makes use of the small variations in the optical index of the gas with temperature [9], or the light emitted or scattered by the air molecules themselves when excited by an electron beam (FFE in [8]) or laser light (Molecular Lidar [7]). Boundary conditions, which are propagated over large distances by the flow, have a fundamental impact on the flow dynamics, so that optical characterization of boundary surface conditions [2] is of the utmost importance for a full understanding of flow dynamics.

Optical diagnostics for reacting flow dynamics

The second part of this Issue is devoted to optical diagnostics for reacting flow dynamics (mostly combustion). Over and above what is needed for non-reacting flows, combustion research calls for quantitative, sensitive and chemical-specific imaging techniques. Combustion science is basically multi-scale (from the molecular level to large scale turbulence) and multi-physics (heat transfer, chemistry, radiation, acoustics, etc.). It is facing new challenges such as environmental protection goals of simultaneously decreasing the consumption of fuel and unwanted emissions (soot, NO_x, CO_x, etc.) or of using alternative fuels with new chemical species. These evolutions call for new approaches in optical diagnostic techniques, such as higher temperature and pressure conditions, greater sensitivity (down to the

ppm level for some pollutants), etc., which are described in [10]. For example, multiphase (spray) combustion studies require new techniques to determine the chemical and physical properties of fuel in its liquid and vapor phases (see for instance [5] and [11]). Chemical sensitivity is particularly important and is determined by the spectroscopic properties, particularly line strength, and the temperature of the species. Laser-Induced Fluorescence (LIF in [11]) consists of imaging the fluorescent light emitted by the molecules present in the flow (OH radicals but also seeded tracers such as NH_3, etc.), when they are excited by a sheet of laser light exactly tuned to their molecular resonance. It allows for a direct two-dimensional mapping of the species concentration and temperature. These molecular resonances are also charted by spectroscopic measurements such as Absorption [13] and Non-linear spectroscopy [12]. These techniques allow for the detection of multiple chemical species and provide enhanced knowledge of the gaseous state (rotational and translational temperatures, metastable species, etc.). They require exceptional mastery of tuneable laser technologies, such as dye lasers or more recently optical parametric oscillators, for which the Onera teams have been world leaders since the early 70's.

An ever-evolving technology

This State of the Art is clearly a snapshot of an ever-evolving technology. New developments and technological breakthroughs lie ahead, as Computational Fluid Dynamics will become more demanding with regard to validations. Femtosecond lasers will bring new opportunities, such as the study of ultra-dense media (e.g. high pressure sprays) using undiffused ballistic photons or time-resolved nonlinear scattering [14]. Progress in data processing will give access to three-dimensional reconstructions. High-power high-repetition rate (>10 kHz) lasers will enhance our knowledge of fluid dynamics over short time scales (turbulence formation, etc.). New sources such as wide bandwidth synchrotron radiation or multiplexed frequency comb-based spectroscopy may also prove useful for simultaneously mapping the concentrations of numerous species ■

Voltaire, in his novel "Candide", wrote in 1759 that there will be "many a century before man knows what is a simple flame". This time is now coming.

References

[1] L. JACQUIN - *Scales in Turbulent Motions.* Aerospace Lab n°1, December 2009.

[2] B. AUPOIX, P. BARRICAU, Y. LE SANT, M-C. MÉRIENNE, G. PAILHAS, P. REULET, Y. TOUVET - *Surface Mapping Methods.* Aerospace Lab n°1, December 2009.

[3] C. BROSSARD, J.-C. MONNIER, PH. BARRICAU, F.-X. VANDERNOOT, Y. LE SANT, F. CHAMPAGNAT, G. LE BESNERAIS - *Principles and Applications of Particle Image Velocimetry.* Aerospace Lab n°1, December 2009.

[4] G. LE BESNERAIS, F. CHAMPAGNAT, A. PLYER, R. FEZZANI, B. LECLAIRE, Y. LESANT - *Advanced Processing Methods for Image-Based Displacement Field Measurement.* Aerospace Lab n°1, December 2009.

[5] V. BODOC, C. LAURENT, Y. BISCOS, G. LAVERGNE - *Advanced Measurement Techniques for Spray Investigations.* Aerospace Lab n°1, December 2009.

[6] N. CÉZARD, C, BESSON, A. DOLFI -BOUTREYRE, L. LOMBARD - *Airflow Charaterization by Rayleigh-Mie Lidars.* Aerospace Lab n°1, December 2009.

[7] A. DOLFI-BOUTEYRE, B. AUGERE, M. VALLA, D. GOULAR, D. FLEURY, G. CANAT, C. PLANCHAT, T. GAUDO, C. BESSON, A. GILLIOT, J-P CARIOU, O PETILON, J. LAWSON-DAKU, S. BROUSMICHE, S LUGAN, L. BRICTEUX, B . MACQ - *Aircraft Wake Vortex Study and Characterisation with 1.5 µm Fiber Doppler Lidar.* Aerospace Lab n°1, December 2009.

[8] A.K. MOHAMED, J. BONNET, S. LARIGALDIE, T. POT, J. SOUTADÉ, B. DIOP - *Electron Beam Fluorescence in Hypersonic Facilities.* Aerospace Lab n°1, December 2009.

[9] J.M. DESSE, R. DERON - *Shadow, Schlieren and Color Interferometry.* Aerospace Lab n°1, December 2009.

10] F. DUPOIRIEUX - *Optical Diagnostics Used at Onera to Characterize Turbulent Reactive Flows and to Validate Aero- and Rocket Engine Combustor Modelling.* Aerospace Lab n°1, December 2009.

[11] F. GRISCH, M. ORAIN - *Role of Planar Laser-Induced Fluorescence in Combustion Research.* Aerospace Lab n°1, December 2009.

[12] B. ATTAL-TRÉTOUT, F. GRISCH, D. PACKAN, I. RIBET-MOHAMED, M. LEFEBVRE - *Laser Spectroscopy for in Situ Diagnostics.* Aerospace Lab n°1, December 2009.

[13] A.K. MOHAMED, M. LEFEBVRE - *Laser Absorption Spectroscopy to Probe Chemically Reacting Flows.* Aerospace Lab n°1, December 2009.

[14] M. BARTHELEMY, L. HESPEL, N. RIVIÈRE, B. CHATEL, T. DARTIGALONGUE - *Pump Probe Experiment for Optical Diagnosis of Very Thick Scattering Media.* Aerospace Lab n°1, December 2009.

Laurent Jacquin
(Onera)

E-mail: laurent.jacquin@onera.fr

Scales in Turbulent Motions

This paper reviews some of the classical dimensional principles used in fluid mechanics to predict the characteristic scales of turbulent flows. The reasoning makes largely reference to the celebrated Kolmogorov theory we first briefly recall. Data obtained in two wind tunnel experiments are then used to exemplify the concepts and to provide typical values of the different length and time scales involved in wind tunnel experiments. Measurement techniques and their role in the scientific research in fluid mechanics are then succinctly commented.

Navier-Stokes equations and the Reynolds number

Navier-Stokes equations correspond to the fundamental law of dynamics applied to a fluid particle (in mechanics, 'particle' means a macroscopic set of molecules of undefined shape and size). For a flow of an incompressible fluid with no volume force, the most standard form of the Navier-Stokes equation is:

$$\underline{u}_{,t} + \nabla \underline{u}.\underline{u} = -\frac{1}{\rho}\underline{grad}\ p + \nu \Delta \underline{u} \qquad (1)$$

In this equation $\underline{u}(\underline{x},t)$ denotes the velocity vector of the fluid particle, $\underline{u}_{,t}$ its temporal variation, $\nabla \underline{u}$ its gradient, ρ the fluid density, p, its pressure and ν its kinematic viscosity. The left hand side of equation (1) is the acceleration of the particle. This acceleration comprises two terms: a variation with time and a variation in space. The flow is steady (or permanent) if the first term is zero; however, this does not prevent the velocity from varying locally in space through the second term, called convective acceleration. The right hand side of equation (1) characterizes the only two mechanisms that can influence the motion of the particle in the absence of volume forces, i.e. the non-homogeneity of the pressure and the viscous diffusion of the momentum. Pressure is a scalar and is involved in equation (1) through a gradient (the particle is accelerated towards the low pressure regions of the flow). As for the second term, it logically takes the form of a Laplacian affected by a diffusion coefficient, which is here the kinematic viscosity of the fluid.

The main difficulty in fluid mechanics relies in the non-linear nature of the acceleration term $\nabla \underline{u}.\underline{u}$ of equation (1). We can only avoid this difficulty when this term is negligible with respect to the viscous diffusion (the last term of (1); the pressure term adapts to the velocity and is therefore not a scaling term). If we introduce the characteristic scales $|\underline{u}| \propto U$ and $|\nabla| \propto 1/l$, the ratio between these two terms is evaluated as:

$$\mathrm{Re} = \frac{|\nabla \underline{u}.\underline{u}|}{|\nu \Delta \underline{u}|} \propto \frac{U^2/l}{\nu U/l^2} = \frac{U\,l}{\nu} \qquad (2)$$

This dimensionless parameter defines the Reynolds number. When $\mathrm{Re} << 1$, the flow is dominated by viscosity and the equations become linear. Observations and theory show that the corresponding flows are generally stable to unsteady perturbations. Starting from this situation, when we increase the Reynolds number, flows progressively destabilize and then turbulence appears. Typically, flows are fully turbulent when $\mathrm{Re} >> 1$ (there are exceptions however, the vortex being an example).

Turbulence

The dissipative and irreversible nature of a fluid motion is due to viscosity. This may be understood if we consider the power per unit mass developed by the viscous friction in equation (1). This power, expressed as $P = \underline{u}.(\nu \Delta \underline{u})$. Simple vector manipulations allow to separate it into two terms:

$$P = \underline{u}.(\nu \Delta \underline{u}) = \nu \Delta\left(\tfrac{1}{2}\underline{u}^2\right) - \nu |\nabla \underline{u}|^2 \qquad (3)$$

We see that viscosity has two effects: it diffuses the kinetic energy in space through the first term, while reducing it with the second term:

$$\varepsilon = \nu\ |\nabla \underline{u}|^2 \qquad (4)$$

This term, defined as positive, is involved in the rate of dissipation of kinetic energy per unit mass. It expresses the irreversible nature of the movement (we find it with an opposite sign in the internal energy and entropy equations). Importantly, (4) shows that dissipation of energy requires high velocity gradients $|\nabla \underline{u}|$, and is thus ascribed to small scale activity. Turbulence is a phenomenon that indeed allows for the development of small scales and intense gradients, which are needed to dissipate energy. The concept of turbulence then leads to a paradox which we can summarize now, instructively.

This paradox appears, for example, when we evaluate the energy dissipated by the movement of an object in a fluid, a sphere in the example of Figure 1. This energy corresponds to the work of the drag force that opposes the motion of the object through the fluid.

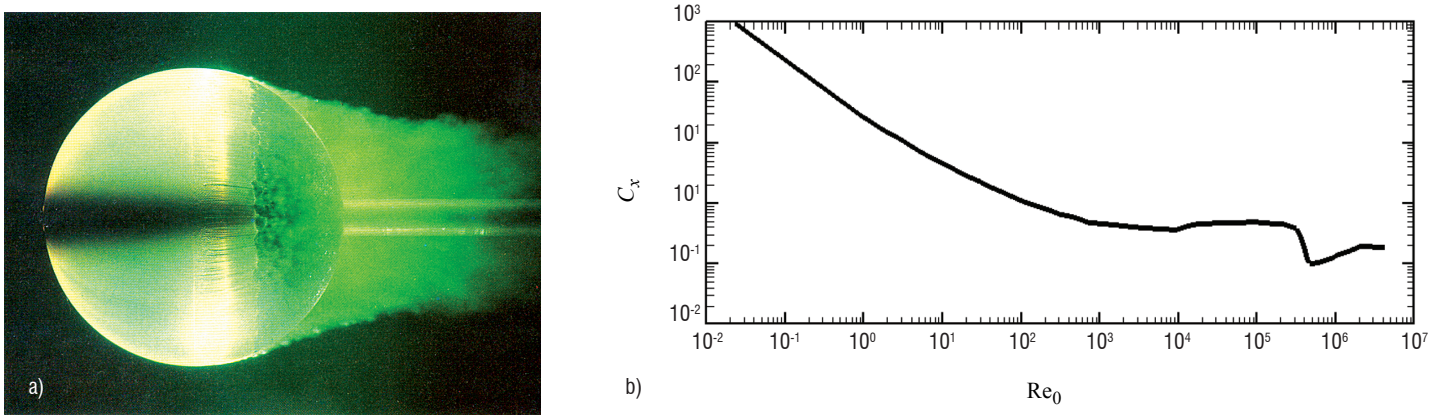

Figure 1 – Influence of the Reynolds number $\mathrm{Re}_0 = U_0 D/\nu$ on the flow around a smooth sphere (U_0 is the speed of flow far upstream of the sphere and D, the diameter of the sphere): (a) dye visualization by colorant in a hydraulic tank for $\mathrm{Re}_0 \approx 400\,000$ (Werlé, 1987), (b) drag coefficient of the sphere $C_x = F_x \Big/ \left(\frac{1}{2}\rho U_0^2 D^2\right)$ as a function of Re_0.

Supposing a sphere of diameter D fixed in a flow of speed U_0 of a fluid of density ρ and kinematic viscosity ν, if we express the three physical dimensions involved in this problem (mass, length and time) using ρ, U_0 and D, the drag force can be written in the form:

$$F_x = C_x(\mathrm{Re}_0)\rho U_0^2 D^2 \qquad (5)$$

The dimensionless coefficient C_x is the drag coefficient. It only depends on the Reynolds number $\mathrm{Re}_0 = U_0 D/\nu$. The power developed by this force, $F_x\ U_0$, is equal to the rate of energy dissipated within the flow. If we consider an average in a volume of fluid $V \sim D^3$ and build the rate of dissipation per unit mass, we obtain:

$$<\varepsilon> = \frac{F_x\ U_0}{\rho V} = C_x(\mathrm{Re})\frac{U_0^3}{D} \qquad (6)$$

To this day, there exists no theory allowing us to go beyond these laws and we must use experiments to determine the behavior of the unknown function $C_x(\mathrm{Re})$. Figure 1b shows the result for the flow past the sphere. The behavior obtained for $\mathrm{Re} \to 0$ is logical: the more viscous the fluid, the more energy must be dissipated to move in it. On the other hand, the saturation of C_x at high Reynolds numbers is not intuitive. We will see that it is in fact quite surprising.

Returning to (6), the experiment of Figure 1b shows that

$\lim_{\mathrm{Re}>>1} C_x(\mathrm{Re}) \approx Cte$, so that:

$$\lim_{\mathrm{Re}>>1} <\varepsilon> \approx Cte \times \frac{U_0^3}{D} \qquad (7)$$

We conclude that at high Reynolds numbers, the power per unit mass absorbed by the viscous friction becomes independent of the viscosity ! This is the very paradox we mentioned. Following (7), this power becomes equal to a constant fraction of the power U_0^3/D injected during the interaction between the object of size D and the flow of velocity U_0; it does not depend on anything else, especially not on the viscosity. Furthermore, in light of (4), relation (7) is equivalent to $\lim_{\nu \to 0} <\nu\ |\nabla \underline{u}|^2> \approx Cte$ which implies that the flow would be capable of developing singularities ($|\nabla \underline{u}| \to \infty$) in the limit case where $\nu \to 0$. Richardson (1922) and Kolmogorov (1941) contributed to assemble these elements into a phenomenological model which unravels the paradox mentioned above. This model, referred to as the Richardson-Kolmogorov cascade, constitutes an essential basis for the interpretation of the physics, and thus the measurement, of turbulent fluid flows.

The model is based on the principle of a fragmentation of scales that adjusts the rate of the energy dissipated within the flow volume to the power developed by externally imposed forces. Sticking to the essential points, in the Richardson-Kolmogorov cascade model turbulence is viewed as a set of imbricated “fluid structures” whose characteristic size decreases according to a dynamic process of successive fragmentations of the structures into smaller and smaller structures. This model is shown schematically in Figure 2. In this way, the

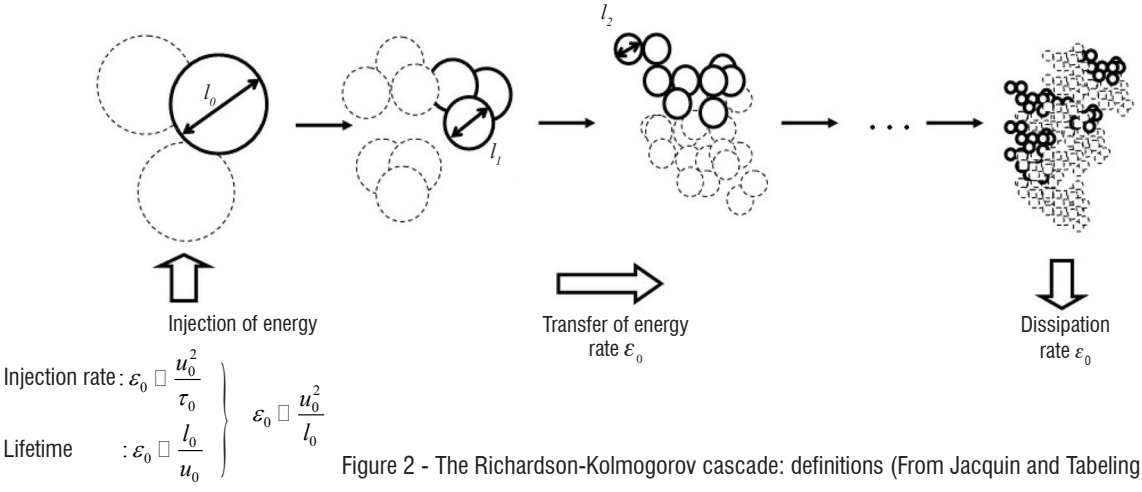

Figure 2 - The Richardson-Kolmogorov cascade: definitions (From Jacquin and Tabeling, 2006)

kinetic energy of the largest scales of characteristic length l_0 and velocity u_0 and on which external forces act, is transferred to the small scales of the motion. In the case of the wake of the sphere of Figure 1, we can consider that these largest scales of the turbulent movement verify: $l_0 \sim D$, $u_0 \sim U_0$. The rate of energy transfer per unit mass is thus in this case:

$$\varepsilon_0 \sim U_0^3 / D \qquad (8)$$

Through this process of scale fragmentation, the kinetic energy per unit mass U_0^2 is transferred from scale to scale without any loss until turbulent structures become small enough to be eliminated by the viscous friction. There, the energy will be finally transformed into heat. Thus, in this cascade, it is not energy that is conserved from scales to scales, but the rate of transfer of this energy. This rate remains constant and equal to ε_0 (see Figure 2). The characteristic velocity scale u_l of the structures of size l is given, whatever l, by the relation $\varepsilon_l \sim u_l^3 / l \sim \varepsilon_0$ or:

$$u_l \sim (\varepsilon_0 l)^{1/3} \qquad (9)$$

For the velocity gradients, we obtain $\nabla u_l \sim u_l / l \sim l^{-2/3}$. According to this law, the decrease in the flow scales within the cascade process is as a matter of fact able to produce the gradients which are necessary to dissipate the energy, see (4).

Figure 3 provides an example that illustrates the relevance of this model in a complex flow. It shows results based on the measurement of the three components of the velocity by PIV in a massive turbulent separation region over a rounded ramp. The geometry of the channel and the mean velocity field determined in several vertical cross sections are shown in Figure 3a. Averaging is made on a set of 1000 images for each of the planes. The images are recorded using a 1376 pixel x 1040 pixel digital camera and the velocity is determined by a standard cross-correlation method. An analysis of the turbulent behavior is done in an exploration window of 100 mm x 200 mm located in the lower part of the section at x = 450 mm. Figure 3b shows the longitudinal velocity averaged on 1000 images. This averaged field corresponds to a shear. Figure 3c isolates one of the images. The variable represented in this latter Figure is not the velocity but the component of the vorticity perpendicular to the observation plane, $\omega_x = \partial V / \partial x - \partial U / \partial y$.

We see that the turbulent vorticity 'superimposed' on the mean shear of Figure 3b presents a very fragmentary and homogeneous aspect that does not in any way reflect the average structure of the flow. Note that in these first three figures, the spatial resolution of PIV is determined by the size N = 32 x 32 pixel^2 assigned to the interrogation window ; the corresponding physical scale is about $L \approx 3$ mm. In Figure 3d, we show the result of an exploration of the scales of this turbulent motion made by modulating the resolution of PIV between N = 16 pixels ($L \approx 1.5$ mm) and N = 512 pixels ($L \approx 48$ mm). We plot in this Figure $\log < |\omega_x| >$ as a function of $\log N$. In accordance with (9), the theory provides the following scaling law for the vorticity:

$$\omega_l \sim \frac{u_l}{l} \sim l^{-2/3} \qquad (10)$$

We see in Figure 3d that the observations correctly reproduce this behavior. Thus, there is a fluctuating movement superimposed on

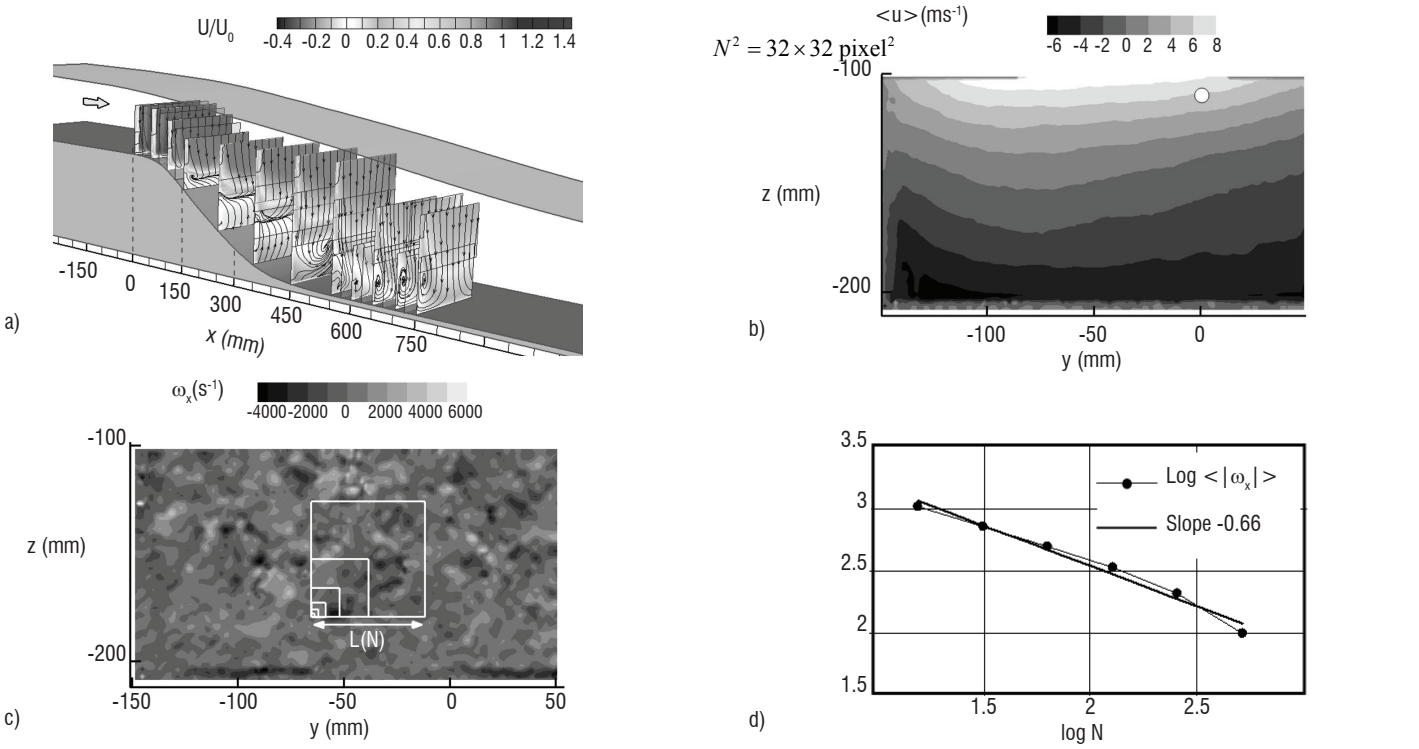

Figure 3 – Separated flow in a curved channel: (a) channel geometry, mean longitudinal velocity and projected stream lines obtained by 3C PIV in planes perpendicular to the upstream flow (averaging is made on 1000 images), (b) mean longitudinal velocity in the plane x = 450 mm (resolution: N^2= 32x32 pixel^2), (c) longitudinal component of the fluctuation of instantaneous vorticity measured in the same window as Figure b (resolution: N^2= 32x32 pixel^2), (d) average of the absolute value of the vorticity ω_x as a function of N for N= 2^n and n = 4-9, log-log plot. The physical sizes $L(N)$ of these windows are shown in superimposition in Figure 3c. The white circle in Figure 3b indicates the point of coordinates (x = 450 mm, y = 0, z = -127 mm) where the spectrum of Figure 4 is determined. Figure 3a is taken from Gardarin and Jacquin (2008).

the well structured mean shear of Figure 3b, which is fragmented according to the scheme of the Richardson-Kolmogorov cascade. Through (10), this movement may be seen as a vorticity field with an intensity which varies as the power -2/3 of the vortex scale. This means that turbulence can be seen as a distribution of more and more intermittent and singular vortices as we refine the scale of observation. The limit of this fragmentation is fixed by a minimum scale where viscous regularization can take place.

The smallest scales of the flow

The Kolmogorov scale

The limit of the inertial process described above is fixed by viscosity which selects the smallest scales of the motion. These scales, of size $l_{\min}$ and characteristic velocity $u_{\min}$, are those for which the Reynolds number is of order unity, $\mathrm{Re}_{\min} = u_{\min} l_{\min} / \nu \approx 1$: in accordance with (2), in these conditions viscosity once again becomes efficient and transforms the kinetic energy into heat. By combining this relation with $\varepsilon_0 \sim u_{\min}^3 / l_{\min}$, we find that the smallest possible scales verify:

$$l_{\min} \sim \left(\nu^3 / \varepsilon_0\right)^{1/4} \equiv \eta \qquad (11)$$

This is the Kolmogorov scale. By combining (8) and (11), we find that the ratio between the largest scale l_0 and the smallest one, η, is:

$$\frac{l_0}{\eta} \sim \mathrm{Re}_0^{3/4} \qquad (12)$$

This demonstrates that the extent of the range of cascading scales adapts to the Reynolds number by evolving as its power 3/4.

As an example, for the wake of the sphere of Figure 2, where $\mathrm{Re}_0 \approx 400\,000$, if we consider a diameter of $l_0 = 0.1$ m (say, an average scale for a sport ball), we obtain $\eta \approx 6\mu m$. At a fixed point located in the turbulent wake of this sphere, the measured frequencies are obtained by taking the local convection velocity of the scales l_0 and η. By taking for this velocity the upstream velocity $U_0 \approx 5$ ms^{-1}, the frequencies obtained are $f_0 \approx U_0 / l_0 \approx 40$ Hz, for the largest scale, and $f_\eta \approx U_0 / \eta \approx 640$ kHz (!) for the smallest one. These are the characteristic scales of this flow.

In the channel flow of Figure 3, at the point of coordinates (x = 450 mm, y = 0, z = -127 mm) indicated in Figure 3b, if we take as a characteristic velocity the difference in the velocities that shears the flow, here $u_0 \approx 30$ ms^{-1}, and if we consider that the scale of energy injection is $l_0 \approx 0.2$ m (the height of the rounded ramp), we obtain the same Reynolds number as previously, $\mathrm{Re}_0 \approx 400\,000$. (12) then yields $\eta \approx 12\ \mu m$ for the Kolmogorov scale. At this point, the local convection velocity is $U_0 \approx 5$ ms^{-1} (see Figure 3b) so that, in terms of frequency, the limits of the turbulent cascade are equivalent to the preceding ones: $f_0 \approx U_0 / l_0 \approx 25$ Hz and $f_\eta \approx U_0 / \eta \approx 417$ kHz.

Figure 4 shows the power spectral density of the fluctuations of the longitudinal velocity measured with a hot-wire probe placed at the point represented in Figure 3b. The hot-wire technique is based on the measurement of voltage variations at the tips of a small heated metallic filament in which a current is modulated so as to maintain a constant temperature of the filament. The voltage fluctuations are proportional to the variations of the flow velocity, that influences the filament temperature, and thus its resistance. This miniature sensor has a low enough thermal inertia to allow resolution of the small spatial and temporal scales of a turbulent flow (when the mean convection velocity is not too large). The hot-wire probe signal is here acquired with a frequency of 9 kHz. It is low-pass filtered with a cut-off frequency of f_c=2 kHz (here, this low value was sufficient for the author's purposes; note that in this flow a hot wire could discriminate the scales up to a frequency of more than 10 kHz). Beyond the frequency f_0 where energy is injected, the spectral density follows the famous "-5/3" power law predicted by the Richardson-Kolmogorov model (the demonstration may be found in any text book dealing with turbulence; see e.g. Jacquin and Tabeling, 2006, in French). The measurement is here under-resolved because, as shown by the theoretical dotted line, the cascade continues until the viscous frequency f_η which is well beyond the low-pass cut-off of the filter. However, the contribution to the total energy of the unresolved scales located in the range $f_c \le f \le f_\eta$ can be considered as negligible. We also see in gray in this Figure the range of the inertial scales of the cascade accounted for by PIV according to the scale of resolution L ($N = 2^n$) with η = 4-9 as indicated in Figure 3c.

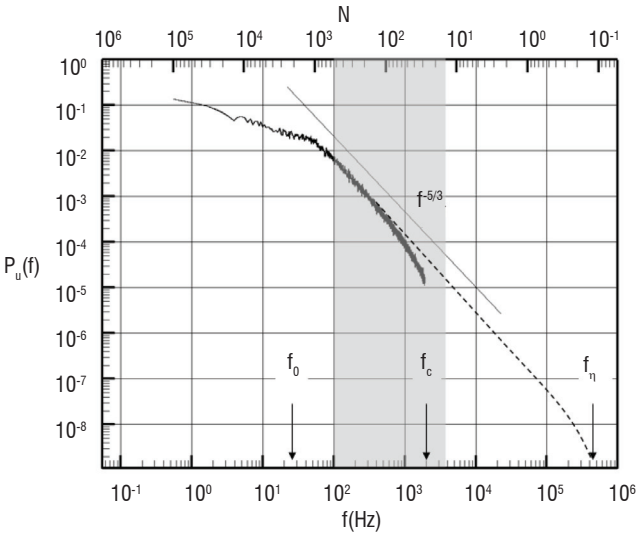

Figure 4 - Power spectral density of the velocity fluctuations at the point indicated in Figure 3b. Solid line: hot-wire measurement (acquisition at frequency f_{acq} = 9 kHz, low-pass filtering at f_{acq} = 2 kHz); dotted line: non-resolved part. The turbulent energy cascade theoretically develops between frequencies $f_0 \approx U_0 / l_0$ 25 Hz and $f_\eta \approx U_0 / \eta \approx 417$ kHz. The gray band represents the frequencies covered by the PIV resolutions tested in Figure 3.

It must be realized that while the cascade produces finer and finer and more intense vortices ($\omega_l \sim l^{-2/3}$, see (10)), these vortices carry less and less energy ($u_l^2 \sim l^{2/3}$, see (9)). The smallest vortices play a fundamental role which is to regulate the energy at the end of its process of injection/transfer/dissipation. But the energetic content of these scales is evanescent and their measurement is a feat that can be judged to be of no value in the case of free flows such as the wake of an object (Figure 1) or in a mixing layer (Figure 3).

But we will see however, that resolving these small scales is of primary importance for wall flows.

Wall flows

On the upstream part of the sphere (Figure 1a), or on the flat plate upstream the rounded ramp (Figure 3a, $X < 0$), the flow is attached and the scales of motion are constrained by the proximity of a solid wall and by the adherence condition $u(z \to 0) = 0$. These flow regions are called boundary layers. This situation is summarized in Figure 5a: when a fluid flows with a velocity U_0 above a solid surface located at $z = 0$, viscous friction, which slows down the flow, is propagated over a thickness δ which defines the boundary layer thickness (usually defined by $u(z = \delta) = 0.99\, U_0$).
In agreement with the preceding, we can seek the smallest scales of the movement taking as a hypothesis that the flow is turbulent, as in Figure 5b.

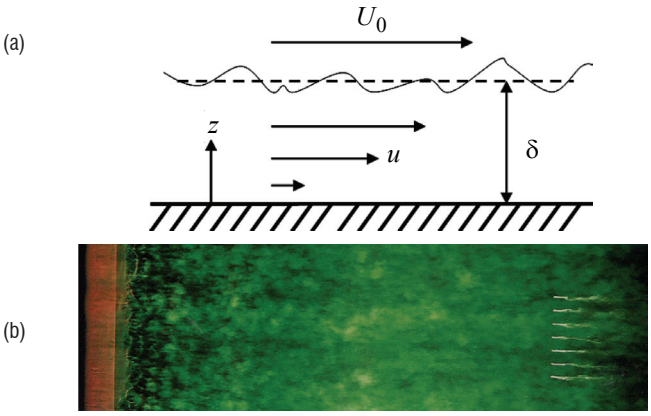

Figure 5 - Boundary layer : (a) definitions, (b) dye visualization of a turbulent boundary layer on a NACA0012 airfoil for a Reynolds number $\mathrm{Re}_c = U_0 c/\nu = 300\,000$, where c is the chord of the profile (view from above; the left and right limits of the image correspond to the leading and trailing edges of the airfoil; taken from Werlé, 1987).

To do this, we must evaluate the length scale l_0 and the velocity scale u_0 which characterize the process of energy injection in the turbulent cascade. For the length scale, one can remark that the physical distance to the wall prevents the motion from developing vertically. The scale of injection of the turbulent energy is thus variable according to the altitude, and we have:

$$l_0 \sim z \tag{14}$$

The evaluation of the corresponding characteristic velocity characterizing the input of energy is a delicate point. Following for example the argument of Landau & Lifchitz (1971), we must remark that the variability of the flow over the thickness of the boundary layer, i.e. between $z = 0$ and δ, is an effect that is caused by the action of the viscous friction on the wall. This introduces the wall friction $\tau_0 = \mu\, \partial u/\partial z\,(z = 0)$ where μ is the dynamic viscosity (the kinematic viscosity being $\nu = \mu/\rho$) as a scaling parameter of the problem. This dynamic parameter allows us to define a characteristic velocity scale: putting $\tau_0 = \rho u_0^2$, we obtain an 'external' velocity scale u_0 of the energy cascade in the form

$$u_0 \sim \sqrt{\tau_0/\rho} \equiv u_\tau \tag{15}$$

This velocity is called the friction velocity and its evaluation usually requires experimental measurements. In that respect, the following reasoning may be considered. If we assume that the flow is turbulent, it must develop an inertial cascade as described previously. The flow at these scales no longer explicitly depends on viscosity ; its properties are only fixed by u_τ and z. For example, the dissipation occurs with a rate $\varepsilon_0(z) \sim u_\tau^3/z$ and the shear $\partial u/\partial z$ must verify $\partial u/\partial z \sim u_\tau/z$. Integrating this latter relation leads to $u(z) \sim \log z$. Therefore, if the flow is turbulent, its velocity must be distributed logarithmically. This is indeed confirmed by the measurements, as will be seen below. Note that these functions do not diverge when $z \to 0$ because there is a minimum physical distance $z_{\min}$ where the flow ceases to be turbulent under a strong action of viscosity. By definition, at this distance the local Reynolds number must be of order unity, i.e. $\mathrm{Re}_{\min} = u_\tau z_{\min}/\nu \approx 1$. Hence:

$$z_{\min} = \nu/u_\tau \tag{16}$$

This scale characterizes the thickness of the laminar sub-layer found at the bottom of boundary layers. To evaluate it, we measure the distribution of velocity u as a function of z and smooth the turbulent fluctuations by taking a time average $< u >$ of u on a sufficiently long period.

We now have enough elements to give some orders of magnitude of the flow scales in a boundary layer, particularly the minimum scale $z_{\min}$ that separates the laminar region from the turbulent one.

Table 1 reports dimensional and non dimensional quantities that characterize three boundary layers of increasing Reynolds number. The first and the third cases are illustrated by the diagrams in figures 6 and 7. These are measurements made with Laser Doppler Velocimetry (LDV) specially adjusted to near wall approaches by minimizing the measurement volume. Following the above dimensional analysis, we traced in these two figures the mean velocity, its standard deviation and the height normalized by their respective reference scales (15) and (16) :

Case	U_0 (ms^{-1})	u_τ (ms^{-1})	$\frac{u_\tau}{U_0}$	$z_{\min}$ (μm)	$z_{z^+=15}$ (μm)	ϕ_v^+	δ (mm)	θ (mm)	Re_θ
1	10	0.46	21.74	33	500	1.2	21.4	25.25	1500
2	40	1.67	23.95	9	135	4.4	16.9	1.57	3400
3	240	9.24	25.97	1.6	24	50	3.46	0.38	6015

Table 1 – Characteristic scales in three boundary layers. Case 1 corresponds to Figure 6, and case 3 to Figure 7. ϕ_v^+ designates the characteristic scale of the LDV measurement volume normalized by the viscous length scale $z_{\min}$. The other parameters are defined in the text. Note the values of the minimal scales $z_{\min}$ (wall unit lengthscale) and $z_{z^+=15}$ (height of the turbulence production region) as well as their reduction when the Reynolds number increases (Losfeld et al. 2003).

$$u^+ = < u > / u_\tau \qquad (17a)$$

$$u'^+ = \sqrt{< u'^2 >} / u_\tau \qquad (17b)$$

$$z^+ = z / z_{\min} = u_\tau z / \nu \qquad (17c)$$

As seen in (17c), z^+ is the Reynolds number that characterizes the flow at height z. Its upper limit, $\delta^+ = \delta / z_{\min} = u_\tau \delta / \nu$, provides a Reynolds number for the whole boundary layer. As the determination of δ and u_τ are generally tricky, it is more convenient to use an integral scale, called momentum thickness, in order to compare various boundary layers:

$$\theta(x) = \int_0^\infty \frac{u}{U_0}\left(1 - \frac{u}{U_0}\right) dz \qquad (18)$$

This provides the values of the Reynolds number $\mathrm{Re}_\theta = U_0 \theta / \nu$ listed in Table 1.

In agreement with the above theoretical prediction, we see in figures 6 and 7 that the measured mean velocity follows a logarithmic law in the region $1 << z^+ << \delta^+$ where a turbulent cascade is possible. In the example of Figure 6, δ^+ is small and the logarithmic region extends over about a decade in z^+. In Figure 7, the Reynolds number $\mathrm{Re}_\theta = U_0 \theta / \nu$ is four times higher (this flow is produced in a transonic wind tunnel ; its Mach number is $M = 0.6$). As the friction velocity u_τ increases with the Reynolds number, the viscous scale $z_{\min}$ decreases, see (16), and the extent of the logarithmic region increases. At $z^+ = O(1)$, by definition, turbulence disappears. A Taylor-expansion then leads to $\tau(z) = \mu \partial u / \partial z(z) \approx \tau_0 z$, whence $u^+ \approx z^+$. This is indeed what is seen in Figure 6a where this linear law is characterized. In the case of Figure 7, the viscous scale $z_{\min}$ falls below 2 μm (!), see Table 1. In this case, the measurement system is no longer capable of characterizing the flow in the laminar sub-layer.

With regard to the fluctuations indicated in the right sides of figures 6a and 7a, we note some remarkable facts. First, the maximum intensity of the fluctuations is not obtained in the fully turbulent region, but at the level of its lower boundary, i..e. at about $z^+ = 15$. This corresponds to about $z = 500$ μm in case No. 1 and $z = 24$ μm (!) in case No. 3. This is the most unstable region of the flow, where production of the fluctuation energy of the turbulent boundary layer is maximal. Lastly, figures 6b and 7b show the probability density functions of the velocities measured at various heights. These distributions become singular in the laminar regions $z^+ = O(1)$ and $z^+ = O(\delta^+)$, and their enlargement in the regions where turbulence may develop characterizes the richness in scales of the turbulent process. Note that most of these histograms are skewed and deviate from a Gaussian distribution: this is one of the characteristics of turbulent shear flows.

The limits of flow simulation

We will now show that to capture all turbulent scales in a turbulent flow, from the larger to the smaller, supercomputers are indeed necessary. In accordance with (12), the minimum number N_{pt} of nodes required to capture all details of a turbulent flow is:

$$N_{pt} \sim \left(\frac{l_0}{\eta}\right)^3 \sim \mathrm{Re}_0^{9/4} \qquad (19)$$

For the case of Figure 1 where $\mathrm{Re}_\theta = 400\,000$, this gives $N_{pt} \approx 4\,10^{12}$ nodes. Furthermore, to solve the Navier-Stokes equations (1) with a numerical method, a minimum number of time steps is also necessary. It can be demonstrated that this number verifies $N_t \sim \mathrm{Re}_0^{1/2}$. A simulation thus requires a spatio-temporal meshing with at least $N_{pt} \times N_t \sim \mathrm{Re}_0^{11/4}$ points which leads to the astronomical number of 2.510^{15} points to handle the case of a simple sport ball. We are still far from having the technology needed to do this. Not to speak of an aircraft, for which Re_θ can reach 10^9, or even a car, for which $\mathrm{Re}_0 \approx 10^7 - 10^8$. Now think of the atmosphere…

Figure 6a gave an example of a direct numerical simulation of a boundary layer sufficiently resolved in 1990 thanks to its moderate Reynolds numbers. Note that once validated, such a direct simulation (DNS), free of any modeling, became a reference because it provides information on quantities that are not measurable. Case of Figure 7 has a larger Reynolds number and requires a meshing that is about 20 times denser. Such a case can be simulated nowadays. But we should now remember that this is just a boundary layer on a smooth flat plate.

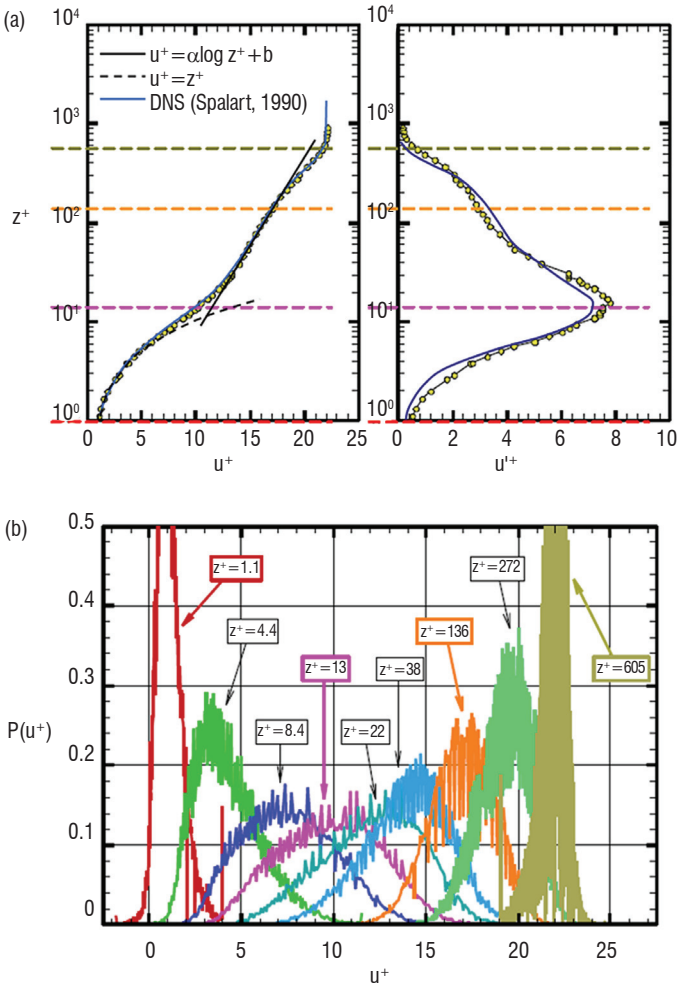

Figure 6 – LDV measurements in an incompressible boundary layer (case N°1 of table 1 : $U_0 = 10$ ms^{-1}, $\mathrm{Re}_\theta = 1500$): (a) average (left) and standard deviation of the fluctuations (right) of the longitudinal velocity component in wall variables and comparison with a direct simulation done at $\mathrm{Re}_\theta = 1410$ (Spalart, 1990), (b) probability density function of the fluctuations at various altitudes. The characteristic scale of the measurement volume is $\phi_v = 40$ μm, to be compared with the viscous scale $z_{\min} = 33$ μm ($\phi_v^+ = 1.2$, see Table 1). Taken from Losfeld et al., (2003).

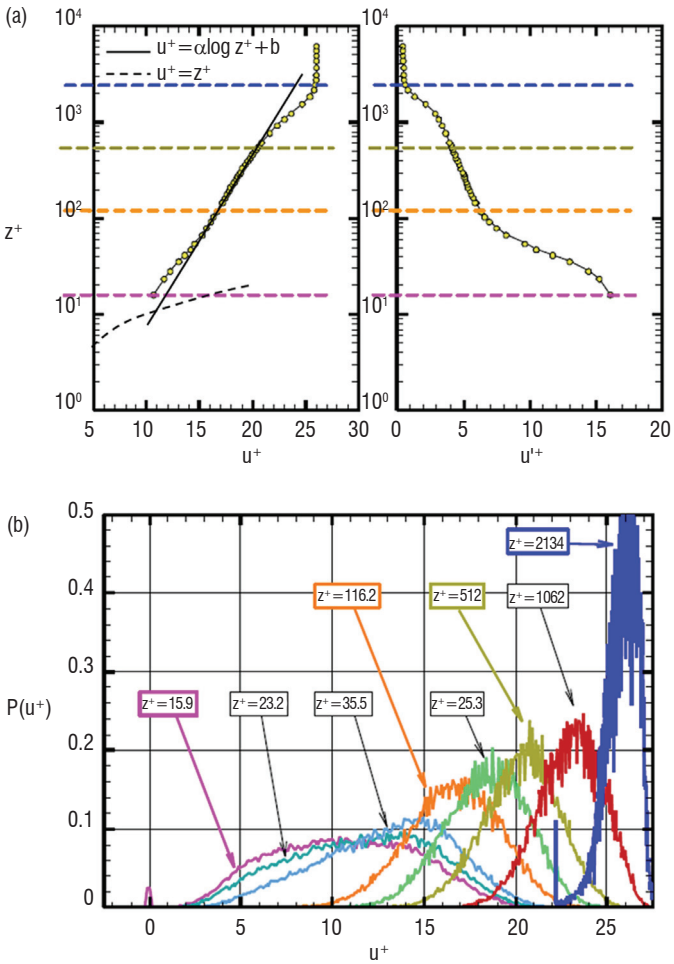

Figure 7 – LDV measurements in a compressible boundary layer (case N°3 of table 1: U_0=240 ms^{-1}, Re_θ=6015): (a) average (left) and standard deviation of the fluctuations (right) of the longitudinal velocity component in surface variables, (b) probability density function of the fluctuations at various altitudes. The characteristic scale of the volume of measurement is ϕ_v =80 μm, to be compared to the viscous scale $z_{\min}$ =1.6 μm (ϕ_v^+=50, see Table 1). Taken from Losfeld et al. (2003).

These limitations not only concern computing time, but also data storage. For each time step and at each point where we solve the equations of fluid mechanics, we must store the three components of velocity and pressure. If the flow is not incompressible, we must add temperature and density. This means recording four or six variables, to which we must add the four indices of the node (space and time), which becomes soon an unmanageable problem. Besides, we are just speaking here of a non-electrically charged and non-reacting flow. This gives an idea of the extent of the problem of simulating (and measuring) high Reynolds number flows from a practical standpoint.

In light of these difficulties, over the course of history, the Navier-Stokes equations were degraded by means of various statistical filtering methods. The success of these methods seems to be guaranteed by the apparently stable and repeatable nature of the statistical properties of turbulent flows (turbulent motion, which is chaotic if we try to follow a trajectory, becomes stable in the sense of ensemble statistics ; we thus realize, at the risk of destroying a stereotype, that turbulence is a fundamentally regularizing process). The activity which consists in formalizing the 'turbulent' terms of the equations resulting from these filtering operations is referred to as 'turbulence modeling'; A great research effort has been made on turbulence modeling in the 1980-90's. It led in particular to the current steady calculation methods, called RANS methods (for Reynolds Averaged Navier-Stokes). The calculation of the flow around a complete aircraft is now feasible thanks to such methods. But models become ineffective when turbulence is not in equilibrium, as it is often the case when it is subjected to mechanisms such as rotation, curvature, compressibility, shock waves, heat release, etc, or when it is no longer separable without ambiguity from a mean field, as is the case in highly unsteady flows. In such cases, turbulence can no longer be easily integrated into an artificial viscosity or in an inter-scale transfer function that are the artifacts used in most practical simulation tools. The success of the simulation then depends on the 'know-how' of the operator who must choose the best compromise among the tools at his disposal. But this also depends on the operator's physical knowledge of the simulated problem and on the availability of measurements he can validate his choices with.

Metrology is challenging flow physics

In the context of the massive investment of computational fluid mechanics which characterizes now the discipline, the role assigned to experimentation has evolved. In recent years, its role has been mainly to validate the numerical solutions by providing information needed for calibration of specific physical models. For instance, flow surveying by LDV played a major role in the development of RANS methods by allowing to measure with a high accuracy the statistical moments of velocity involved in the RANS equations. But measurements are also constantly challenging the researcher and accompanying him in both his theoretical analyses and modeling efforts. This is exemplified by PIV, a technique which is supplanting progressively LDV: while the commercial success of PIV came from a significant reduction of operational difficulties (compared to LDV), it opens up new possibilities that are not covered by the current simulation tools and their modeling capacities. In a near future, thanks to continuous progress in the field of lasers and digital cameras, PIV should provide a direct and complete description of the spatio-temporal kinematics of turbulent flows. Only direct numerical simulation of the Navier-Stokes equations (DNS), which is model-free, could be comparable to this. The current limitation of PIV lies in the handling of the considerable mass of data it produces. What can we do with all this information? What kind of model could use it? We should expect that PIV will contribute to modifying the landscape of modeling in fluid mechanics by giving rise to new theoretical proposals. Presently, on the fundamental basic research side, PIV is already at the core of modern analyses of hydrodynamic stability and flow control.

Conclusion

In this article, we first presented the physical principles that determine the characteristic scales of monophasic and incompressible flows at high Reynolds numbers, which are that found in wind tunnel experiments. The key analysis tool is the famous phenomenological theory of Kolmogorov, the basics of which we have outlined. The two experiments used here to illustrate the introduced concepts involve three main velocimetry techniques of fluid mechanics: PIV, LDV and hot wire anemometry. Note that beyond the limited framework of monophasic flows considered here, specific measurement methods exist to investigate multiphase flows, reactive flows, or plasmas; other physical scales are involved in these problems, which make the measurements more complex. Finally, we emphasized how challenging turbulence is for computational fluid mechanics and how important measurement is for the stimulation and development of scientific research in fluid mechanics ■

Acknowledgements
The author would like to thank his PhD student Benoit Gardarin and his colleagues Gilles Losfeld and Philippe Geffroy for kindly providing him with the two data commented on in this article. Benjamin Leclaire is acknowledged for his useful remarks.

References

[1] B. GARDARIN, L. JACQUIN - *Flow Separation Control with Vortex Generators.* AIAA-4th Flow control conference, Seattle, 23-26 June 2008.
[2] L. JACQUIN, P. TABERLING - *Turbulences et tourbillons.* Cours de l'école Polytechnique, édition 2006.
[3] G. LOSFELD, F. MICHELI, P. GEFFROY, R. SOARES, Y. LE SANT - *Vélocimétrie laser à frange, amélioration des mesures en couche limite.* Rapport Technique Onera N° RT 223/07382, DAFE, December 2003.
[4] A.N. KOLMOGOROV - *The Local Structure of Turbulence in an Incompressible Fluid with Very Large Reynolds Numbers*. Dokl. Akad. Nauk. SSSR, vol. 30, pp. 301-305, 1941.
[5] LANDAU, LIFCHITZ - *Physique théorique*. vol.6: Mécanique des fluides, Editions Mir, 1971.
[6] L.F. RICHARDSON - *Weather Prediction by Numerical Process*. Cambridge University Press, 1922.
[7] P. SPALART - *Direct Simulation of Turbulent Boundary Layer up*. Journal of Fluid Mechanics, 187, 1988.
[8] H. WERLÉ - *Transition et turbulence*. Note Technique 1987-7, Onera, 1987.

Acronyms

PIV (Particle Image Velocimetry)
RANS (Reynolds Averaged Navier-Stokes)
LDV (Laser Doppler Velocimetry)
DNS (Direct Numerical Simulation)

AUTHOR

Laurent Jacquin Research Director, Director of the Fundamental/Experimental Aerodynamics Dept of Onera. Associated Professor in Mechanical Engineering at Ecole Polytechnique (from1996 to 2007). Background: Master Degree in Mechanical Engineering from University of Marseille. PhD from University of Marseille in 1983. Research Habilitation Thesis (thèse d'état) from University of Lyon in 1987. Joined Onera in 1987.
Research topics include: Turbulence, Hydrodynamic stability, Vortex Dynamics, Compressible Flows, Aerodynamics, Experimental Methods.

Y. Le Sant, B. Aupoix,
P. Barricau, M-C. Mérienne,
G. Pailhas, P. Reulet,
Y. Touvet
(Onera)

E-mail: yves.le_sant@onera.fr

Surface Mapping Methods

The first measurement method used was measuring the forces on the model tested in a wind tunnel. This raised more questions that could only be solved by measuring the pressure on the model's surface. This is still done with pressure taps, but the advent of new optical methods provides a real insight into the flow over the model's surface. Nowadays, all the physical quantities are adressed: pressure, temperature, heat flux, model shape and shear stress.

Introduction

Wind tunnel testing often involves taking physical measurements on the model's surface. These measurements are pressure, temperature and shear stress. There are also derived physical quantities such as heat flux and boundary layer transition. Finally, the surface's shape must be known in order to measure properties, which calls for new measuring methods. All of these variables can be determined using single point sensors or optical methods. The following article mostly concerns the latter type since most of today's research efforts are related to them.

The optical methods are always compared to single point sensor methods and often the end customer has to make a decision taking into account their claimed relative uncertainty. Optical methods undoubtedly have an advantage for temperature measurements and model deformation. In the case of other methods, such as Pressure Sensitive Paint (PSP), the uncertainty of the optical methods is roughly an order of magnitude greater than that of the single point sensors. However, experience has shown that the pressure map offers information of great value that cannot be extracted from a limited number of measurement points. This leads to a rather unexplored field: how can dense experimental results be compared to computational ones? Though this question is obviously also at the heart of flow measurement methods, it is however more challenging for surface mapping methods since the surface pattern of the measured property is of great value because it usually cannot be inferred from single point measurements.

Surface temperature determination is of primordial importance for aerodynamic studies and Infrared thermography, developed over more than 20 years, is the pioneering mapping method. It was an alternative method to thermocouple measurements but is now highly reliable and is even capable of seeing "through the wall", as it will be shown. Temperature Sensitive Paint has been developed at the same time.These two methods are routinely used for many applications.

Surface pressure mapping is also an important issue. Pressure Sensitive Paint or PSP has recently been developed. It consists of measuring the pressure with a luminescent paint. The 90's were the golden age of this method, which is now widespread. It has important advantages and drawbacks which are explained. In this method, the camera's location in relation to the model must be precisely determined and compensation must also be made for model deformations created by wind loading.

The article then contains the seminal works for a new technique for determining the model's shape called Model Deformation Measurement (MDM). This technique requires unusual precision, which makes it a full method. Finally, shear stress determination, which is the Holy Grail of metrologists, is addressed in final part, which describes how the oil-film method may be the first step in this quest.

Heat flux measurement using infrared thermography

Temperature measurement is probably the most well known surface measurement, due to the widespread use of infrared thermography (*IrT*). Everyone knows that it can be used to "see" where there are hot spots, which is useful in many applications, such as detecting heat sinks and defects in thermal insulation. These kinds of applications are qualitative and quantitative applications that are more connected with R&D fields. There are two kinds of applications for wind tunnel testing. The first one is detecting where the transition from laminar to turbulent is in the boundary layer. Since the heat transfer level is higher in the turbulent area, a temperature discrepancy can be measured through the transition area. The second one is more complicated since it concerns heat flux measurement, which is a derived quantity of the temperature map.

Another technique can also be used for these two kinds of applications. This is TSP, standing for Temperature Sensitive Paint. TSP is very similar to PSP and uses the same devices and nearly the same paints [1]. So when should *IrT* or TSP be used? Both methods have advantages and disadvantages: *IrT* offers an excellent temperature resolution (the best cameras have a resolution of 0.02 K) while the resolution of TSP is usually greater than 0.5 K. On the other hand TSP works in the visible range and therefore has no limitation because of the wide choice of cameras and lenses. This is the really bad point for *IrT* since special windows must be used and the lens choice is dramatically poor.

The paint could be an argument for *IrT*, but *IrT* suffers from an extra problem which is emissivity, that is usually too low for metallic parts. As a consequence a special paint is often used with *IrR* in order to increase the emissivity.
Anyway, *IrT* is more used than TSP since it is often simpler to apply and does not require any specific post processing to obtain the temperature. But there are some cases in which TSP is used, typically when there is no optical access for *IrT*.
Measuring heat flux Φ is much more challenging than measuring temperature. The former is deduced from the latter by solving the heat equation [2] which in the 1D case is:

$$\frac{\delta T(x,t)}{\delta t} = \frac{a}{\lambda}\frac{\delta \Phi(x,t)}{\delta x} \quad \text{with} \quad \Phi(x,t) = \lambda \frac{\delta T}{\delta x} \tag{1}$$

This equation shows that Φ depends on the thermal properties (a=diffusivity, λ =conductivity) and on time. That means that the entire temperature histogram must be known. The worst situation is the 3D case where the spatial temperature map must also be taken into account!

However, solving the heat equation is no longer an issue due to dedicated 1D [3] or 3D codes. The output is the heat flux history, which is usually noisy since the heat flux noise is proportional to the first temporal derivative of the temperature noise. A time filter or a space filter based on a small kernel is usually efficient enough to provide smooth results.

As said before, there are two kinds of applications of IrT in wind tunnel testing: boundary layer transition assessment [4] and heat flux measurements in hypersonic facilities. The former is a qualitative application since the aim is simply to visualize the location of the transition area from the laminar part to the turbulent part that enhances the heat flux exchanges between the model surface and the flow. For transonic applications, the temperature step is often lower than 1 K, which is why *IrT* is a valuable tool since it can be used to visualize temperature changes as low as 0.02 K. Figure 1 shows an old example in a hypersonic facility. The newest cameras (that have improved temperature resolution as well a double image size) have been used in transonic facilities but the images cannot be shown here.

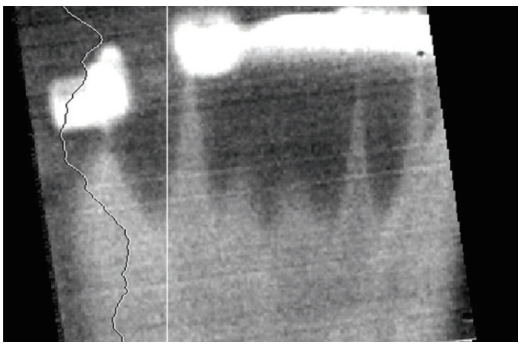

Figure 1 - Visualization of the boundary layer transition in a hypersonic facility. The camera was not well aligned so the image has been mapped on the model grid. This is why there are black parts where the camera did not see anything. The white parts are reflections of the test section's hot spots. The vertical cut shows the temperature profile along a vertical line.

The second application is heat flux measurement in hypersonic facilities [3,5]. The aim is to gather enough quantitative information to design the thermal protection system. As shown in figure 2, the model is heated quickly by the flow and the three curves have a typical pattern: a parabolic rise followed by a linear rise. The parabolic part at the beginning of the run is the solution of the heat flux equation for a semi-infinite wall while the linear part appears when the thickness of the model surface cannot be neglected.

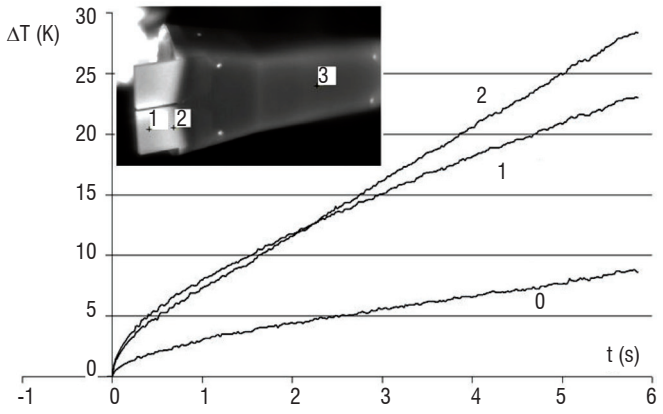

Figure 2 - Temperature history for three points on the PREX model.

Data reduction provides the heat flux history, which is in turn used to provide a unique heat flux value at the beginning of the run, which is presented in figure 3. As expected, the hottest parts are on the flaps while the heat flux level is quite low on the main body and even decreases before the flaps because of flow separation.

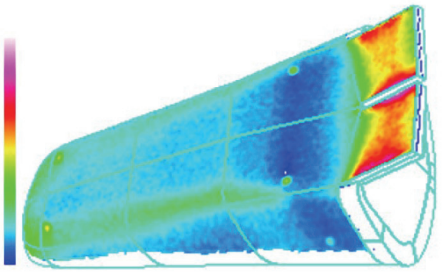

Figure 3 - Heat flux map on the PREX model.

Data reduction is done with a 1D code with some correction to take the 3D lateral conduction into account. However, under severe conditions, this 1D solution is not relevant and a 3D code should be used. This solution is under development and is based on studies carried out in the Onera.

DMAE (Department Aerodynamics and Energetics Modeling) has developed a 3D code that solves the 3D heat flux equation. The applications are to assess the heat flux on a flat plate heated by some heating source like a plasma. Since the heated face cannot be imaged, the opposite face is imaged with an infrared camera. This makes the problem much more complicated since the heat flux level on the heated face has to be deduced from measurements on the non heated face, which is like "seeing through the wall" and is a difficult inverse problem. It is solved by minimizing the functional:

$$E = \int_S \left[T(x) - \int_S f(x,u)\Phi(u)\,du \right]^2 dx \tag{2}$$

Where S is the model's surface and f is a sensitivity function that returns the effect of the heat flux at the point u on the point x. A regularization method must be used as the Beck's method [6] which assumes that the heat flux is constant for some time duration

Δt, i.e. assessing values at time t by using temperatures at future times. The functional is then:

$$E = \int_{\Delta t} \int_{S} \left[T(x,t) - \int_{S} f(x,u,t)\Phi(u)\,du \right]^2 dx \qquad (3)$$

The minimization can be done but often provides noisy results due to the noise on the temperature measurements, which are enhanced. The input data, which is the temperature map, then has to be smoothed using some tool such as the Discrete Cosinus Transform.

The inverse method [7] is used routinely to check the efficiency of heating sources and has even been used in wind tunnel testing [8] as shown in figure 4. The next step is to apply the method to a model with a high 3D feature.

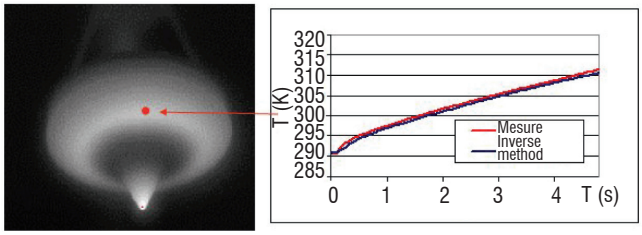

Figure 4 - Infrared measurement on the heated face. A dense thermocouple distribution was used on the non heated face to apply the inverse method. The agreement is fairly good except at the beginning of the run, where the Beck's method fails since the heat flux cannot be considered to be constant.

Box 1- Infrared thermography: uncertainty

Uncertainty for the temperature measurement: 0.03 K for *IrT*, close to 0.5 K for TSP.
Uncertainty for the heat flux measurement: since the heat flux is a derived quantity and depends on many quantities, the uncertainty is larger and is often close to 10%.

Surface pressure measurement using Pressure Sensitive Paint

Until recently, surface pressure measurements in wind tunnel testing were taken solely by pressure taps. Since the 1980's, an optical method has been introduced in order to replace these instruments and is now commonly used in industrial wind tunnels: Pressure Sensitive Paint, or PSP, which is a method generating an image of the pressure surface [9, 10, 11, 12]. The enthusiasm for this technique is prompted by the considerable savings it offers in terms of model instrumentation costs and model construction time, while the wealth of information that can be extracted from the images makes it a preferred investigation tool for complex flows[13]. Moreover, the measured pressure over an entire surface can be integrated to calculate the forces and moments of the complete model, or parts thereof. This article presents the basics of PSP and the way it is used. The PSP principle is relatively simple but requires many precautions if a high level of accuracy is desired.

Pressure sensitivity of luminescence

Practically all existing materials are luminescent in that they emit light when they are excited at a certain wavelength. The emission wavelength is always greater than the excitation wavelength according to Stoke's law. Emission may follow immediately upon excitation, in which case it is called fluorescence, or it may occur later, as in the phenomenon of phosphorescence. The emission intensity and spectrum depend on many parameters[14].
For the molecules used in PSPs, the oxygen captures a part of the decay energy as shown in Figure 5. The molecules used belong to three broad families: porphyrins, ruthenium complexes and pyrene derivatives. These molecules are excited in ultraviolet (pyrene) or in visible wavelengths (ruthenium). Some (porphyrins) can be excited over a large spectrum covering the ultraviolet and visible. Emission occurs in the visible portion of the spectrum.
The sensitivity to oxygen, more commonly called oxygen quenching, thus endows the molecule with sensitivity to air pressure, because the oxygen concentration is constant in the air. So, it is not a matter of sensitivity to pressure in the mechanical sense.

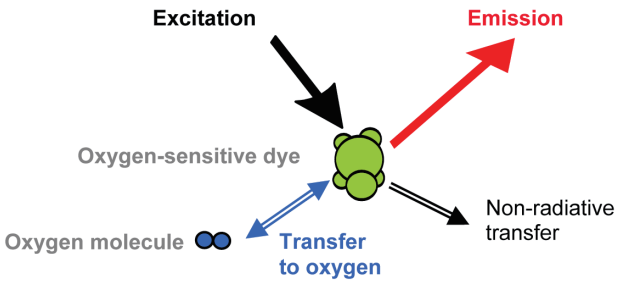

Figure 5 - Pressure sensitivity principle.

Composition of a PSP coating

In practice, the application of paint on the model requires two different layers. The model is first coated with a screen layer, which hides the luminescence of the model and increases the emission intensity by reflecting both the incident excitation radiation and the PSP emission. Then the active layer consists of a porous binder mixed with the luminescent molecule. The binder must be porous because the PSP principle is based on transfers with oxygen molecules. Only if the binder is porous enough will the oxygen partial pressure in the paint be equal to that in the flow. The PSP response time depends on the paint porosity and thickness and is usually about one second. The thickness of the paint is in the range 30–50 μm. PSP coatings are applied with a spray gun.

Intensity measurement method

The intensity method considers the luminescence emitted under a continuous illumination. Another method considers that the rate of luminescence decreases after a brief excitation (see box 2).It can be shown that the sensitivity obeys the Stern– Volmer law over a large range. This law is:

$$\frac{I_{ref}}{I} = A_{pref} + B_{pref}\frac{p}{p_{ref}} \qquad (4)$$

Box 2- Lifetime method

If a PSP molecule is excited briefly, it can be shown that its response is:

$$I(t) = I_{t=0} e^{-t/\tau} \text{ (i)}$$

where τ is the radiance lifetime. It can be shown that τ is expressed in the form:

$$\frac{\tau}{\tau_0} = 1 + \alpha p \text{ (ii)}$$

where τ_0 is the lifetime without oxygen. The lifetime varies considerably from one dye to another. It is of the order of 100 ns for pyrene-based paints and of the order of 100 μs for porphyrin-base paints.

The response under continuous excitation is found by integrating Eq. (i):

$$I = I_{t=0} \int_0^{t\to\infty} e^{-\eta/\tau} d\eta = I_{t=0}\tau \text{ (iii)}$$

$$\frac{I_{ref}}{i} = \frac{1+\alpha p}{1+\alpha p_{ref}} = \frac{1}{1+\alpha p_{ref}} + \frac{p}{1+\alpha p_{ref}} \frac{p}{p_{ref}} \text{ (iv)}$$

According to the Stern–Volmer equation (4), the values of coefficients A and B are:

$$A = \frac{1}{1+\alpha p_{ref}}, \quad B = \frac{p_{ref}}{1+\alpha p_{ref}} \text{ (v)}$$

So there is a strict equivalency between the Stern–Volmer law and the radiance lifetime law.

In this equation, the subscript *ref* indicates a reference value, generally taken at atmospheric pressure. I_{ref} is the intensity emitted under continuous excitation at the reference pressure p_{ref}, while I is the intensity emitted at the pressure p.

Constant A_{pref} gives the ratio of the intensities between the reference pressure (usually atmospheric) and the value at vacuum (i.e., with no oxygen). Since the oxygen captures a part of the excitation energy, the emission intensity decreases with an increasing partial pressure of oxygen, i.e., as the pressure rises

As I/I_{ref} is equal to one at the reference pressure, the sum $A_{pref} + B_{pref}$ is also equal to one and therefore B_{pref} is always less than one. However, Eq. (4) is only approximate because it does not take many effects into account – especially that of temperature. Polynomials of the following form are therefore used in practice:

$$\frac{I_{ref}}{I}(T,p) = \sum_{i=0}^{n} A_i T^i + \sum_{i=0}^{n}\sum_{j=1}^{m} B_{ij} T^i \frac{p^j}{p_{ref}} \quad (5)$$

where the temperature T can have a large effect. Usual PSP temperature sensitivity is between 0.4 to 1%/K. For a sensitive PSP (B∼1), an uncontrolled 1K increase in the temperature produces a considerable error of 400 Pa to 1kPa around the ambient pressure.

Sources of errors

Temperature

The temperature is one of the main sources of error even for a low temperature sensitive PSP, like pyrene-based paints which have a temperature sensitivity of 0.4% / K leading to an error in pressure of 500 Pa for 1 K. The temperature difference between the reference (or wind-off) image, which is taken when there is no flow in the wind tunnel, and the wind-on image, taken under the flow, must be taken into account as well as the temperature gradient on the model surface under the aerodynamic flow.

Temperature measurements taken using a few temperature sensors are limited to uniform variation of temperature, which is never the case. Such sensors can be useful for the reference image when thermal equilibrium is reached.

We can assess the temperature map for the wind-on images by calculating the recovery temperature. Since this temperature depends on the local Mach number, the calculation is then an iterative method.

Another possibility is to measure the temperature map with an infrared camera. This solution can be difficult to install in wind tunnel test sections because special infrared optics are required (see § Example of applications).

Binary paints can also be used to correct for the temperature variation. The principle is to add a second dye in the PSP (see box 3). This dye must be insensitive to pressure and, if it has the same temperature sensitivity as the pressure dye, the ratio between the two emissions will be insensitive to temperature. The measurements are also corrected for the intensity variations. This is the ideal case.

The second dye can be used as a temperature sensor, like in TSP (Temperature Sensitive Paint) where the emission spectra exhibits two different wavelength ranges with different temperature sensitivities. In this case, three images are required: one for the pressure, one the temperature and one for the intensity variations.

Intensity variation

Each uncontrolled variation in intensity will lead to a pressure uncertainty in the final results. Variations in intensity measured by the camera can be due to an unstable excitation source or to a model movement and/or deformation between the reference image and the wind-on image.

Source stability can be checked on a sequence of images. Continuous stable sources provide stability better than 0.1% (rms value) on a sequence of 20 images which are needed to reduce the camera shot noise (see § Instrumentation). The sequence duration is about 5 minutes and is representative of wind tunnel test acquisition conditions.
Model displacement between wind-off and wind-on images under aerodynamic loads and model deformation leads to a change of illumination field on the surface. Binary paint (see box 3) can be used to correct for these effects provided that the two set of images are properly aligned before processing, taking the 3D model geometry into account. Dedicated software called AFIX_2 has been developed at Onera to process the images [15] (one of its main tasks is to calibrate the camera, see box 5).

Instrumentation

PSPs can be excited by ultraviolet or visible spectrum light, depending on the dye used. Onera's paint contains a pyrene derivative as the pressure sensor and a rare earth oxysulfide as the reference component, which require UV light as excitation. We use a continuous Mercury-Xenon lamp which is extremely powerful (100 times standard Hg lamp) and very stable.
The PSP technique is a photometry technique and therefore the camera used for intensity measurements has to satisfy specific requirements. Scientific grade CCD cameras are cooled in order to reduce the dark current. They have a quantum efficiency up to 90 % in the visible range and a high full well capacity (300,000 electrons) which provides high sensitivity and dynamics (16 bits). Note that photon shot noise is a fundamental property of the quantum nature of light. As a consequence, photon shot noise is unavoidable and always present in imaging systems. Image averaging is the only way to reduce its effect.
In the case of binary paints that include a reference dye, there are two images so two filters are needed and three for the TSP/PSP application. A filter holder can be used to change the filter in front of the camera, but then the two images are no longer synchronous. This means that the excitation intensity should not change between the two images, requiring a source stability better than 0.1 %.
Some additional corrections can be achieved like the camera linearity and the flat field defects. The flat field correction is made to compensate for the non-uniformity of the CCD response. A flat field image is usually obtained by imaging a uniform field of view. Since it is nearly impossible to create a uniform scene, dedicated devices are used as integrating spheres. However, vignetting created by the lens is often larger than the non uniformity of the CCD. Therefore the lens must be calibrated too. This is a tedious task since vignetting depends on the aperture and on the focus distance.

Box 3 - Binary paint and TSP principle

PSPs that use a second dye are called binary paints. The second dye, used as reference to correct for variation of illumination, should be insensitive to the pressure and its emission spectrum must be clearly distinguishable from that of the pressure-sensitive dye (Figure B3 - 01).

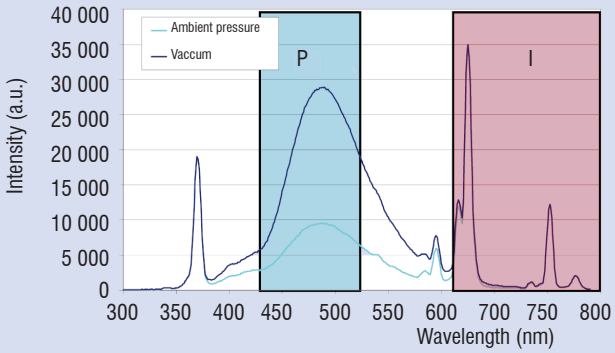

Figure B3 - 01 - Emission spectra of the Onera's PSP binary paint showing the pressure sensitivity (P filter) and the reference measurement (I filter).

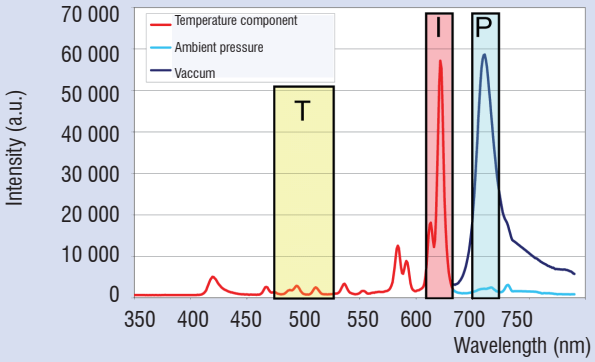

Figure B3 - 02 - Emission spectra of a PSP/TSP binary paint showing the pressure sensitivity (P filter), the temperature measurement (T filter) and the reference measurement (I filter).

The image corresponding to the reference dye can then be selected out by a filter. This view is often called the intensity image. The pressure image provided by the pressure sensitive dye is then divided by the intensity image, which compensates for the intensity fluctuations. The main drawback of the binary paint strategy is that two images are required: this means using two cameras or a single camera equipped with a filter holder.
An extension of the binary paint concept is using the second component as a temperature sensor, thus combining the PSP and TSP (Temperature Sensitive Paint) measurement techniques (Figure B3 - 02). In this case three images are required. The temperature image is used in the calibration law (eq. 5) to correct pressure measurements.

Box 4 - Pressure Sensitive Paint: uncertainty

The pyrene-based paint developed at Onera has a pressure sensitivity of 80%/100 kPa and a temperature sensitivity of 0.4%/ K. Thus the uncertainty on pressure due to a temperature variation of 1 K is 500 Pa.
Similarly, any variation in intensity due to the source stability or to the model's movement of 0.1% represents an uncertainty of 100 Pa (50 Pa rms). PSP is an absolute measurement technique, so this value corresponds to a more important uncertainty on the Cp coefficient which is a relative pressure parameter under low speed flow where pressure variations are small ($\Delta Cp=0.04$) than under transonic flow conditions ($\Delta Cp=0.01$).

Example of applications

PSP was initially developed for transonic applications where the demand was greatest. Since low speed tests play an important role for the design phase of aircraft, PSP technology has also been developed for small pressure variations in the pressure range between 80 and 100 kPa. A great deal of effort has been put into controlling all of the sources of errors which limit the accuracy of the technique [16, 17, 18].
We present a test performed in a low speed wind tunnel located at Onera Lille center with wind speed at 40 m/s. The test item was a fighter aircraft and the PSP was applied on the right wing, both on the pressure side and on the suction side. The model was equipped with canards located upstream of the wings. The canards have a strong effect on the wing and the aim of the test was to understand the decrease in efficiency on the trailing edge flap at high angle of attack (figure 6).
Simultaneously, temperature measurements were taken using an infrared camera with 70 mK of resolution. The temperature maps obtained on the suction side are uniform with a temperature variation of 0.2 K. On the pressure side, the IR images show a pattern which represents the structure of the model (figure 7). The main part of the wing is made of steel while the other part is filled with a resin. The temperature variation on the surface remains low (0.7 K) however temperature correction needs to be done on the pressure images. If not, the PSP images will show the same pattern as the temperature image and, in this case, we have checked that the discrepancy in pressure represents 300 Pa.

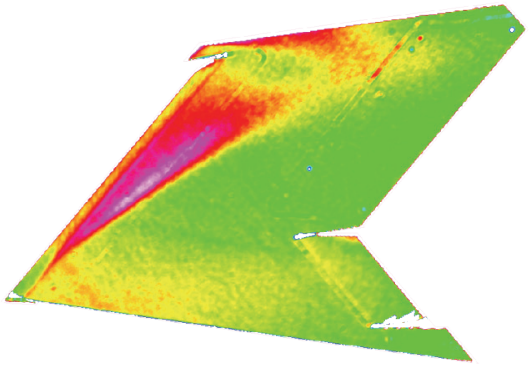

Figure 6 - PSP image on the wing suction side at 18° of angle of attack. The canard effect is visible near the wing fuselage junction.

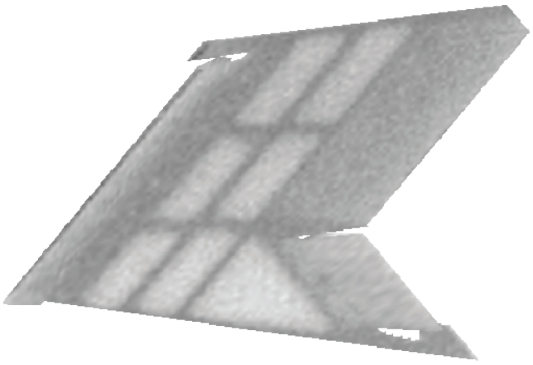

Figure 7 - Infrared image on the pressure side. $\Delta Tmax=0.7K$.

Unsteady PSP measurements

Application to unsteady pressure measurements is a new challenge for the PSP technique as it requires a fast responding coating [19]. Highly gas diffusive materials are needed as a binder for the unsteady PSP because the response time of the PSP depends on the gas diffusivity in the binder. One solution is to remove the binder and to use a fast responding PSP based on porous anodized aluminum with the dye adsorbed on the surface (AA-PSP) [20, 21, 22]. This type of coating (figure 8) gives a quite short response time of the order of 100 μs. AA-PSP has been used in a blow down supersonic wind tunnel to investigate the flow field topology inside a nozzle during the transient phase and to assess the pressure gradient at the outlet region during the steady state phase (figure 9). Images are acquired by using a fast frame rate camera equipped with a CMOS sensor, 12 bits dynamic range, at a rate up to 5,000 images per seconds (figure 10).

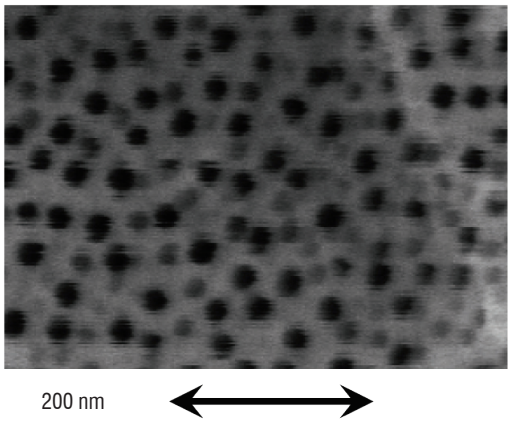

Figure 8 - Self organized formation of hexagonal pores on the Anodized-Aluminum surface (scanning electron microscopy)

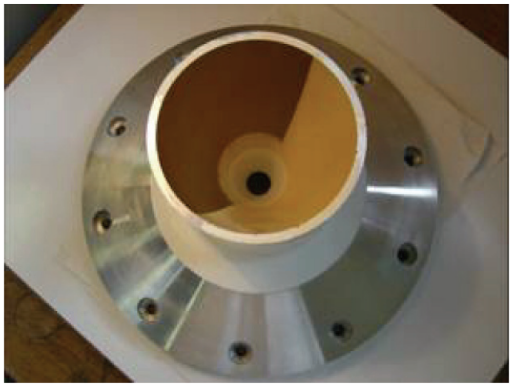

Figure 9 - Nozzle model with AA-PSP on half part of the inner surface

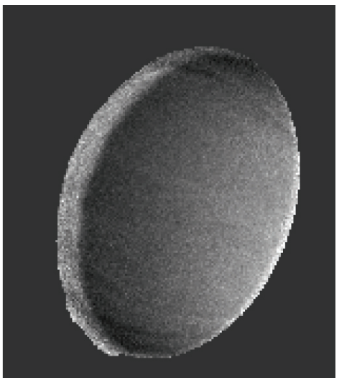

Figure 10 - Pressure image obtained during the transient phase.
Video - http://www.aerospacelab-journal.org/al1/Surface-mapping-methods

Box 5 - Camera calibration

Imaging methods address this question: where is the object in the image? The answer for the earliest mapping methods, such as infrared thermography, was very simple: the camera axes were aligned with the object axes. Assuming that this one was planar, which was often the case, a linear relation was established between the image and the object. This approach is still valid for some methods, such as 2C PIV. However, most of the applications have to deal with 3D objects and/or with a 3D camera arrangement. So the original question becomes: where is the camera in relation to the object? This problem is known as the pose problem [26] and is well known by the Computer Vision (CV) community. It was solved very early (Grüner, 1841!) and requires at least four known imaged points. Six parameters are identified which are three rotations and three translations. They are called the external parameters. The image is then created using the pinhole model (Figure B5 - 01).
However, using only the external parameters is not sufficient: the focal length must be known. You might think that the focal length number provided with the lens system could be used, but… this is only a rough estimate! Every photographer knows that changing the focus distance changes the viewed size of the object slightly, which means that the focal length depends on the focus distance! As a consequence it is also a parameter and is called an internal parameter since it only depends on the lens, not on the camera's location.
But this is only the beginning of the story: adjusting the external parameters and the focal length is done with a minimization criteria and the final standard deviation is often greater than 1 pixel, which is really too much for a lot of quantitative methods. Then extra parameters were added: the first ones were the pixel ratio and the skew factor, which models the possible rhomboid shape of the camera sensor. These two parameters were firstly identified by CV because they can be determined with analytical methods [27]. But the real world is more complex and in practice these two parameters are negligible in relation to other parameters that model lens distortions. All of these parameters along with the focal length are grouped together in the internal parameter set.
The first one is the radial distortion parameter K1, which creates a symmetric cushion effect. Then comes the lateral distortion, modeled with two parameters called P_1 and P_2. The equations that give the lens distortion are:

$$x_d = x + x r^2 K_1 + P_1(r^2 + 2x^2) + 2 P_2 x z \qquad y_d = y + y r^2 K_1 + P_2(r^2 + 2y^2) + 2 P_1 x z$$

where x,y are the image coordinates and xd,yd are the corrected coordinates. Note that the lens distortions could be modeled with two polynomial of the third order, which would introduces 20 parameters, which is much more than the 3 lens deformations parameters! Figure B5 - 02 shows the (exaggerated) effect of these parameters. In practice, at least two other parameters are used which are the coordinates of the lens axis in the image plane. It can usually be assumed to be exactly at the center of the image, but this may be not true for some cameras or for 3C PIV measurements that use a Sheimpflug device.
Calibration is done with a calibration body that is a flat plate covered with markers, as shown in Figure B5 - 02. The white ones are used for an automatic alignment and then the calibration is fully automatic. Several images are used. The calibration plate must be moved in the measurement volume and must be turned so that the upper left corner becomes the lower right corner. The reason is that the calibration body always suffers from small defects. Changing the plate orientation compensates for them. However, it has been demonstrated that no compensation can be made some defects, such as a twist. The marker locations then have to be adjusted, which is known in CV as "bundle" adjustment.
The uncertainty can be as low as 0.06 pixels, which is the uncertainty of the marker detector. However, this is usually difficult to achieve because of blurring created by the out-of focus effect or by some small calibration body motion since this one is often moved manually. Usual values are closer to 0.4 pixels, while an uncertainty greater than 1 pixel means that something is going wrong.
Using all the latest tools, such as bundle adjustment, calibration is more a matter of know-how and skills than a scientific task, even if it can be deeply involved in scientific applications. However decreasing the uncertainty would require an advanced investigation into marker detection (the existing tool is already rather sophisticated) as well as modeling small sensor defects.
Visit the Onera web site www.onera.fr to learn more about calibration.

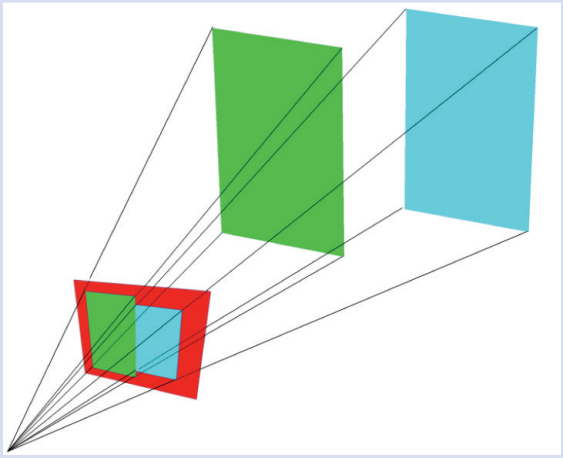

Figure B5 - 01 - The pinhole model.

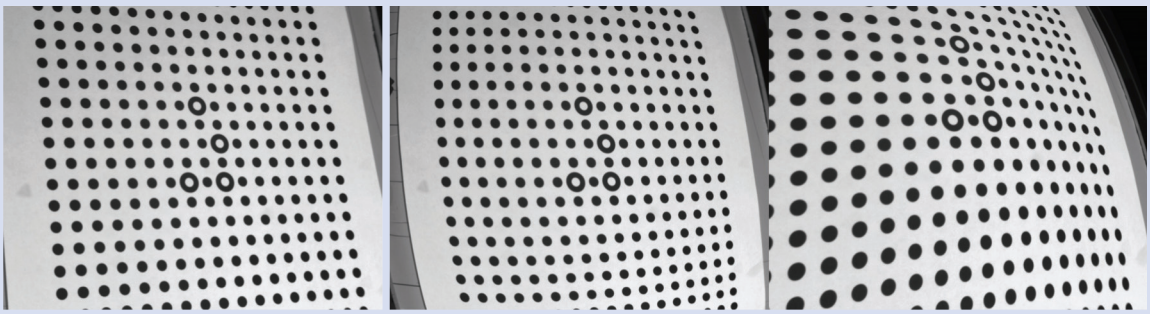

Figure B5 - 02 - The original image, enhanced cushion effect with K_1, enhanced lateral distortion with P_1 and P_2.

Model Deformation Measurement

Models used in wind tunnel testing are deformed by the aerodynamic loading. This may create a wing twist as large as 1°, while the acceptable uncertainty is lower than 0.1°! As a consequence there are differences between the tested shape and the shape used for computations. As a matter of fact, for a long time these differences were thought to be caused by wind tunnel wall interference or by sting effects, while the real reason, wing deformation, was ignored. The likely reason is that the deformation level was unknown and barely measurable because of the lack of an appropriate method. Indeed, it is only recently [23] that model deformation has been considered to be a major source of errors that must be measured for every test.

There are several methods but the only one that provides real time results is based on marker detection and stereovision which is very well known by the Computer Vision (CV) community. Markers are stuck on the model surface which is imaged with two cameras. Figure 11 shows two typical images as well as a marker. The angle between the two cameras is close to 45°. These cameras (usually 2,000 x 2,000 pixels) must have been calibrated previously (Box 5). The challenge for applications in large facilities is the size of the calibration body. It has to be stiff but must not be too heavy and then cannot be expected without defects. This is why the calibration method includes a tool (known as bundle adjustment by CV), which is used to compensate for shape defects.

The basic tool for stereovision is marker detection. The final uncertainty depends on it, which is why a fast and accurate marker detector has been developed. Its uncertainty is of 0.06 pixels, which provides a measurement uncertainty lower than 0.1mm for a full scale of 1m. The twist uncertainty is lower that 0.05°, even at the wing tip.

The 3D location of the marker is obtained using the stereovision principle which is simple: a marker in an image defines a viewing line and the real point is located at the intersection of the two lines. However, they never intersect exactly and there is a small error which is called the epipolar error. The average epipolar error is a good indicator for camera calibration quality. It can be lower than 0.1 pixels and it is considered to be acceptable for values lower than 0.5 pixels. Larger values mean that the cameras start to become uncalibrated, because of the relative displacement relative to each other.

The Onera MDM system [24] is monitored by the wind tunnel control system as a usual measurement tool. It can work at a frequency of 10Hz and is mostly limited by the frame rate. Figure 12 is an example of bending measurement along a wing.

Up to now, this system could be compared to industrial vision systems and is more of an engineering application than a scientific one. However recent developments are scientific matters. The first development is related to the effect of thick windows (several centimeters) or a change of medium (air/pressurized air) that makes the standard pinhole model not completely reliable. A second one is tracking small parts of the wing and moving the cameras to track them when the model moves. The cameras would become uncalibrated (only the external parameters) and may be recalibrated to minimize the epipolar error [25]. A real scientific challenge would be to assess the effects of air density changes on the MDM measurements. These effects are created by the pressure changes, especially through the shock waves.

The MDM method can be used for other applications than wind tunnel testing. It can be used for conventional shape measurement, for flight testing or for scientific applications that require knowledge of an object's shape with a non contact method. This would be the case for PIV or LDV measurements close to the model's surface.

Box 6 - Model Deformation Measurement: uncertainty

The standard measurement uncertainty is 0.1mm for 1m, and twist uncertainty of 0.05°

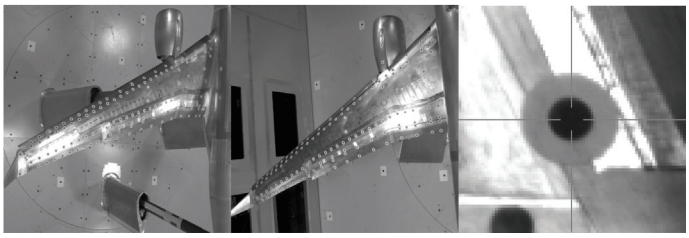

Figure 11 - The two images obtained by the two cameras and a marker.

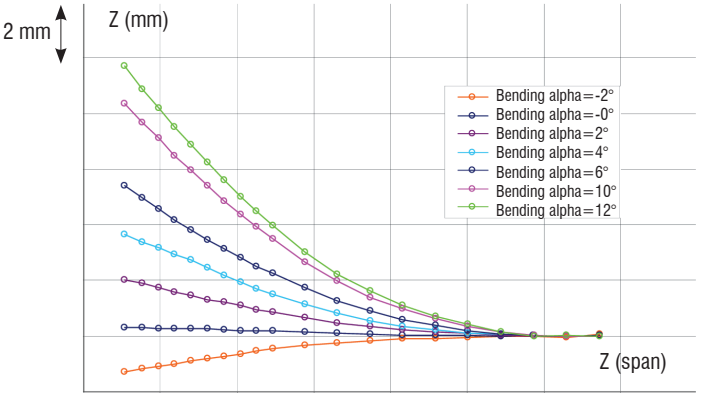

Figure 12 - A typical example of wing bending.

Wall Friction Measurement Using The Oil Droplet Technique

The drag of an airplane is due to pressure forces and friction forces, both contributions being nearly equal in cruise conditions. While surface pressure distribution is quite easy to measure, the direct measurement of wall friction is still a major challenge.

The friction force is generally determined indirectly, i.e. either from velocity measurements above the surface with an assumption for the velocity distribution or from analogies between friction and heat transfer. There are however several methods for directly determining the wall friction, some having been known for a long time, such as the use of surface balances or the oil film technique, and some being more recent, such as the use of micro-balances or flexible micro-cylinders.

The oil film technique [28] is based upon the analysis of the law governing the spreading of a very thin film of viscous fluid under the action of the wall friction. In the simple case of a uniform wall friction, except close to the ends where capillarity effects are important, the film grows linearly in space. Moreover, the film gets thinner as time increases and it spreads. The film height h is thus given by the relation

$$h(x,t) = \frac{\mu_0 x}{\tau_w t} \qquad (6)$$

where μ_0 is the oil viscosity, τ_w the wall friction, x the abscissa and t the time. The film thickness can be determined by an interferometric technique. When the film is illuminated by a monochromatic light, fringes can be observed, which can be related to the changes in the film thickness, as shown in figure 13. This figure also shows the spreading of the film and changes in film thickness leading to changes in the fringe spacing.

When the wall friction is not constant, the expression of the film thickness is very tricky, so that the determination of the friction from the film thickness is far from simple and accurate. Moreover, the film thickness can also increase or decrease longitudinally, which cannot be determined by the fringe pattern which only gives information about a change in thickness, not its sign.

Firstly, Onera [29] proposed the use of at least two illumination wavelengths, so that the comparison of the information given by the fringe patterns for the various wavelengths gives the sign of variation of the film thickness. Another strategy developed at Onera is to use only very little droplets, a few square millimeters in surface, so that the wall friction can be assumed constant. Moreover, an analysis of the interfringe process has given deep insight in the optical properties of the material the oil droplet has to be deposited on [30]; small Mylar stamps are good candidate. This analysis also shows that the method can work looking at the fringes from under a glass surface. Onera has applied this technique from low speed to transonic and supersonic speeds. Figures 14 and 15 provide examples of measurements, taken in the WALLTURB European project, respectively for a nearly zero pressure gradient flow and for a severe positive pressure gradient flow. The measured skin fiction is compared with micro-PIV results and with indirect determination from the Clauser plot. This approach is shown to be reliable and able to measure very low friction levels [30].

This technique can be used on any model, without special equipment, provided an optical access is possible.

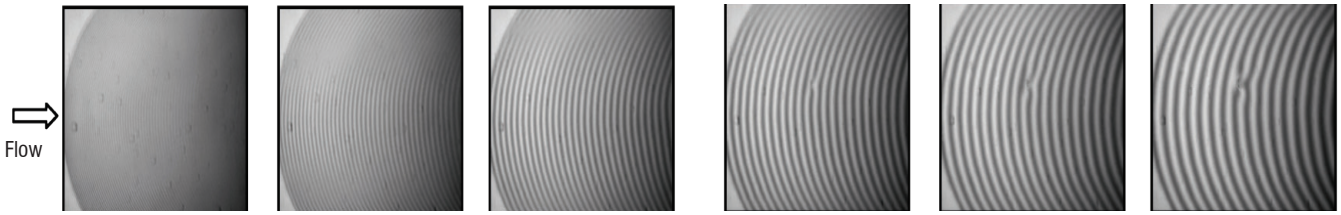

Figure 13 - Changes in the fringe pattern on the oil droplet with time.

Conclusion

The methods presented here are quite mature and are used routinely in wind tunnel testing. However significant progress has been made recently concerning the "details". For example, an accurate calibration of the camera used for PSP has significantly decreased the uncertainty of PSP. Uncertainty is the keyword: this is the right guide to selecting the required developments. From this point of view, may be the most important recent progress is this rigorous assessment of uncertainty that has nothing in common with the old rules of thumb. The research into PSP concerns its application for unsteady measurements, for which there are many requests. In the case of two other methods, *IrT* and MDM, the aims are quite similar: to reach the limits, which is a 3D data reduction for *IrT* and measuring small details for MDM. This would be the final step and highlights the lack of a full mapping measurement method for shear stress. This measurement is often considered to be as important as pressure, but there is still no practical method for large wind tunnels. There are some solutions, such as the oil droplet method presented in this article, but none of them are as developed as PSP, for example. This, then, is a major scientific challenge and we can expect to see more and more effort put into it in future ■

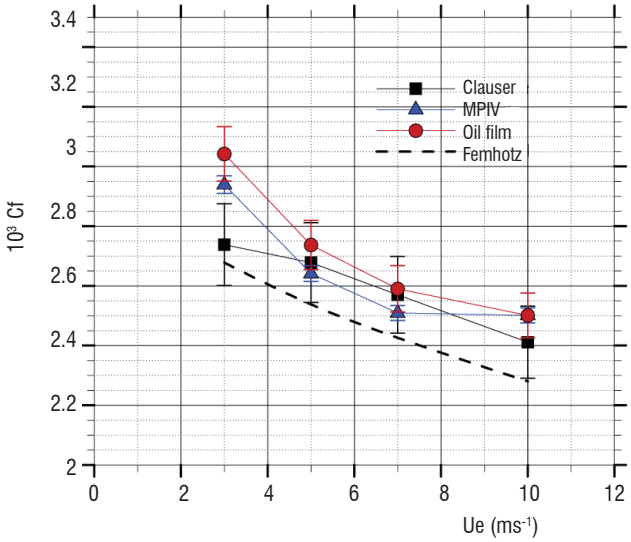

Figure 14 - Skin friction coefficient determination for nearly zero pressure gradient flow.

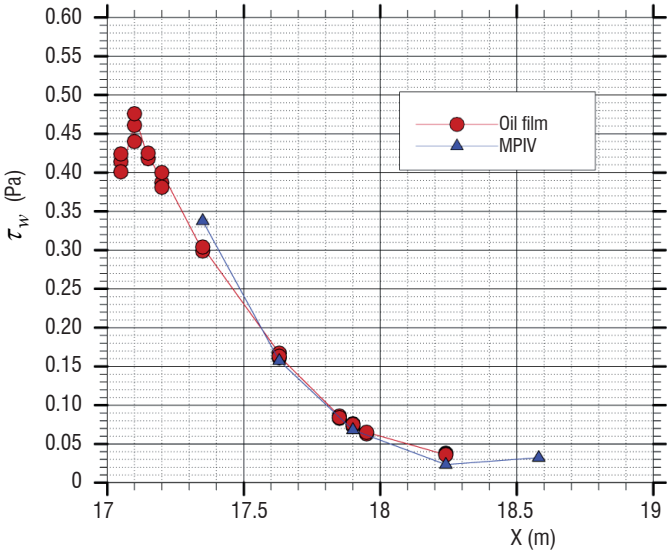

Figure 15 - Wall shear stress measurements for a strong adverse pressure gradient boundary layer.

References

[1] U. FEY - *Transition Detection by temperature Sensitive Paint at Cryogenic Temperatures in The European Transonic Windtunnel (ETW)*. 20th International Congress on Instrumentation in Aerospace Simulation Facilities, ICIASF 2003 Record, Göttingen, Germany, August 25 –29 , pp. 77 – 88, 2003.

[2] H.S. CARSLAW, J.C. JAEGER - *Conduction of Heat in Solids*. Oxford University Press, New-York, 1959.

[3] D.L. SHULTZ, T.V. JONES - *Heat Transfer Measurements in Short Duration Hypersonic Facilities.* AGARDograph 168, 1973.

[4] L. DE LUCA, G. M. CARLOMAGN, G. BURESTI - *Boundary Layer Diagnostics by Means of An Infrared Scanning Radiometer*. Experiments in fluids 1990, vol. 9, n° 3, pp. 121-128.

[5] Y. LE SANT, M. MARCHAND, P. MILLAN AND J. FONTAINE - *An Overview of Infrared Thermography Techniques Used in Large Wind Tunnels.* Aerospace Science and Technology, Vol. 6 Issue 5. Pages 355-366, September 2002.

[6] J. V. BECK, B. BLACKWELL, C. ST CLAIR - *Inverse Heat Conduction: Ill Posed Problems*, Wiley Interscience, New York, 1985.

[7] D. NORTHAUSER, P. MILLAN - *Resolution of Three-Dimensional Unsteady Inverse Problem by Sequential Method Using Parameter Reduction and Infrared Thermography Measurements.* Numerical Heat Transfer, Part. A, vol. 37, pp. 587-611, 2000.

[8] A. HOORNAERT, C. PELISSIER, Y. LE SANT, F. THIVET, P. MILLAN - *Rear Infrared Thermography in Heat Fluxes Determination on Hypersonic Vehicles*. 7th International Conference on Quantitative Infrared Thermography, QIRT 2004, von Karman Institute for Fluid Dynamics, 5-8 July 2004, Rhode-St-Genèse, Belgium

[9] T. LIU, J.P. SULLIVAN - *Pressure and Temperature Sensitive Paints.* Springer-Verlag, 2004.

[10] Y. LE SANT, M.-C. MÉRIENNE - *Surface Pressure Measurements by using Pressure-Sensitive Paints*. Aerospace Science and Technology, 9, 2005, pp. 285-299.

[11] Y. MEBARKI - *Pressure Sensitive Paints: from Laboratory to Wind Tunnel,* 22nd ICAS congress, Harrogate, England, 2000.

[12] J.H. BELL, E.T. SHAIRER, L.A. HAND, R.D. MEHTA - *Surface Pressure Measurements Using Luminescent Coatings, in: Annual Review of Fluid Mechanics,* Vol. 33, March 2001, pp. 155–206.

[13] C. KLEIN, R.H. ENGLER, U. HENNE, W. SACHS - *Application of Pressure Sensitive Paint for Determination of the Pressure Field and Calculation of the Forces and Moments of Models in Wind Tunnel.* Experiments in Fluids, 2005, Vol. 39, pp475-483.

[14]Y. MÉBARKI, *Peintures Sensibles à la Pression: Application en Soufflerie Aérodynamique*. Thesis presented at Lille 1 University, 1998.

[15] Y. LE SANT, A. DURAND, M.-C. MERIENNE - *Image Processing Tools Used for PSP and Model Deformation Measurements*. 35th AIAA Fluid Dynamics Conference and Exhibit, Toronto, Paper AIAA 2005-5007.

[16] R. ENGLER, M.-C. MERIENNE, K. KLEIN, Y, LE SANT - *Application of PSP in Low Speed Flows.* Aerospace Science and Technology, Vol. 6, N° 5, 2002.

[17] J. H. BELL - *Applications of Pressure Sensitive Paint to Testing at Very Low Speeds*. 42nd AIAA Aerospace Sciences Meeting and Exhibit, Reno, Nevada, Paper AIAA 2004-0878.
[18] M.C. MERIENNE, Y. LE SANT - *Reliable PSP Application and Data Processing at Low Speed Flow Conditions*. 24th AIAA Aerodynamic Measurement Technology and Ground Testing Conference, San Francisco, Paper AIAA 2006-3632.
[19] C. KLEIN, U. HENNE, W. SACHS, R.H. ENGLER, Y. EGAMI, V. ONDRUS, U. BEIFUSS, H. MAI - *Application of Pressure-Sensitive Paint for Determination of Dynamic Surface Pressures on a Rotating 65° Delta wing and an oscillating 2D profile in transonic flow*. ICIASF, Pacific Grove, 2007.
[20] H. SAKAUE, K. ASAI, J.P. SULLIVAN, Y. IIJIMA, T. KUNIMASU - *Anodized aluminum Pressure Sensitive Paint in a Cryogenic Wind Tunnel.* 45th Int. Instrumentation Symposium, Instrument Society of America, Albuquerque, NM, 1999.
[21] M. KAMEDA, T. TABEI, K. NAKAKITA, H. SAKAUE, K. ASAI - *Image Measurements of Unsteady Pressure Fluctuation by a Pressure-Sensitive Coating on Porous Anodized Aluminum*. Measurement Science an Technology, Vol. 16, 2005, pp. 2517-2524.
[22] M.C. MERIENNE, D. COPONET, J.M. LUYSSEN. - *Unsteady Pressure Field Investigation in a Nozzle by Using Anodized-Aluminum PSP Technique Under Supersonic Flow Conditions*. 26th AIAA Aerodynamic Measurement Technology and Ground Testing Conference, Seattle, Paper AIAA 2008-3946.
[23] T. LIU, R. RADEZTSKY, S. GARG, L. CATTAFESTA - A *Videogrammetric Model Deformation System and its Integration with Pressure Paint.* 37th AIAA Aerospace Sciences Meeting and Exhibit, AIAA 99-0568, January 11-14, 1999, Reno, NV.
[24] Y. LE SANT, A. MIGNOSI, G. TOURON, B. DELÉGLISE, G. BOURGUIGNON - *Model Deformation Measurement (MDM) at Onera.* 25th AIAA Applied Aerodynamics Conference, paper 2007-3817, Miami, FL, 25-28 June 2007.
[25] R. HARTLEY, A. ZISSERMAN - *Multiple View Geometry in Computer Vision*. Cambridge University Press, 2000.
[26] R. HARALICK, C.N. LEE, K. OTTENBERG, M. NÖLLE - *Review and Analysis of Solutions of the Three Points Perspective Pose Estimation Problem*. International Journal of Computer Vision, vol. 13, n°3, pp 331-356, 1994.
[27] R.Y. Tsai - *An Efficient and Accurate Camera Calibration Technique for 3D Machine Vision*. Proceedings of IEEE Conference on Computer Vision and Pattern Recognition, Miami Beach, FL, USA, 1986, pp. 364-374.
[28] L. H. TANNER, L. G. BLOWS - *A Study of the Motion of Oil Films on Surfaces in Air Flow, With Application to the Measurement of Skin-Friction.* Journal of Physics E, vol. 9, N° 3, 1976.
29] J. M. DESSE - *Oil-Film Interferometry Skin-Friction Measurement Under White Light.* AIAA Journal, Vol. 41, N° 12, pp. 268-2477, December 2003.
[30] G. PAILHAS, P. BARRICAU, Y. TOUVET, L. PERRET - *Friction Measurement in Zero and Adverse Pressure Gradient Boundary Layer Using Oil Film Interferometric Method.* Experiments in Fluids Volume 47, Issue 2 (2009), 195-207. (ONERA TPND 2009-141).

Acronyms

PSP (Pressure Sensitive Paint)
MDM (Model Deformation Measurement)
CARS (Coherent Antistokes Raman Spectroscopy)
IrT (Infrared Thermography)
TSP (Temperature Sensitive Paint)
AA-PSP (Anodized Aluminum - PSP)

AUTHORS

Yves Le Sant Researcher at Onera since 1983. His first studies concerned wall interferences and the development of an adaptive test section. Then he was involved in applying and developing many measurements methods, such as heat flux assessment, temperature and pressure sensitive paints and model deformation. His current activities are in the field of image processing applications, such as in Particle Image Velocimetry.

Bertrand Aupoix graduated from Supaero in 1976. He was awarded a PhD in 1979 and a "Thèse d'Etat" in 1987, both in the field of turbulence modeling. He is currently Research Director and head of the TMP, Turbulence, Modeling and Predictions, Research Unit at Onera Toulouse.

Philippe Barricau graduated in solid state physics from the «Institut National des Sciences Appliquées». Since 1998, he has worked in the field of instrumentation applied to aerodynamics. He has developed the optical arrangement of a Doppler Global Velocimetry system. He has also implemented the PIV technique in various Onera facilities and used the oil film technique to measure skin friction in various flows. Since 2008, he has been working on the development of sparkjet actuators for flow control applications.

Marie-Claire Mérienne joined Onera in 1980 as a technician in the composite materials department. She received her Engineering Diploma in Physical Measurements and Instrumentation from the Conservatoire National des Arts et Métiers, in 1989. Then, she joined the experimental Aerodynamics Department and, since 1994, she has been involved in the development of the PSP technique. Recently, a large part of her activity has been focused on unsteady applications.

Guy Pailhas, a research engineer at Onera is in charge of experimental studies in the Turbulence Modeling and Prediction Unit. A large part of his activity is devoted to the analysis of the structure of turbulent shear flows. Recently, he focused his efforts on skin friction measurement in complex flows by means of the interferometric oil film technique.

Philippe Reulet, Dipl. Ing. Dr., responsible of Aerothermics activity in C2A Research Unit, graduated in 1992 from the «Ecole Centrale Paris». In 1997, he received his Ph.D. in Fluid Mechanics and Energetics from «Ecole Nationale Supérieure de l'Aéronautique et de l'Espace». Since 1998, he has been working at Onera in the field of experimental and numerical thermal analysis.

Yann Touvet, graduated from the Institut Universitaire de Technologie in Toulouse. He is currently working as a technician at the Turbulence Modeling and Prediction Unit of the Aerodynamics and Energetics Modeling Department at Onera Toulouse.

C. Brossard, J.-C. Monnier,
P. Barricau, F.-X. Vandernoot,
Y. Le Sant, F. Champagnat,
G. Le Besnerais
(Onera)

E-mail: Christophe.Brossard@onera.fr

Principles and Applications of Particle Image Velocimetry

In this paper, the principles of two-component Particle Image Velocimetry (PIV) and stereoscopic PIV are first recalled. Recent improvements in the camera calibration procedure for stereoscopic PIV are highlighted. The advantages of the PIV technique are illustrated through different studies performed in Onera laboratories for non-reacting or reacting flows, and various issues raised by the nature of fluid, flow dynamics, spatial and temporal resolutions, as well as data utilization, are examined. Finally, recent advances in the technique, time-resolved PIV and tomographic PIV, as well as potential gains from novel processing and post-processing algorithms, are presented.

Introduction

Particle Image Velocimetry appeared 25 years ago and since then has become an essential measurement technique in fluid mechanics laboratories in both research institutes and industry. Papers related to PIV have represented approximately half of the total papers presented in the Lisbon International Symposia on Applications of Laser Techniques to Fluid Mechanics held since 2000 [1]. This success, boosted by the progress in laser technologies as well as electronic image recording, can be explained by the large quantity of information that can be recorded instantaneously and simultaneously, for a reasonable implementation effort, compared to other measurement techniques. It is also related to the development of several commercial systems that have made the technique easily available worldwide, for a very large variety of applications, ranging from microfluidic scales ($\sim$ a few hundred microns) to large fields ($\sim$ 1 m) in wind tunnels. This spectacular development has been largely supported through collaborative networks such as EUROPIV or PIV Challenge ([2-5]), set up to foster international cooperation and organize worldwide comparison of algorithm performances.

The purpose of this paper is not to provide a detailed course on PIV. We recommend that readers with that aim in mind consult the reference books in the field [6] or follow one of the high quality courses fully or partly dedicated to PIV, such as the ones proposed by the DLR (Deutsches Zentrum für Luft- und Raumfahrt, [7]), VKI (Von Karman Institute, [8]) or AFVL (Association Francophone de Vélocimétrie Laser, [9]). Rather, after a brief reminder of the principles of the technique, its high potential will be illustrated using some selected studies performed at Onera. We will then present the most significant directions of progress that this continuously evolving technique has followed recently.

Fundamentals of PIV

Principles of two-component PIV (2C-PIV)

Based upon the definition of velocity, i.e. the first derivative of position with respect to time, the technique consists in measuring the displacement of fluid (Δx) over a given time interval (Δt). The position of the fluid is imaged through the light scattered by liquid or solid particles illuminated by a laser light sheet. In most applications, such particles are not naturally present in the flow which, therefore, has to be seeded with tracer particles, assumed to be sufficiently small and light to move with local flow velocity. Figure 1 shows a typical standard two-component PIV (2C-PIV) setup. A plane within the flow is illuminated twice by means of two superimposed laser light sheets. The light scattered by the particles is recorded on two separate frames on a special cross-correlation CCD camera sensor. For evaluation, the digital PIV recording is divided in small areas called “interrogation windows”. The local 2C-displacement vector of the particle images between the two illuminations is determined for each interrogation window by means of a spatially statistical cross-correlation function, defined in Box 1. Given the time interval between the two laser pulses and the image magnification obtained from camera calibration, the projection of the local flow velocity vector onto the plane of the light sheet, attributed to the center of the interrogation window, can then be deduced. Neighboring interrogation windows can be partially overlapping in order to reduce the spacing between two vectors in the resulting vector grid. Typically, a 50% overlap is used, which doubles the number of vectors in each direction and thus quadruples the total number of vectors.

Figure 1 - Typical PIV setup

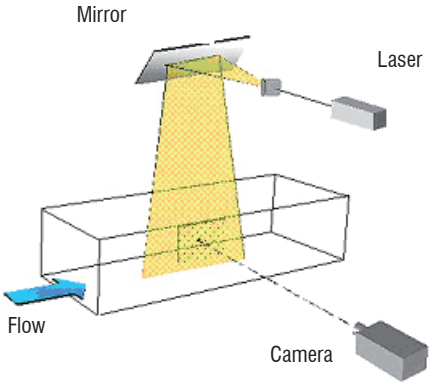

In standard PIV, though several types of laser sources are suitable, the most commonly used is the pulsed Neodyme-YAG (Nd:YAG) laser, doubled in frequency (532 nm). Pulse duration is typically 5-10 ns, and repetition rate is on the order of 10 Hz. Laser energy can reach 400 mJ/pulse. PIV systems are made of two independent laser cavities, but the laser beams should be superimposed in the near- and far-fields so that the two laser sheets illuminate the exact same area.
In most cameras, digital image recording is done via a CCD (Charge-Coupled Device) sensor which converts photons to an electric charge based on the photoelectric effect. The CCD sensor consists of many individual sensors that are arranged in a rectangular array. Each pixel has a size on the order of 10x10 μm. Their repetition rate in PIV double frame mode is on the order of 10 Hz.

Box 1 - Cross-correlation of a pair of two singly exposed recordings

Let $\boldsymbol{X}_i$ be the position vector and $\boldsymbol{x}_i$ the image position vector of particle i in the first exposure, respectively, related by $\boldsymbol{X}_i = \boldsymbol{x}_i / M$, where M is the magnification factor.

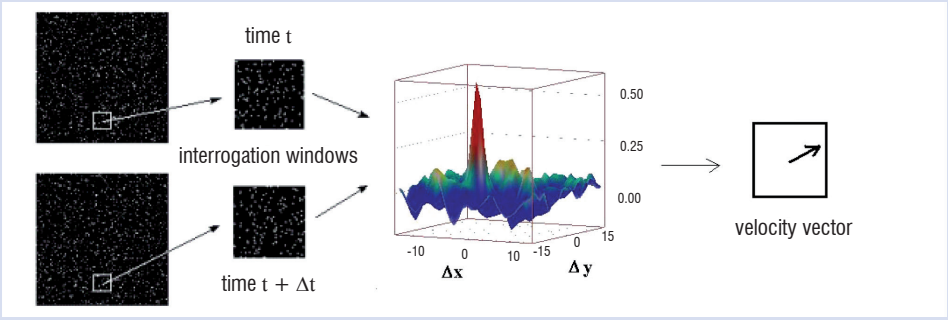

The image intensity field of the first exposure may be expressed by:

$$I(\boldsymbol{x}) = \sum_{i=1}^{N} V_0(\boldsymbol{X}_i)\,\tau(\boldsymbol{x} - \boldsymbol{x}_i)$$

where $V_0(\boldsymbol{X}_i)$ is the transfer function giving the light energy of the image of an individual particle i inside the interrogation volume and its conversion into an electronic signal, and $\tau(\boldsymbol{x})$ is the point spread function of the imaging lens, which is commonly considered to be Gaussian in both directions of the plane.
Assuming that between the two exposures all particles inside the interrogation window have moved with a same displacement vector $\boldsymbol{\Delta X}$, the image intensity field of the second exposure may be expressed by:

$$I'(\boldsymbol{x}) = \sum_{j=1}^{N} V_0'(\boldsymbol{X}_j + \boldsymbol{\Delta X})\,\tau(\boldsymbol{x} - \boldsymbol{x}_j - \boldsymbol{\delta x})$$

where $\boldsymbol{\delta x}$ is the particle image displacement, which can reasonably be approximated by $\boldsymbol{\Delta X} \cong \boldsymbol{\delta x}/M$
The cross-correlation of the two interrogation windows is defined as:
$R(\boldsymbol{s}) = \langle I(\boldsymbol{x})\, I(\boldsymbol{x}+\boldsymbol{s}) \rangle$, where $\boldsymbol{s}$ is the separation vector in the correlation plane, and $\langle\ \rangle$ is the spatial averaging operator over the interrogation window.
R can be decomposed into three parts:

$$R(\boldsymbol{s}) = R_C(\boldsymbol{s}) + R_F(\boldsymbol{s}) + R_D(\boldsymbol{s})$$

where R_C is the correlation of the mean image intensities, and R_F is the fluctuating noise component, both resulting from the $i \neq j$ terms. The displacement-correlation peak R_D represents the component of the cross-correlation function that corresponds to the correlation of images of particles from the first exposure with images of identical particles present in the second exposure ($i = j$ terms). This peak reaches a maximum for $\boldsymbol{s} = \boldsymbol{\delta x}$. Therefore, the determination of the location of this maximum yields $\boldsymbol{\delta x}$, thus $\boldsymbol{\Delta X}$. This location is commonly obtained through systematic exploration in the interrogation window by using Fast-Fourier Transform algorithms for computing cross-correlation. In the general case when all particles inside the interrogation window do not have uniform velocities (turbulence, velocity gradients), the location of the maximum yields the most probable displacement within the interrogation window. The value of $\boldsymbol{s}$ is determined with sub-pixel accuracy from correlation data interpolation, obtained through a fit of these data to some modeling function (e.g. Gaussian profile).

Although PIV relies on a simple principle, care should be taken in its practical implementation in order to obtain a reliable measurement and reduce uncertainties (see Box 2). The major asset of the PIV technique is its capacity to deliver a quantitative and instantaneous measurement of the velocity not only at one point, like Laser Doppler Velocimetry, but over a whole plane simultaneously: both visualization and quantification of the 2D flow structure become available. This, together with advances in electronic imaging and computing tools, explains its success over the past two decades.

Computation of the cross-correlation function

The computation of the cross-correlation function forms the heart of most commercially available data processing software and is commonly based on Fast-Fourier Transform (FFT) algorithms. Nowadays, most of them are iterative and based on an initial evaluation of velocity vectors using large interrogation windows, associated with a high SNR due to the large amount of particles taken into account in the statistics, but with poor spatial resolution. These velocity vectors and their gradients can then be used in the next step to adequately shift and deform the interrogation windows in each of the two exposures in order to reduce in-plane loss of correlated particle images. The interrogation window size is also progressively reduced to reach a final size of 32x32 or 16x16 pixels in practice, depending upon the density of particle images. Processing algorithms have been constantly developing with additional features aimed at enhancing signal-to-noise ratio (SNR) and removing spurious vectors. Recent efforts have mainly focused on improving spatial resolution by using adaptive interrogation windows parameters (size, shape, orientation). In particular, Theunissen et al. [13] reported, for cases when the interest lies in the mean flow field, an original scheme based upon statistical adaptivity, i.e. taking into account ensemble statistics over an entire image set.
Pre-processing is usually applied to raw images prior to cross-correlation computation in order to enhance contrast, reduce background noise (e.g. generated by particles deposits on windows), or homogenize particle intensities in order to avoid the bias of the cross-correlation function towards large particles. Following vector computation, post-processing operations are used to remove spurious vectors. This paper cannot cover all of the available declinations of PIV processing algorithms, so for specific detailed information the reader is invited to consult the references recommended in the introduction.

Principles of stereoscopic PIV (3C-PIV)

Adding a second camera to the setup, and arranging both cameras with different viewing axes, provides access to the otherwise unknown third component of the velocity vector, perpendicular to the laser light sheet and usually referred to as the out-of-plane component. This technique, known as stereoscopic PIV, can also reduce measurement uncertainty for the two in-plane components compared to a 2-C PIV setup, by accounting for the perspective projection caused by the displacement of the particles within the laser sheet thickness. Because what is measured when using only one camera is the projection of the local flow velocity vector onto one plane in the light sheet, the deduced displacement vector of the particle images results from two contributions: the in-plane displacement to be measured, but also the projection onto the plane of the out-of-plane component of velocity. In other words, the displacement of a particle animated with a purely out-of-plane velocity would be erroneously interpreted as a non-zero in-plane displacement. Note that this error is unrecoverable, although potentially significant in a highly three-dimensional flow.
By using two cameras with different viewing angles, projections of the velocity vector are obtained in two planes and in-plane can be differentiated from out-of-plane displacements. Whenever space and optical access constraints allow, the usual practice is to install the cameras so that the opening angle between them approaches 90°, as in this configuration the measurement uncertainty for the out-of-plane component is minimum and similar to the uncertainty for in-plane components. In order to obtain a satisfying image quality toward the edges of the field-of-view, the lens principal axis should be aligned with the principal viewing direction when the viewing direction is different than 90°. To make sure that the complete image is in focus, the plane of the CCD sensor should be tilted according to the Scheimpflug criterion, in which the image plane, lens plane and object plane intersect in a common line. In practice, this is performed by mounting the camera on a so-called Scheimpflug adaptor, which allows it to rotate with respect to the lens.
This optical arrangement has the side-effect of introducing a strong perspective distortion, which means that the magnification factor is no longer constant across the field-of-view. Therefore, the full spatial calibration matrix has to be determined for each camera. Quality of calibration is a key prerequisite for measurement reliability in stereoscopic PIV. The usual calibration procedure consists in taking several images of a flat calibration grid, placed first in the light sheet plane, then in a few other parallel planes. Based upon these images, a fit mapping function is computed for each camera and is used to dewarp raw particles images, i.e. to perform a back-projection in order to convert image coordinates into true “world” coordinates. Recent work performed at Onera has contributed to significant improvements

Box 2 - Measurement uncertainties in PIV

A reliable quantification of uncertainties is of prime importance for utilizing and interpreting experimental data, for PIV as much as for other metrological means. Even though numerous significant papers have already been published on this topic (e.g. see [10-11]), most of them focus on one particular cause of uncertainty, such as the presence of velocity gradients inside interrogation windows. Such studies are essential for selecting the best operating parameters to be implemented. However, the values they provide are not alone sufficient for a global estimation of an error bar for each computed velocity vector. In particular, many experimental studies indicate a displacement uncertainty of 0.05-0.1 pixel; however, this uncertainty refers only to the determination of the position of the correlation peak through sub-pixel interpolation of the correlation data [12]. As part of its quality management system processes, in 2007 Onera initiated an ambitious work program for a global and systematic assessment of measurement uncertainties in PIV. This work is still in progress, but preliminary results have already provided orders of magnitude for the relative significance of sources of uncertainty in the case of 2C-PIV: roughly 90% of the total uncertainty comes from the determination of the displacement in pixels from raw images; roughly 10% is due to camera calibration; compared to these causes, the uncertainty on the time interval between the two laser pulses is negligible.

in this field, leading to a new, more accurate and easier-to-use calibration procedure (Box 3). Finally, the calibration data obtained from the calibration grid can be further improved to account for the slight residual misalignment of the calibration plate with respect to the light sheet. The principle of this method, often referred to in the literature as "self-calibration", is to detect and correct small discrepancies between de-warped images recorded by the two cameras at the same time, which should contain identical information. Its implementation is based upon the computation of the cross-correlation function inside interrogation windows between these images (similarly to a standard PIV computation, see § "Computation of the cross-correlation function"), which results in disparity vectors being brought iteratively to a near-zero value.
Once calibration parameters have been determined for both cameras, two corresponding two-component vector fields can be computed from the de-warped images. The three velocity components can be deduced from these vector fields by solving a system of linear equations. The velocity vectors and their gradients can be utilized within an iterative scheme, in order to adequately shift and deform the interrogation windows in the next step.

Applications of PIV at Onera

Considering the large variety of experimental studies in its laboratories in which knowledge of the velocity field is of prime interest, the PIV technique has found at Onera a natural environment where it has been thoroughly implemented. Several research groups are equipped with PIV systems, in which data acquisition and processing software is either commercial or home-developed. The fields of application cover fundamental or applied aerodynamics and energetics for non-reacting or reacting flows. In this section, the advantages of the PIV technique are illustrated through different studies performed in Onera laboratories for non-reacting or reacting flows, and various issues raised by the nature of fluid, flow dynamics, spatial and temporal resolutions, as well as data utilization, are examined.

Multiple-camera PIV in aerial wakes of flying aircraft models

In the last decade, a lot of research on the wake vortex characterization and their alleviation has been carried out jointly by Onera and DLR [15, 16]. Vortex sheets shed off the wings of large aircraft, roll up, and organize into a multiple-vortex system in the aircraft's wake. Such large-scale coherent vortical structures usually are considerably stable and energetic. If an aircraft passes through this phenomenon during its takeoff or landing, it can dangerously affect its flight. As a consequence, regulatory separation distances have been imposed between the aircrafts. This safety regulation limits the airport's capacities. Therefore, the alleviation of wake vortices remains an important issue in commercial aviation.
The experimental campaign presented here was carried out in close cooperation with DLR. In the framework of the AWIATOR program, the main objectives of these tests were, on the one hand, to characterize the alleviation of wakes generated by different aircraft models and for various high lift configurations, and, on the other, to demonstrate the benefits of wing devices and span loading. This experimental campaign was carried out in the Onera B20 Free Flight Laboratory, shown in Figure 2. Compared to wind tunnels, in this facility the evolution of wakes can be studied from the near-field to far-field (from 0 to 100 wingspans). In this laboratory, non-motor-

Box 3 - Polynomial calibration versus pinhole calibration

The PIV community often uses polynomial calibration while the Computer Vision (CV) community only uses pinhole calibration (see Box 5 in [30]). Polynomial calibration can be implemented easily and usually gives a calibration error slightly lower than the pinhole method. However, it does not model the real world. During a 3-C PIV test, it was found that a significant error can be introduced by polynomial calibration [14]. This was demonstrated by comparing two overlapping PIV velocity fields, for which on the overlapped area the results were identical with pinhole calibration but different with polynomial calibration.
The reason is that the image velocities (see figure below) are equivalent to the spatial derivatives of the calibrations. The two following matrixes provide the 3-C velocity components from the two 2-C image velocity components. It can be seen that the differences are around 3% on the W component, the last line.

$$\begin{pmatrix} u \\ v \\ w \end{pmatrix}_{poly.} = \begin{bmatrix} 0.0726 & 0.0000 & 0.0743 & 0.0001 \\ -0.0006 & -0.0525 & 0.0008 & -0.0523 \\ -0.0718 & -0.0001 & 0.0714 & 0.0002 \end{bmatrix} \begin{pmatrix} u_1 \\ v_1 \\ u_2 \\ v_2 \end{pmatrix} \qquad \begin{pmatrix} u \\ v \\ w \end{pmatrix}_{pinhole} = \begin{bmatrix} 0.0736 & 0.0000 & 0.0734 & 0.0001 \\ 0.0000 & -0.0525 & 0.0001 & -0.0523 \\ -0.0742 & 0.0001 & 0.0739 & 0.0001 \end{bmatrix} \begin{pmatrix} u_1 \\ v_1 \\ u_2 \\ v_2 \end{pmatrix}$$

This surprising result can be explained: polynomial calibration uses too many parameters, which gives an improved calibration fit but creates unrealistic effects, enhanced by the derivative nature of the previous matrixes.
The pinhole model is then highly recommended and has just been extended at Onera in order to take into account thick window effect and even medium changes (air/glass/water) along the viewing direction. Combining it with the CV calibration method (see Box 5 in [30]), which does not require translation of the calibration body at known z-locations (Soloff's method), makes the pinhole model more reliable and easier to use than polynomial calibration.

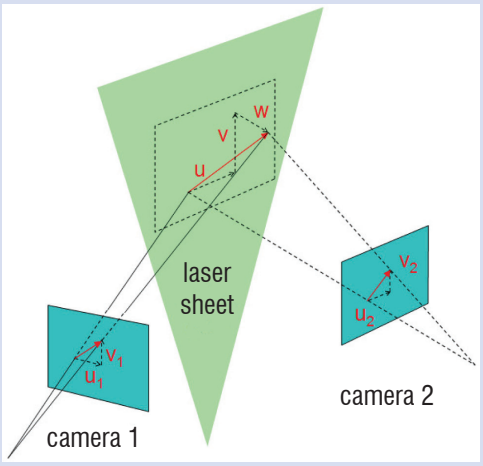

Projected velocities on the two cameras images

ized free flying scaled models are propelled by means of a pneumatic catapult via a trolley. Once launched, the model flies freely, i.e. without any wall or mounting interference, in a 90 m long, 20 m wide and 20 m high observation area. At the end of its free flight, it lands in a recovering system. An example of an aircraft model is shown in Figure 2 (wingspan b ≈ 2.1 m and weight M ≈ 23 kg).
In order to investigate a very large field of observation (≈ 1.7 m²) without loss of spatial resolution, 12 high-resolution PIV cameras were used for recording images (see Figure 2). This solution meant that the small eddies in the near field could be measured accurately as well as the coherent vortical structures in the far field. The arrangement of the cameras was chosen to provide a fine resolution in the center region of the wake and a coarser one in the outer regions. During flight, the wake of aircraft model has a descending movement. In order to follow this displacement, both light sheet optics and cameras were mounted on a traversable gantry so as to be translated simultaneously. The flow tracers were DEHS (synthetic oil) particles. The mean size of these droplets was around 1 micrometer. The flow was only seeded 15 minutes before each run of the model. The illumination of the particles in a very large field required a particularly high energy density in the light sheets. Therefore, two frequency-doubled, double-cavity high-energy (300 mJ/pulse) Nd:YAG lasers were used, instead of only one, in order to double the energy in each light sheet formed at the two exposures. Under these conditions, the energy was 600 mJ in each of the two light sheets. As the cameras are limited in repetition rate, PIV images were recorded at 3 Hz, which was the largest value compatible with the capabilities of all components of the PIV recording setup. During one launch, each camera recorded around 40 PIV pairs of images.
Figure 2 shows two examples of velocity fields. In the left one, obtained in the near-wake field, the two main vortices generated by the wing tip and the tail are clearly visible. However, a single coherent vortical structure is detected in the second velocity field, measured in the mid-wake field. Each velocity map includes around 60,000 instantaneous velocity vectors. Three axial vorticity fields are presented in Figure 2. The left one, obtained in the near-wake field of the model (X/b<2), reveals the formation of the different vortices mainly generated by the Horizontal Tail Plane (HTP), flaps (Inner/Board Co-rotating Vortex) and wing tips. After a few wingspans (extended near-wake field), the roll-up and merging of dominant vortices occurs, gradually leading to one main vortex. In the mid-wake field of the model (10 < X/b < 100), the axial vorticity map (on the right in Figure 2) shows the lingering resulting vortex which drifts downwards in the atmosphere. The full post-processing of the whole data sets was used not only to determine the trajectory, size and intensity of individual vortices detected (see figure 2, [17, 18]), to follow in detail the wake alleviation in all model configurations investigated, but also to evaluate quantitatively the efficiency of different wing devices tested.
During another campaign in the B20 Free-Flight Laboratory, PIV and LIDAR measurements were performed simultaneously. Comparisons between these two optical measurement techniques are presented in references [18] and [31].

Mean and turbulence measurements of wake vortices

In the wake vortices generation process, the initial roll-up vortex is due to the variation of the circulation distribution along the wingspan. Many experimental studies have been carried out on wake vortices, most of them in the near wake [19]. Jacquin and al. [20] investigated the extended near wake of a small scale A300 up to 9 wingspans downstream by the means of LDV and hotwire probe. The aim of the experimental study presented here was to characterize the vortex roll-up behind a generic wing equipped with an inboard flap deflected at different angles. A half-wing model of 75 mm chord, 150 mm half-span (aspect ratio equal to 4), rounded wingtip and NACA0012 wing section was tested in the Onera/Thales hydrodynamic tunnel (upstream velocity: 4 m.s^{-1}; Reynolds number based on chord: around 3 10^5) shown in Figure 3. The flap was 80% of the half-span large and 30% of the chord long. The flap angle could be set to 0° (clean case), 4°, 6° or 8°. The double-cavity pulsed laser, cameras and sheet optics of a stereoscopic PIV system were mounted on a traversable gantry in order to investigate several cross plane configurations, up to almost 9 wingspans downstream. The cameras were installed on both sides of the test section under a symmetrical configuration. The water flow was seeded with silver-coated hollow glass spheres (mean diameter: 10 microns). In this experiment, the presence of internal water prisms induced distortion effects on the recorded images. To correct these, an original and efficient solution was adopted: external water prisms were installed close to the windows.
For all angles of incidence investigated, the mean fields of the three velocity components, of the axial vorticity, and the six Reynolds stresses were successfully measured, as shown by the color maps represented in Figure 3. However, turbulence measurements carried out in a wind or a water tunnel are altered by a phenomenon called vortex wandering, which is a slow side-to-side movement of a vortex, probably due to a receptivity of the background turbulence of the facility. Devenport and al. [21] proposed a method to remove the wandering effects from hot wire measurements, in particular on the turbulence by high-pass filtering. PIV, which supplies instantaneous velocity fields, was used to develop an original and more objective procedure [22]. The vortex location was first detected in each instantaneous field based upon the so-called λ_2 criterion computed from the gradient tensor [23]. Assuming that the vortex has a solid motion, the average and standard deviation fields were then calculated after translating the instantaneous fields so that each instantaneous vortex center is at the same location. Taking vortex wandering into account leads to a dramatic correction of the turbulence levels in the vortex center, as shown by the plots of Root Mean Square (RMS) values in Figure 3, and explains why important peaks of turbulence are usually reported in the literature. This experiment demonstrated the great potential of the PIV technique for the qualification of wake vortices in the presence of the wandering phenomenon. Indeed, this optical diagnostic technique is the only one which is able to provide instantaneous velocity fields, required to correct this random effect encountered in aerodynamic or hydrodynamic facilities.

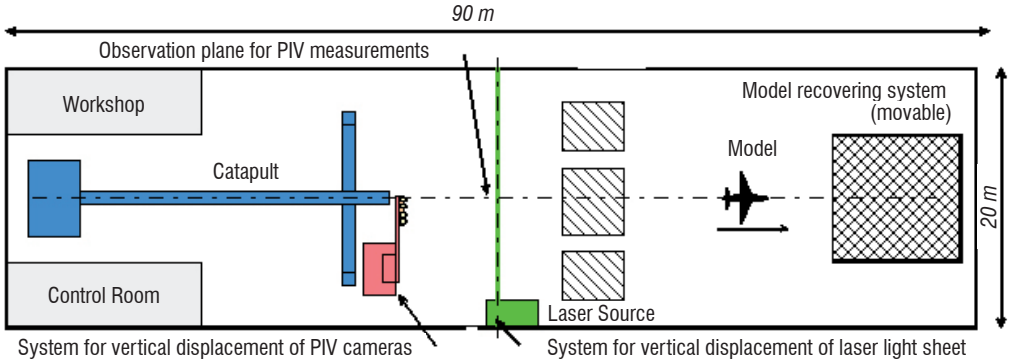

Schematic View of Onera B20 Free-Flight Facility and PIV setup

Large Transport Aircraft (LTA) Model

12 PIV cameras mounted on rails

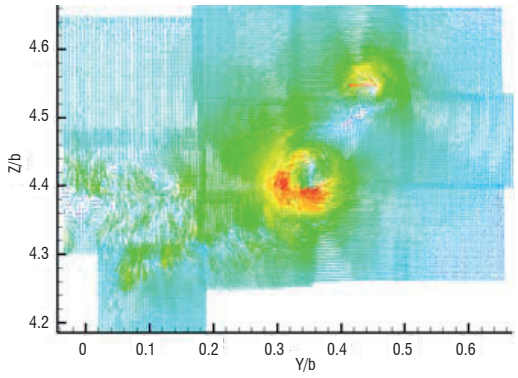

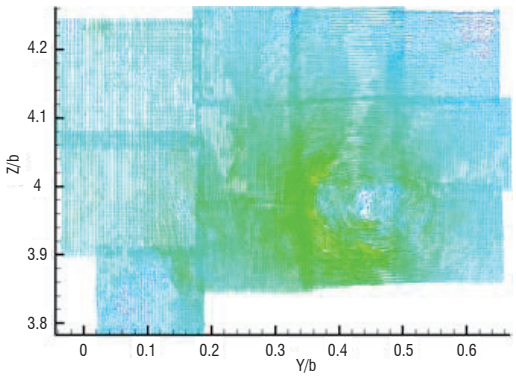

Velocity fields measured at longitudinal locations X/b= 1.3 and 30.4 - X: longitudinal distance downstream of the aircraft model, b: wingspan.

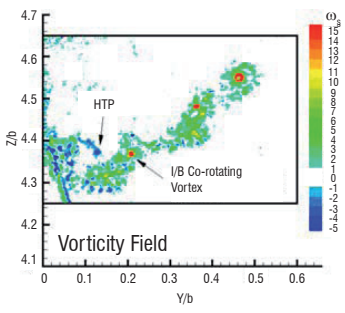

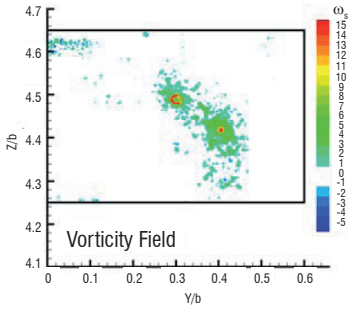

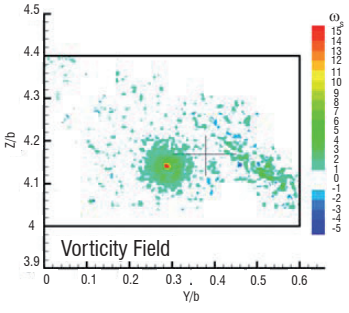

Axial vorticity fields at longitudinal locations X/b=1.3, 4.5 and 14.2 [18]

Figure 2 - Multiple-camera PIV in aerial wake of flying aircraft model

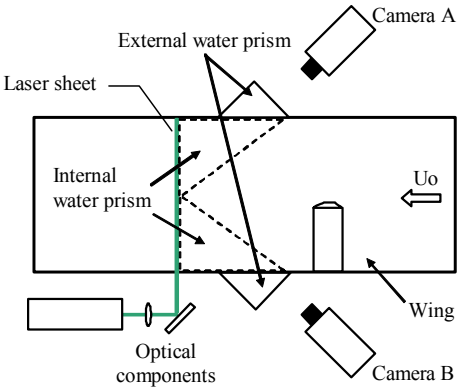

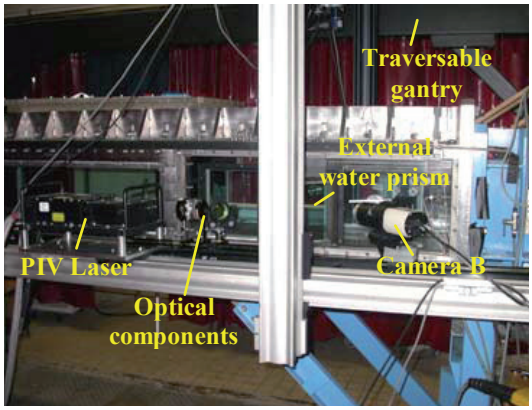

Implementation of the stereoscopic PIV technique in Onera hydrodynamic tunnel (top view and right side view)

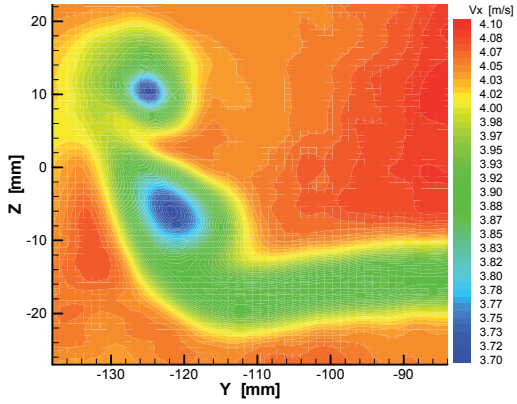

Axial velocity at X = 1.3b

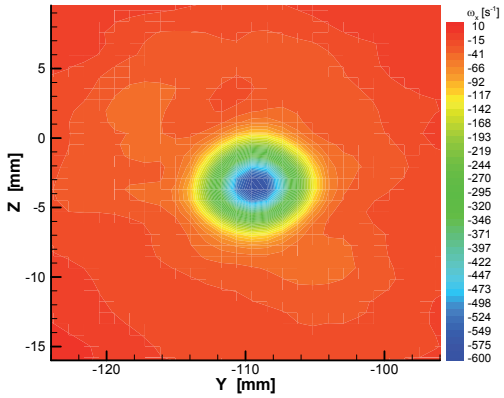

Axial vorticity at X = 3b

Mean fields in two cross planes. Angle of attack: 1.25°. Flap angle: 4°. X: distance downstream of the trailing edge; b: wingspan

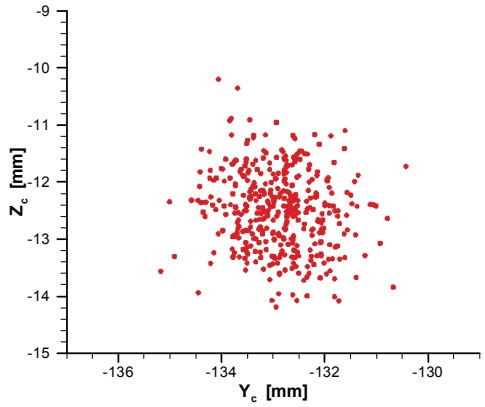

Instantaneous positions of the vortex center (400 samples)

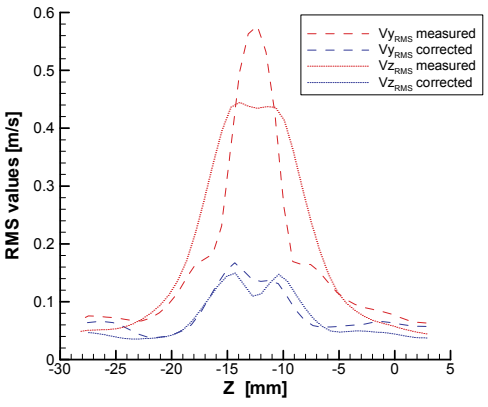

Effect of wandering correction on the transverse RMS values

Example of vortex wandering and effects of the correction. Angle of attack: 5°. Flap angle: 0°

Figure 3 - Mean and turbulence measurements of wake vortices

Thermo-acoustic flame instabilities in high turbulence flow

The purpose of this study [24] was to investigate low-frequency combustion instabilities in a model lean-premixed stepped combustor. Lean-premixed combustion has become one of the most promising means of meeting stringent environmental requirements for the reduction of NOx emissions produced by gas turbine engines. However, operating under lean premixed conditions often leads to the occurrence of undesirable combustion-driven pressure oscillations and intense heat release fluctuations that can severely damage the combustor or turbine hardware. The specific feature of this study, compared to most of research works published in the literature, was that it used high turbulence flow conditions representative of industrial combustors. Figure 4 shows a photograph of the methane/air flame anchored at the step in the combustion chamber, illuminated by one of the two superimposed vertical laser sheets used for PIV in the axial plane. Micronic solid magnesium oxide (MgO) seeding particles were used as flow tracers due to their capacity of withstanding the high-temperature reacting environment. For an unstable flame, the power spectrum of the unsteady pressure signals showed a dominant 154 dB peak at 66 Hz, corresponding to the ¼-longitudinal acoustic wave of the inlet duct. This raised the following question: how can a cyclic phenomenon at 66 Hz be studied using a standard PIV system with a repetition rate of less than 10 Hz? The usual answer is to phase-lock the PIV data acquisition with the signal from a high-frequency sensor, e.g. in our experiment the unsteady pressure trace. By using adequate time delays to trigger the PIV data acquisition with respect to the time reference from the pressure trace, the full cycle can be resolved. This procedure can be repeated at the PIV system repetition rate in order to perform a statistical analysis of all measured instantaneous vector fields. Though this method is frequently used, it requires the investigated cycle to be perfectly constant in frequency and amplitude, since lasers require a constant frequency trigger. This was not the case in our experiment, in which the pressure signals were highly modulated in frequency (in the range 55-80 Hz) and amplitude. Therefore, an alternative solution was adopted, which consisted in synchronizing the PIV acquisition with that of a digital high-speed (4,000 Hz) camera recording the chemiluminescence signal of the OH* radical, used as a natural tracer of the flame front. This method allowed to identify the instant, pressure, and flame location in the cycle to which each measured velocity field corresponded. An example of an instantaneous PIV velocity field synchronized with high-speed images, taken as the flame propagated downstream toward the step before re-attachment, is provided in Figure 4. This result showed that this motion was associated with the formation of a strong vortex behind the step and an induced acceleration near the step edge. The PIV technique was also particularly well-suited to this study due to its large dynamic range, which meant that it could measure the highly fluctuating levels of velocity (from 0 to 200 m/s) revealed during the experiments.

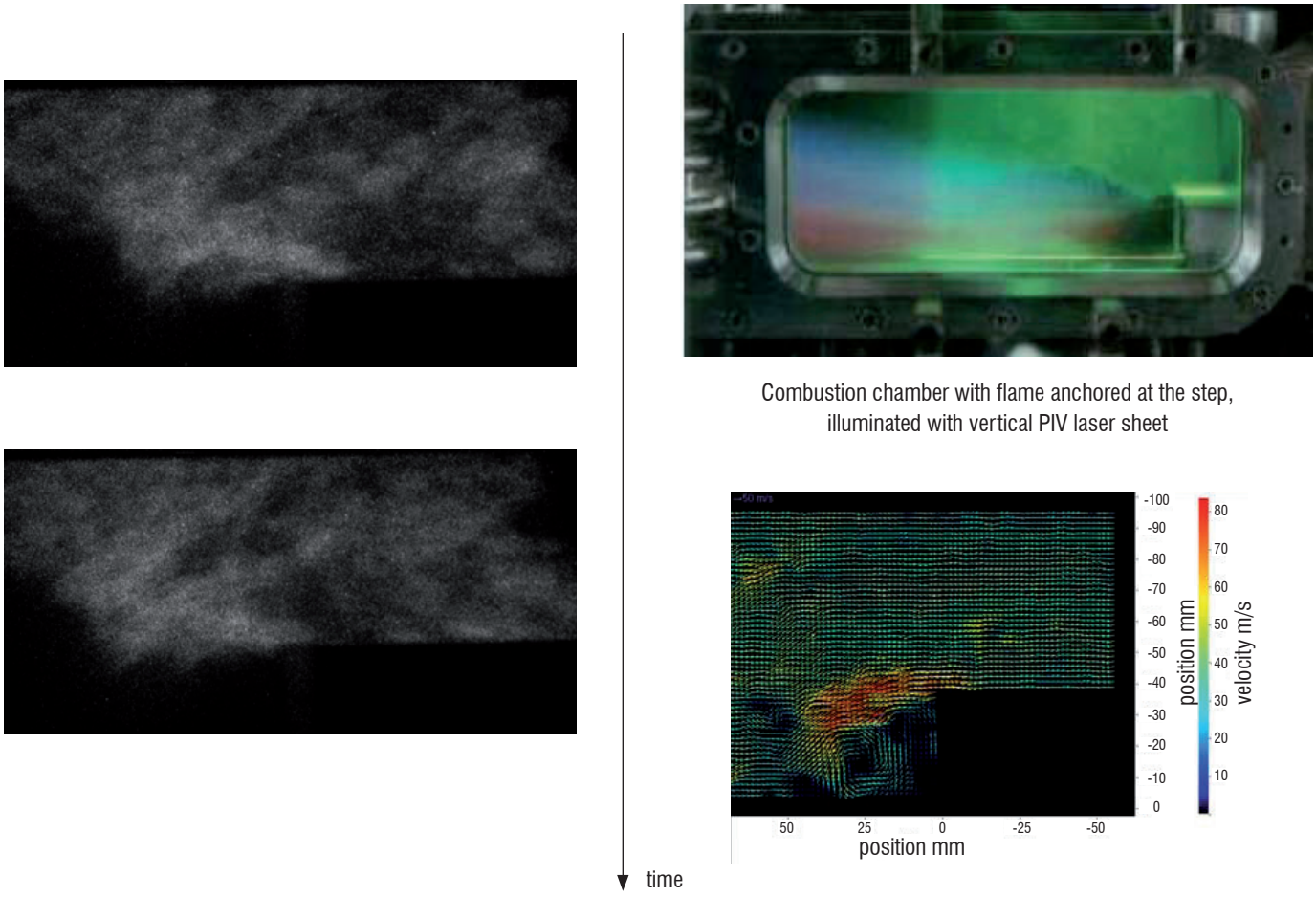

Combustion chamber with flame anchored at the step, illuminated with vertical PIV laser sheet

Instantaneous PIV velocity field synchronized with high-speed OH* chemiluminescence images at 4,000 Hz.

Figure 4 - Thermo-acoustic flame instabilities in high turbulence flow

Recent advances in PIV

Time-Resolved PIV

The technological limits of PIV have been pushed further into the distance by the still ongoing progress in laser technologies and electronic imaging systems. In particular, the new high repetition rate lasers and cameras available today have led to the development of time-resolved PIV (often referred to as TR-PIV in the literature). Some high-speed cameras available today, based on CMOS (Complementary Metal Oxide Semiconductors) sensors, can reach a repetition rate of more than 80 kHz (with a resolution reduced to 256x256 pixels), i.e. a PIV repetition rate of more than 40 kHz (2 images per PIV acquisition). The major drawback of these cameras with respect to standard PIV CCD cameras is a larger pixel size, slightly less than 20x20 μm, but this difference has been significantly decreased in recent camera models. TR-PIV systems are currently limited by laser energy: a few mJ/pulse at 10 kHz for a high-speed Nd:YLF laser, versus up to 400 mJ/pulse at tens of Hz for a Nd:YAG laser used in standard PIV (see Figure 1). In addition, high-speed laser pulse widths increase with repetition rate and range between 100 and 300 ns: this is much higher than the 5-10 ns pulse width of a Nd:YAG laser, and can be a severe limitation when investigating high-speed flows. Despite these drawbacks, the recent success of TR-PIV systems can be explained by the jump in time resolution from the Hertz to the kilohertz range that they provide. One particular PIV hardware system can also be used in a broad frequency range, typically from 1 to 10 kHz: as the product of repetition rate and energy per pulse stays roughly constant over the operating range, this offers some flexibility for finding the best compromise between energy and repetition rate based upon the experimental constraints. Technological progress is so fast that, according to some researchers [25], TR-PIV could replace standard PIV in a few years.Time-resolved PIV has opened the way to quantitative measurement of velocity fields for unsteady flows or transient phenomena, which is a requirement for validating computation codes [32,33]. Until now, the highest operating (i.e. with sufficient energy per pulse) repetition rates of high-speed lasers have been limited to 20 kHz, which is borderline for resolving the smallest time scales of turbulence in many practical flows: Laser Doppler Velocimetry (up to several tens of kHz repetition rate) is still the most suitable optical diagnostic technique for accessing such information. However, this could change in the very near future, as highest available repetition rates have kept increasing very fast recently.

Tomographic PIV

A natural development of the PIV technique has been its extension to the third dimension in space, i.e. from a 2D planar to a 3D volumetric technique. Several different 3D techniques now exist: holographic PIV, scanning PIV, dual plane PIV, 3D PTV (Particle Tracking Velocimetry), defocusing PIV and, more recently, tomographic PIV [26, 27]. This latter technique is a very powerful one, compared to the others, that offers the simultaneous advantages of being fully volumetric, truly instantaneous and based on fully digital data recording and analysis. It is based on an extension of the stereoscopic PIV concept by using the principle of tomographic volume reconstruction. The 3D light intensity field of the illuminated particles is reconstructed for each voxel (the 3D equivalent to a pixel) from the images of typically four cameras viewing from different angles, by using a tomographic reconstruction algorithm. The entire volume is kept in focus by using a relatively small lens aperture (typically f-numbers > 8) and applying the Scheimpflug condition (see § “Principles of stereoscopic PIV”). The particle displacement (hence velocity vector) within an interrogation volume is then obtained by the 3D cross-correlation of the reconstructed particle distributions at the two exposures. Combining TR-PIV hardware under a tomographic PIV arrangement leads to time-resolved tomographic PIV, which is used to obtain what ultimately most fluid mechanics researchers look for: a full sequence showing the time-resolved evolution of the three-component velocity vectors inside a volume. Reference [28] is a particularly good illustration of this technique’s potential. It enabled the researchers to carry out for the first time a topological investigation of the flow structures in a turbulent boundary layer, within a temporally and spatially highly resolved Lagrangian and Eulerian frame.

The MEMFIS research project at Onera

The importance of the PIV technique in many research labs and the current development of more advanced techniques, presented previously, can generate extremely large amounts of data, which raises the question of using the adequate numerical data processing. Compared to progress recently made in the experimental setting and acquisition devices, data processing in most commercial PIV systems still relies on window correlation techniques dating back from the 80’s, and seems rather cautious about recent developments in motion estimation techniques originating from the Computer Vision community. The MEMFIS project (which stands for “Methods for Movements and deFormations Estimations by Imaging and Stereoscopy”), initiated in 2007 by the Modeling and Information Processing Department at Onera, aims to spread these developments to Onera’s physicists both in the Fluid Mechanics and Energetic branch and in the Materials and Structures branch. MEMFIS promotes federative research in three main directions:

Algorithm

Study of fast and parallel techniques for flow field computation (multigrid, domain decomposition, etc.), to pave the way for massive dataset processing in TR-PIV and 3D tomographic PIV. Reference [34] presents recent work conducted at Onera on this subject.

Variational approaches for flow field estimation

Although many iterative refinements and post-processing are included in modern software to extend their use, window correlation methods are fundamentally based on the prior assumption that the flow field investigated is locally uniform. Such an assumption is necessary for increasing the signal-to-noise ratio, at the cost of a bias in the deduced velocity, which is a form of spatial regularization of the flow field estimation. Recently, new regularization principles based on variational approaches have been proposed, some of them dedicated to fluid dynamics [29]. These techniques, which are studied in the MEMFIS project, can be considered as an attempt to bridge the gap between experimental data processing and numerical simulation.

Post-processing and PIV data interpretation

Up to now, PIV data have been mostly used in terms of temporal statistics (average and fluctuations). Post-processing algorithms to

be developed in the frame of the MEMFIS research project open the way to an interpretation in terms of instantaneous flow structures, hence a more adequate comparison with newly developed LES-based (Large Eddy Simulation) computation codes [32].
Regarding the latter subject, a topic of interest to many applications is the detection of vortices in the flow field. Previouly (see § "Mean and turbulence measurements of wake vortices") was illustrated how a detection scheme can take the effects of wandering on turbulence measurements into account and correct them. Applied to time-resolved PIV data, algorithms dedicated to vortices detection should also allow the temporal tracking of these vortices.Therefore, the MEMFIS research project constitutes an excellent interface between the advances in PIV supported by new technologies on one side, and those in numerical simulations on the other side.

Conclusion

The very high potential of the PIV technique has been illustrated through some experimental studies performed at Onera. The examples presented show that this technique can provide detailed, qualitative and quantitative information on flow structure and turbulence, whether in the wake behind a wing or inside a combustion chamber. Progress in laser technologies and electronic imaging systems has brought new innovative and powerful improvements to the technique. Time-resolved PIV allows flow unsteadiness investigation. Tomographic PIV extends digital PIV from the planar to the volumetric domain. Novel processing algorithms developed at Onera in the framework of the MEMFIS research project are possible answers to a more efficient data processing and a better use of the vector fields obtained ■

References

[1] L. DAVID and P. GICQUEL - *Evolutions de la technique PIV à travers quelques conférences internationales de 2000 à aujourd'hui*. Congrès Francophone de Techniques Laser, CFTL 2006, Toulouse, France, September 19-22, 2006.
[2] M. STANISLAS, J. WESTERWEEL, J. KOMPENHANS - *Particle Image Velocimetry : Recent Improvements*. Proceedings of the EUROPIV2 workshop held in Zaragoza, Spain, March 31, April 1, 2003.
[3] M. STANISLAS, K. OKAMOTO, C.J. KÄHLER - *Main Results of the First International PIV Challenge*. Measurement Science and Technology, Vol. 14, pp. R63-R89, 2003.
[4] M. STANISLAS, K. OKAMOTO, C.J. KÄHLER, J. WESTERWEEL - *Main Results of the Second International PIV Challenge*. Exp. Fluids, Vol. 39, pp. 170-191, 2005.
[5] M. STANISLAS, K. OKAMOTO, C.J. KÄHLER, J. WESTERWEEL, F. SCARANO - *Main results of the Third International PIV Challenge*. Exp. Fluids, Vol. 45, pp. 27-71, 2008.
[6] M. RAFFEL, C. WILLERT, J. KOMPENHANS - *Particle Image Velocimetry – A practical Guide*. Springer-Verlag Berlin Heidelberg, 1998.
[7] DLR PIV Course - *Application of Particle Image Velocimetry* – Theory and Practice. http://pivcourse.dlr.de/
[8] VKI Lecture series, http://www.vki.ac.be/
[9] Ecole d'Automne de Vélocimétrie et Granulométrie Laser en Mécanique des Fluides, http://www.afvl.ensma.fr/
[10] B. LECORDIER, M. TRINITÉ - *Accuracy Assessment of Image Interpolation Schemes for PIV from Real Images of Particle*. 13th Int. Symp. on Applications of Laser Techniques to Fluid Mechanics, Lisbon, Portugal, June 26-29, 2006.
[11] J. WESTERWEEL - *On Velocity Gradients in PIV Interrogation*. Exp. Fluids, Vol. 44, pp. 831-842, 2008.
[12] J. WESTERWEEL - *Theoretical Analysis of the Measurement Precision in Particle Image Velocimetry*. Exp. Fluids, Vol. 29, N°7, pp. S3-S12, 2000.
[13] R. THEUNISSEN, F. SCARANO, M.L. RIETHMULLER - *Statistical Adaptivity in PIV Interrogation for Mean Flow Estimation*. 14th Int. Symp. on Applications of Laser Techniques to Fluid Mechanics, Lisbon, Portugal, 07 -10 July 2008.
[14] Y. LE SANT, B. GARDARIN, B. LECLAIRE, P. GEFFROY, D. SOULEVANT - *Polynomial Calibration vs Pinhole Calibration*. 7th Int. Symp. on Particle Image Velocimetry, Roma, Italy, September 2007.
[15] E. COUSTOLS, L. JACQUIN, F. MOENS, P. MOLTON - *Status of Onera Research on Wake Vortex in the Framework of National Activities and European Collaboration*. European Congress on Computational Methods in Applied Sciences and Engineering, ECCOMAS 2004 Conference, Jyväskylä, Finland, 24-28 July. P. Neittaanmäki, T. Rossi, S. Korotov, E. Oñate, J. Périaux, and D. Knörzer (Eds.).
[16] E. COUSTOLS, L. JACQUIN, G. SCHRAUF, 2006 - *Status of Wake Vortex Alleviation in the Framework of European Collaboration: Validation Attempts Using Tests and CFD Results*. European Conference on Computational Fluid Dynamics, ECCOMAS CFD 2006, P. Wesseling, E. Oñate, J. Périaux (Eds).
[17] C.F.V. CARMER, R. KONRATH, A. SCHRÖDER, J.-C. MONNIER - *Identification of vortex pairs in aircraft wakes from sectional velocity data* - Exp. Fluids, Vol. 44, pp. 367-380, 2008.
[18] E. COUSTOLS, A. DOLFI-BOUTEYRE, A. GILLIOT - *Developments of PIV and Lidar Measurements for Wake Vortex Tracking at the Onera B20 free-Flight Facility*. Aerospace 08, Testing – Design – Manufacturing, European Ground Testing Instrumentation Symposium, Munich, Germany, April 15-16, 2008.
[19] J. S. CHOW, G. G. ZILLIAC, P. BRADSHAW - *Mean and Turbulence Measurements in the Near Field of a Wingtip Vortex*. AIAA Journal, Vol. 35, N°. 10, October 1997.
[20] L. JACQUIN, E. COUSTOLS, P. GEOFFROY, S. BRUNET, G. PAILHAS - *Experimental Study of the Vortex Wake Behind a A300 Airbus Model.* Technical report N° RT 14/2496 DAFE/Y, April 1998.
[21] W. J. DEVENPORT, M. C. RIFE, S. I. LIAPIS, G. S. FOLLIN - *The Structure and Development of a Wing-Tip Vortex*. J. Fluid Mech., Vol. 312, pp. 67-106, 1996.
[22] F.-X. VANDERNOOT, P. BARRICAU, H. BEZARD, H.-C. BOISSON - *Mean and Turbulence Measurements of Wake Vortices*. 14th Int. Symp. on Applications of Laser Techniques to Fluid Mechanics, Lisbon, Portugal, 07 -10 July 2008.
[23] J. JEONG, F. HUSSAIN - *On the Identification of a Vortex*. J. Fluid Mech. Vol. 285, pp. 69-94, 1995.
[24] V. SABEL'NIKOV, C. BROSSARD, M. ORAIN, F. GRISCH, M. BARAT, A. RISTORI, P. GICQUEL - *Thermo-Acoustic Instabilities in a Backward-Facing Step Stabilized Lean-Premixed Flame in High Turbulence Flow*. 14th Int. Symp. on Applications of Laser Techniques to Fluid Mechanics, Lisbon, Portugal, 07 -10 July 2008.
[25] R. HAIN, C. J. KÄHLER - *Advanced Evaluation of Time-Resolved PIV Image Sequences*. 6th Int. Symp. on Particle Image Velocimetry, Pasadena, California, USA, September 21-23, 2005.
[26] G.E. ELSINGA, F. SCARANO, B. WIENEKE, B.W. VAN OUDHEUSDEN - *Tomographic Particle Image Velocimetry*. 6th Int. Symp. on Particle Image Velocimetry, Pasadena, California, USA, September 21-23, 2005.
[27] F. SCARANO - *Tomographie en PIV: nouveaux développements et perspectives en vélocimétrie tridimensionnelle résolue dans le temps*. Congrès Francophone de Techniques Laser, CFTL 2006, Toulouse, France, September 19-22, 2006.
[28] A. SCHRÖDER, R. GEISLER, K. STAACK, B. WIENEKE, G.E. ELSINGA, F. SCARANO, A. HENNING - *Lagrangian and Eulerian Views into a Turbulent Boundary Layer Flow Using Time-Resolved Tomographic PIV.* 14th Int. Symp. on Applications of Laser Techniques to Fluid Mechanics, Lisbon, Portugal, 07 -10 July 2008.

[29] P. RUHNAU, C. SCHNÖRR - Optical Stokes Flow Estimation: an Imaging-Based Control Approach. Experiments in Fluids, Vol. 42, pp. 61-78, 2007.
[30] Y. LE SANT, B. AUPOIX, P. BARRICAU, M-C. MÉRIENNE, G. PAILHAS, P. REULET, Y. TOUVET - *Surface Mapping Methods. Aerospace Lab n°1*, December 2009.
[31] A. DOLFI-BOUTEYRE, B. AUGERE, M. VALLA, D. GOULAR, D. FLEURY, G. CANAT, C. PLANCHAT, T. GAUDO, C. BESSON, A. GILLIOT, J-P CARIOU, O PETILON, J. LAWSON-DAKU, S. BROUSMICHE, S LUGAN, L. BRICTEUX, B . MACQ - Aircraft Wake Vortex Study and Characterisation with 1.5 μM Fiber Doppler Lidar. Aerospace Lab N°1, December 2009.
[32] L. JACQUIN - *Scales in Turbulent Motions.* Aerospace Lab N°1, December 2009.
[33] F. DUPOIRIEUX - *Optical Diagnostics Used at Onera to Characterize Turbulent Reactive Flows and to Validate Aero- and Rocket Engine Combustor Modelling*. Aerospace Lab N°1, December 2009.
[34] G. LE BESNERAIS, F. CHAMPAGNAT, A. PLYER, R. FEZZANI, B. LECLAIRE, Y. LESANT - *Advanced Processing Methods for Image-Based Displacement Field Measurement.* Aerospace Lab N°1, December 2009.

Acronyms

CCD (Charge-Coupled Device)
CMOS (Complementary Metal Oxide Semiconductors)
CV (Computer Vision)
DEHS (Di-Ethyl-Hexyl-Sebacate)
DLR (Deustches zentrum fur Luft und Raumfahrt)
FFT (Fast-Fourier Transform)
HTP (Horizontal Tail Plane)
LDV (Laser Doppler Velocimetry)
LES (Large Eddy Simulation)
LIDAR (Light Detection And Ranging)
MEMFIS (Methods for Movements and deFormations Estimations by Imaging and Stereoscopy)
PIV (Particle Image Velocimetry)
2C-PIV (Two-Component PIV)
3C-PIV (Three Component PIV)
PTV (Particle Tracking Velocimetry)
RMS (Root Mean Square)
SNR (Signal-to-Noise Ratio)
TR-PIV (Time-Resolved PIV)

AUTHORS

Christophe Brossard received his Engineering Degree in Energetics from the "Institut National des Sciences appliquées" in Rouen, France, in 1991. He received his Doctoral Degree in Energetics from the University of Rouen in 1995. From 1996 to 2001, he worked at the Propulsion Engineering Research Center at Pennsylvania State University, USA. Since 2001, he has worked as a research scientist in the Fundamental and Applied Energetics Department at Onera, focusing on flow field characterization, in non-reacting or reacting environments, using optical diagnostic techniques (PIV, LDV, Phase Doppler). His current research addresses the investigation of swirl-stabilized flames using time-resolved PIV, and the post-processing of PIV vector fields for flow structures motion detection.

Jean-Claude Monnier received his doctoral degree in Mechanics from the University of Lille. Since 1990, he has been employed as a research scientist in the Applied Aerodynamics Department at Onera. He started with experimental work on problems of Fundamental Fluid Mechanics. For eighteen years, he has worked mainly on the development of Particle Image Velocimetry (PIV) and its use for aerodynamic applications and in large industrial scale wind tunnels. Since 1998, he has managed the PIV team of the Applied Aerodynamics Department.

Philippe Barricau graduated in solid state physics from the "Institut National des Sciences Appliquées". Since 1998, he has worked in the field of instrumentation applied to aerodynamics. He has developed the optical arrangement of a Doppler Global Velocimetry system. He has also implemented the PIV technique in various Onera facilities and used the oil film technique to measure skin friction in various flows. Since 2008, he has been working on the development of sparkjet actuators for flow control applications.

François-Xavier Vandernoot graduated as an engineer at Supaero (French Engineering School of Aeronautics and Space) in 2005. He developed a research activity on wake vortices within the aerodynamics laboratory. His student work was rewarded with the Ludwig Prandtl prize. After a Master of Research in Fluid Dynamics at the University of Toulouse, rewarded by the Onera prize for the best Master of Research project in 2005, and a training period, he continued to work at Onera for three years as part of a PhD on the experimental and numerical study of wake vortices. In 2009, he joined Airbus in the wake vortex team and now works on evaluating the criticality of wake vortex encounters.

Yves Le Sant Researcher at Onera since 1983. His first studies concerned wall interferences and the development of an adaptive test section. Then he was involved in applying and developing many measurements methods, such as heat flux assessment, temperature and pressure sensitive paints and model deformation. His current activities are in the field of image processing applications, such as in Particle Image Velocimetry.

Frédéric Champagnat graduated from the Ecole Nationale Supérieure de Techniques Avancées in 1989 and received a Ph.D. degree in physics from the Université de Paris-Sud, Orsay, France, in 1993. From 1994 to 1995, he held a Postdoctoral position with the Biomedical Engineering Institute, Ecole Polytechnique, Montreal, QC, Canada. Since 1998, he has been with the Onera, Chatillon, France. His main interests are in the field of spatio-temporal processing for space or aerial image sequences, in particular registration, motion estimation, super-resolution, and detection.

Guy Le Besnerais graduated from the Ecole Nationale Supérieure de Techniques Avancées in 1989 and received a Ph.D. degree in physics from the Université de Paris-Sud, Orsay, France, in 1993. He joined Onera in 1994, where he is now a senior scientist in the Modeling and Information Processing Department. His work concerns inversion problems in imagery and computer vision, with an emphasis on embedded perception for autonomous aerial robots.

G. Le Besnerais, F. Champagnat,
A. Plyer, R. Fezzani,
B. Leclaire, Y. Le Sant
(Onera)

E-mail:
guy.le_besnerais@onera.fr

Advanced Processing Methods for Image-Based Displacement Field Measurement

We present recent developments in data processing for velocity field estimation and visualization originating from computer vision. We review the current paradigm of PIV data processing, based on window correlation, and the regularization or variational approach which is dominant in optical flow estimation. We propose a novel unifying framework via the optimization of a compound regularized criterion written in terms of a dense displacement (or velocity) field. The paper then focuses on algorithmic issues. A fast iterative window correlation method leading to a highly parallel algorithm termed FOLKI is described. Thanks to a GPU (Graphical Processing Unit) implementation, FOLKI reaches video rate for typical PIV data. Then we present more sophisticated solvers able to deal with the regularization term of the criterion, notably multigrid methods.
In our view, these two components form the foundation of a video rate velocity field visualization and interpretation toolbox which, together with recent advances in experimental apparatus and numerical simulation, opens the way to a major development in experimental fluid science.

Introduction

Photometry and photogrammetry are the two main image-based methods for measuring physical quantities. In photometry, the parameter investigated is a function of the intensity level: an example is the measurement of pressure on the surface of an object in a wind tunnel by means of Pressure Sensitive Paint (PSP). In photogrammetry, we are interested in the shape of some image patterns or in their apparent motion from one image to the other so as to measure geometric quantities such as distance, velocity, strain, etc.; classical examples are Model Deformation Measurement (MDM) and Particle Image Velocimetry (PIV) (see the other contributions on these techniques in this issue).

This paper looks at photogrammetry, and focuses on the measurement (or estimation) of displacement fields from image sequences. Estimation problems like these occur in the experimental study of fluid dynamics via dedicated imaging techniques such as Laser Tomoscopy and PIV and also in experimental characterization of strain on solids. These techniques, which are related to the domain of image motion or optical flow estimation in computer vision, are the subject of Onera's research project MEMFIS which associates computer vision specialists with physicists from fluid mechanics and materials science.

Following on seminal work dating back from the 80's [1, 2], motion estimation in computer vision is now rapidly developing again under three main driving forces: (i) the renewal of the methodological framework – notably physically sound regularization models tailored for fluid dynamic, see § "Regularisation framework for displacement field estimation"; (ii) assimilation of the applied mathematics corpus into the estimation algorithm (i.e. multi-grid methods [3], sub-domain decomposition, etc.); (iii) technological advances in generic computing hardware, notably the development of one-chip massively parallel architectures, such as multi-core CPUs and GPUs.

These recent developments are still widely ignored in the PIV community. This paper is one of a series of recent initiatives that the computer vision community has taken in the field of PIV [4, 5]. Contrarily to most of these works it emphasizes the points (ii) and (iii), i.e. algorithm and architecture for fast computation of the displacement field. Indeed, we believe that computational efficiency is the key to the spread of methodological advances on fluid displacement estimation and interpretation within the PIV community, for two main reasons:

1. advances in experimental PIV (Time Resolved PIV, 3D tomographic PIV) yield a huge data flow to be processed;
2. advanced processing methods usually come up with more tuning parameters, whose influence is often more difficult to predict, so their use requires a high level of interaction with the user.

The rest of the paper is divided in three parts: the firt one formulates displacement field estimation within a general regularization framework and presents the main algorithmic issues, the second one focuses on fast window-based estimation algorithms, then we briefly presents algorithmic trends for solving the large non linear systems yielded by regularized approaches. To conclude remarks and prospects are gathered together.

A regularization framework for displacement field estimation

PIV and interrogation windows

Fundamentally, in PIV or in other fields where image velocity is required, such as video coding or optical flow estimation in computer vision, the problem at hand is to estimate a displacement field $d(x)$ from two images $I(x, t_1)$ and $I(x, t_2)$ – velocity is derived from the time interval $t_2 - t_1$ between images. At this point, most authors in PIV introduce the notion of an "interrogation window" (IW), i.e. a square area containing a certain number of particles (say 10) that form some random pattern that can be detected and localized in the next image. This search leads to a displacement vector which is attributed to the center of the interrogation window. The size of the interrogation window is the main parameter of this approach: it defines the resolution of the result, i.e. the spatial sampling of the estimated displacement fields (typically half the IW size). Moreover, the window size tunes the "bias versus variance" trade-off of the estimation process. Larger windows lead to smoother estimated fields. The variance of the estimation error is lowered but so are small-scale motions, which means a bias toward the constant displacement field. There are of course several developments in modern PIV software that improve on this trade-off: image preprocessing, iterative window refinement, vector field post-processing, etc. The concept of an interrogation window still influences and, as we will try to demonstrate here, essentially limits the development of innovative PIV processing.

Modern optical flow and regularization

Modern optical flow estimation starts from a more abstract problem: if $I(x,t)$ is the image intensity at position x and time t and assuming that the recorded images correspond to time instants t_1 and t_2, the problem can be expressed as the search for a displacement field $d(x)$ which satisfies the so-called image registration condition

$$I(x,t_1) = I(x + d(x), t_2), \quad \forall x \tag{1}$$

In practice, this condition is relaxed by searching the peak of the cross-correlation or by minimizing the least-square criterion

$$\sum_x \left(I(x,t_1) - I(x + d(x), t_2) \right)^2 \tag{1b}$$

see box 1. This image registration problem is in general indeterminate: very different and often "non-physical" displacement fields lead to a low criterion. Indeterminacy stems from two facts: (i) being a scalar equation of a 2D unknown vector, the registration condition clearly yields less than half the number of equations that would be necessary; (ii) moreover, the recorded images are blurred, noisy and sampled versions of the image intensity, which means that only an approximation of the registration criterion (1b) is computable.

Box 1 - Optical flow and optical flow

The term "optical flow" has various meanings depending on the domain and context. In the PIV community, optical flow is often associated with the work of Quénot et al. [25]. This is an unfortunate confusion, because [25] describes a particular technique based on window correlation and dynamic programming, two elements which depart notably from the vast majority of optical flow estimation methods in computer vision. A much more "main-stream" application of optical flow to PIV can be found in [4].

Optical flow is also often associated with a first order expansion of the registration condition (1) for small motion d and time interval $dt = t_2 - t_1$:

$$\frac{\partial I}{\partial t} + (\nabla I)^t \, d = 0 \tag{I.1}$$

This so-called "optical flow constraint" (OFC) is central to historical references on optical flow such as the work of K.B. Horn and B. Schunck [1], and is still used in several recent references such as [10]. However, OFC is valid only for very small displacements and since the end of the 90's, many authors have proposed that the more general condition (1) should be considered to deal with large displacements. The expression "modern optical flow" which is used in the text refers to this large displacement context which is, in our opinion, the right framework for PIV processing.

Let us emphasize that the main difference between (I.1) and (1) is that the latter is non linear with respect to the displacement field. To deal with the non linearity, the estimated field is iteratively refined, by means of a first order development of (1) around a previous estimate d_0. Writing $d = d_0 + \delta d$, the flow increment satisfies a first-order condition which is similar to the OFC constraint:

$$I(x + d_0(x), t_2) - I(x, t_1) + (\nabla I(x + d_0(x), t_2))^t \, \delta d = 0 \tag{I.2}$$

Hence classical optical flow approaches based on the OFC often appear inside the iterative process of modern "large displacement" optical flow estimation.

Finally, we should discuss implementation issues, related to the fact that the images are recorded on a square grid of pixels positions. Assuming, without loss of generality, that the sampling step is 1, equation (I.2) is written for discrete positions m, associated with pixels of image $I(m, t_1)$. However, (I.2) also includes values of image $I(m, t_2)$ for real positions such as $m + d_0(m)$ which are shifted by the initial displacement field d_0. The resulting image $m \rightarrow I(m + d_0(m), t_2)$ is a warped version of $I(m, t_2)$. In image processing, warping an image $I(m, t_2)$ consists in interpolating its values on real warped positions by means of a spatial interpolation, using for instance a kernel-based interpolation such as

$$\tilde{I}(x,t) = \sum_m \gamma(x - m) I(m,t) \tag{I.3}$$

This interpolated image is also used to define the spatial gradient values required in (I.2).

The classical answer to such ill-posed problems is regularization [6]. It consists of complementing the data with prior information on the investigated object, here the displacement field. In the line of the works of Philips-Twomey-Thykonov in the 60-70's (see references in Chapter 1-2 in [6]), this information is often expressed as a constraint on some derivative functional of the displacement field $f(d)$. For optical flow estimation, a popular choice is the Horn and Schunck regularizing functional [1]:

$$f(d) = \|\nabla d_u\|^2 + \|\nabla d_v\|^2, \quad for \quad d = [d_u, d_v] \tag{2}$$

The estimated displacement field is then defined as the minimizer of a regularized criterion such as:

$$J(d) = \int \psi\left((I(x,t_1) - I(x+d(x),t_2))^2\right)dx + \lambda \int \Phi\left(f(d)\right)dx \tag{3}$$

where ψ and Φ are potential functions, and λ is the regularization parameter. The simplest choice is the quadratic penalization, associated to trivial potentials $\psi(s^2) = \Phi(s^2) = s^2$. Such approaches are often termed "variational optical flow estimation" in recent papers such as [4, 7]

Qualitative comparison on a real PIV dataset

Box 2 presents a comparison of estimated displacement fields on the central (512 x 512) part of images 25-26 of the PIV Package3 dataset of the European interdisciplinary FLUID project [5]. This package is made of experimental PIV images of a slightly turbulent air flow seeded with small water droplets: see one frame in figure B2 - 01.
The left part of figure B2 - 02 shows the estimated displacement field using a window-based method. It is derived from the dense window-based algorithm FOLKI, which is the topic of Section 3. Except for the density of the estimated field (one vector per pixel), this result is a typical output of current PIV software. On the right is the result of the minimization of regularized criterion (3) with regularizing functional (2). In other words, this variational optical flow estimate does not use any interrogation window; the goodness-to-fit term is simply a pixel-wise registration criterion. As can be seen, despite their very different rationales both approaches give similar results with this example.
Finally, figure B2 - 03 presents several results for varying parameters. The four fields on the top line are estimated using the window-based method with a Gaussian weight function of standard deviation 4, 6, 12 and 26 from left to right. The four fields on the bottom line are derived from the minimization of (3) with regularizing functional (2) and four different choices of the regularization parameter ($\lambda =$ 100, 1000, 1.10^4, 3.10^4, from left to right). Except for the two estimates on the left, which exhibit large errors, all other reconstructions appear correct. Looking at the various degrees of smoothness of the estimates, it should be clear to the reader that the regularization parameter in (3) plays a role similar to the window size in the aforementioned "bias vs. variance" trade-off: the higher λ, the smoother the solution.
The window-based approach then appears as a form of spatial regularization, which assumes that the motion field is constant at the scale of the interrogation window. As always, this regularization principle is only approximately true – actually it is absolutely wrong near regions of high velocity gradient, such as a vortex center or other discontinuities. Note, however, that the Horn and Schunck functional (2) is not particularly well suited to fluid dynamics: it has been noted, for instance in [8], that it leads to underestimation of the velocity near a vortex.

A unifying framework

As already noted by [4], the real advantage of the optical flow approach is its versatility. Contrarily to window-based approaches which all rely on the same regularization principle, modern optical flow techniques use various regularizing functionals f and various potentials ψ and Φ, which opens the way to completely different estimators [7] and in particular to techniques tailored for the particular situations of fluid dynamics [8,9,10,22,24].
In our view, regularization appears here as the expected interface between experimental and numerical studies, because choosing the right regularization tool is essentially a matter of modeling the phenomenon being studied. However, we will not discuss further the design of such regularization tools, and turn toward the essential problem of the computing the estimates. In order to do so, let us introduce a generalized version of (3), where the registration criterion includes a local window. Defining the weighted average of squared intensity differences

$$D(d,x) = \int w_\rho(x-y)\left(I(y,t_1) - I(y+d,t_2)\right)^2 dy, \quad \forall (x,d) \tag{4}$$

using the normalized and separable (i.e. isotropic) Gaussian kernel w_ρ of standard deviation ρ, this unifying regularized criterion is written:

$$J(d(\cdot)) = \int \psi\left(D(d(x),x)\right)dx + \lambda \int \varphi\left(f(d;I)\right)dx \tag{5}$$

Convolution of the squared intensity difference with a Gaussian kernel introduces a spatial integration of the registration criterion over the essential support of w_ρ. Such a criterion is a generalization of the CLG approach of Bruhn *et al*. [3] to the large displacement context. It unifies a window-based approach (ρ typically around 16 pixels and $\lambda = 0$) and a regularized criterion like (3) ($\rho \to 0$ and $\lambda > 0$). Note also that the regularization functional f in (5) depends on the image intensity I: indeed, some authors use the local image gradient to tune the regularization (it is called "image driven regularization" in [7]).

In the sequel we focus on numerical methods for fast optimization of criterion J of (5) with respect to the dense vector field d for various values of ρ and λ. Next section will discuss the optimization in the case $\lambda = 0$, and the final part of the article will discuss current approaches for the general case.

Window-based estimation of dense velocity fields at video rate

Introduction

In this section, we consider the optimization of (5) for $\lambda = 0$. As there is no longer a regularization term in this case, the optimization boils down to a separable problem where each vector of the field is sought in order to minimize a local registration criterion, spatially integrated on a local window whose extension is given by the shape of the weight function w_ρ. This approach belongs to the paradigm of window-based methods that underlies commercial PIV software and has been reviewed in previously. The main difference lies in the optimization process. The proposed iterative process, described in the following section and box 3, allows for fast computation of a dense field, whereas FFT-based PIV software yields under sampled vector fields, typically by a factor of 16 on each dimension (considering for instance an interrogation window size of 32*32 pixels with 50% overlap between adjacent windows, which can be a standard setting in PIV campaigns).

Box 2 - Estimation with window-based and variational methods on real PIV data

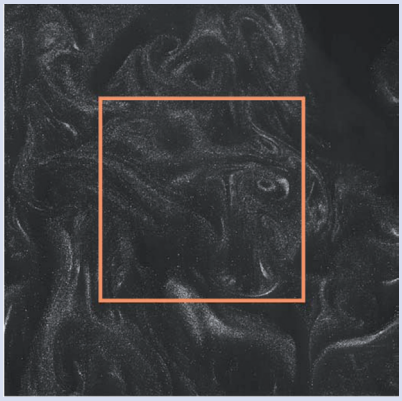

Figure B2 - 01. One image of the dataset “Package3” from the FLUID project [5]: experimental PIV on a slightly turbulent air flow seeded with small water droplets. Only the central part (512 x 512 orange square) of the motion field has been computed in the sequel.

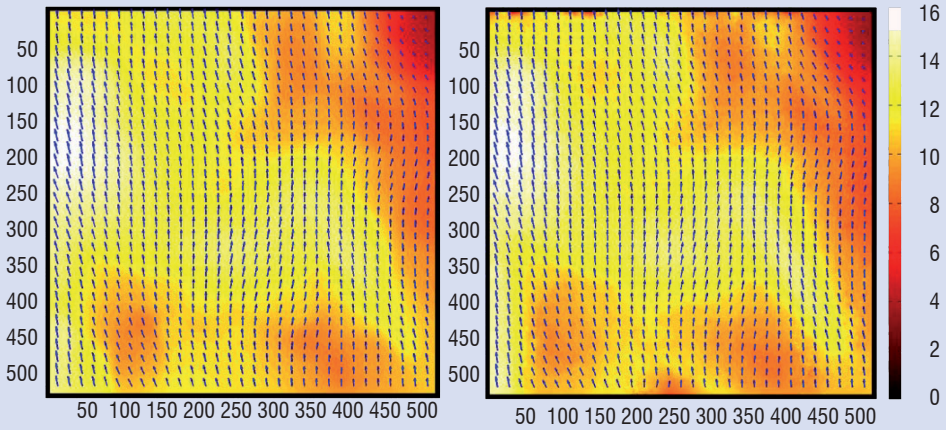

Figure B2 - 02. Results of displacement field estimation for two images of the dataset “Package3” from the FLUID project [5]. Norm of the field in color (see color map) Left: window-based dense approach (algorithm FOLKI, see Section 3) with a Gaussian window of standard deviation 12. Right: variational approach, estimation obtained by minimization of criterion (3) with Horn and Schunck’s regularizing functional (2) and a regularization parameter $\lambda = 1000$. Note the similarity between both methods, despite their different rationale.

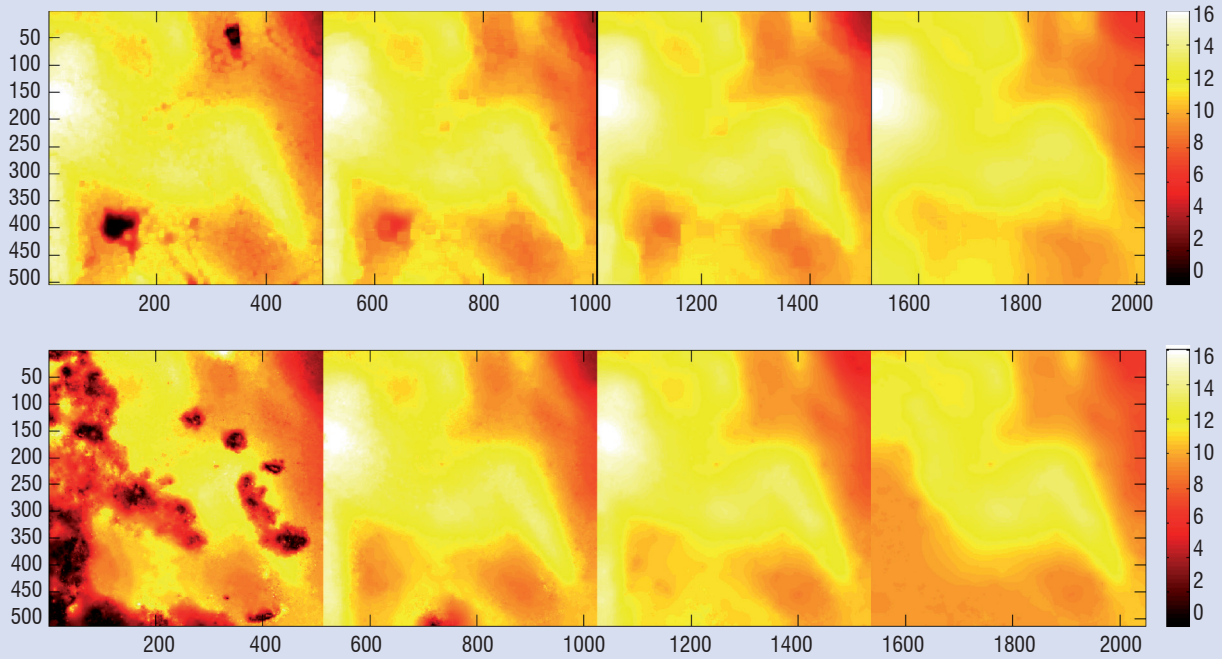

Figure B2 - 03 - Results of displacement field estimation for two images of the dataset “Package3” from the FLUID project [FLUID]. Top: norm of the optical flow estimated using a window-based dense approach with a Gaussian window of standard deviation 4, 8, 16 and 32 (from left to right). Bottom: norm of the estimate obtained by minimization of the regularized criterion (3) with regularizing functional (2), regularization parameter set to 100, 1000, 1.10^4, 3.10^4 (from left to right). The degrees of smoothness of the result can be controlled in both methods, either by the window radius (i.e. standard deviation of the Gaussian) or the regularization parameter.

Box 3 - Iterative window registration

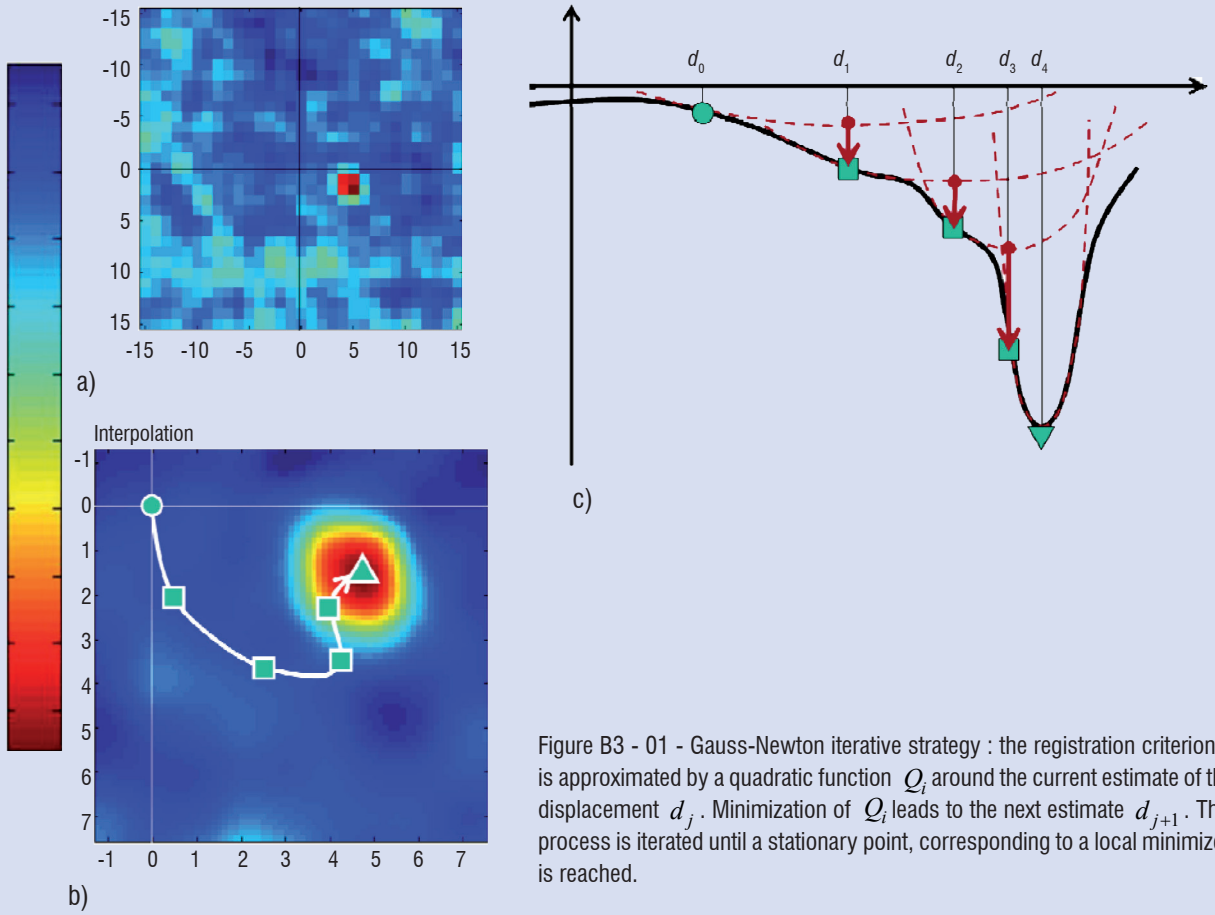

Figure B3 - 01 - Gauss-Newton iterative strategy : the registration criterion *A* is approximated by a quadratic function Q_i around the current estimate of the displacement d_j. Minimization of Q_i leads to the next estimate d_{j+1}. This process is iterated until a stationary point, corresponding to a local minimizer, is reached.

The cross-correlation function $R(d)$ associated with the search of an interrogation window W from image $I(x,t_1)$ to image $I(x,t_2)$ was defined in [21, box 1]. It is usually computed all over a grid of possible displacements d so as to find a maximum. Here, we use a quadratic distance between interrogation window intensities (sometimes weighted by a window profile w):

$$A(d) = \sum_m w(m-k)\left(I(m,t_1) - \tilde{I}(m+d,t_2)\right)^2 = E_{t1}^2 - 2R(d) + E_{t2}^2(d) \qquad \text{(III-1)}$$

An example of registration criterion A is represented in Figure B3 - 01 - a for integer displacements d. In general, the energy of the image integrated on a window is approximately stationary and A varies as the opposite of the cross-correlation function R.
In this work, we first consider all possible real-valued displacements d: The registration criterion A is then written in terms of an interpolated image defined in Box 1, equation (I.3). Figure B3 - 01 - b shows that the criterion A appears as a smooth surface, whose maximum is sought using an iterative optimization algorithm. The Gauss-Newton iterative scheme, sketched in Figure B3 - 01 - c in the 1D case, is derived from a first order development of the residuals appearing in (III-1) in $d = d_0 + \delta d$. Around d_0, the criterion is approximated by a quadratic function

$$Q_0(\delta d) = \sum_m w(m-k)\left(I(m,t_2) - \tilde{I}(m+d_0,t_1) - \nabla\tilde{I}(m-d_0,t_2)^{\mathrm{t}}\delta d\right)^2 \qquad \text{(III-3)}$$

whose minimization yields the new estimated displacement d_1. It is interesting to derive another form of Q_0:

$$Q_0(\delta d) = [\delta d^{\mathrm{t}} \quad 1]\, H_0 \begin{bmatrix}\delta d \\ 1\end{bmatrix}, H_0 = \sum_m w(m-k)q(m)q^{\mathrm{t}}(m), \quad q(m) = \begin{bmatrix} -\nabla\tilde{I}(m+d_0,t_2) \\ I_t(m,t_1) - \tilde{I}(m+d_0,t_2)\end{bmatrix} \qquad \text{(III-4)}$$

From (III-4) it is clear that the Hessian matrix H_0 only depends on spatio-temporal derivatives of the image intensity integrated on the chosen window support.

Local search by iterative optimization

As detailed in Box 3, the search for the matching window is considered to be the iterative optimization of a nonlinear least squares registration criterion. The usual Gauss-Newton iterative optimization process relies on successive local quadratic approximations of the criterion. Since its introduction into computer vision by Lucas and Kanade [2], numerous contributions have concerned improvements of this scheme. The most significant development is conducting the search in a multi-resolution framework. These iterative and multi-resolution techniques are capable of fast window registration with a good accuracy, typically less than the tenth of a pixel, even when the true displacement is large, for instance equal to the window size [11].

Parallel Implementation for dense estimation

The previous iterative approach provides 2C velocity fields whose quality is similar to that obtained with classical FFT-based cross-correlation peak detection techniques. But the true advantage of such approaches is their highly parallel structure, when combined with dense estimates. Let us apply the Gauss-Newton strategy simultaneously to all local registration criteria whose sum forms the global criterion J of (5) with $\lambda = 0$. This global iterative scheme uses an approximate quadratic criterion which is the sum over all pixels of the quadratic forms given by (III-3 and III-4) in Box 3. Updating the whole field simply amounts to solving NxN independent 2 x 2 systems each one with a Hessian matrix given by in (III-4). A remarkable result is that in a dense framework, the coefficients of all these systems can be computed simultaneously by 2D linear filtering of the images; essentially differentiation on the pixel scale and integration on the window scale, as shown by the form of the Hessian matrixes in (III-4) of Box 3. This result has been known for years in the case of an initial null displacement, and has been generalized to further iterations in a recent paper [12]. This yields an algorithm christened FOLKI (for *Flot Optique Lucas-Kanade Iteratif*), which, on a conventional architecture, can compute a dense field for a computational cost equivalent to the computation of a 16 times under sampled field with the classical FFT-based cross-correlation.

The structure of FOLKI is ideally suited to massively parallel architectures like GPUs (*Graphics Processing Unit*). Boosted by the video games market, graphic units have become cheap, ubiquitous and powerful parallel co-processors. FOLKI has been implemented on a GPU this year [20], leading to performances unchallenged by previous techniques: the processing of a 1000 x 1400 pixel PIV image pair requires less than 30ms. This performance means that a typical PIV data set (1000 PIV pairs, each 2000 x 2000 pixel) can be processed in a few minutes. One interesting result is that the computational gain of FOLKI-GPU compared to an implementation on a classical CPU architecture increases with the image size. Table 1 below shows the computing time per-pixel on FOLKI for increasing image sizes. FOLKI-GPU yields a gain of a factor 10 for small (512 x 512) images but the factor reaches 100 for large (4096 x 2048) images. More informations on the FOLKI-GPU algorithm, including a downloadable open source software (under L-GPL license), can be found on the website www.onera.fr/dtim/gpu-for-image, which is dedicated to image and vision applications of GPU computing.
These unchallenged performances open the way to on-the-fly PIV processing inside fluid flow visualization and interpretation software. A video of the results obtained in real-time with FOLKI on dataset "Package3" from the FLUID project [5] is provided on the previously mentioned website.

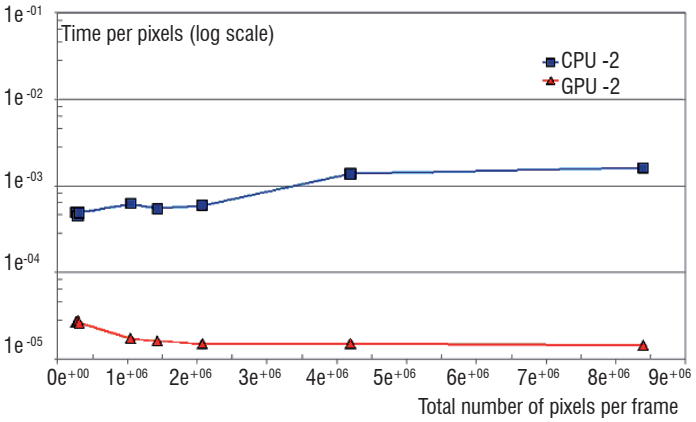

Figure 1 - Computing time per-pixel of FOLKI for increasing size of images. Comparison between computing time on a classical CPU architecture and on a GPU architecture.

Extension to Stereo PIV

The regularization framework presented before also provides a direct formulation of the Stereo PIV problem [13][14]. Stereo PIV uses the simultaneous acquisition of "left" and "right" PIV images in a stereoscopic setting to recover the out-of-plane velocity component. The classical technique consists of separately estimating velocities in each image plane (using one of the previously described techniques), then combining these two 2C estimates to estimate the 3C velocity V. We have recently proposed a direct formulation of the estimation of V [15]. This formulation introduces a nonlinear least squares criterion that cumulates the registration errors associated with left and right images. The resulting criterion is a simple generalization of J in (5) (with $\lambda = 0$) which involves the four PIV image intensities, the 3C velocity V, and projection matrices for left and right cameras derived from the geometric calibration of the system. Such a direct formulation is interesting because it makes use of the epipolar geometry during the correlation step to constrain the search domain and remove potential ambiguities. Moreover, the overall Gauss-Newton iterative multi-resolution scheme introduced for 2C estimation is entirely transferable to 3C estimation.

Toward fast global regularized estimation

Introduction

We now consider the problem of the optimization of (5) in the general case where $\lambda > 0$. Because of the regularizing functional f, typically made of spatial derivatives of the displacement field, the problem is no longer separable. In other words, in an iterative optimization scheme, based on successive linearization of the registration term following equation I-2 in Box 1, the system which has to be solved at each iteration is no longer diagonal (or 2x2 block diagonal, like the one in § "Local search by iterative optimization") but involves a $2N$x$2N$ matrix. In general the optimization of such a non linear coupled criterion of around 2 million variables would be a formidable, if not intractable, task. Two elements simplify the problem: (i) the non linearity of the registration term can be dealt with in a multi-resolution framework, see next section and Box 4; (ii) inside an iteration of the algorithm, efficient multigrid solvers can be used thanks to the structure of the linearized problem.

Multi-resolution estimation

Multi-resolution estimation is closely linked to the theory of scale-space in computer vision and image analysis [16]. It consists in associating with an image a one-parameter family of smoothed images (the "scale-space representation") parameterized by the size of the smoothing kernel used for suppressing fine-scale structures. The most popular smoothing kernel is the 2D separable Gaussian kernel $g_\sigma(x)$, which is parameterized by its standard deviation σ. The resulting representation can be written as $I(x;\sigma) = (g_\sigma * I)(x)$.
As the spectral content of $I(x,\sigma=2)$ is halved in both directions with respect to the original image, it can be represented with sampling periods twice the original ones, i.e. using $N/2 \mathrm{x} N/2$ coefficients if the original image was discretized on $N \mathrm{x} N$ pixels. We then get a pyramid of images $\{I^{(j)}(x)\}$ by setting $I^{(0)}(x) = I(x)$ and recursively convolving by g_2 and down-sampling the previous image, the level j image $I^{(j)}$ being discretized on $N/2^j \mathrm{x} N/2^j$ pixels if the original ones was $N \mathrm{x} N$. A discrete version of this so-called Gaussian pyramid has been proposed in 1983 by Burt and Adelson [17], an example on a PIV image is presented in Box 4.
The rationale for such a redundant representation is the fact that several phenomena of interest in image and video analysis (edges, segments, motions, etc.) have a characteristic scale. Analyzing the image at this particular scale, by using the corresponding image in the chosen scale-space representation, gives better detection of the phenomenon. For instance, in motion estimation, large displacements are usually easier to estimate on coarse scale images. From a theoretical point of view, Lefébure and Cohen showed that the registration of coarse-scale images yields a criterion "more convex" than the registration of the original fine scale images [18]. The multi-resolution estimation scheme then consists in a coarse-to-fine refinement of the estimated motion. Using for instance the Burt-Adelson Gaussian pyramid, we initialize the estimated displacement by the null field at level J, registers $I^{(j-1)}(x,t_1)$ and $I^{(j-1)}(x,t_2)$ estimate a first displacement field $d^{(J)}$. Transition to the next finer scale consists in up-sampling and magnifying the estimated field by a factor 2 to initialize the registration of $I^{(j-1)}(x,t_1)$ and $I^{(j-1)}(x,t_2)$ – usually this initialization is done by warping one of the images (the warping operation is explained in box 1, Eq. (I.3)). This process is reiterated until the original $(j=0)$ resolution level is reached.
An example of multi-resolution estimation is given in box 4. Figure B4 - 01 compares the displacement field obtained with a multi-resolution process on the left to the one obtained with multiple iterations at the original resolution level on the right. The latter field is presented with a scale factor of 50 on the vectors, which are largely under estimated and appear trapped in several local minima of the registration criterion. The multi-resolution process avoids these minima and yields a correct flow. Note that recently Ruhnau et al. [4] have proposed a true multi-scale estimation process, using not only the reduced images of the Gaussian pyramid, but also intermediate smoothed images $I(x,\sigma)$. According to this reference, this approach is particularly beneficial for PIV image processing, because PIV images are usually very spiky and, even using a multi-resolution scheme, one could be trapped in a local minimum.

Box 4 - Multi-resolution coarse-to-fine scheme

We present experimental evidence about the benefits of a coarse-to-fine multi-resolution scheme for estimating displacement fields in PIV. We first compare the results obtained with a multi-resolution scheme and those obtained with iteration at level 0, i.e. by working directly on the original image resolution. As can be seen in the right part of Figure B4 - 01, the latter strategy leads each vector to the closest local minimizer.

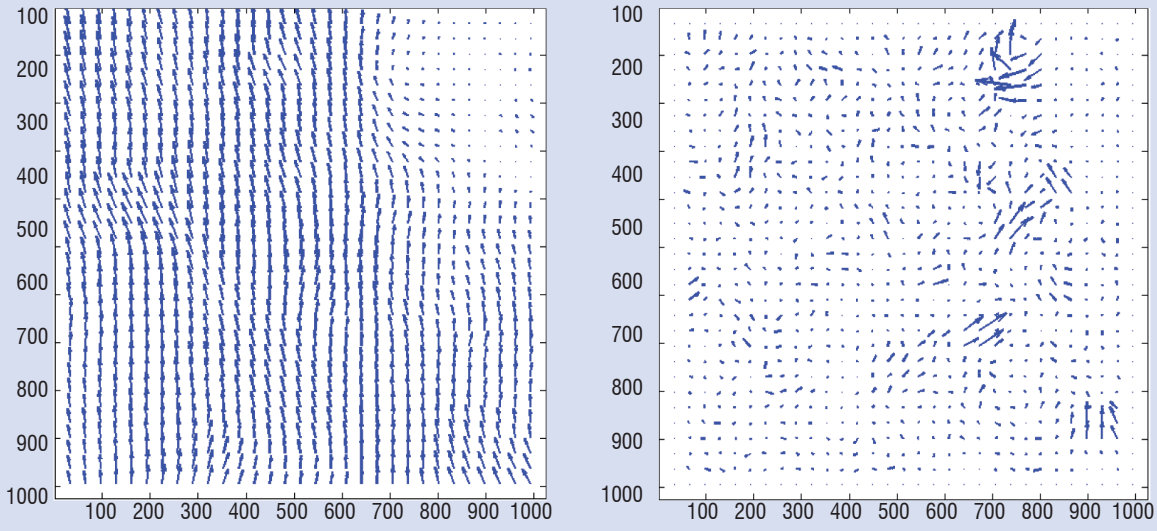

Figure B4 - 01 - Comparison of estimated displacement fields with the FOLKI window-based algorithm (Gaussian weight function with standard deviation 12) on 2 images of the dataset "Package3" from the FLUID project [5]. Left: result of a multi-resolution scheme, 3 resolution levels, 2 iterations on each level, vectors magnified by a factor of 2; right: result of 4 iterations at level 0, vectors magnified by a factor of 50.

Then we present intermediate results (only their norm is shown) for three levels of a multi-resolution coarse-to-fine strategy, in front of the corresponding sub-sampled image. The main motions are already correctly estimated on the level 3 (128 x 128) result. At this scale, the maximum displacement is 2 pixels. This estimate is up-sampled and multiplied by a factor of 2 and then refined at resolution level 2, while descending the resolution pyramid until the original scale (not shown here) is reached.

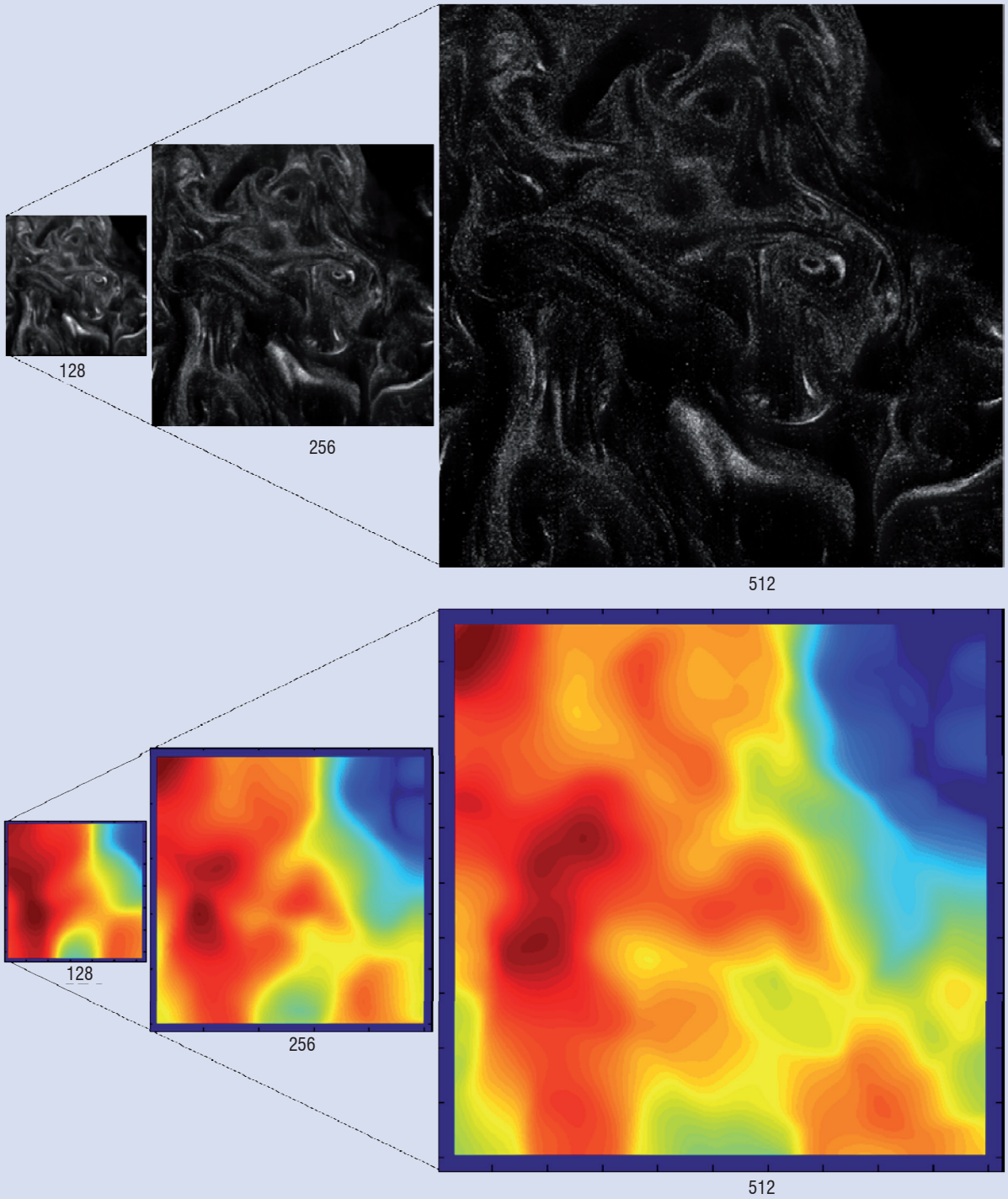

Figure B4 - 02. Three steps of a multi-resolution coarse-to-fine estimation on 2 images of the dataset “Package3” from the FLUID project [5]. Top: image pyramid, from left to right, level 3, 2, 1). Bottom: estimated displacement field norm, window-based FOLKI method with Gaussian weight function of standard deviation 12. From left to right, intermediate results at level 3 (norm max = 2) , 2 (norm max = 4), 1 (norm max = 8).

Efficient solvers for the internal linearized problem

As already mentioned, at each iteration of the optimization, an internal linearized problem has to be solved, with a very large Hessian matrix made of blocks with a diagonal band structure defined by the chosen regularizing functional. Most regularizing functionals imply low-order derivatives and lead to short-range interactions between pixels. For instance, using the Horn and Schunck functional (2) and a quadratic regularization, the stationary equations for the 1D case take the following form:

$$ad_k + b + \frac{d_{k-1} - 2d_k + d_{k+1}}{2h} = 0 \quad \forall k \tag{6}$$

In 2D this model only involves the 4-nearest neighbors of each pixel. The Gauss-Seidel (GS) algorithm (and variants like Jacobi or SOR techniques) is a simple and popular solver for these problems. GS is essentially a pixelwise updating scheme: for each pixel, the displacement d_k is updated by solving (6) with all other displacements $d_l, l \neq k$ fixed. The whole algorithm repeats several sweeps on the image.

The GS algorithm is considered to be an efficient smoother. In $Ad = b$ linear problems, with local dependencies such as (6), GS is very efficient at reducing the high frequency part of the error – in other terms, if d^* denotes the exact solution, d_0 an initial estimate and d_1 the output of a GS iteration, $d_1 - d^*$ has a lower frequency content than $d_0 - d^*$, i.e., it is smoother. Conversely, short-range dependencies mean that GS is very slow in propagating the low-frequency components of the solution. A large number of sweeps are required to achieve a correct convergence.

The logic of multigrid (MG) [19] methods is to use a smoother such as GS but at coarser scales. Indeed, working at coarse scale accelerates the propagation of low-frequency characteristics by GS. Moreover, as problem dimensions are reduced at coarse scales, running the GS algorithm is also cheaper. Therefore, MG methods are theoretically the most efficient techniques for elliptical PDE.

Multigrid methods should not be confused with the multi-resolution estimation process. Multi-resolution estimation deals with the non linearity of the registration criterion with a coarse-to-fine strategy. Multigrid methods are used to speed up the resolution of the linearized sub-problems and use various cycles on the resolution levels (or scales), not only coarse-to-fine: see Box 5.

MG methods are becoming the new standard of fast variational optical flow computation, providing gain factors higher than 20 when compared to classical GS-like algorithms for real-time (i.e. 60 Hz) processing, as been reported on small images (120 x 160 pixels) in [7].

Conclusion

This paper reports the work on fluid dynamics estimation and visualization conducted in the Onera's project MEMFIS. Window correlation methods, popular in the PIV community, have been reviewed, together with the regularization framework (also called variational approach) usually adopted in computer vision. In the line of [3], a unified framework merging the two approaches in a compound criterion has been proposed. But the main subject has been to describe recent algorithmic developments, such as fast iterative correlation techniques, which are at the heart of the window-based FOLKI algorithm [12], and multi-resolution/multigrid optimization schemes. Combined with a GPU implementation, these approaches can already process PIV data at video rate, based on a simple window correlation paradigm. In the near future, there is no doubt that real-time performance will be also achievable using more sophisticated techniques, based on physically-sound models.

These new algorithmic solutions could be the basic engine of a video rate velocity field visualization and interpretation toolbox. They will provide real time computing of the velocity fields inside the visualization tool, so that neither pre-computing nor storing of displacement fields will be necessary. Thus, based on PIV images alone, the user will be able to visualize the salient phenomena while browsing the PIV image sequence, in order to select a spatiotemporal zone and suitable processing in real-time, like, for instance, the detection and tracking of a vortex.

Such combination of recent data processing solutions open the way to a major development in fluid dynamics studies of experimental data. Indeed, the profound changes that we have reported in terms of data processing takes place in a context of great changes both on the experimental side, with new acquisition settings (Time Resolved PIV, tomographic PIV, etc.) and on the numerical side, where finer simulation tools have become available. We think that there is a major opportunity for advanced data processing techniques, based on physical regularization and variational approaches, to realize a smart interface between both sides. We have tried to show that several recent results concerning algorithmic and architectural problems provide solutions to meet this challenge in the near future. In our view, the next step is to launch multidisciplinary studies between experimentalists, physicists and data processing specialists to develop innovative interpretation tools ■

Box 5 - Multigrid schemes

MG methods are used to speed up the resolution of a linear system such as $Ad = b$ based on a smoother like Gauss-Seidel (GS). Let d^* be the true solution of the system, d_0 the current solution and $e_0 = d_0 - d^*$ the current error. As mentioned in the text, a few sweeps of the GS algorithm starting from d_0, an operation that we denote by GS(A, b, d_0), leads to another estimate d_1 and reduces the high-frequency part of the error, i.e. the resulting error $e_1 = d_1 - d^*$ is smoother than e_0.

MG methods consist of solving the problem on coarse grids using few iterations of a smoother (here Gauss-Seidel or SOR) and to correct back d_0 on the finest grid. Two things are then required: a reduction operator $\mathcal{R}$ that projects the smoothed error e_0 and the linear system (A,b) to a coarser level and a prolongator $\mathcal{P}$ that interpolates the correction at some coarse level to the finer level. The interpolation in $\mathcal{P}$ will generally introduce high frequency errors in the solution: this error is reduced by smoothing again (post-smoothing) using GS.

The simplest "two grids" scheme algorithm is:

- Get a first solution on the fine grid GS$(A, b, 0) \rightarrow d_0$
- Compute residual: $r_0 = b - Ad_0$
- Error approximation on coarse grid (reduction/smoothing) : GS$(\mathcal{R}A, \mathcal{R}r_0, \mathcal{R}0) \rightarrow e_1$
- Correction of the current solution: $d = d_0 + \mathcal{P}e_1$
- Smooth the corrected solution: GS$(A, b, d) \rightarrow d_1$

This procedure can be generalized to more than two grids by recursion on the error e, and there are several MG "cycles", such as the V and W-cycles (see Figure B5 - 01).

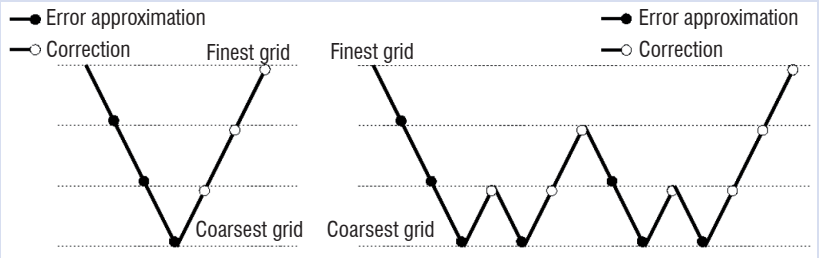

Figure B5 - 01 - Multigrid methods. V-cycle (left) and W-cycles (see text).

In the "full multigrid" scheme, sketched in Figure B5 - 02, we start the algorithm on the coarsest grid with some iteration of the chosen smoother GS (we can also perform a direct resolution because at this scale, the linear system is of small and its resolution is cheap). This approximation is used as an initialization for a multigrid W-cycle (or V-cycle) starting from the next finer grid. But we also merge this process into a multi-resolution estimation process, as explained: the prolongated displacement field is used to change the current registration problem and update the linearized system. Recursively, every solution found on a coarse grid is used for initialization/relinearization by prolongation for the solver on the next finer grid. We can also perform multiple consecutive multigrid cycles on the same resolution to get a better approximation.

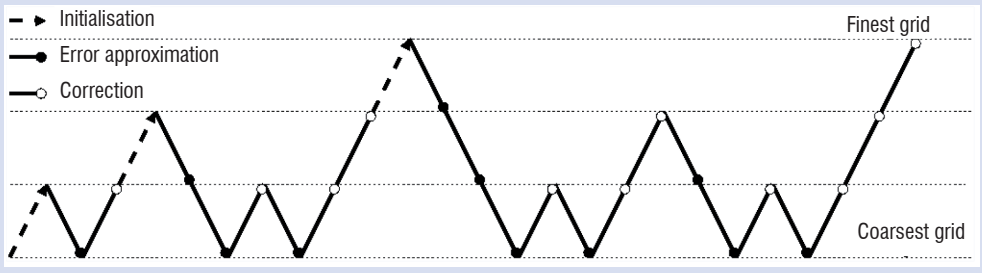

Figure B5 - 02 Full multigrid method. The basic scheme is a W-cycle, which is merged into a coarse-to-fine multi-resolution process.

References

[1] B. HORN, B. SCHUNCK - *Determining Optical Flow,* Technical Report, Massachusetts Institute of Technology, April 1980.

[2] B. LUCAS, T. KANADE - *An iterative Image Registration Technique with an Application to Stereo Vision*. Proceedings DARPA Image Understanding Workshop, pp. 121-130, April 1981.

[3] A. BRUHN, J. WEICKERT - *Lucas/Kanade Meets Horn/Schunck: Combining Local and Global Optic Flow Methods*. International Journal of Computer Vision, vol. 61, n° 3 pp. 211-231, 2005.

[4] P. RUHNAU, T. KOHLBERGER, C. SCHNÖRR, H. NOBACH - *Variational Optical Flow Estimation for Particle Image Velocimetry.* In Experiments in Fluids, vol. 38, pp. 21-32, 2005.

[5] *Interdisciplinary Projet FLUID (FLUid Image analysis and Description)* website http://fluid.irisa.fr/ (data used in the illustrations: http://fluid.irisa.fr/Data/Package3LaVision/), 2006.

[6] J. IDIER (Ed.) - *Bayesian Approach to Inverse problems*. Coll. Digital Signal and Image Porcessing, ISTE – Wiley, London, 2008.

[7] A. BRUHN, J. WEICKERT, T. KOHLBERGER, C. SCHNÖRR - *A Multigrid Platform for Real-Time Motion Computation with Discontinuity-Preserving Variational Methods.* in International Journal of Computer Vision, vol 70, n °3 pp. 257-277, 2006.

[8] T. CORPETTI, E. MÉMIN, P. PÉREZ - *Dense Estimation of Fluid Flows*. IEEE on Pattern Analysis and Machine Intelligence, vol 24, n° 3, march 2002.

[9] P. RUHNAU, C. SCHNÖRR - *Optical Stokes Flow Estimation: An Imaging-Based Control Approach.* in Experiments in Fluids, vol. 42, pp. 61-78, 2007

[10] P. RUHNAU, A. STAHL, C. SCHNÖRR - *Variational Estimation of Experimental Fluid Flows with Physics-based Spatio-temporal Regularization*. Measurement Science and Technology, vol. 18, pp. 755-763, 2007.

[11] S. BAKER, I. MATTHEWS - *Lucas-Kanade 20 years on: A unifying framework*. International Journal of Computer Vision, vol. 56, n° 3, pp. 221–255, 2004.

[12] G. LE BESNERAIS, F. CHAMPAGNAT - *Dense Optical Flow by Iterative Local Window Registration.* ICIP 2005. IEEE International Conference on Image Processing, pp. 137-140, vol. I, 2005.

[13] M. RAFFEL, C. WILLERT, J. KOMPENHANS - *Particle Image Velocimetry: A Practical Guide*. Springer-Verlag, Berlin Heidelberg, 1998.

[14] A. K. PRASAD - *Stereoscopic particle image velocimetry.* Experiments in Fluids, vol. 29, pp. 103-116, 2000.

[15]B. LECLAIRE, B. JAUBERT, F. CHAMPAGNAT, G. LE BESNERAIS, Y. LE SANT - *FOLKI-3C: a Simple, Fast and Direct Algorithm for Stereo PIV.* Proc. 8th Symposium on Particle Image Velocimetry, PIV'09, Melbourne, Victoria, Australia, August 25-28, 2009.

[16] T. LINDEBERG - *Scale-space theory in computer vision*. Kluwer Academic Publishers, 1994.

[17] P. BURT, T. ADELSON - *The Laplacian Pyramid as a Compact Image Code*. IEEE Trans. Communications, vol. 9, n°4, pp. 532–540, 1983.

[18] M. LEFÉBURE, L.D. COHEN - *Image Registration. Optical Flow and Local Rigidity*. Journal of Mathematical Imaging and Vision, vol 14, pp. 131-147, 2001.

[19] P. WESSELING - *An introduction to multigrid methods*. John Wiley and sons, 1991.

[20] F. CHAMPAGNAT, A. PLYER, G. LE BESNERAIS, B. LECLAIRE AND Y. LE SANT - *How to compute dense PIV vector fields at video rate?* Proc. 8th Symposium on Particle Image Velocimetry, PIV'09, Melbourne, Victoria, Australia, August 25-28, 2009.

[21] C. BROSSARD, J.-C. MONNIER, P. BARRICAU, F.-XAVIER VANDERNOOT, Y. LE SANT, F. CHAMPAGNAT, G. LE BESNERAIS - *Principles and Applications of Particle Image Velocimetry.* Aerospace Lab n° 1, December 2009.

[22] T. CORPETTI, P. HÉAS, E. MÉMIN, AND N. PAPADAKIS - *Pressure image assimilation for atmospheric motion estimation*. Rapport de recherche INRIA/RR6507, 2008.

[23]G. LE BESNERAIS, F. CHAMPAGNAT - *B-Spline Image Model for Energy Minimization-Based Optical Flow Estimation*. IEEE Trans. on Image Processing, vol. 15, n° 10, pp. 3201-3206, oct. 2006.

[24]T. CORPETTI, D. HEITZ, G. ARROYO, E. MÉMIN, A. SANTA-CRUZ - *Fluid Experimental Flow Estimation Based on an Optical-Flow Scheme*. Experiments in Fluids, vol 40, n° 1, pp. 80-97, jan. 2006.

[25] G. M. QUÉNOT, J. PAKLEZA, T. A. KOWALEWSKI - *Particle image velocimetry with optical flow*. Experiments in Fluids, vol. 25, pp. 177-189, 1998.

Acronyms

GPU (Graphical Processing Unit)
PSP (Pressure Sensitive Paint)
MDM (Model Deformation Measurement)
PIV (Particle Image Velocimetry)
IW (Interrogation Window)
OFC (Optical Flow Constraint)
MG (Multi Grid)

AUTHORS

Guy Le Besnerais graduated from the Ecole Nationale Supérieure de Techniques Avancées in 1989 and received a Ph.D. degree in physics from the Université de Paris-Sud, Orsay, France, in 1993. He joined Onera in 1994, where he is now a senior scientist in the Modeling and Information Processing Department. His work concerns inversion problems in imagery and computer vision, with an emphasis on embedded perception for autonomous aerial robots.

Frédéric Champagnat graduated from the Ecole Nationale Supérieure de Techniques Avancées in 1989 and received a Ph.D. degree in physics from the Université de Paris-Sud, Orsay, France, in 1993. From 1994 to 1995, he held a Postdoctoral position with the Biomedical Engineering Institute, Ecole Polytechnique, Montreal, QC, Canada. Since 1998, he has been with the Onera, Chatillon, France. His main interests are in the field of spatio-temporal processing for space or aerial image sequences, in particular registration, motion estimation, super-resolution, and detection.

Aurelien Plyer has been a Onera-Laga PhD student since 2008. He received his Master of Science in Computer Science from Universite Pierre et Marie Curie (Paris 6) in 2008. His research deals with video analysis and interpretation of aerial videos within a urban context. He uses GPU programming in order to implement real-time processing.

Benjamin Leclaire graduated from the Ecole Polytechnique in 2001 and received his Ph.D. degree from the same university in 2006. During his Ph.D., he worked on the dynamics of turbulent rotating flows in the Fundamental and Experimental Aerodynamics Department of Onera. He now holds a position of research scientist in this department. His activity includes industrial wind-tunnel tests and fundamental research on vortex breakdown and PIV (Particle Image Velocimetry). In this latter field, his interests are focused more specifically on motion detection and flow characterization.

Riadh Fezzani holds a Masters in mathematical modeling and computational methods from the University Paul Sabatier (Toulouse 3) and is currently preparing a PhD thesis in the French Aerospace Lab (Onera).

Yves Le Sant Researcher at Onera since 1983. His first studies concerned wall interferences and the development of an adaptive test section. Then he was involved in applying and developing many measurements methods, such as heat flux assessment, temperature and pressure sensitive paints and model deformation. His current activities are in the field of image processing applications, such as in Particle Image Velocimetry.

V. Bodoc, C. Laurent,
Y. Biscos, G. Lavergne
(Onera)

E-Mail: gerard.lavergne@onera.fr

Advanced Measurement Techniques for Spray Investigations

The objective of this paper is to present recent advances at Onera in the spray diagnostic and simulation fields. In the context of the reduction of engine pollutant emissions, the optimization of fuel spray injection represents phenomena of great fundamental and practical interest and is an important feature in the design of new prototypes of turbojet injection devices. The physics of spray formation, transport, evaporation and combustion are not completely understood and the models must be improved to make better predictions of air fuel mixing inside combustion chambers. Onera, in cooperation with CNRS, has developed new optical diagnostics to obtain more detailed validation databases for validating numerical approaches. New techniques are presented for characterizing the dispersed liquid phase in sprays in terms of droplet temperature, size and velocity. During the last few years, important work has been done on measuring the mean and local droplet temperature, by coupling Standard Rainbow Refractometry (SRR) and Laser Induced Fluorescence (LIF) for a monodisperse droplet stream [8]. Local characterizations of the discrete phase inside a polydisperse spray have also been carried out by the simultaneous use of the Global Rainbow Refractometry (GRR) method and the well known Phase Doppler Anemometry (PDA) technique. This paper describes the principle of these techniques and the different levels of application from basic configurations involving monodisperse droplet streams to polydisperse sprays in a high pressure and temperature environment. Experimental results are compared with the numerical ones for some simple configurations.

Introduction

The reduction of pollutant emissions and the development of alternative fuels require a better understanding of multi-component spray transport, evaporation and combustion in a turbojet combustion chamber. The movie (Video1) presents the spray behavior before (Figure 1), during and after ignition in a rectangular sector of a combustion chamber (Onera MERCATO Facility). These images show the spray's unsteadiness with a high liquid concentration zone close to the atomizer's orifice. The challenge is to develop accurate techniques to characterize the temporal and spatial multi-component droplets' evolutions in the different zones of the spray and for the different phases of the ignition process. In this field, the understanding of the time dependent evaporation mechanism is essential for the prediction of the local equivalence ratio, ignition delays and pollutant levels [10].

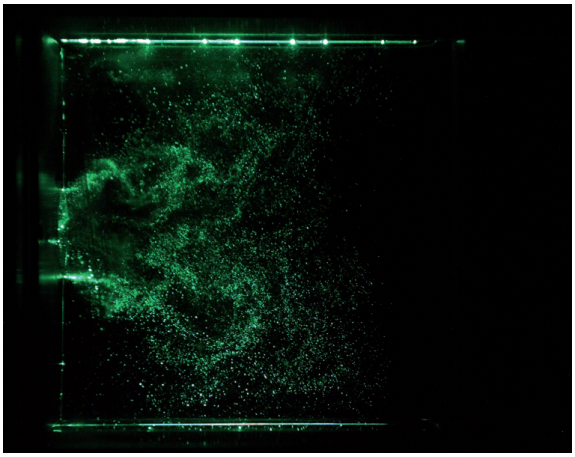

Figure 1 - Spatial distribution of the dispersed phase before ignition in a combustion chamber

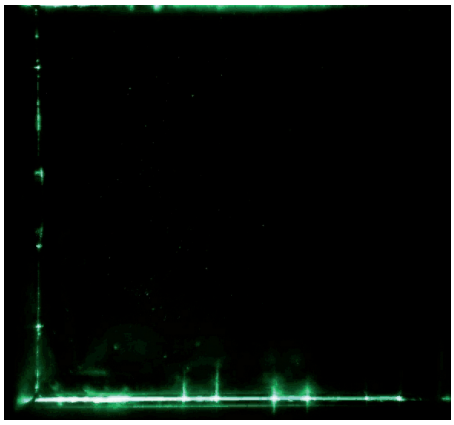

Video 1 - Spray behavior before, during and after ignition [10]

At high altitude, the droplet evaporation rate is weak, due to the low pressure and temperature, and it is important to understand the real dynamic of the evaporation process for each component correctly.

Improving the multi-component droplet vaporization models is very useful for optimizing the composition of new generation fuels. More accurate optical techniques for simultaneously measuring the spatial and temporal evolutions of the droplet size, velocity and temperature must be developed for validating these detailed droplet evaporation models. During the few last years, important work has been done at Onera in cooperation with CNRS (CORIA, IMFT, LEMTA) in the framework of a national program entitled: "Experimental diagnostics and numerical simulations for the analysis of the multi-component sprays evaporation". The objective is to characterize the droplet and its environment during the evaporation process [3, 4, 5, 6, 7, 9, 23, 24].
This paper focuses on the recent advances in droplet temperature measurement by coupling SRR and LIF techniques for individual droplets and the use of GRR and PDA techniques for simultaneous measurements of the droplet size, velocity and temperature inside sprays. First of all, these techniques and methods are tested on basic configurations, involving monodisperse droplet streams. Secondly, polydisperse sprays in non confined and confined configurations are investigated. Finally, the experimental results are compared to the numerical simulation for different configurations.

Description of the techniques

Box 1 - Phase Doppler Anemometry

Phase Doppler Anemometry is a well-established optical technique for the simultaneous measurement of particle velocity, size, flux and concentration. Its usefulness has been demonstrated in a wide range of multiphase flows applications: automotive and aircraft fuel injectors, nozzle design, etc. This technique finds its origins in the refractive properties of droplets. The Mie and Debye's theories furnish rigorous analytic solutions of the light scattering by a homogeneous sphere of any size and refractive index. The principle of the PDA technique is the scattering of lit planes by spherical particles. Based on the geometrical optics, for spheres much larger than the wavelength of the incident light, the Mie scattering can be approximated by the interference of diffracted, refracted and reflected rays [20]. The principle will be explained by an intuitive geometrical optics approach rather than the more rigorous Mie theory (Figure B1-01)

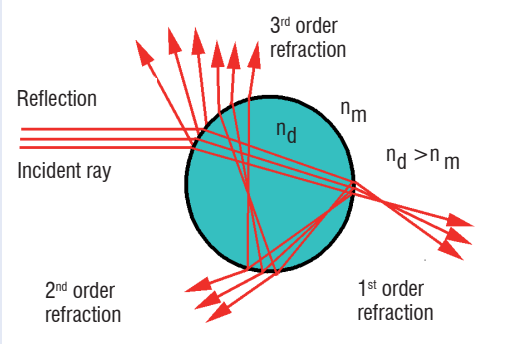

Figure B1-01 - Ray trace for a droplet.

The measurements are performed at the intersection of two laser beams, forming an interference fringe pattern of alternating light and dark planes. The transmitting system generates the measurement volume, which has a Gaussian intensity distribution in all 3 dimensions (Figure B1-02).
Particles scatter the light, as the particle passes through the light planes of the interference pattern. Receiving optics, placed at an off-axis location focus scattered light onto multiple detectors (2 or 3 for each velocity component).
Each detector converts the optical signal into a Doppler burst with a frequency linearly proportional to the particle's velocity

$$f = \frac{1}{t} = \frac{v}{\delta_f} = \frac{2\ v\ \sin(\frac{\theta}{2})}{\lambda}$$

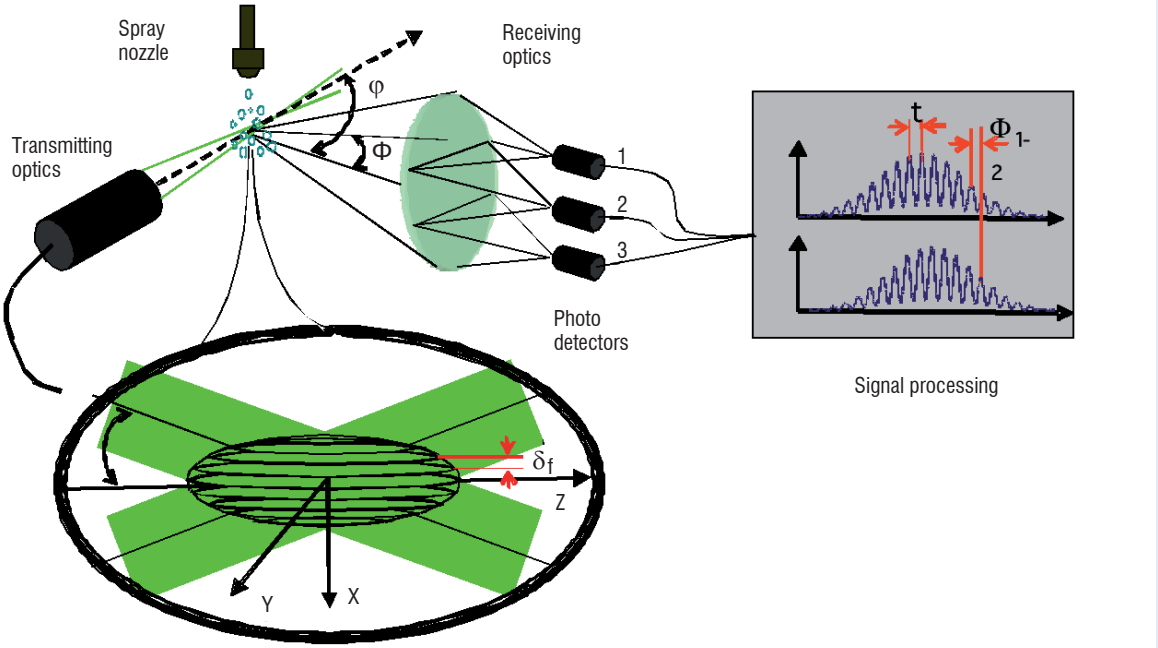

Figure B1-02 - PDA technique setup

The signal-processing unit measures the phase difference between the droplets' signals, from two different detectors (Figure B1-02). This is a direct measurement of the droplet size since the phase shift, $\Delta\Phi$ between the Doppler signals of two different detectors can be linearly correlated with the droplet's diameter (Dg). This linear relationship exists if the detectors are positioned such that only one light scattering mode dominates (equations below). Note that there is no calibration constant in these equations. Simultaneous detection of different scattering modes of comparable intensity leads to a non-linear phase-diameter relation.

$$\Delta\Phi = \frac{2\pi \ Dg}{\lambda} \frac{\sin\theta \ \sin\psi}{\sqrt{2(1-\cos\theta \ \cos\psi \ \cos\varphi)}}$$

reflection mode ($80^0 < \Phi < 110^0$)

$$\Delta\Phi = \frac{-2\pi \ Dg}{\lambda} \frac{n_{rel} \ \sin\theta \ \sin\psi}{\sqrt{2(1+\cos\theta \ \cos\psi \ \cos\varphi) \ (1+n_{rel}^2 - n_{rel}\sqrt{2(1+\cos\theta \ \cos\psi \ \cos\varphi)})}}$$

first order refraction mode ($30^0 < \Phi < 70^0$)

The third detector is added in order to improve the droplet size measurement's accuracy.

Box 2 - Rainbow Refractometry

Rainbow refractometry consists of analyzing interference patterns diffused by a laser lit droplet.
Rainbow phenomenon appears when a droplet crosses an incident parallel light beam (sunbeam or laser beam). In nature, the rainbow phenomenon occurs when the human observer looks at the rain, with the sun shining behind it (Figure B2-01 a.). Two rays can be defined. The first connects the observer and the cloud of droplets, while the second links the sun and the same cloud of droplets. The size of the angle between these two rays is a function of the droplets' refractive index (temperature) and size distribution. As for the different colors in the rainbow, they are the expression of the dependence of the refractive index on the wavelength of the incident light.
In laboratory, a laser replaces the beam of sunlight and different experimental set-ups can be developed to investigate isolated droplets, monodisperse droplet streams and polydisperse sprays (Figure B2-01 b.) [1].

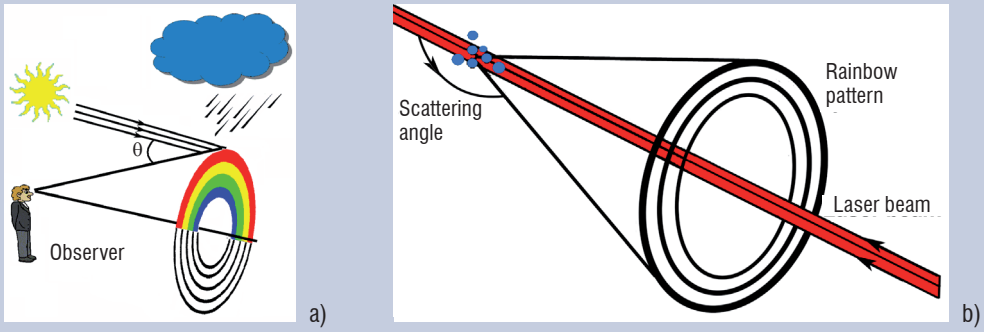

Figure B2-01 - a) Natural rainbow; b) Monochromatic rainbow formation in laboratory

In the case of a single droplet (Standard Rainbow Refractometry technique), the backward diffusion pattern is mainly created by the superposition of two interference patterns: the Airy fringes and the ripple structure (Figure B2-02). The latter is a result of the optical interference between the once internally and once externally reflected light (Figure B1-01). The angular position of the 1st order rainbow depends especially on the droplet's refractive index (and consequently its temperature) and the droplet's shape [9, 17, 19].

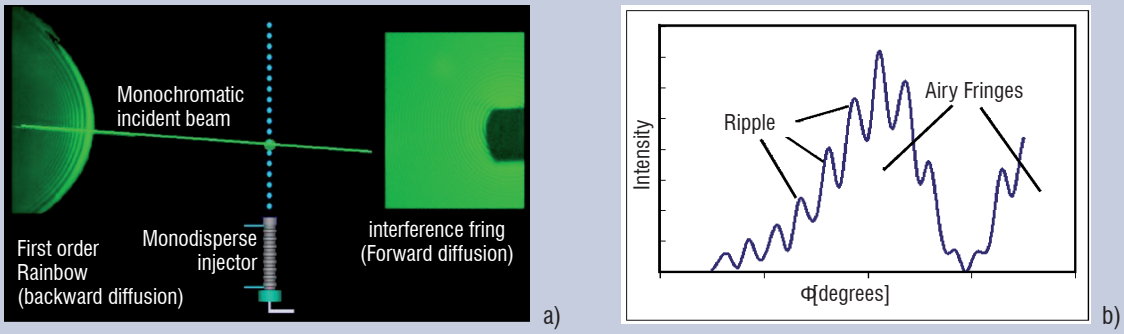

Figure B2-02 - Scattered light around an individual droplet

When a cloud of droplets is investigated, the technique is known as Global Rainbow Refractometry (GRR) or Global Rainbow Thermometry (GRT). The basic principle of the GRR technique is the summation of the rainbow signals corresponding to droplets of different shapes, dimensions and temperatures [2, 14, 16, 18, 21-24]. A pattern is formed by constructive interference of laser light scattered by the spherical droplets of different sizes. As in the natural rainbow case, the effect of non-spherical droplets is eliminated by destructive interference yielding a uniform background (Figure B2-03).

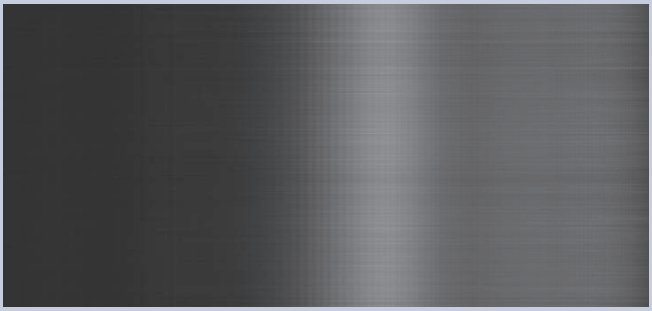

Figure B2-03 - A typical global rainbow pattern

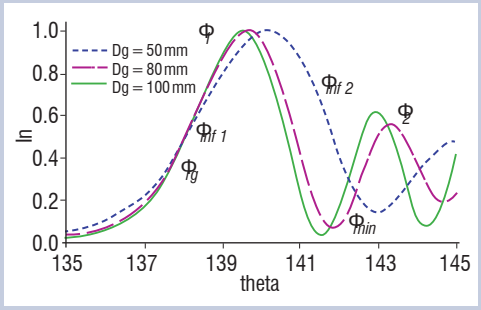

Figure B2-04 - Simulation of the typical global rainbow pattern

The temperature and size are determined from the recorded global rainbow optical signal with an inversion algorithm. Up to now, several inversion algorithms, based on the Airy and Complex Angular Momentum theories have been proposed. The most interesting results are obtained using the one based on the inflexion points around the main rainbow maximum, i.e. Φ_{inf1}, Φ_{inf2} (Figure B2-04)

$$Dg = 823.14 \quad \lambda \quad (\theta_{\inf 2} - \theta_{\inf 1})^{-3/2}$$
$$\theta_{rg} = \theta_{\inf 1} - 18.62 \quad (\lambda / Dg)^{2/3} \qquad [22]$$

where Φ_{rg} is the so-called geometrical rainbow angle, which only depends on the refractive index, and thus on the droplet's temperature.

Box 3 - Laser Induced Fluorescence In Liquid Phase

The principle of this method is based on the dependency of the fluorescence intensity of the dye which is added to the droplets (Figure B3-01).

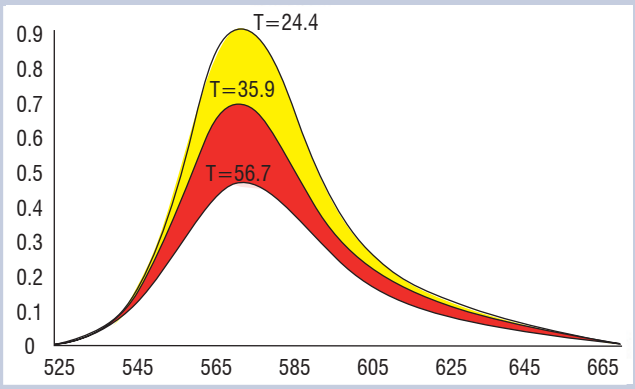

Figure B3-01 - Fluorescence spectra of Rhodamine B

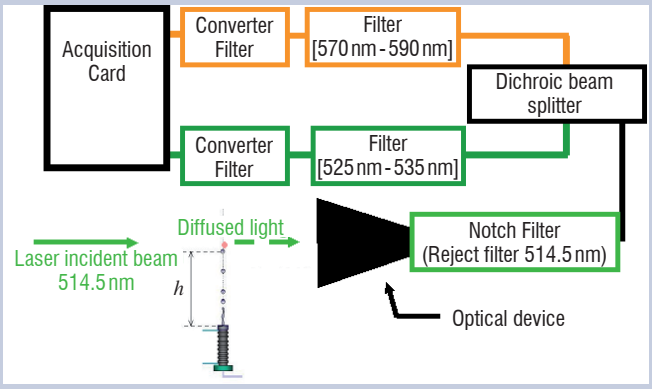

Figure B3-02 - LIF experimental set-up for different temperatures

However, as the fluorescence depends on other physical properties such as tracer concentration or collection volume, intensity ratios must be considered. The fluorescence signal is first collected by a lens and then split between two spectral bands using a dichroic beam splitter. The acquisition card receives the two signals converted by the photomultipliers (Figure B3-02).
The liquid is seeded with Rhodamine B (the concentration lies between 10^{-6} and 10^{-5} mol.l^{-1}). This dye was chosen by P. Laveille and F. Lemoine [12, 13]. A detailed study was done to determine the spectral bands. The spectral bands used here are [535 nm - 545 nm] and a high-pass at 575nm (Figure B3-03). Contrary to the first spectral band, the second is very sensitive to temperature.

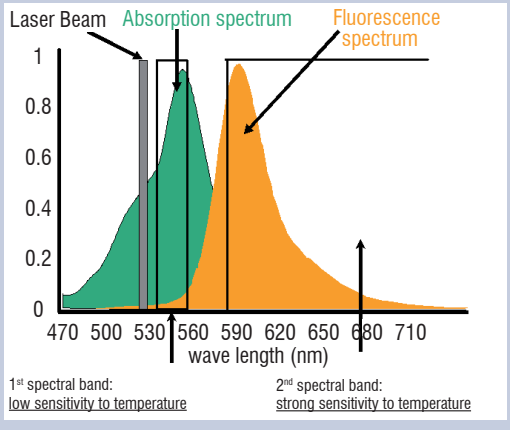

Figure B3-03 - Selection of the two spectral bands

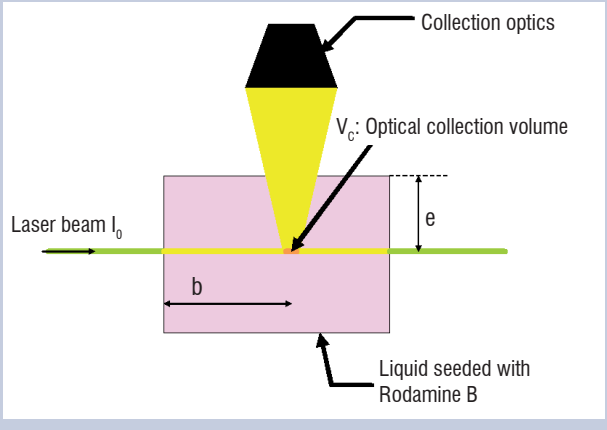

Figure B3-04 - Calibration device

The coefficients of sensitivity to temperature are determined by a previous calibration inside a cell controlled in temperature by a Peltier module (Figure B3-04).

Applications

Monodisperse droplet stream

This basic configuration was chosen first because it gives good control of the droplet characteristics during injection: size, velocity, temperature. It is relatively simple to set up and can be used to develop different investigation techniques. Another objective is to build up a large data base of experimental data in order to model the droplet evaporation.

Experimental set up

The experimental set-up is arranged around a monodisperse droplet injector (Figure 2). The monodisperse droplet stream is generated by Rayleigh disintegration of a liquid jet, with the use of mechanical vibration obtained by using a piezoceramic device [15]. At a particular frequency range, the liquid jet breaks into equally spaced and sized droplets. The resulting droplet diameter for a calibrated orifice of 50 μm is about 100 μm. The droplet injection velocity can range from 2 m/s to about 10 m/s. The fuel can be pre-heated in the injector body by means of a thermostat. The liquid temperature is measured exactly at the injection point with a thermocouple. All droplets have the same characteristics at each position in the stream. In this way the changes over time in the droplets' properties can be obtained from measurements at several positions in the stream.
Electrostatic deviation of droplets can be used to adjust the droplet spacing, without changing the droplets' diameter. The deviator is mounted at the injector exit (Figure 3). The stream passes through a positively charged ring, positioned at the break-up location of the cylindrical jet, so that the droplets can be negatively charged by electrical impulses. Consequently, a periodically selected number of droplets can acquire a negative electrical charge. After being charged, the droplets pass between two plates where a high intensity electrostatic field is created. The charged droplets are deviated onto the side of the positive plate and picked up. The rest of the jet is not deviated and presents a different droplet spacing from the initial jet, depending on the number of the initially charged droplets. With the use of this device, from 1/2 up to 64 out of 65 droplets can be eliminated.
A vertical heated plate can also be mounted above the electrostatic droplet deviator (Figure 2) in order to generate the thermal boundary layer. The plate is made of ceramic and is electrically heated. The electrical power dissipated in the wire resistance is around 300 W. The droplet stream is generated very close to the plate at 0.8 mm where the temperature is between 800 and 900 K (Figure 3).

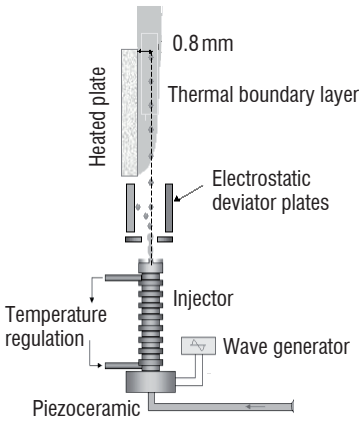

Figure 2 - Droplet stream generator

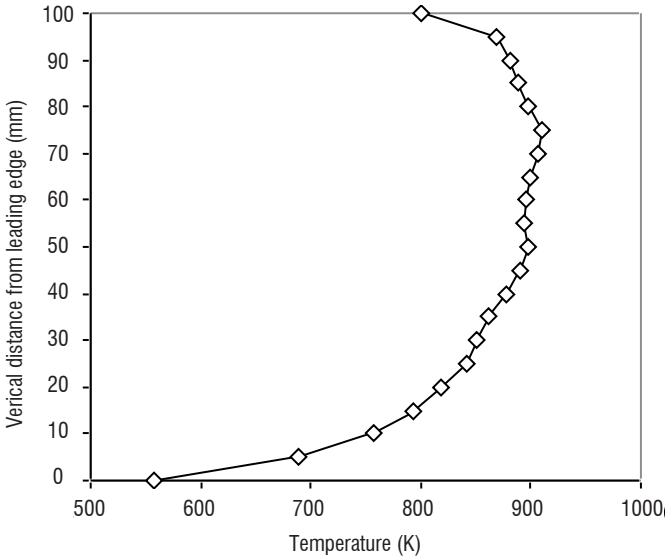

Figure 3 - Temperature profile at 0.8 mm from the heated plate

The velocity of droplets is measured by Laser Doppler Anemometry (see LDA on Figure 4). Their diameter is measured from the angular interference pattern in forward diffusion recorded by Camera 1. Using this method, droplet size is determined with an accuracy of 1.5 %. The characterization of the droplet temperature is performed using two measuring techniques: Rainbow refractometry using backward diffusion (Camera 2 on Figure 4) and Laser Induced Fluorescence (see LIF optical device on Figure 4).

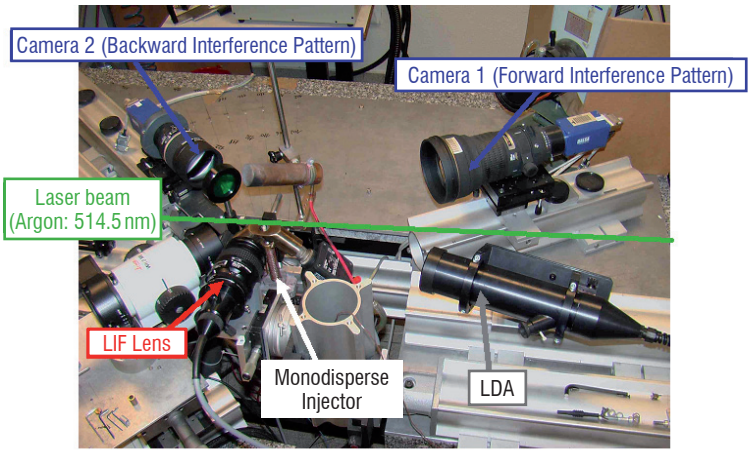

Figure 4 - Experimental set-up

Analysis of droplet diameter measurement for a two component droplet

The tests were performed with the deviator device. To get isolated droplet conditions, 32 out of 33 drops are deviated and the explored range of initial spacing parameter is 54 to 72. The spacing parameter is the ratio of the distance between two droplets and the droplet diameter.
The two components used are ethanol and n-butanol whose boiling temperatures are respectively 351.5 K and 390.9 K. The initial velocity is 6 m/s and the injection temperature is 296 K. The pure components and three mixtures are investigated.

The experimental setup was originally developed for a pure ethanol droplet. The evolution of the dimensionless droplet surface for both pure components and the three binary mixtures are presented in Figure 5. The initial mass compositions of the mixtures are ethanol 75 % - n-butanol 25 %, ethanol 50 % - n-butanol 50 % and ethanol 25% - n-butanol 75 %. All of the liquids present an almost constant evaporation rate after the heating phase at the beginning of the droplet lifetime. The period of this heating phase increases with the initial proportion of n-butanol in the droplet. Few values for ethanol 25 % - n-butanol 75 % and pure n-butanol are equal to or greater than the initial diameters at the beginning of the droplet lifetime. That can be explained by the droplet's thermal expansion, since the droplet does not vaporize enough to compensate for its expansion.

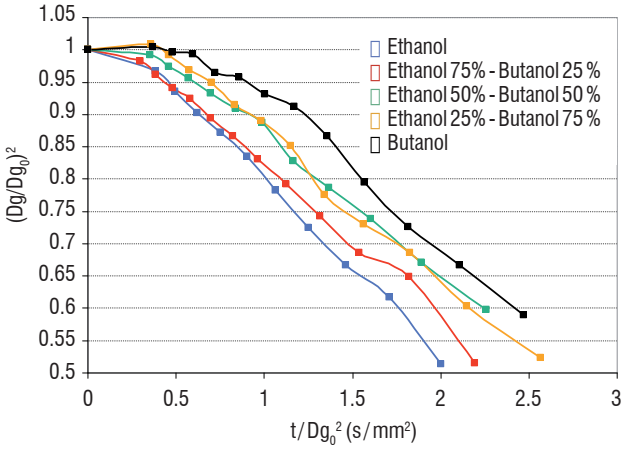

Figure 5 - Temporal evolution of the non-dimension droplet surface

Due to the presence of the vertical heated plate, the droplet's temperature cannot be measured. For the numerical prediction the initial temperature was chosen at 298 K for all liquids, which seems to be a correct value. A difference of 10 K in this initial temperature predicts a gap of only 1 μm at the end of the measurement range.
The model used here for comparisons with experimental data is the effective conduction model [9]. This model assumes a spherical distribution of the temperature inside the droplet but a correction factor for the liquid conduction coefficient is used to take the internal vortex effects into account. At the beginning of the vaporization process, the droplet heats up and there is a thermal expansion of the droplet's diameter. The thermal equilibrium is then reached and the droplet size follows the well-known d2-law behavior:

$$Dg^2 = Dg_0^2 - Kt$$

The results plotted on Figure 6 show this change. The comparison between the numerical results and the experimental measurements were used to validate the model. The results fit correctly, except for the pure n-butanol where a gap appears but the curves have identical slopes.

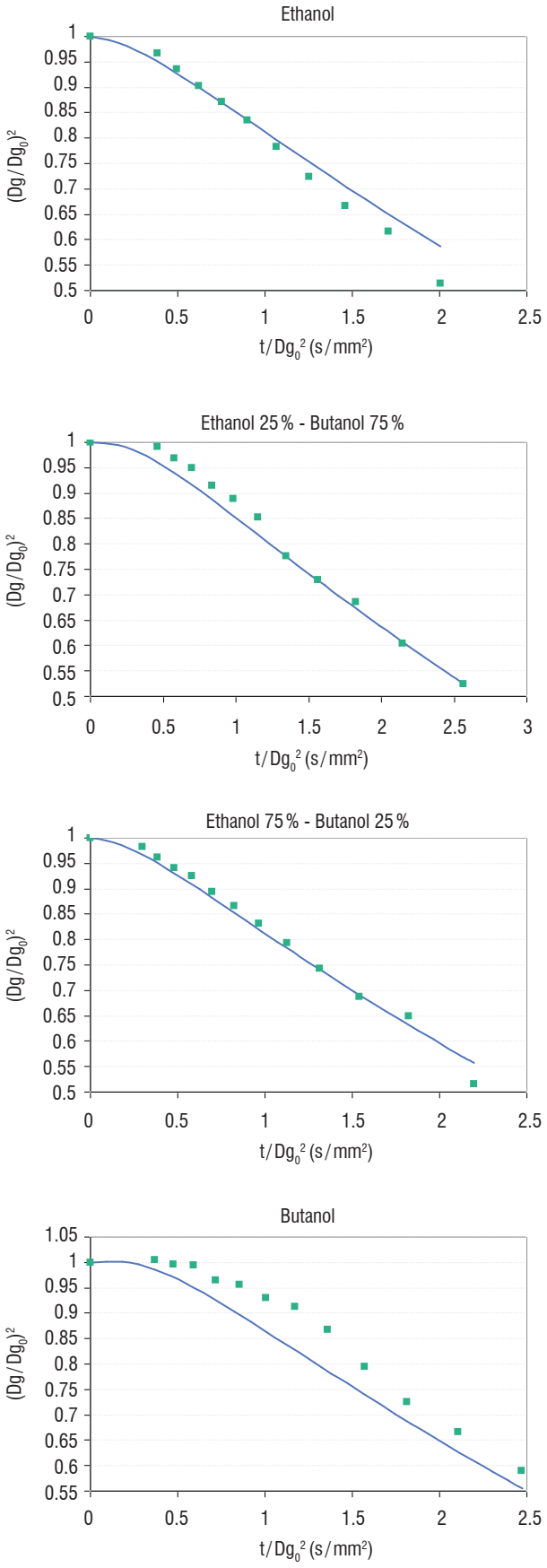

Figure 6 - Evolutions of non-dimensional droplet surface versus non-dimensional time along the heated plate. Comparison between experimental measurements (dots) and numerical predictions (line)

Droplet temperature measurement for ambient conditions vaporization

Two temperatures were experimentally measured. The first one was obtained from LIF technique and the measured temperature T_{LIF} was assumed to be the droplet's mean temperature. This was used to obtain a relationship between T_{LIF} and the temperature at the droplet's surface T_S and the temperature at the droplet's centre T_C. Considering a parabolic radial temperature profile in the droplet, the relationship which can be established is therefore

$$T_{LIF} = \frac{3}{5}T_s + \frac{2}{5}T_c$$

The second experimental technique used to measure the droplet temperature was the rainbow refractometry. The measured temperature is very sensitive to the thermal gradient inside the droplet. Consequently, a parametric study was performed to quantify the effect of the thermal gradient on the temperature measurement. The following equation was obtained for a parabolic change of the temperature in the droplet [9]:

$$T_{Rainbow} = -0.223(T_S - T_C) + T_C$$

Consequently, the temperature at the droplet's surface T_S and the temperature at the droplet's centre T_C were experimentally estimated from the measured temperatures T_{LIF} and TRainbow using the relationships obtained for each technique. These temperatures were compared with those computed by the effective conduction model which solves the heat conduction equation inside the droplet (Figure 7).
As expected, for every case, the experimental rainbow temperature was higher than LIF temperature measurement. The slope of the experimental curves is in a good agreement with the numerical computation. However, the experimental thermal gradient is more important than the computed one. Other experiments are in progress to understand these results and to solve this difficult point.

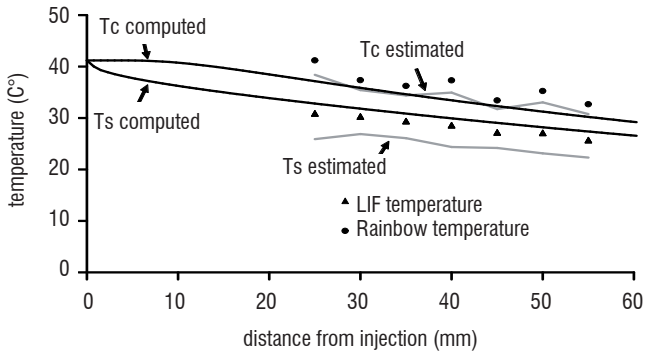

Figure 7 - Droplet temperature changes in a vaporizing monodisperse droplet stream

Investigation of a non-confined spray configuration

Introduction

In the real applications, such as turbojet combustors, polydisperse fuel sprays are injected. Thus, the measuring techniques cited in the previous section must be extended to the investigation of the more complex two phase flows configurations.
An experimental setup was developed at Onera in order to perform droplet temperature, size and velocity measurements (Figure 18).

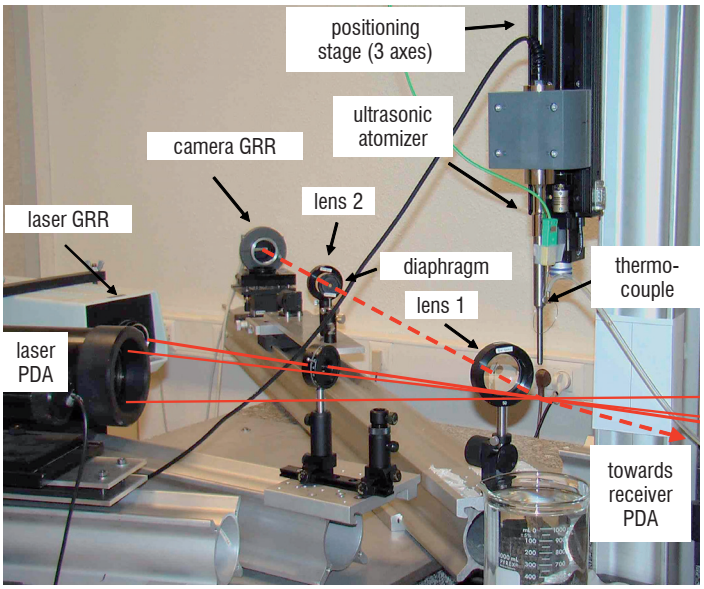

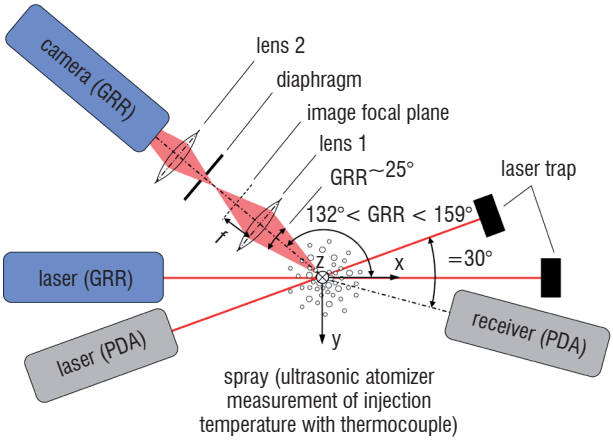

Figure 8 - Photograph and top-view of the experimental setup

The polydisperse spray is generated using an ultrasonic atomizer. The size distribution and the spray expansion are controlled by the amplitude of the generator excitation and by the liquid flow rate. The liquid temperature is measured with a thermocouple placed in the atomizer, close to the nozzle.
A commercial PDA system was used to measure the diameter and axial velocity of each droplet. The PDA receiver was placed in forward diffusion at 30° angular position. The scattered light at this position is dominated by the first order refraction for a parallel polarization.
An HeNe continuous laser, delivering a power of 30 mW, was used for the GRR technique. The droplets in the probe volume are illumi-

nated by the incident laser beam. The light scattered by the droplets is submitted to an optical Fourier transform through the first lens of the optical system. In this way, in the focal plane of the first lens, the scattered light intensity is expressed only as a function of the scattering angle and is independent of the droplet position in the probe volume. The image of the optical Fourier transform is reproduced by the second lens on the CCD linear sensor. A diaphragm placed in the image plane of the first lens can be used to control the size of the probe volume. The optical arrangement can be rotated in so that a large range of angles can be measured.

To successfully measure the temperature using the GRR technique, a relationship has to be found between the pixel number and the angular position of the scattered light intensity. This is done by using the same incident laser beam, reflected by a mirror placed in the probe volume. The mirror is fixed on a micrometric rotating plate. The reference angular position is established by superposition of the incident and reflected laser beams. Afterwards, the position of the illuminated pixel is recorded for different angular positions of the scattered light. A 3rd order polynomial correlation is used and the error is $\pm 0.001°$.

Since GRR only provides the refractive index of the droplets, a correlation between the refractive index and the liquid temperature needs to be determined. For some liquids, the literature gives such correlations. However, these results can be obtained by using the multispectral refractometer available in the laboratory. The results show a systematic linear change in liquid temperature as a function of the refractive index.

The droplet's mean temperature is determined from the global rainbow optical signal by using an inversion code, developed at the CORIA laboratory by S. Saengkaew and G. Gréhan [16, 18]. A mean refractive index and a size distribution are extracted by using the Non-Negative Least Square method (NNLS) with light intensity computed by the Nussenzveig theory and minimizing the distance between the recorded and computed global rainbow pattern.

For all of the measurements, the incident laser beam absorption is assumed to be too weak to influence the spray's temperature or droplets' evaporation.

A first feasibility study was carried out using the n-hexadecane (T_b=559 K), because of its very low evaporation rate, in order to avoid the thermal gradient in the droplet. The liquid was injected at the ambient temperature (T_{amb}~298 K).

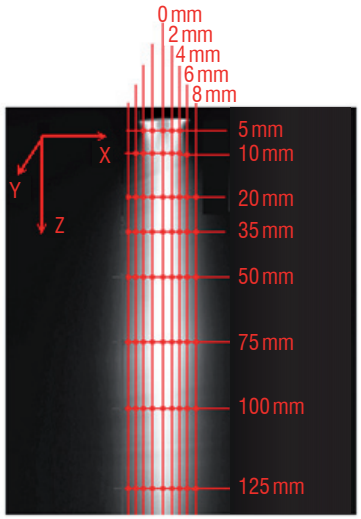

Figure 9 - Grid measurements in the spray

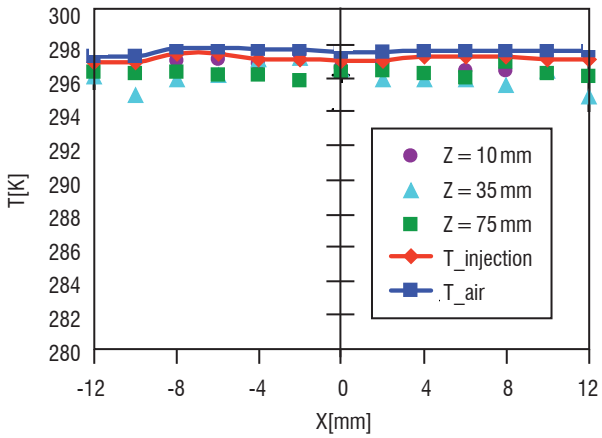

Figure 10 - Radial evolution of the temperature for the n-hexadecane

If the liquid and the air temperatures are equal, the spray temperature is constant and this parameter was recorded by the thermocouple placed inside the atomizer. Measurements were taken in the XZ plane in different locations in the spray (Figure 9). The grid was refined enough to build a very detailed data base for use in the validation of numerical approaches and available for other research work [3, 4].

The radial temperature changes, for three different distances from the nozzle, are plotted in Figure 10. The discrepancy between the GRR results and the thermocouple values is low, about 1 K. This can be explained by the effect of the very low droplet evaporation, due to the convection effect (relative velocity ~1 m/s) and by the accuracy of the technique.

Later, a more volatile liquid was studied. Experimental and numerical results are compared in the next section. The operating conditions are detailed in the Table 1.

Liquid	**n-octane**
Liquid temperature	~317.5 K
Air temperature	26.5±0.5 K
Volume flow rate	35 ml/min

Table 1 - Operating conditions for the non-confined flow

Spray numerical simulation

Spray numerical simulation is performed using a RANS approach. The code provides multiple modules, making it useful in the multiphase flow investigation.

As the experimental results show a quasi-symmetrical evolution of the spray pattern, a two dimensional configuration has been chosen for the computation. This approach significantly reduces the computing cost.

A two-way coupling processing of the spray behavior is performed through an Eulerian-Lagrangian stochastic approach using an effective conduction evaporation model. The unsteady technique used in this numerical computation consists of tracking a large number of numerical droplets representing a number of real droplets with similar properties: position, radius, velocity, temperature. The modeling of the droplets is done taking into account gravity, drag (Shiller & Neuman-model), heating (Ranz-Marshall model for the Nusselt number),

vaporization (Ranz-Marshall model for the Sherwood number) and turbulent dispersion (Langevin model)

The main advantage of a Lagrangian tracking technique is that it allows a detailed study of the droplets' dispersion, heat and mass transfer. However this approach needs as input data the initial droplet size and velocity distributions.

The size and velocity distributions as well as the temperature were measured at 5 mm from the atomizer.

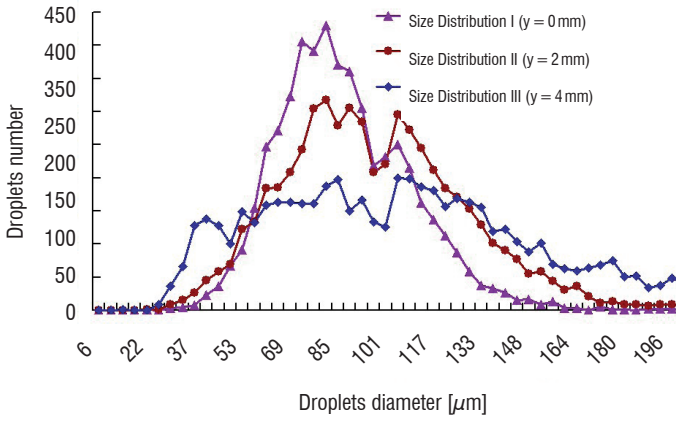

Figure 11 - Droplet size distributions at the exit of the atomizer (Z = 5mm)

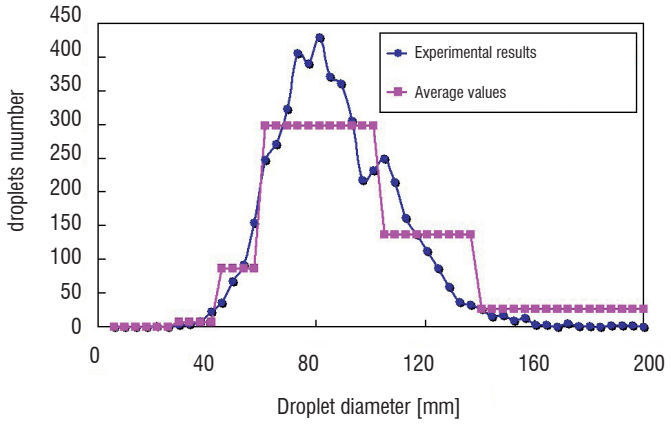

Figure 12 - Droplet size distribution modeling

The size distribution shape changes with the position of the measurement volume within the spray (Figure 11). This heterogeneity is taken into account as follow: every size distribution is supposed to be characteristic to a limited interval of the injector surface. Moreover, as it is almost impossible to use the real distributions provided by the PDA because of the great number of classes, the use of a simplified distribution is proposed. Thus only 5 classes are retained and the average technique is explained in Figure 12. In the case of the velocity, a mean value balanced with the droplet's mass is calculated for every class.

The droplet temperature, velocity and size results are of great interest for the comparison with the experimental data. Figures 13 and 14 present the axial and radial changes in the droplet's temperature. As the radial experimental measurements were carried out symmetrically in respect to the spray axis, the X^+ (GRR_I) and X- (GRR_II) changes were represented on the same side of the Z-axis.

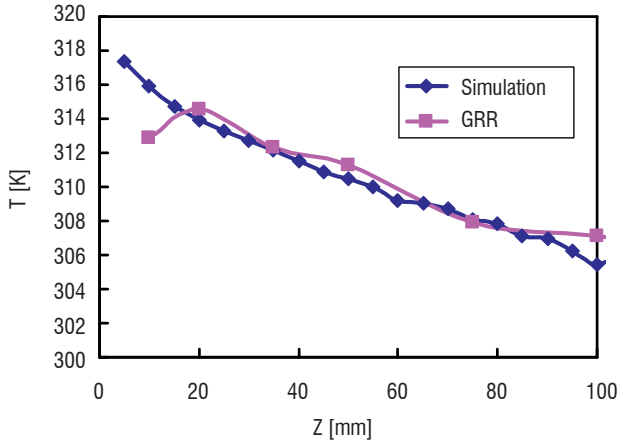

Figure 13 - Longitudinal change of the droplet temperature (Y=0 mm)

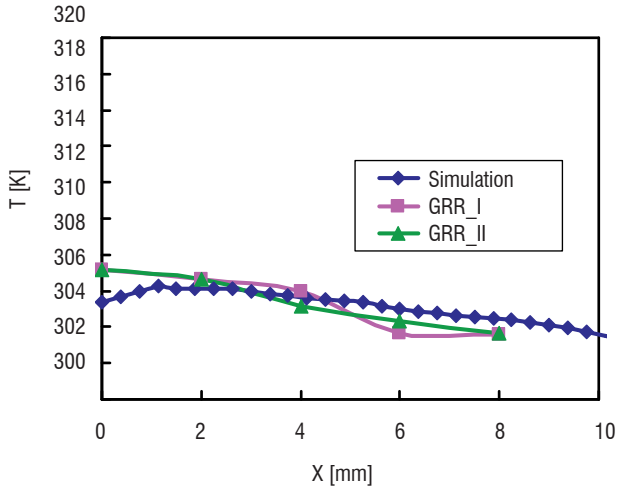

Figure 14 - Radial change of the droplet temperature (Z=100 mm)

Numerical and experimental results are in good agreement except in the near injector area. It seems that at Z = 5 mm and Z = 10 mm the temperature values provided by GRR technique are non-realistic as these values are significantly inferior to the liquid temperature. The liquid temperature is measured at the injector nozzle by the thermocouple. Actually, during the experimental measurement campaign it was realized that it is very difficult to obtain a realistic temperature under 20 mm from the spray nozzle. On the one hand, the high density of the dispersed phase suppresses the Global Rainbow optical signal by multiple scattering. On the other hand, the quality of the optical signal is altered by the non-spherical shape of the droplets present in this region of the spray. In order to avoid this problem, in the numerical simulation the injected droplet temperature is considered equal to the value gien by thermocouple located inside the atomizer (Figure 10). The temperature decreases with the radius because of the high thermal transfer between the two phases at the spray boundaries (Figure 14).

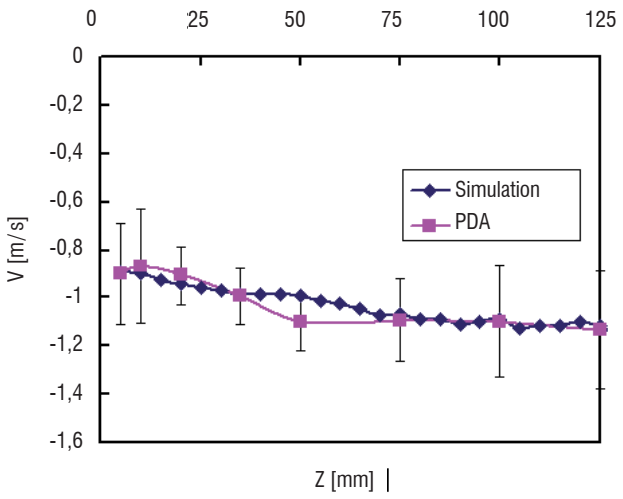

Figure 15 - Longitudinal change in the droplet's velocity (Y=0 mm)

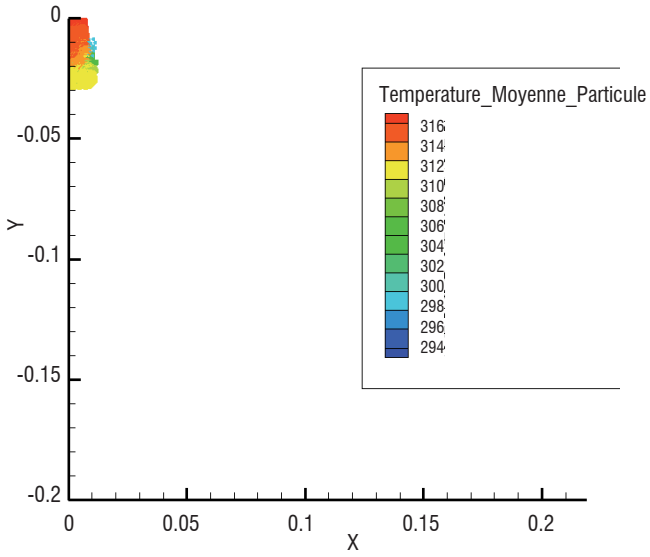

Video 2 - Numerical simulation of the emerging spray [3]

In the case of velocity, a close match was found in its change over time between the experiment and simulation, although there are local differences (Figures 15). Note that the plotted mean values for both curves were obtained by balancing the measured velocity values with the droplet mass.
The Video 2 concludes this work, showing the computed spray transition to the stable state. The droplets' behaviors inside a spray emerging in free stagnant air can be identified here.
As the numerical results seem to match the experimental ones, a numerical tool is available and can be used for different configurations. This tool must be extended to multi-component droplets if real fuels are concerned.

Spray investigation in turbulent and high pressure environments

Evaporating spray in highly turbulent flow at ambient pressure

The GRR and PDA techniques can also be used to measure the mean temperature, size and velocity distributions locally in confined flows. A special experimental facility was developed [4] during work to investigate the droplets' evaporation in a turbulent flow. A polydisperse spray is injected in a square cross-section channel in the presence of a highly turbulent flow (Figure 16). The nozzle of the ultrasonic injector is located at the entrance of the channel. The air enters the channel at a temperature of 410.5 K and the liquid is injected at 285.5 K. The measurements are taken in the XZ plane at different locations in the spray. The operating conditions are detailed in the Table 2.
For this experimental setup, Figure 17 presents, as example, the change in the droplet temperature for different radial positions. The temperature increases close to the channel's walls. Two different mechanisms can contribute to this behavior. On the one hand, the turbulent structures of the flow inside the duct are responsible for the non-homogenous droplet dispersion, especially for highly inertial droplets. The result is a spatial non homogeneity of the dispersed phase temperature. On the other, the channel's walls are at a higher temperature than the continuous phase. For this reason the droplets transported close to the channel borders heat up more.

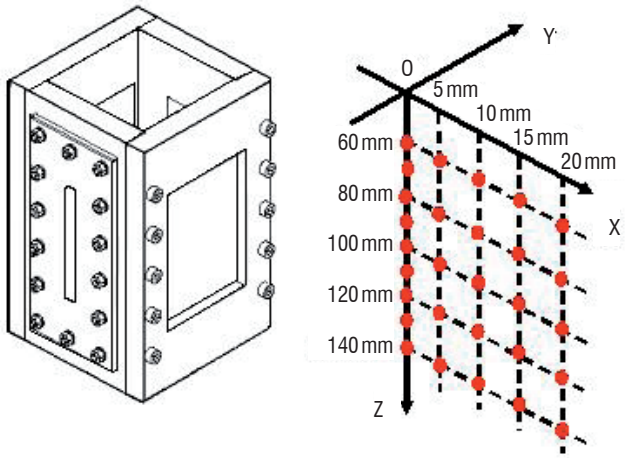

Figure 16 - Measurement positions inside the channel flow

Liquid	n-octane
Air temperature (at the nozzle position)	410 K
Air bulk velocity	1 m/s
Liquid mass loading	8.7 %
Liquid flow rate	0.41 g/s
Liquid temperature	285 K

Table 2 - Operating conditions for the confined flow

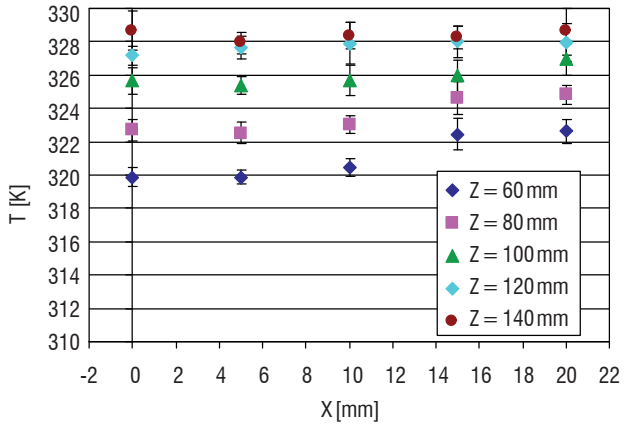

Figure 17 - Radial change in the droplets temperature in a square cross-section duct.

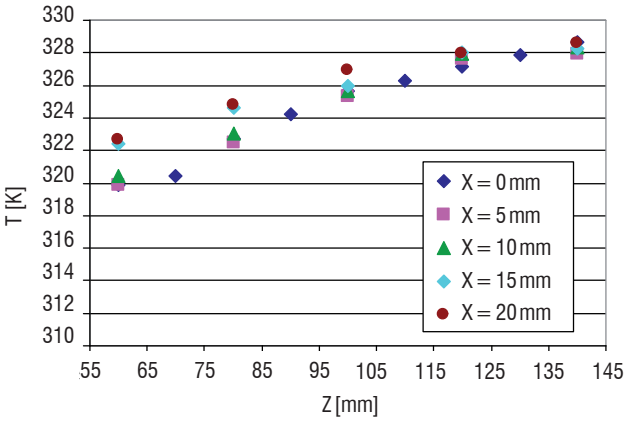

Figure 18 - Longitudinal change in the droplets temperature in a square cross-section duct.

The increase of the longitudinal temperature (Figure 17) proves that the droplets are still in the heating phase in the investigated distance range. Due to their large size, the droplets have not yet reached the equilibrium temperature. The investigations have to be extended downstream to get an overall change in the droplets temperature.
This work is on-going. A detailed data base on droplet size, velocity and temperature change will be built and used to validate the modeling of the behavior of droplet dispersion phase in a highly turbulent flow.

Pressurized spray characterization

Various experimental set-ups are available at Onera for reproducing the operating conditions in a turbojet combustion chamber. Thus, the LACOM test facility is used to characterize sprays in a high pressure and temperature environment by using optical techniques to build a very precise database for the validation of physical models in real conditions. Spray atomization, transport, evaporation, ignition phenomena are studied for kerosene or alternative fuels. The test rig is equipped with different windows for optical diagnostics (Figure 19). Laser tomography using high speed video camera gives the structure of the spray (Figure 20) and shows the different mechanisms leading to spray formation (Video 3).

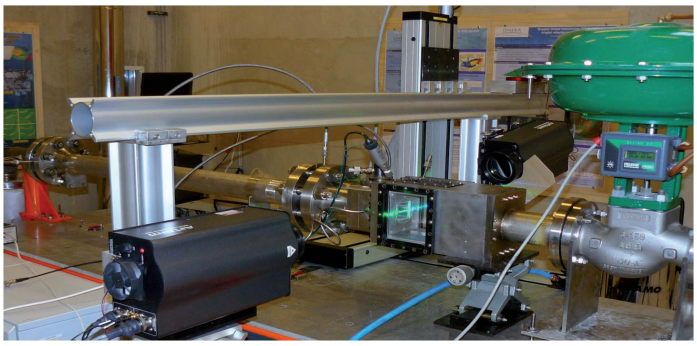

Figure 19 - LACOM facility

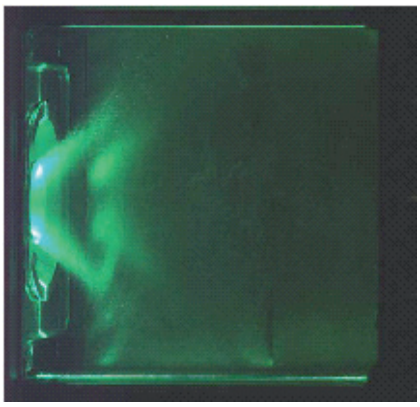

Figure 20 - Structure of the spray for a real injector (P = 4 bar, T = 450 K)

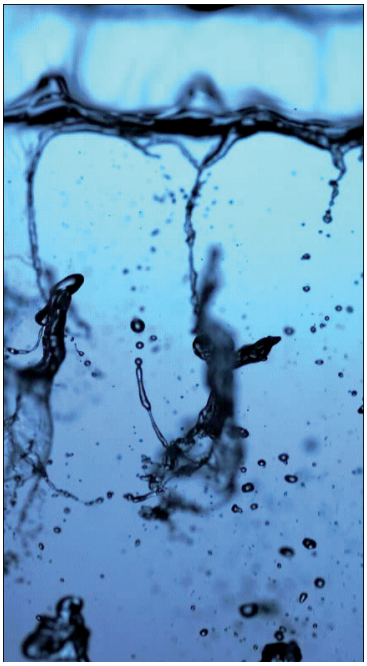

Video 3 - Liquid annular film atomisation for a simplified injector[11]

As an example of the PDA results, the Figures 21 and 22 present the radial change in the droplet size and velocity for two injected mixtures. This work has been done in the framework of the national program (CALIN) on the research for alternative fuels. This database will be completed in the near future with GRR temperature measurements.

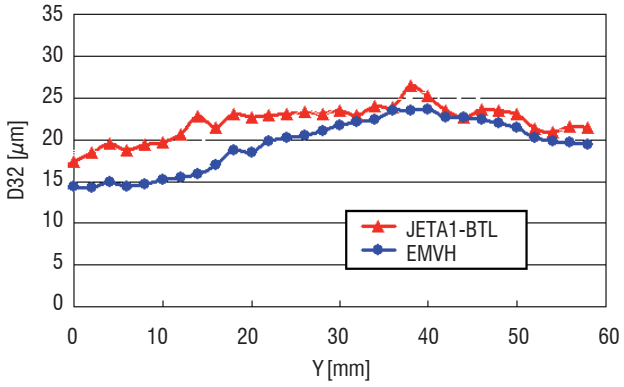

Figure 21 - Radial change in the droplet Sauter Mean Diameter (P=4 bar, T=450 K).

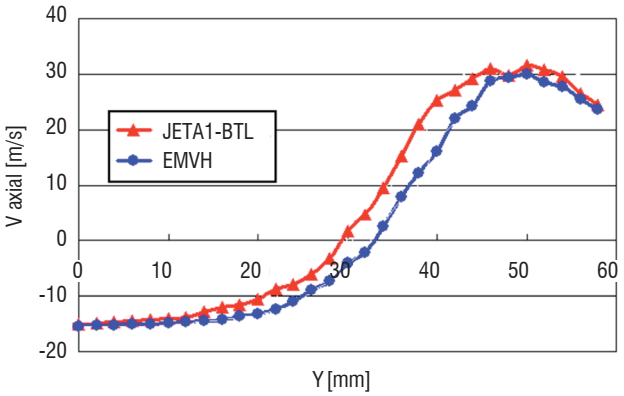

Figure 22 - Radial change in the droplet velocity (P = 4 bar, T = 450 K)

The influence of the environmental pressure (up to 12 bar) on the atomization process is now investigated for a planar liquid sheet configuration (Video 3).
The GRR technique will be applied in the near future to a burning cloud of multi-component droplets in the LACOM facility. The challenge is to demonstrate the capacity of the GRR technique to measure the droplet temperature in real burning sprays. To achieve this objective experimental and numerical investigations must be conducted in parallel.

Conclusions

The aim of this paper is to present the state of the art at Onera in the field of spray investigation using experiments and numerical simulation.
New optical techniques are developed and tested on different two phase flow configurations from monodisperse droplets stream to a highly turbulent evaporating flow in unconfined and confined conditions. The local and simultaneous acquisitions of droplet size, velocity and temperature by the coupling of these techniques present real advances in quantifying the air-fuel mixing and then the local equivalence ratio.
This research, carried out in cooperation with other laboratories, has made crucial progress in the understanding and the modeling of evaporating sprays. The local equivalence ratio measurement is a great challenge for the near future for investigating new injector designs and new fuels and then designing combustion chambers with low pollutant emissions. In parallel, the progress in the unsteady numerical approaches (LES) needs very detailed databases for validation □

Nomenclature

SRR	Standard Rainbow Refractometry	
GRR	Global Rainbow Refractometry	
GRT	Global Rainbow Thermometry	
LDA	Laser Doppler Anemometry	
PDA	Phase Doppler Anemometry	
LIF	Laser Induced Fluorescence	
EMVH	Mixture of biofuels	
BTL	Mixture of paraffin	
T_S	Temperature at the droplet surface	[K]
T_C	Temperature at the droplet centre	[K]
T_b	Boiling temperature	[K]
T_{amb}	Ambient temperature	[K]
K	Vaporization constant	[m2/s]
N	Refractive index	[-]
Φ	Laser wavelenght	[nm]

Acknowledgments
The authors are grateful to the ASTRA program founded by CNRS and Onera. This program deals with the study of multi-component sprays. They also would like to thank their Onera colleagues for their support.

References
[1] J.P.A.J. VAN BEECK - *Rainbow phenomena: Development of a Laser-based, Non-Intrusive Technique for Measuring Droplet Size, Temperature and Velocity.* PhD Thesis, Eindhoven University of Technology, 1997.
[2] J.P.A.J. VAN BEECK, L. ZIMMER and M.L. RIETHMULLER - *Global Rainbow Thermometry for Mean Temperature and Size Measurement of Spray Droplets.* Particle & Particle System Characterisation, vol. 18, pp. 196-204, 2001.
[3] V. BODOC, J. WILMS, Y. BISCOS, G. LAVERGNE and O. ROUZAUD - *Experimental and Numerical Investigation of a Monocomponent Polydisperse Spray*. 22nd European Conference on Liquid Atomisation and Spray Systems - ILASS 2008, Como, Italy.
[4] V. BODOC, F. MOREAU, YVES BISCOS, R. BASILE and G. LAVERGNE - *Experimental Investigation of Evaporating Bi-Component Droplets in a Turbulent Channel Flow*. 11th International Annual Conference on Liquid Atomisation and Spray Systems - ICLASS 2009, Vail, Colorado, USA.
[5] G. CASTANET - *Étude aérothermique d'un jet de gouttes monodispersé en évaporation et en combustion à l'aide de méthodes optiques*. PhD Thesis. Henri Poincaré University, Nancy, 2004.
[6] G. CASTANET, A. DELCONTE, F. LEMOINE, L. MEES, G. GREHAN - *Evaluation of Temperature Gradients within Combusting Droplets in Linear Stream Using Two Colors Laser-Induced Fluorescence*. Experiments in Fluids, vol. 39, pp .431-440, 2005.
[7] N. DOUÉ - *Modélisation de l'évaporation de gouttes multicomposants*. PhD Thesis, École Nationale Supérieure de l'Aéronautique et de l'Espace, 2005.
[8] C. LAURENT - *Amélioration et validation des modéles d'évaporation multi-composant*. PhD Thesis, ISAE 2008.
[9] C. LAURENT et al - *Thermal Gradient Determination Inside Vaporizing Droplets by Combining Rainbow and Laser Induced Fluorescence Measurements*. FEDSM 2006, July 17-20, Miami, USA.
[10] N. GARCIA ROSA, G. LINASSIER, R. LECOURT, P. VILLEDIEU, G. LAVERGNE - *A Two-Phase Model for Ignition in a Model Turbojet Combustor*. 11th International Annual Conference on Liquid Atomisation and Spray Systems - ICLASS 2009, Vail, Colorado, USA.
[11] V. GUTIERREZ FERNANDEZ et al - *Primary Atomisation in Water and Kerosene Liquid Sheets at High Pressure*. 11th International Annual Conference on Liquid Atomisation and Spray Systems - ICLASS 2009, Vail, Colorado, USA.
[12] P. LAVEILLE, F. LEMOINE, M. LEBOUCHÉ, G. LAVERGNE - *Mesure de la température de gouttelettes en combustion par fluorescence induite par laser à deux couleurs*. Résultats préliminaires et perspectives, comptes rendus de l'académie des sciences série IIB Mécanique, vol. 329, pp.557-564, 2001.
[13] P. LAVEILLE - *Étude expérimentale du comportement aérothermique de gouttes en écoulement, réactif ou non, par utilisation de la fluorescence induite par laser à deux couleurs*. PhD Thesis, Henri Poincaré University, Nancy I, 2001.
[14] P. LEMAITRE et al - *Développement de la réfractometrie arc-en-ciel global pour mesurer la température des gouttes en chute libre*. Proc. Symp. 9e Congrès Francophone de Vélocimétrie Laser, pp. F.2.1-F.2.9, 2004.
[15] N. ROTH, K. ANDERS, A. FROHN - *Simultaneous Measurement of Temperature and Size of Droplets in the Micro-Metric Range*. J. Laser Appl., vol.2, pp.37-42, 1990.
[16] S. SAENGKAEW et al - Rainbow refractometry: *On the Validity Domain of Airy's and Nussenzweig's Theories*. Optics Communications. vol. 259, pp. 7-13, 2006.
[17] S. Saengkaew et al - *Rainbow Refractometry on Particles with Radial Refractive Index Gradient*. Exp. Fluids, vol. 43, pp. 595-601, 2007.
[18] S. SAENGKAEW - *Study of Spray Heat Up: On the Development of Global Rainbow Techniques*. PhD Thesis, Rouen University, 2005.
[19] S. SAENGKAEW, Y. BISCOS, N. GARCIA-ROSA, T. CHARINPANITKUL, H. VANISRI, G. LAVERGNE, G. GOUESBET, L. MÉÈS, G. GRÉHAN - *Processing of Rainbow Signals from Individual Droplets*. The 20th ILASS-Europe Meeting, Orléans, September 2005.
[20] SUBRAMANIAN V. SANKAR, WILLIAM D. BACHALO - *Response Characteristics of the Phase Doppler Particle Analyzer for Sizing Spherical Particles Larger than the Light Wavelength*. Applied Optics, vol. 30, n°. 12.
[21] M.R. VETRANO et al - *Mesures de la température d'un spray d'eau chaude par la méthode globale par arc-en-ciel : effet du gradient de la température dans les gouttes*. Proc. Symp. 9e Congrès Francophone de Vélocimétrie Laser, pp. F.3.1-F.3.8, 2004.
[22] D. YILDIZ, J.P.A.J. VAN BEECK, M.L. RIETHMULLER - *Global Rainbow Thermometry Applied to a Flashing Two-Phase R134-A Jet*. Laser-Symposium, Lissabon 2004.
[23] J. WILMS, Y. BISCOS, S. SAENGKAEW, G. GRÉHAN and G. LAVERGNE - *Precision and Applicability of Global Rainbow Refractometry for Measurements in sprays*. Optics Communications , 2007.
[24] J. WILMS, G. GRÉHAN and G. LAVERGNE - *Global Rainbow Refractometry with Selective Imaging Method*. Part. Part. Syst. Charact., vol 25, pp. 39-48, march 2008.

Acronyms
GRR (Global Rainbow Refractometry)
GRT (Global Rainbow Thermometry)
NNLS (Non-Negative Least Square)
SRR (Standard Rainbow Refractometry)
LIF (Laser Induced Fluorescence)
PDA (Phase Doppler Anemometry)

Virginel Bodoc graduated from Military Technical Academy of Bucarest in 2003. Research engineer at the Military Equipment and Technology Research Agency between 2003-2006. Master Degree at the National Polytechnic Institute of Toulouse in 2007.
PhD Student in the multiphase flow group of Onera in the frame of the Marie Curie EST project ECCOMET. The thesis objective is the modelling of multicomponent droplet evaporation with application to alternative fuels.

Claire Laurent masters degree in Fluids Mechanics in 2005, PhD in Energetics and Transfers in 2008. Research engineer in the Onera multiphase flow group studying the droplet vaporization phenomenon (thermal conduction inside droplets, multi-component vaporization, …). Research activities focused on experimental validation of vaporization models and their development for implementation in CFD codes. Currently in charge of the development of thin film flow modelling in the multi-physics Onera CFD code CEDRE.

Yves Biscos a former engineer at Onera, now retired, has developed many experimental test benches for basic studies of evaporation and the combustion of jets of monodisperse drops. He is a specialist in new measurement techniques in diphasic flows.

Gerard Lavergne, PhD in Fluid mechanics in 1978, University of Toulouse (France) and HDR. Director of Research, in charge of multiphase flow research at Onera for propulsion systems applications. The research team is well known for the modelling of the main physical processes in combustors, namely: primary and secondary liquid-sheet breakup, droplet / wall (cold and hot) interaction, including shear-driven liquid film modelling, mono-component and multi-component droplet evaporation spray ignition under high-altitude conditions and droplet interactions in dense sprays (evaporation, collision, etc.).

N. Cézard
C. Besson
A. Dolfi-Bouteyre
L. Lombard
(Onera)

E-mail: nicolas.cezard@Onera.fr

Airflow Characterization by Rayleigh-Mie Lidars

This paper deals with lidar systems applied to airflow measurements. The properties of the two main light scattering processes, Rayleigh and Mie scattering, are presented and correlated to general but important rules for lidar design. The Rayleigh lidar developed at Onera for short-range wind speed measurements is also presented, and the Doppler analysis technique using Michelson fringe imagery is briefly discussed.

Introduction

The principle of LIDAR (Light Detection and Ranging) is very similar to that of RADAR (Radio Detection and Ranging). Radars emit radio wavelengths to detect echoes on targets of a significant size (typically >1 mm) whereas lidars use optical wavelengths generated by lasers to detect signals backscattered by much smaller elements, like dust, particles, or even gas molecules. For aeronautic applications, weather radars are commonly used to locate and characterize clouds, rainfall and storms. Lidar systems can be very useful for determining physical and chemical properties in the atmosphere, especially in clear air (no clouds).
With regard to airflow characterization, lidar systems fall into two main categories:

- Systems that detect or characterize the airflow disturbances imprinted by an aircraft on the atmosphere. These are generally ground-based systems (sometimes airborne), well-suited for ground tests or measurements during take-off and landing phases. These measurements are important because aircraft-generated airflows can be dangerous for the aircraft itself or for neighboring ones (see wake vortices, detailed in paper [6]).

- Systems that characterize the natural state of the atmosphere in front an aircraft. These are airborne systems, as shown in figure 1. For example, a long-range forward-looking lidar could be used to detect hazardous turbulence early enough to avoid it, or at least to secure passengers and crew. Shorter-range lidars could also be used to anticipate atmospheric parameters (such as air speed, temperature, density), so as to improve automatic flight control systems and reduce turbulence-induced stresses [1-5].

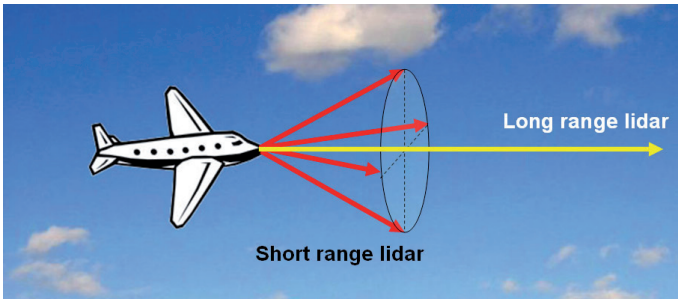

Figure 1 - Long-range lidars could be used for turbulence detection, at least early enough to warn passengers to sit down and fasten their seat belts. Short-range lidars could be used for air data measurements to provide accurate input for automatic flight control systems.

Light scattering in the atmosphere and lidar design

Light scattering in the atmosphere occurs by two main processes: Rayleigh and Mie scattering. Rayleigh scattering involves essentially gas molecules (diameter of about 0.1 nm), while Mie scattering implies airborne aerosols of much bigger size (10 nm to 10 μm). These processes have very different characteristics, which are summarized in Box 1. For lidar design, the particularly important factors are the backscattering coefficient β ($m^{-1}.sr^{-1}$) and the width γ ($m.s^{-1}$) of the velocity distribution of scatterers along the lidar line of sight (LOS).

The key role of β and γ for lidar design can be highlighted by considering the example of wind speed measurements with a pulsed laser. The measurable speed u is the wind speed projected on the lidar LOS. It is deduced from the measurement of the Doppler frequency shift $\Delta\nu = 2\mu/\lambda_L$, between the laser spectrum (assumed to be monochromatic of wavelength λ_L here), and the central frequency of the backscattered signal. Because the lidar signal is always corrupted by at least the photon noise, carried by the signal itself, the achievable accuracy of Doppler-shift measurements is fundamentally limited. The minimum error standard deviation ε in m/s is given by:

$$\varepsilon = \kappa \frac{\gamma}{\sqrt{N_e}} \quad \text{with } \kappa > 1 \qquad (1)$$

where κ is a constant depending on the Doppler-shift analysis technique (for optimized systems, κ can be as low as 2), γ is the standard deviation of the scatterer's velocity distribution along the lidar LOS, and N_e is the number of charge carriers generated by the lidar signal impinging on the photodetector, given by the so-called "lidar equation":

$$N_e = N_P T \eta \beta \frac{A}{z^2} \Delta z \qquad (2)$$

where N_p is the total number of emitted photons (in one or several laser pulses), T is the global optical transmission factor, η the photodetector quantum efficiency, β the backscattering coefficient, A/z^2

the solid angle of reception (receiver area A at distance z), and Δz the thickness of the atmospheric cell considered as the measurement volume (selected by time gating).

Equation (1) shows that for Doppler measurements, the Mie signal is far more valuable than the Rayleigh signal, because of the ratio between γ_{Mie} and γ_{Ray}. For example, to reach an accuracy of $\varepsilon = 1$ m/s with an instrument working at $\kappa = 2$, the required number of charge carriers N_e would be only 100 for a Mie signal, but 350,000 for a Rayleigh signal (assuming $\gamma_{Mie} = 5$ m/s and $\gamma_{Ray} = 295$ m/s - see box 1)!

On the ground or at low altitudes, the particle concentration can be high. Since the Mie signal level required to reach a good accuracy is low, it is possible to use lidar systems of moderate powers. Nowadays, using telecom components, compact and efficient infrared Mie Doppler lidars can be built (see paper [6]). These systems are not

Box 1 - Light scattering in the atmosphere

	Rayleigh Scattering	Mie Scattering
Named after	British scientist John W. Strutt, also known as Lord Rayleigh (1842-1919)	German scientist Gustav Mie (1869-1957)
Scatterers *type*	Essentially molecules. In air, the major contributors are O_2 and N_2.	Dust, water droplets, ice crystals, soots… Generally referred to as "particles" or "aerosols"
size	The typical size is about 0.1 nm	Between 10 nm and 10 µm (depending on the particle type)
1-D velocity distribution (a)	* Quasi-Gaussian distribution * Average velocity = wind speed * Standard deviation γ_{Ray} depends on temperature T and scatterer mass m $\gamma_{Ray} = \sqrt{k_B T / m}$ (k_B: Boltzmann constant) For air, γ_{Ray}=295 m/s at 288 K	* Lorentzian distribution * Average velocity ≈ wind speed * Standard deviation γ_{Mie} is small because particles are much heavier than molecules γ_{Mie} ≈ a few m/s
Light Polarization	Rayleigh scattering leaves polarization almost unchanged (less than 2 % depolarized)	Mie scattering by spherical particles (e.g water droplets) does not affect polarization, but non spherical particles (e.g ice crystals) can strongly depolarize
Backscattering coefficient β $\beta = \sigma\rho$ σ: backscattering cross-section ($m^2.sr^{-1}$) ρ : scatterer concentration (m^{-3})	* σ is strong wavelength dependent: it is proportionnal to λ^{-4} * ρ decays exponentially with altitude h The decay parameter is called the "scale height" (average value 8 km). → Backscattering coefficient β_{Ray}: $\beta_{Ray} \approx 8.10^{-6} \exp\left(-\frac{h(km)}{8}\right)\left(\frac{355}{\lambda(nm)}\right)^4$	* σ is proportionnal to λ^{-r}, with $1.2 < r < 2.4$, depending on the particle type. * ρ varies by orders of magnitude due to a variety of factors, mainly altitude and weather conditions but also local pollution. → Backscattering coefficient β_{Mie} is often expressed in terms of β_{Ray}. A parameter $\alpha > 1$ is defined, called « scattering ratio ». $\beta_{Mie} \approx (\alpha - 1)\beta_{Ray}$

(a) The one-dimensional velocity distribution is the 3D-distribution projected on the lidar line of sight (LOS)

powerful enough to make use of the Rayleigh signal but they do not need to. The Rayleigh signal is then ignored or discarded.

The situation changes at high flight altitudes however, because the particle concentration can drop by several orders of magnitude and becomes unpredictable. The constant availability of Doppler measurements with Mie lidars cannot therefore be guaranteed over a whole flight path. Rayleigh lidars then appear as a possible solution to this problem, inasmuch as molecules are always available in the atmosphere. They are also valuable because they can provide information about the air density and temperature (not measurable with Mie lidars). Today, most Rayleigh lidars operate in the ultraviolet wavelength range to maximize the backscattering coefficient β_{Ray} (proportional to λ_L^{-4}), and reach the high signal levels that are required to obtain satisfactory accuracy. The lidar range is also frequently reduced to gain more signal and to increase accuracy. Long-range applications nonetheless remain possible, but require higher integration times.

An example of a Rayleigh lidar system at Onera

Studies at Onera have covered various applications of Rayleigh lidars, from long-range systems for turbulence detection to short-range systems for air data measurements. We present here as an example a short-range system developed at Onera, demonstrating the feasibility of an all-altitude air speed sensor using a Rayleigh lidar. For this system, it was necessary to design a Doppler shift measurement method that would remain unbiased regardless of the strength of the Mie component. The selected spectral analysis technique uses interferometric fringe imagery, which is an efficient technique at short-range. Michelson interferometry was chosen from among the various possibilities because of its simplicity. The principle is detailed in box 2. In short, the atmospheric backscattered signal generates an interference fringe pattern on a detector, and the phase of the fringes varies linearly with the wind speed.
The lidar built at Onera (laboratory prototype) is depicted on figure 2. It uses a 355 nm laser source. Because the laser frequency can vary slightly from pulse to pulse, the instrument derives the wind speed from a differential phase measurement. With each laser pulse, the fringe patterns produced by the lidar signal and by the emitted laser pulse are recorded with a very small time delay, and their phases are compared. This measurement method has allowed robust daytime

Box 2 - Speed measurement using Michelson fringe imagery

A Michelson interferometer is depicted below:

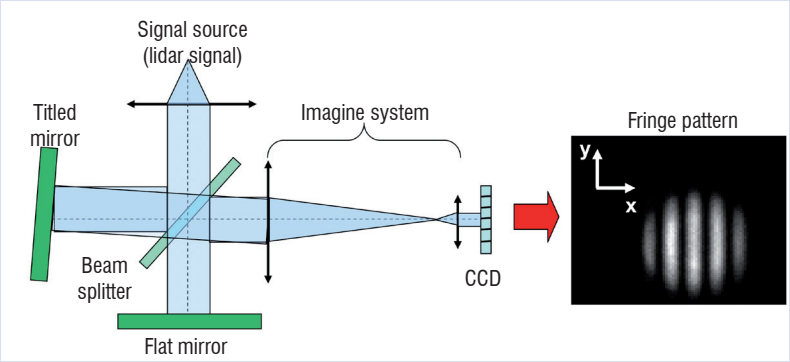

Michelson interferometer in mathematical terms

The Michelson interferometer "computes" the auto-correlation function of the lidar signal. This latter is equal to the Fourier Transform of the signal power spectrum (Wiener-Khinchine theorem). A Doppler shift in the frequency domain thus naturally translates into a phase variation of its Fourier Transform (= fringe phase shift).

The interference between the waves traveling in the flat mirror arm and tilted mirror arm produces a periodic pattern of straight fringes, which can be imaged on a CCD camera. The fringe phase, which refers to an arbitrary point of the detector, depends on the path difference of the waves at that point, and thus on the mean wavelength of the analyzed spectrum. Consequently, the fringe phase variation $d\phi$ is proportional to the wind speed variation du according to following equation:

$$d\phi = \frac{4\pi\Delta_0}{c\lambda_L} du$$

where Δ_0 is the interferometer path difference, λ_L the laser wavelength, and c the light velocity. Two important characteristics may be noted:

- the phase sensitivity $d\phi/du$ remains unchanged whatever the strength of the Mie component. Thus the fringe phase shift measurement method is unbiased regarding Mie scattering,
- the phase sensitivity is proportional to the path difference Δ_0. However, one cannot increase Δ_0 indefinitely because the fringe contrast decreases with Δ_0. Indeed, the coherence length of the Rayleigh signal is quite short (broad spectrum). Consequently, there is an optimal value of Δ_0 that minimizes the wind speed measurement error ($\Delta_0 \approx 3$ cm for a 355 nm Rayleigh lidar).

measurements. The Michelson fringe imagery method also allows for unbiased speed measurements regardless of the strength of the Mie signal. Without the Mie signal, pure Rayleigh fringes are obtained, and if a Mie signal is added, fringes with a higher intensity, higher contrast, but the same phase, are obtained. Consequently, rather than being a disturbing effect, the occurrence of Mie scattering is beneficial, though not essential, to this technique.

Conclusion

Lidar systems optimized for Rayleigh or Mie signals are quite different systems, operating with different wavelengths, power levels and spectral analysis methods. Nevertheless, they are complementary instruments to characterize airflows. Rayleigh signals are more reliable, and can provide more information (speed, temperature, density), but generally require high energies. Mie signals require lower energies and are well-suited for speed measurements when the particle concentration is sufficiently high ■

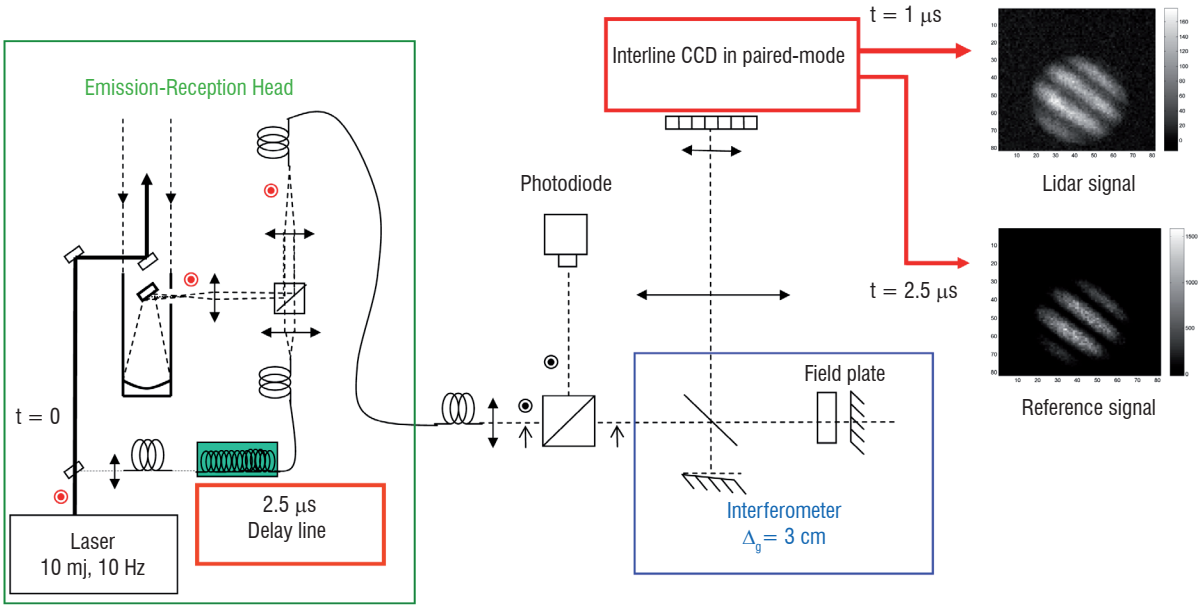

Figure 2 - This 355 nm Rayleigh-Mie Doppler lidar derives the wind speed from the differential phase measurement between fringes generated by the emitted laser pulse fringes and the atmospheric signal. With each laser pulse, the small time delay (2.5 µs using a 500 m fiber delay) between fringe records allows for minimization of the thermo-mechanical disturbances in the interferometer. The interferometer also comprises a field plate to match the fiber field angle at the interferometer input.

References

[1] N. CEZARD, A.DOLFI-BOUTEYRE, J.-P. HUIGNARD, P. FLAMANT - *Performance Evaluation of a Dual Fringe-Imaging Michelson Interferometer for Air Parameter Measurements with a 355 nm Rayleigh-Mie Lidar.* Appl. Opt. 48, 2321-2332 (2009).

[2] P. FENEYROU, J.-C. LEHUREAU - *A Performance Evaluation for Long-Range Turbulence Detection Using UV Lidar.* Proc. of 24th ILRC, p.252 (2008).

[3] N. P. SCHMITT, W. REHM, T. PISTNER, P. ZELLER, H. DIEHL, P. NAVÉ - *Airborne Direct Detection UV LIDAR.* Proc. of 23rd ILRC, p.167 (2006).

[4] R. TARG, M. J. KAVAYA, R. M. HUFFAKER, AND R. L. BOWLES - *Coherent Lidar Airborne Windshear Sensor: Performance Evaluation.* Appl. Opt. 30, 2013-2026 (1991).

[5] P. TCHORYK, C. WATKINS, S. LINDEMANN, P. HAYS, C. NARDELL - *Molecular Optical Air Data System (MOADS).* Laser Radar Technology and Applications VI, SPIE Proc. Vol. 4377 (2001).

[6] A. DOLFI-BOUTEYRE, B. AUGERE, M. VALLA, D. GOULAR, D. FLEURY, G. CANAT, C. PLANCHAT, T. GAUDO, C. BESSON, A. GILLIOT, J-P CARIOU, O PETILON, J. LAWSON-DAKU, S. BROUSMICHE, S LUGAN, L. BRICTEUX, B . MACQ - *Aircraft Wake Vortex Study and Characterisation with 1.5 µm Fiber Doppler Lidar.* Aerospace Lab n°1, December 2009.

AUTHORS

Nicolas Cézard graduated from the "Institut National des Sciences Appliquées" Toulouse, in 2003, and received a Ph.D degree in physics from Ecole Polytechnique, Paris, in 2008. He is currently working as a lidar engineer at Onera.

Agnès Dolfi-Bouteyre graduated from the "Ecole Supérieure d'Optique", Orsay, (1986) and received a PhD degree in Physics from University Paris XI Orsay (1990). She joined Onera in 1990 where she has been involved in lidar systems development for defence or aerospace.

Claudine Besson received her Ph.D. degree in physics from the Optics Graduate School, Paris, France in 1989. She is currently a senior scientist and research group leader at Onera. Her current research interests are fiber lasers and LIght Detection And Ranging systems.

Laurent Lombard received the Engineering Diploma from the "Ecole Superieure d'Optique, Institut d'Optique" Orsay, France, in 2002 and the Ph.D degree from the University of Paris XI, France, in 2005. Since 2006, he is a research scientist at Onera, Palaiseau, France. His current research deal with high power fiber lasers, lidars and optical beam processing.

A. Dolfi-Bouteyre, B. Augere, M. Valla, D. Goular, D. Fleury, G. Canat, C. Planchat, T. Gaudo, C. Besson, A. Gilliot (Onera)
J.-P. Cariou, O. Petilon, J. Lawson-Daku (Leosphere)
S. Brousmiche, S. Lugan, L. Bricteux, B. Macq
(Université catholique de Louvain)

E-mail: Agnes.Dolfi-Bouteyre@onera.fr

Aircraft Wake Vortex Study and Characterization with 1.5 μm Fiber Doppler Lidar

For ten years now, Onera has been developing lidar tools for wake vortex detection and studies. Since 2003, new developments based on 1.5 μm fibered laser sources have been achieved in parallel with extensive research work on the laser sources themselves. Three innovative lidars have been developed and are presented in this paper:
1) A mini-lidar, based on a CW (continuous-wave) 2 W / 1.5 μm laser source, for aircraft model wake vortex characterization in a catapult facility. A self-triangulation technique allows the vortex core position to be found with 10 cm error, and the circulation error is 10 %.
2) A pulsed 1.5 μm lidar, based on a 50 μJ / 15 kHz MOPA (Master Oscillator Power Amplifier) source, for lateral wake vortex monitoring at airports. The range is 400 m, the core position error is about $\pm$ 2 m and the circulation error is about 10 %.
3) A pulsed 1.5 μm lidar, based on a 120 μJ / 12 kHz MOPA source, for onboard axial wake vortex detection. Ground based lidar tests at Orly airport have demonstrated wake vortex detection up to 1.2 km.

Introduction

Detecting atmospheric hazards such as wind shear, clear air turbulence and wake vortices has been a major concern for twenty years. The lift force exerted on the aircraft wing creates a counter-rotating pair of trailing vortices (wake vortex) which constitute a potential hazard to following aircraft. Detecting these vortices is of crucial importance for flight safety, airport capacity and aircraft design [1].
The experimental techniques used to study wake vortices include coherent lidar (light detection and ranging), also called coherent laser radar or CLR. Coherent lidars are practical and efficient tools to characterize and monitor wind fields and more specifically wake vortices [2], [3], [4]. The measurement of the Doppler shift of light (from a laser source), after scattering from atmospheric particles, implies the line-of-sight flow velocity and allows a picture of vortex flow to be built up. Monitoring of vortices at ranges exceeding a few hundred meters is best carried out using pulsed lidar. Detailed measurements at short range are better obtained with CW (continuous-wave) lidar [5]. Lidars have the potential to help with low-vortex wing design and for quantifying the vortex hazard from existing aircraft.
Because low-vortex wing design requires extended measurements, reduced-scale test facilities such as wind tunnels, water tanks or catapults have been used to perform easy and low-cost measurements. Full-scale measurements are however necessary to check the atmospheric impact on wake vortex evolution and lidar is the link between reduced-scale and full-scale approaches.

Onera has been developing these coherent detection lidar tools for wake vortex characterization and monitoring for ten years now. New developments are based on 1.5 μm fiber laser sources, which have a high electrical to optical efficiency $\sim$10 %, thus allowing for low electrical consumption. This wavelength is also the most favorable for eyesafe lidar designs: as the maximum laser energy imposed by eye safety regulations is high, the laser power can be increased with little constraint on the lidar operation or design. It is now well-established that a fiber architecture is easy to adjust and mechanically reliable in a vibrating environment; other advantages are the compactness and flexibility in terms of onboard installation. The lidar can be split into subsystems, far apart in the aircraft body and linked by fiber optics. 1.5 μm fiber coherent lidars have recently been flown with success [5], [6].
In this paper we will present the most recent lidar developments at Onera for wake vortex characterization and monitoring. The coherent detection lidar technique and architecture are first described. Then we present reduced-scale measurements with a self-triangulation CW technique. The measurements are compared with PIV (particle imaging velocimetry) for ground-based tests (Box 1). The rest of this article deals with full-scale measurements at airport sites with pulsed lidar. The lidar developed for transverse wake vortex measurements is presented. Finally, we describe a future onboard pulsed lidar for axial wake vortex detection based on a high-brightness large-core fiber amplifier (Box 2: comparison between full-scale and reduced-scale measurements).

Coherent detection lidar principle and wake vortex detection application

Coherent detection lidar principle

Accurate distant wind velocity measurements are possible with laser anemometry based on coherent detection lidar (Figure 1). A laser beam is focused on atmospheric aerosols, and then reflected by Mie diffusion. The reflected beam is frequency shifted because of relative displacement between the aerosols and the lidar (the Doppler effect). In order to measure the radial velocity information contained in the beam phase, the backscattered beam is mixed in an optical interferometer with a reference beam (the LO or local oscillator). Thanks to a close optical frequency match between the backscattered beam and the LO, this coherent beam combining allows for a convenient transposition into the radiofrequency domain. The electric current given by the optical detection (the so-called heterodyne current) is described by:

$$i_{het}(t) = \sqrt{2.K.P_S.P_{LO}}.\cos(2\pi(f_s - f_{LO} + f_D).t + \phi) \quad (1)$$

where K is a coefficient taking into account heterodyne efficiency and detector efficiency, P_s is the backscattered beam power, P_{LO} is the local oscillator beam power, fs is the laser source frequency, f_{LO} is the local oscillator frequency, φ is the heterodyne signal phase, f_D is the Doppler frequency given by $f_D = \frac{2.V_r}{\lambda}$ where V_r is the radial velocity, and λ is the laser beam wavelength. The shift f_D is 1.3 MHz per m/s for a laser wavelength of 1.54 μm.

In practice, the LO beam is additionally shifted (via an acousto-optic modulator) by typically F = 40 MHz or 70 MHz, depending on the application.The heterodyne signal frequency is then $f_S - f_{OL} + f_D = \Delta f + f_D$. Moreover, the term $\sqrt{2.K.P_S.P_{LO}}$ in the heterodyne current shows that coherent detection enhances the detection sensibility by multiplying the very weak backscattered signal power by the local oscillator power.

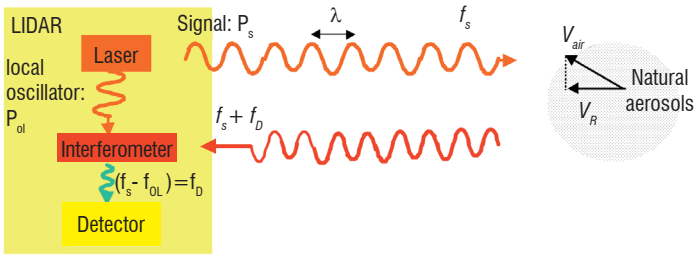

Figure 1 - Coherent detection lidar principle.

Wake vortex characterization

An aircraft in flight always creates vortices in its wake, and their strength increases with the mass of the aircraft. In a plane perpendicular to the aircraft path, the largest vortices are generated at the wingtips. These are large masses of rotating air with induced tangential velocities as high as 30 m/s.
In order to characterize wake vortices with a lidar, a scanning device is used as shown in Figure 2.

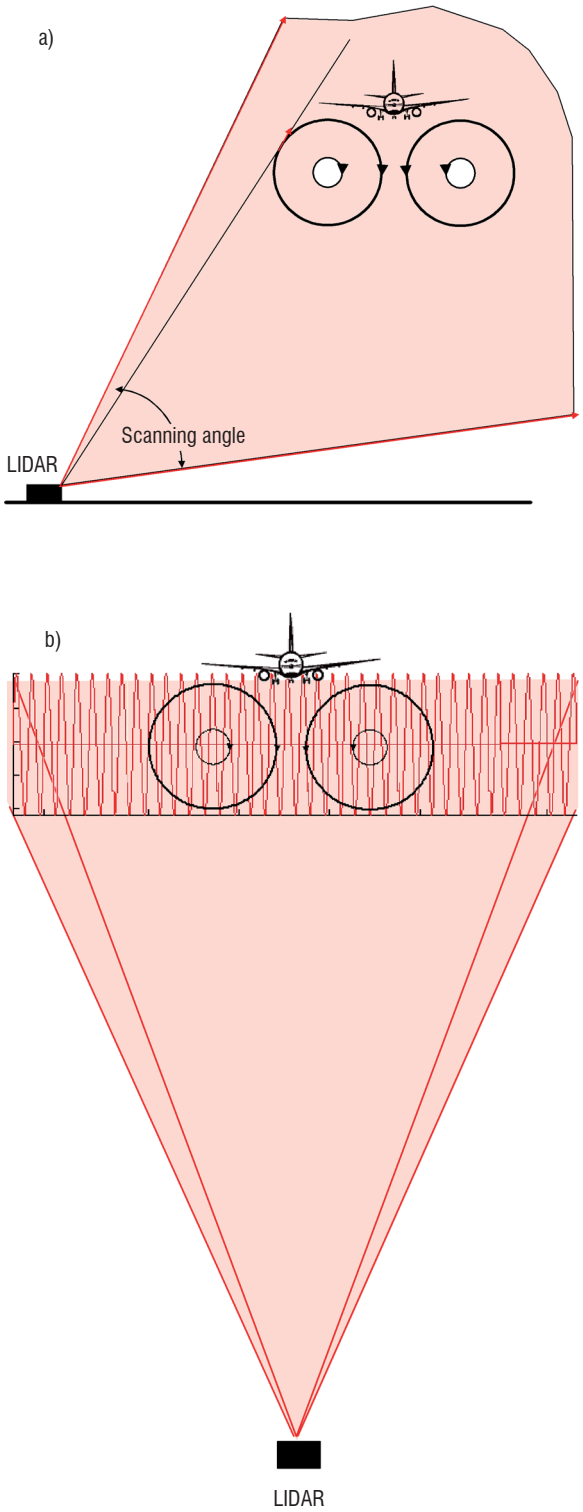

Figure 2 - Lidar scanning pattern: (a) for lateral wake vortex detection, (b) for axial wake vortex detection.

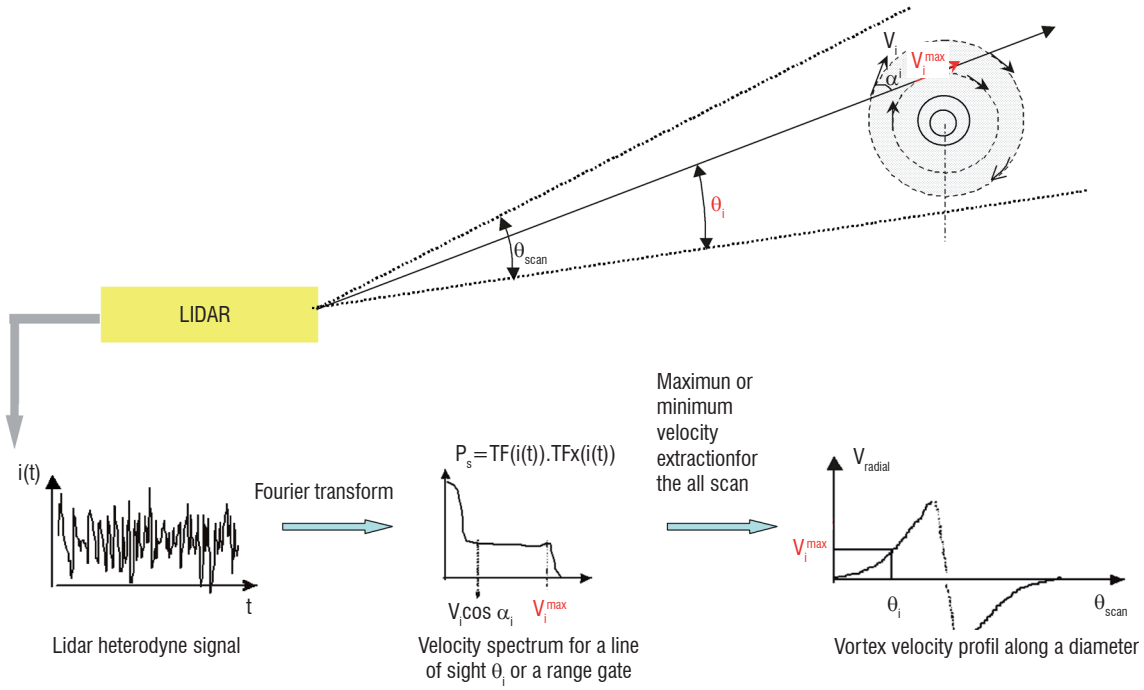

Figure 3 - Signal processing scheme for lidar lateral characterization of a vortex.

Lateral detection and characterization

For lateral detection, the scan is in a plane perpendicular to the aircraft path (Figure 2a) so the measured tangential velocities are very high. The signal processing usually associated with this lateral (sideways on) detection is detailed in Figure 3. A Fourier-transform power spectral estimate for the heterodyne signal yields a weighted velocity distribution (weighted along the whole line of sight for CW lidar, or within the range gate for pulsed lidar). For a scan angle θ_i the highest velocity measured (in absolute value) is the tangential one shown as V_i^{max}. The maximum (or minimum) velocity extraction for each line of sight or range gate enables us to reconstruct the velocity profile along a diameter of the wake vortex.

Axial detection

A pulsed laser allows the wind field to be spatially resolved along its line of sight, and scanning of the laser (e.g. the sinusoidal scan of Figure 2b) allows for the generation of an accurate 3D velocity image of the wind field.

Wake vortex axial detection is more difficult because the radial velocity components (the projections of the 3D air velocity on the lidar beam axis) are very low. Instead of radial velocity, it is easier to detect the spectral broadening due to vortex turbulence.

Reduced-scale measurements

The Onera catapult facility offers the possibility of observing the total lifetime of the wake, starting from its origin at the wing, up to about a hundred wingspans. In this facility, non-motorized free-flying scale models are propelled by means of a pneumatic catapult via a trolley. Once launched, the model flies freely without any wall or mounting interference in a 90 m long, 20 m wide and 20 m high observation area. Afterwards, the model is recovered from a volume of plastic foam (Figure 4). Reduced-scale aircraft models have wingspans in the 2 m range (Figure 5).

Oil droplets are generated to seed the vortices. Lidar measurements in vertical observation planes, transverse to the flight path of the model,

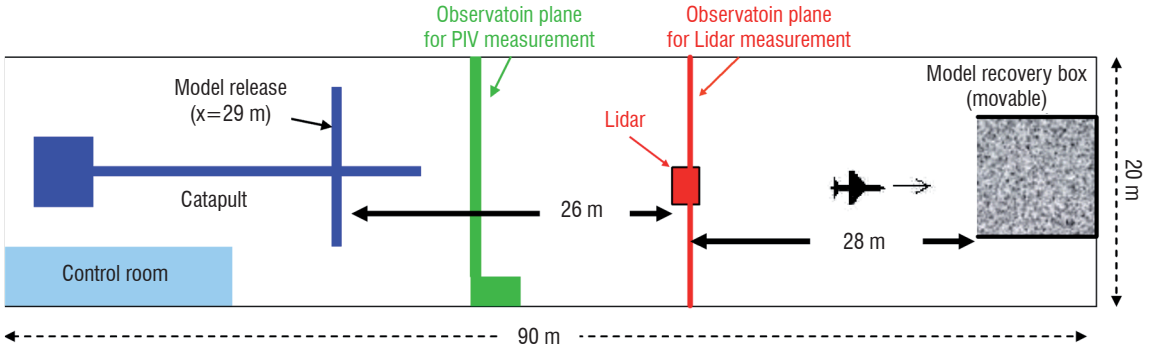

Figure 4 - B20 catapult facility (view from above): observation planes for PIV and lidar measurements.

allow for tracking of the wake vortex development, giving a precise description of the secondary flow field as well as of the velocity profiles. Because the phenomena to be analyzed are small, a CW lidar is used. But with a single CW lidar, only angular vortex core positions can be derived. Triangulation has proved a successful way to characterize full-scale wake vortices with 2 CW lidars [7]. An innovative setup for the mini-lidar was developed by Onera in order to apply the triangulation method and thus obtain the vortex trajectory as a function of time (or of distance up to ~100 spans). In this autonomous (self-triangulation) configuration, a second beam scanner was added to investigate the same wind field from an offset viewpoint (Figure 6). It is therefore possible to determine the positions of the cores and their trajectories over time. The scanning is carried out sequentially on each scanner with a measurement rate of 1.25 Hz (period of 0.4 s for each scanner).
The accuracy of the core location depends on the triangulation base length (distance between the two scanners), and on the angular measurement accuracy (dependent on the number of spectra averaged). Our base length is around 5 m and the precision of the core positions is better than 10 cm.

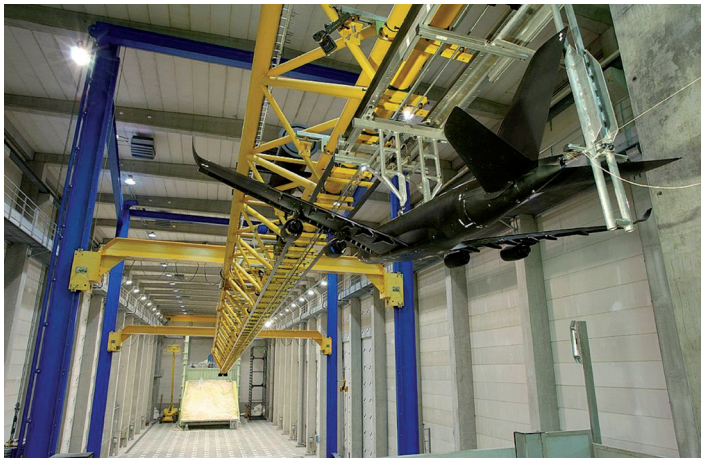

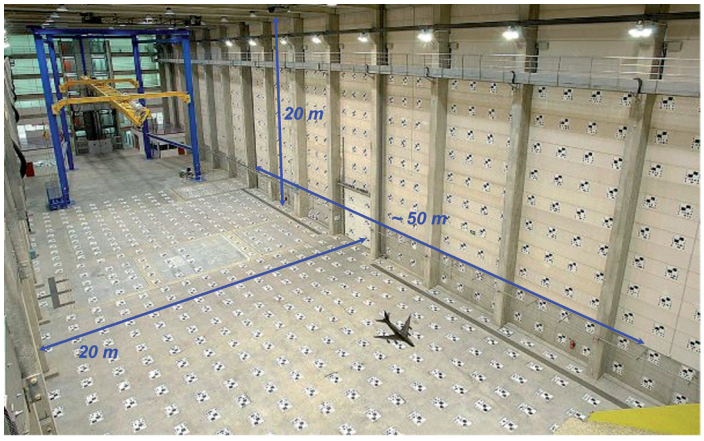

Figure 5 - B20 catapult facility with a very large transport aircraft model.

The mini-lidar has a 2W CW 1.5 μm laser, an aperture diameter of 20 mm, and a measurement depth (given by the weighting along the line of sight) of 2 m at 8 m height.
Figure 7 shows an example of vortex velocity spectra viewed alternatively from scanner 1 (circle a) and from scanner 2 (circle b). The horizontal axis is the time after over flight (or the scanning angle), the vertical axis is the velocity, and the color scale gives the power spectral density. The vortex velocity profiles are extracted from those images as explained in Figure 3 and are drawn in white. Core positions are extracted automatically from the derivative of these profiles. Then a value of circulation (m^2/s, related to the vortex strength) is calculated.

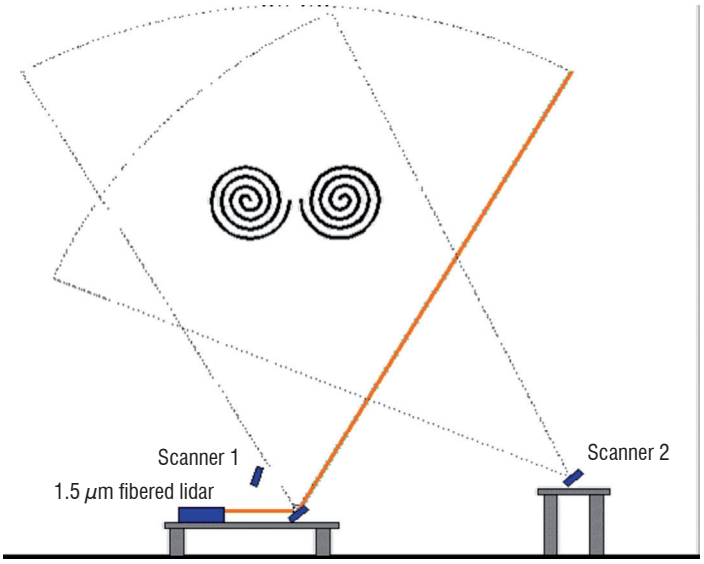

Figure 6 - Mini-lidar in self-triangulation configuration.

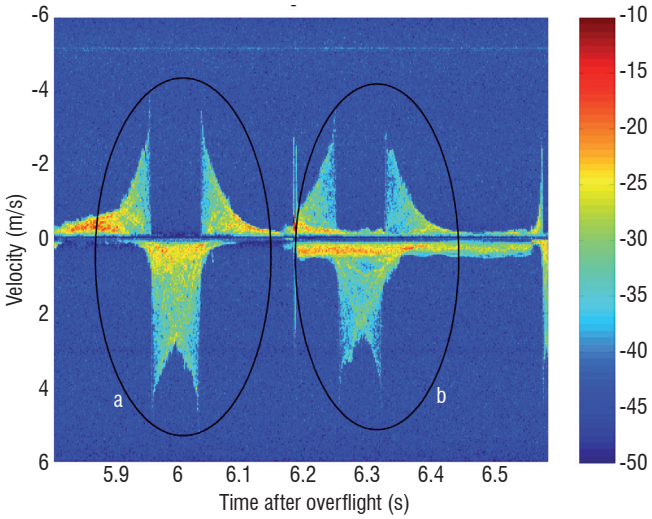

Figure 7 - Vortex velocity spectra: (circle a) viewed from scanner 1, (circle b) viewed from scanner 2).
(Horizontal axis) time after over flight. (Vertical axis) velocity (m/s).

Figure 8 gives an example of measurement results: a) vortices' positions in the measurement plane with an accuracy of 10 cm in each direction; b) the circulation values as functions of wingspan.

Wingspan units are equivalent to time units (number of wingspans = time after overflight x aircraft model velocity) and allow for the easiest comparisons between reduced-scale measurements and full-scale measurements (see Box 2).
In addition to lidar measurements, PIV is performed simultaneously to analyze the vortices. PIV (particle imaging velocimetry) gives the 2D wind field perpendicular to the trajectory [16]. PIV and lidar measurements were performed on two different observation planes (Figure 4). However, they are complementary, since the first method allowed for detailed characterizations of the wake flow to ~40 wing spans behind the model, while the second ones tracked the vortices up to ~100 spans. PIV allows for measurements ofmultipolar structures in the near field whereas

lidar is more useful when there is only one vortex in the far field. Measurement adequacy was demonstrated and the data provide mutual support for result interpretation. Comparisons between PIV measurements and lidar measurements are presented in Box 1.
Using lidar in a catapult facility is a cheap and easy way to perform extensive studies for low-vortex wing design. However full-scale measurements are mandatory to study the atmospheric impact.

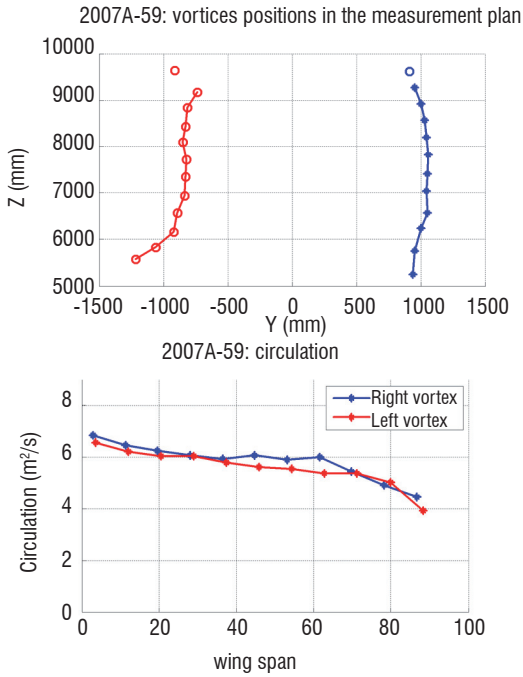

Figure 8 - (a) Example of descending vortex trajectory in the measurement plan, (b) circulation values as functions of wingspan.

Lateral full-scale wake vortex measurements

For wake-vortex lateral full-scale measurement purposes, various systems have been developed using CO_2 [7] and HoTm: YAG sources [9]. Onera has developed the first eye safe pulsed fiber lidar for wake vortex monitoring and characterization. Its design is based on a 1.5 μm fiber laser and high power telecom components. This new lidar was installed at Frankfurt airport field in February and March 2007 in order to perform wake vortex measurements for aircraft departures as part of the CREDOS EU project.
The lidar is composed of three innovative sub-systems: a pulsed fiber laser based on a Master Oscillator Power Fiber Amplifier (MOPFA) architecture, a compact Brewster circulator, and a user-friendly human-machine interface (HMI) with real-time wake vortex monitoring. The MOPFA architecture allows the pulse duration, shape and repetition rate to be optimized for lidar applications. For wake vortex detection, a pulse duration of 250 ns was chosen as a trade off between velocity resolution and spatial resolution.
The main characteristics of Onera's wake vortex lidar (SWAN) are:

- Wavelength: 1.55 μm
- Range: 400 m
- Min distance: 50 m
- Longitudinal resolution: 2.4 m after signal processing
- Lateral resolution: 3 mrad (1 m at 300 m)
- Speed resolution: 1 m/s
- Frame rate: ~0.25 Hz for a scanning angle range of 60°

- Fibered polarization-maintaining (PM) laser 50 μJ / 15 kHz designed and built at Onera
- Fibered PM architecture
- Real time velocity field signal processing and display.
- Eye safety

Figure 9 gives a schematic view of the lidar design. Figure 10 shows the optical architecture.

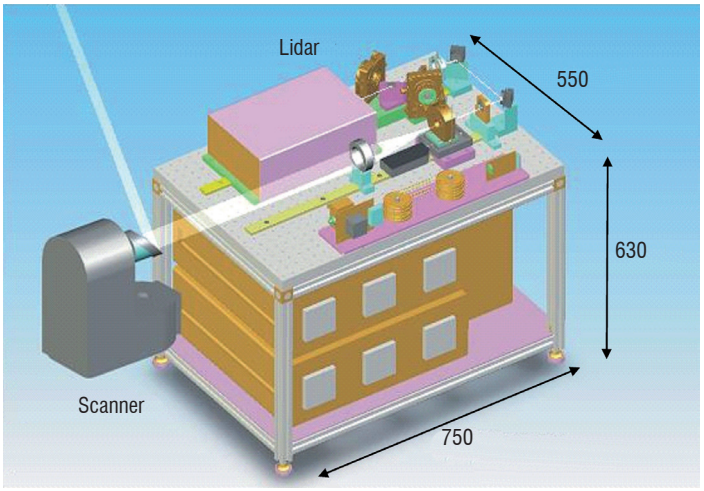

Figure 9 - Drawing and size of SWAN lidar.

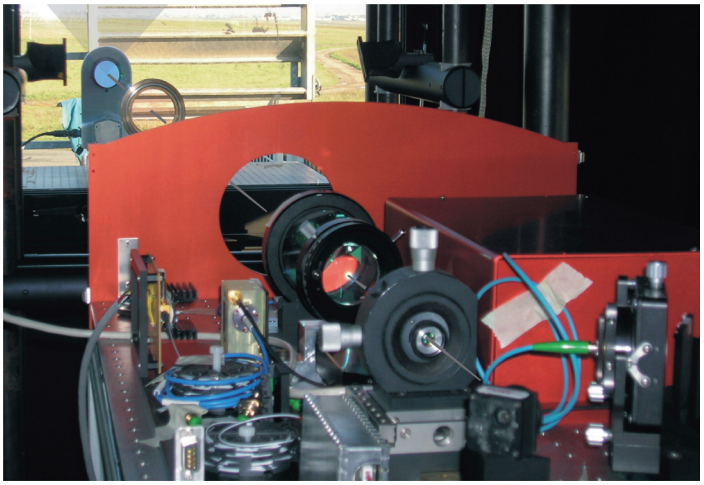

Figure 10 - Picture of lidar optical design.

Laser

The MOPFA using Erbium-Ytterbium doped fibers is well-suited for 1.5 μm high energy pulse generation. The peak power is however limited by stimulated Brillouin scattering (SBS) because of the narrow spectral linewidth. To overcome this limitation, large-mode-area (LMA) fibers are required [8]. These fibers must also have low core numerical apertures to avoid multimode operation and minimize amplified spontaneous emission (ASE). We recently developed a 3-stage all-fiber amplifier. The third amplification stage is built with a large core fiber which guides up to 6 LP mode groups. Thanks to proper packaging, the beam quality is still compatible with coherent detection requirements (the beam quality factor M^2 was measured to be close to 1.3). The beam is better than 98 % linearly polarized. With an 8 W pump power source, pulse repetition frequencies (PRFs) of 15 kHz have been reached, allowing hundreds of lidar signals to be averaged on each line of sight and thus significantly reducing the speckle noise.

Optical architecture

The optical architecture is based on collimated beams, and can thus be used with different fiber lasers, even with multimode fibers, as the laser output is collimated in free space. A compact circulator has been specially designed with both robustness and very good optical isolation (60 dB). The output beam has an effective Gaussian diameter of 50 mm (at $1/e^2$ intensity, with $M^2 = 1.3$), allowing a focus range up to 300 m. The received beam is focused on a single mode PM fiber before being mixed with the fibered local oscillator. The LO beam is frequency shifted by f = 70 MHz before being injected into the amplifier, allowing the sign of the Doppler shift to be measured (see § Coherent detection lidar principle, page 5).

Signal processing and display

In order to display the wake vortex measurements in real time, three maps are computed, having range and angle as the main axes. These maps are calculated with the first three spectral moments (respectively the CNR, the velocity centroid, and the velocity dispersion). The CNR map is useful for the lidar alignment setting and focus adjustments. The velocity map gives the position and trajectory of the vortex cores. The dispersion map provides information about wind turbulence.
Figure 11 shows a capture of the real time display with a wake vortex pair 325 m away from the lidar. The Y-axis is the range in m from the lidar, and the X-axis is the index of the line of sight, linearly dependent on the scan angle. The scanner executes symmetric sawtooth trajectories so that the right hand side of the display roughly mirrors the left hand side. The color scale gives the velocity information (spectrum centroid value) on each point of the scan plane. The real time display does not provide information about the maximum velocity component in the spectra, related to the wake vortex circulation. However, the presence and position of a wake vortex are clearly visible on the velocity map: a wake vortex has a characteristic signature.

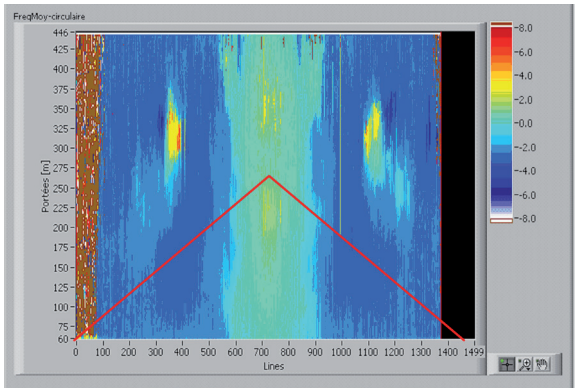

Figure 11 - Real time display of velocity map.

In order to determine the wake vortex age exactly, we installed a video camera, looking vertically above the Onera position, with a GPS time insert (see Figure 12). For each measurement, we know the time of the aircraft overflight.

The range resolution of 2.4 m is obtained by performing FFT analysis on 92 % overlapping 30 m-long gates (corresponding to the 200 ns pulse length); each gate is shifted by 2.4 m from the previous gate, as described by Köpp et al. [10]. The FFT spectral estimates are real time processed with DSP and displayed (Figure 11).

Figure 12 - Video recording for wake vortex aging.

The vortex velocity profiles are evaluated by searching for the maximal values (Figure 13, red line) and minimal values (Figure 13, blue line) in the frequency spectra of each range gate (Figure 13: each red line or blue line corresponds to one range gate).

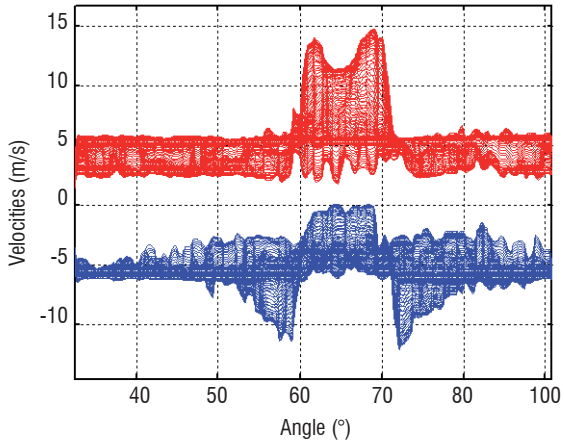

Figure 13 - Example of vortex spectra extraction from frequency spectra.

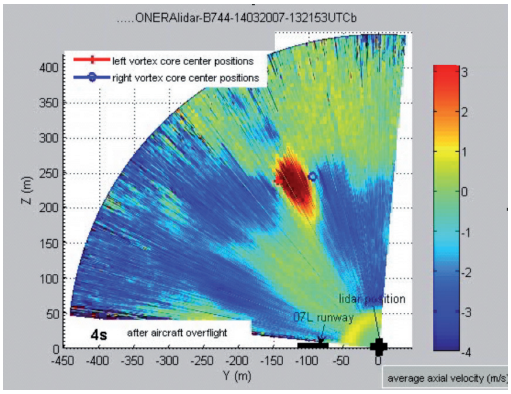

Figure 14 - Example of average velocity map display. The core positions are post processed. This shows the first measurement of a B747-400 on March 14th. This is a movie (Click on it to run).

The circulation is evaluated using the Smalikho method described in Köpp et al. [10]: the circulation is calculated by summation along an arc passing through the core center and between the radii 5 m and 15 m. The core position error is about ± 2 m and the circulation error is about 10 %.

Box 1 - Comparisons between lidar and PIV measurements

In the observation of vertical planes, transverse to the flight path of the model, PIV (particle imaging velocimetry) and lidar measurements allowed for tracking the wake vortex development in the B20 catapult facility, giving a more precise description of the secondary flow field as well as of the velocity profiles. Onera developed an innovative triangulation setup to obtain the vortex trajectory as a function of time. A PIV system, including several PIV cameras, was designed by DLR and Onera colleagues in the framework of the AWIATOR project; the evolution of the wake vortex could then be captured during a single shot. Catapult measurement results are presented in [13],[14] and [1]. During the AWIATOR project, PIV and lidar measurements were performed alternately, whereas during the DPAC project they were performed simultaneously on two different observation planes. They are complementary, since the first method allowed for detailed characterizations of the wake flow to ~40 wing spans behind the model (Figure B1-01), while the second one allowed for the tracking of vortices up to ~100 wing spans (Figure B1-02).

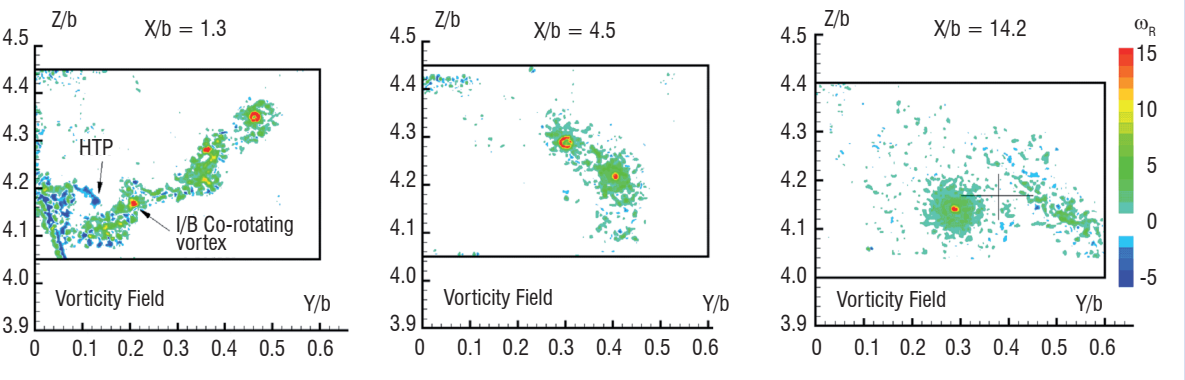

Figure B1-01 - Illustration of PIV measurements: Vorticity field recorded at different longitudinal locations X/b (four-engine type large aircraft model).

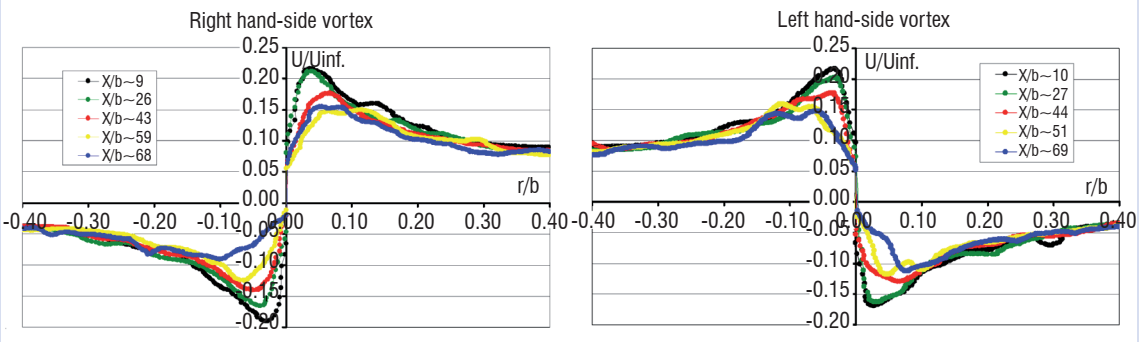

Figure B1-02 - Illustration of lidar measurements: Tangential velocity profiles recorded at different longitudinal locations X/b (generic very large transport-type aircraft model).

The PIV and lidar measurements are compared in Figure B1-03.
The velocity profile on the lidar line of sight is computed from the PIV velocity field and then compared with the results from the lidar measurements. In Figure 3, the lidar velocity profile is shown (in black) for X/b ~ 10, and the PIV velocity profile for X/b ~ 8 and X/b ~ 12. Although the PIV velocity maxima are slightly different from the lidar ones (because the vortex evolves from X/b ~ 8 to ~10 to ~12), the maxima are similar and the velocity profiles are very close.

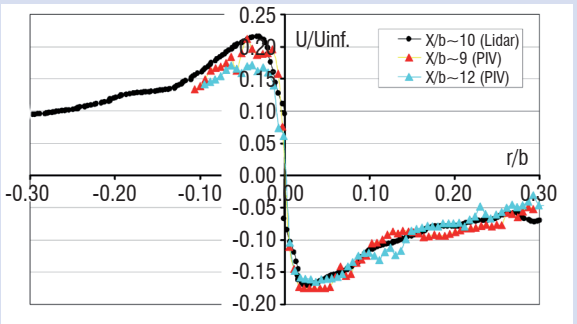

Figure B1-03 - Comparison between lidar and PIV measurements of tangential velocity profiles recorded at about the same longitudinal location (generic very large transport-type aircraft model)

The adequacy of lidar and PIV measurements has been demonstrated and the data provide mutual support for interpreting results.

Box 2 - Comparison between reduced-scale measurements and full-scale measurements

During the AWIATOR project, the wake vortex of a large transport aircraft-type configuration was characterized in the catapult facility with Onera's mini-lidar. This mini-lidar uses a 5W CW CO_2 laser, a transmitter-receiver telescope with a 1.5 cm objective lens and two 60 degree beam scanners, heterodyne coherent detection, and a triangulation technique. Measurements were obtained at high spectral frequency accuracy ($dV = 5$ cm/sec) and the precision of the core location was better than 15 cm.
Later, full-scale measurements were done at Tarbes airport by Onera's 10 μm CW lidar and DLR's 2 μm pulsed lidar. The pulsed lidar monitored the seeded vortices of a large transport aircraft (vortex position and circulation) while the CW lidar made detailed measurements of velocity profiles. During a previous EU project, CWAKE, an inter-comparison was already done for simultaneous wake vortex measurements by the DLR pulsed 2 μm lidar and two triangulating 10 μm CW lidars, one from QinetiQ and one from Onera. This CW Onera lidar used a 5W continuous wave CO_2 laser, a transmitter-receiver telescope with a 30 cm diameter aperture and a 50 degree beam scanner, and heterodyne coherent detection. The spectral resolution was $dV = 5$ cm/sec and the angular resolution was 2.2 mrad.

In order to compare reduced-scale and full-scale measurements, we normalized the parameters as suggested by T. Gertz et al. [1]. The evolution of the wake field behind an aircraft is usually described by the longitudinal distance X, normalized by *b/2* (half the geometrical wing span):
$X^* = X / (b/2)$.
X=0 refers to the trailing edge of the wing tip, at a given value of the angle of attack or lift coefficient C_L.
Wake vortex evolution is usually plotted versus the dimensionless vortex lifetime t^*:
$t^* = t / t_0$,
where $t_0 = 2\pi b_0^2 / \Gamma_0$. Here b_0 is the initial vortex spacing after roll-up; $b_0 = s.b$ (s, the spanwise load factor, is equal to $\pi/4$ for an elliptically loaded wing), and Γ_0 is the reference circulation.
$\Gamma_0 = C_L V_0 b / (2s.A_R)$ is expressed in terms of lift coefficient C_L, aircraft or model speed V_0, wingspan *b* and reference wing aspect ratio $A_R (= b^2 / S_{ref}).S_{ref}$ is the wing reference surface.
The vortex velocity profiles are normalized by the aircraft or model speed V_0:
$V^* = V / V_0$

Table 1 below compares experimental normalized resolutions of reduced-scale measurements at the catapult and airfield measurements.

	Reduced-scale measurement	Full-scale measurement
Normalized velocity resolution: dV / V_0	0.002	0.0006
Normalized spatial resolution: $dx / (b/2)$	0.015	0.015
Normalized temporal resolution T / t_0 (T = time between two full vortex measurements)	0.21	0.28

Table 1 - Experimental normalized resolutions of reduced-scale measurements at the catapult and field measurements

Only flights with the same wing configuration (reference configuration) can be compared. For the B20 tests, flights 9, 10 and 23 of the second campaign were in the reference configuration; for the Tarbes experiments, flights 1-13 , 2-07 and 2-10 were in the reference configuration.

Figure B2-01 and Figure B2-02 provide examples of wake vortex trajectories measured by the DLR pulsed lidar for field measurement, and by the self-triangulation mini CW lidar for catapult measurement.
Whereas for field measurement the vortex trajectories are strongly driven by local wind and turbulence, the main left and right vortices generated downstream from the aircraft model descend uniformly in the catapult facility, disturbed only by local indoor turbulence. It is therefore easier to analyze wake vortex velocity profiles and temporal evolution in the catapult facility.
Figure B2-03 and Figure B2-04 give examples of velocity profile evolution, for field and catapult measurements respectively. Velocity profiles obtained in field measurements are smoother than catapult measurements because of the averaging of 100 spectra, despite a better normalized velocity resolution for the catapult data. Maximum tangential velocity peaks are higher for catapult measurement because of the better signal to noise ratio due to seeding. Nevertheless, reduced-scale and full-scale velocity profiles as well as the evolution in distance (or time) are in very good agreement.

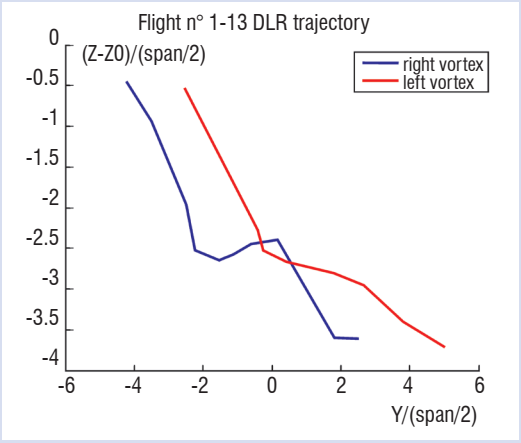

Figure B2-01 - Field test wake vortex measurements: left and right vortex trajectories measured by the 2 μm pulsed DLR lidar

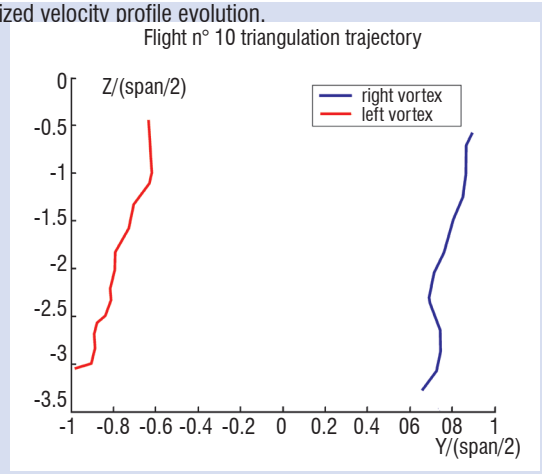

Figure B2-02 - Catapult (reduced-scale) vortex measurements: left and right vortex trajectories measured with self-triangulation CW mini-lidar.

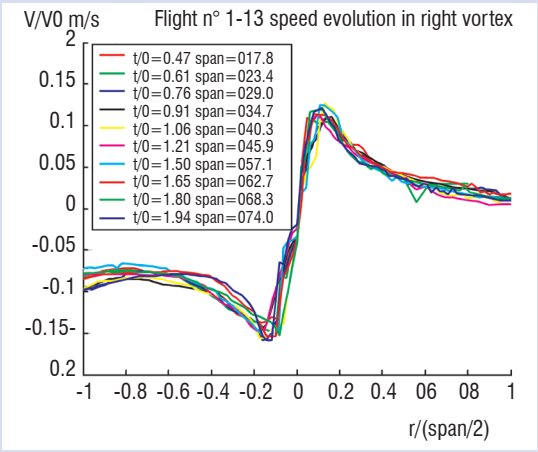

Figure B2-03 - Field test wake vortex measurements with Onera CW lidar: normalized velocity profile evolution.

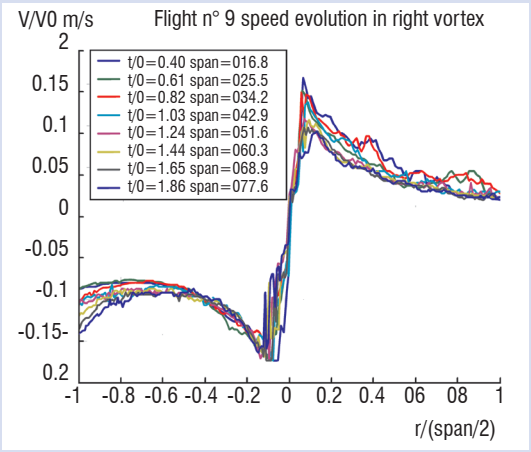

Figure B2-04 - Catapult (reduced-scale) vortex measurements with CW mini-lidar: normalized velocity profile evolution.

Figure B2-05 29 and Figure B2-06 give examples of circulation evolution, for field and catapult measurements respectively. Flight 2-07 took place in very quiet atmospheric conditions so the circulation decay was very low, and identical for both vortices. It fits very well with the circulation evolution in the catapult up to $t^* = 2$. After $t^* = 2$, at the catapult, the two vortices become unsymmetrical and their circulations differ.

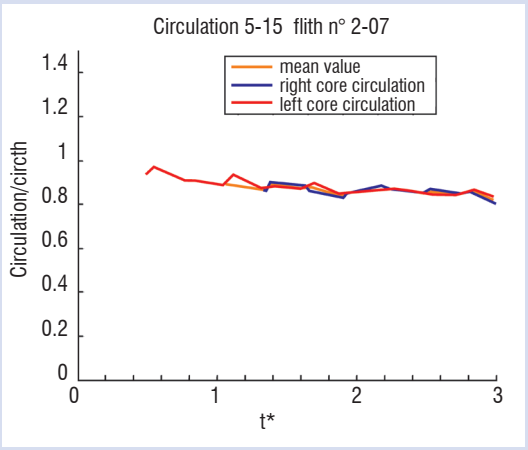

Figure B2-05 - Field test wake vortex measurements with Onera CW lidar: normalized circulation evolution.

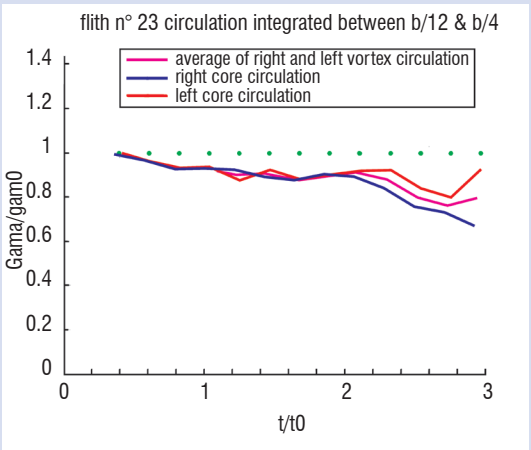

Figure B2-06 - Catapult (reduced-scale) vortex measurements with CW mini-lidar: normalized circulation evolution.

The scale factors between the model and true aircraft have been checked, and normalized results for reduced and full-scale measurements are in very good agreement. Lidar is the link between reduced-scale and full-scale approaches. Reduced-scale measurements are easier, cheaper and well-suited for fundamental research on aircraft configuration and devices. Full-scale measurements are however necessary to check the atmospheric impact on wake vortex evolution.

Figure 14 show examples of average velocity map displays for the first and last measurements of a B747-400 overflight on March 14th 2007. The core positions are post processed. Figure 15 displays the results from the measurements shown in Figure 14.

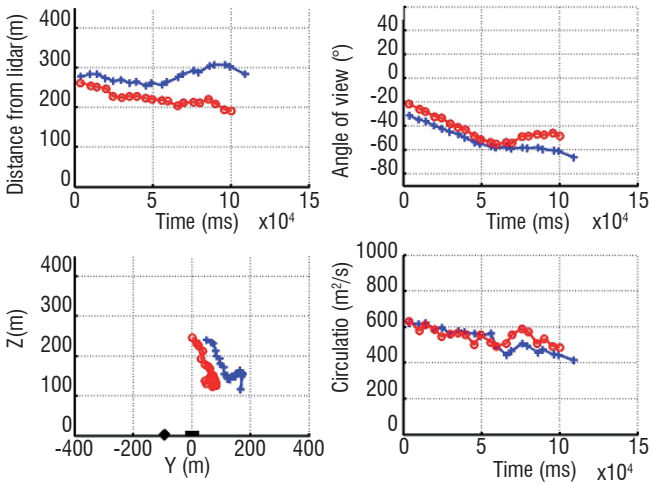

Figure 15 - Top left: distance of vortex cores from the lidar as a function of time after overflight (t.a.o); top right: angle of view of vortex core as a function of t.a.o.; bottom left: vortex core trajectories in the measurement plane; bottom right: circulation values of left and right cores as functions of t.a.o.

Measurements of 187 departures at Frankfurt were obtained in only 8 days.

No particular effort was made to reduce the lidar size and there is still room for further reduction. This campaign proved that the fibered technology is now reliable and mature and little effort should be required to build a fully automatic system. Thanks to the good optical efficiency of fibered lasers, a fully autonomous temperature regulated system should require less than 500 W electrical power. The next steps are the size reduction and the automation of the lidar system.

Axial wake vortex detection

The purpose of the FIDELIO European project is to introduce a unique fiber laser technology geared for the aerospace industry requirements, enabling onboard realization of an atmospheric hazard detection lidar system. The FIDELIO lidar measures wind tracer velocities using coherent detection and a fiber architecture based on mainstream telecommunications components. The goal is to detect wake vortices along their axis at a range of 2 km.
In-flight demonstration of axial wake vortex detection was done during the IWAKE UE program [11].
FIDELIO project activities encompass the fiber laser design, the lidar simulations and design, and the field tests at Orly airport. A detailed presentation is available in [12].

Simulations

During FIDELIO, extensive simulation has been performed in order to specify an adequate laser. Onera has developed an end-to-end simulation tool including the observation geometry, the wake vortex velocity image, the scanning pattern, the lidar instrument, the wind turbulence outside the vortex, and the signal processing. A simulation of large aircraft wake vortex evolution in a turbulent atmosphere has been performed by UCL/TERM.
The simulation's main conclusion is that the pulse duration must be at least 800ns. A 1600 ns pulse gives very good simulation results but was not chosen for the lidar design because such a large range gate (240m) would lead to a system sensitive to wind gradient.
Extensive simulations were carried out with varying laser energy E, pulse duration, PRF, and turbulence strength. The main conclusions are:
- At medium range (>1km), the vortex is easier to detect by measuring the spectrum broadening. These results confirm the IWAKE conclusions. [11]
- Longer pulse duration (800 ns) gives better results than the nominal value of 400 ns and leads to a high velocity resolution.
- The vortex is easier to detect at old ages than at young ones, since dissipation increases the velocity dispersion on the observation axis.
- Low PRF cannot be compensated for by increasing the laser energy. Indeed a high PRF value enables incoherent summation, reduced speckle effects and therefore a better velocity resolution.
- For PRF = 4 kHz, E = 1 mJ, and nominal atmospheric conditions the theoretical lidar range is 2400 m. For PRF = 10 kHz and E = 0.1 mJ, the theoretical lidar range is 1200 m.

Lidar architecture

Within FIDELIO, an innovative high-brightness pulsed 1.5 μm laser source was built, based on a MOPFA architecture with a large core fiber. The beam quality is excellent (M^2 = 1.3). The pulsed energy achieved is 120 μJ with a PRF of 12 kHz and a pulse duration of 800 ns. With a further amplification stage, 750 μJ pulses were obtained in Onera lab at 5 kHz and 1 μs with excellent beam quality. This last prototype has not been integrated in the field test.
The lidar optical architecture developed at Onera has the same base as SWAN, except for the larger output optic in order to focalize at 800 m.

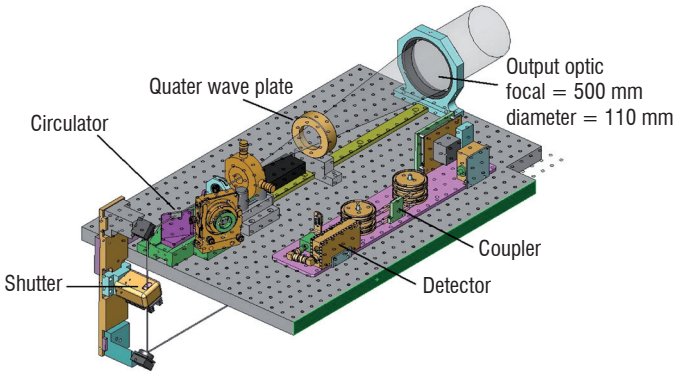

Figure 16 - Lidar optical layout.

The lidar includes a real-time display of the wind field, developed by UCL. Wind dispersion is post-processed.

Field tests

Field tests were carried out at Orly airport in April 2008. The lidar was placed about 800 m in front the runway touchdown threshold, facing the landing aircraft. The scanning configuration is presented in Figure 17. The total field of view is 12° horizontal × 3° vertical.
The image resolution was set to 128 x 32 pixels, giving an angular resolution of 1.6 mrad.

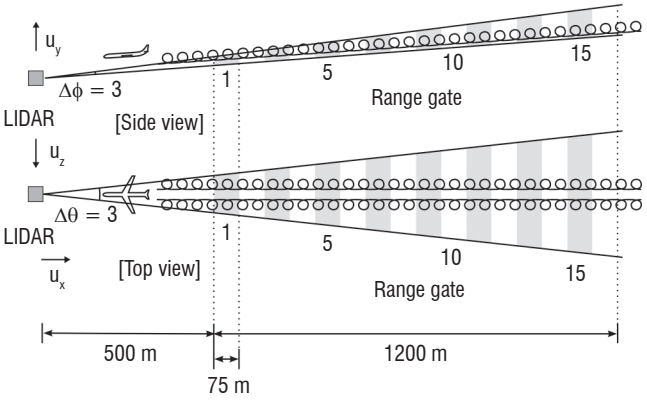

Figure 17 - Scanning configuration.

The overall average wind velocity displayed in the main window was validated with the atmospheric information coming from the tower.

In order to validate the vortex detection, video recordings were made of the landing aircraft during the test campaign. A real-time aircraft detection, tracking and geometric reconstruction algorithm was used to track the distance between the aircraft and the sensor.
Figure 18 shows a set of wind velocity dispersion images computed after the passing of two successive aircraft. Each box represents the 12° x 3° field of view image acquired at different ranges (vertical axis) and at different times (horizontal axis). We can clearly see the vortex signatures in scans 0 and 1 for the first plane and in scans 4 and 5 for the second one. The time elapsed between two scans is 6 seconds. The disappearance of the turbulence is mainly due to the lateral wind, which blows the vortices outside of the spatial region of scan. The distance from the vortex signature corresponds to the distance between the aircraft and the sensor as measured by the video detection and tracking system.

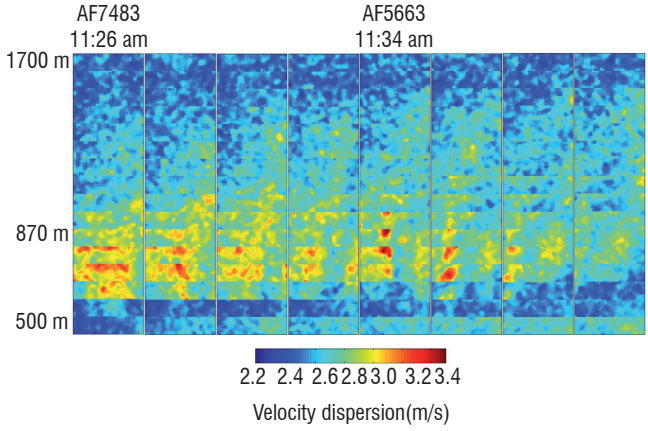

Figure 18 - Velocity dispersion images, calculated by UCL, obtained for 8 successive scans of 16 range gates of 75m after the passing of two successive aircraft. Each box represents the 12° x 3° field of view image acquired at different ranges (vertical axis) and at different times (horizontal axis).

Figure 19 and Figure 20 show a 3D representation of wake vortex detection on two consecutive scans a few seconds after a B747 landing. Each rectangle corresponds to a range gate. The X-axis represents the 12° horizontal field of view, the Z-axis the 3° vertical field of view and the Y-axis the distance of the range gates from the lidar. The detection was possible because the wind velocity showed strong discontinuities. The blue regions (gates 7 to 10 around 1.2km) are

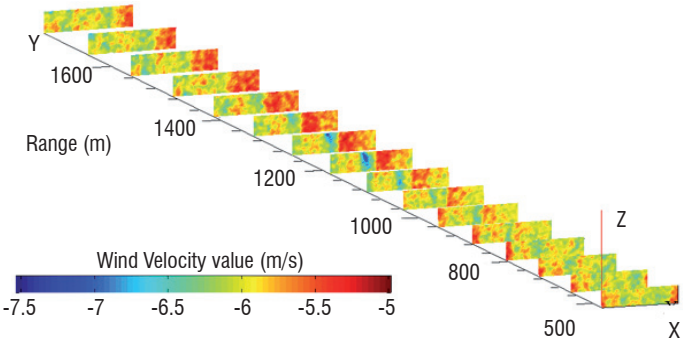

Figure 19 - 3D view of mean velocity images, calculated by UCL, obtained during the landing of a B747. (X axis = azimuth scan, Y axis = 16 range gates, and Z axis = elevation scan; color chart: = line-of-sight wind speed).

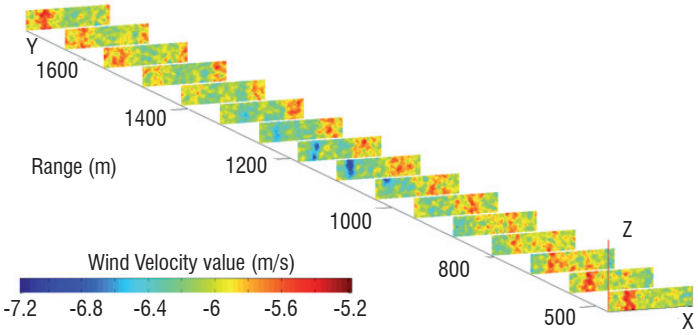

Figure 20 - 3D view of mean velocity images calculated by UCL, obtained during landing of a B747 (Xaxis = azimuth scan, Y axis = 16 range gates, and Z axis = elevation scan; color chart = line-of-sight wind speed).

again consistent with the aircraft location. We can see the wake vortex decay on the two consecutive scans. This range detection is in accordance with the simulated results.
This work was undertaken in the FIDELIO program and aims at meeting commercial aircraft requirements for onboard implementation of a wake vortex sensor. Among its results, the project has generated important advances in research and development on fiber laser technology.

Conclusions

For ten years now, Onera has been developing lidar tools for wake vortex detection and studies. Since 2003, new developments based on 1.5 μm fiber laser sources have been achieved, in parallel with extensive work on the laser sources themselves leading to breakthrought achievements. Recently three innovative lidars have been developed:
1) A mini-lidar with a CW 2W 1.5 μm laser source for aircraft model wake vortex characterization in the catapult facility. A self-triangulation technique allows for core location with 10cm precision and circulation estimation with 10% error.
2) A pulsed 1.5 μm lidar based on a 50 μJ / 15 kHz MOPA source for lateral wake vortex monitoring at airport sites. The range is 400 m, the core position error is about $\pm$ 2 m, and the circulation error is about 10 %.
3) A pulsed 1.5 μm lidar based on a 120 μJ / 12 kHz MOPA source for onboard axial wake vortex detection. The ground-based lidar test at Orly airport has demonstrated wake vortex detection up to 1.2 km. Our 1.5 μm fiber laser research continues and aims at increasing the laser source brightness and the lidar detection range for applications 2 and 3 ■

Acknowledgments

This work was supported by the European Union under grant No. 30837 (CREDOS) and grant No. 12008 (FIDELIO) and by DPAC-SPAé (Service Technique des Programmes Aéronautiques). The work presented in the inserts was supported by the European Union through the AWIATOR and CWAKE projects.

The authors thank Eric Coustols from Onera in Toulouse for the coordination of wake vortex research at Onera, and Frederic Moens from Onera in Meudon for the analysis of the PIV measurements.

The authors thank Thomas Peschel from the Fraunhofer Institute for lending the scanner in the FIDELIO project.

Thanks also to the FIDELIO project partners: ELOP (Israel, coordinator, laser integration), Thales R&T (France, laser research), INESC Porto (Portugal, laser research), IPHT (Denmark, fiber research and design), CeramOptec (Denmark, fiber packaging) and Thales Avionics (France, aircraft integration specifications).

References

[1] T. GERTZ, F HOLZÄPFEL and D. DARRACQ - *WakeNet Position Paper on Aircraft Wake Vortices*. European Union, April 2001.

[2] S. M. HANNON and J. A. THOMSON - *Aircraft Wake Vortex Detection and Measurement with Pulsed Solid-State Coherent Laser Radar.* J Modern Opt, vol.41 (1994), p. 2175.

[3] S. RAHM, I. SMALIKHO and F. KÖPP - *Characterization of Aircraft Wake Vortices by Airborne Coherent Doppler Lidar*. Journal of aircraft, vol. 44, no3, 2007, pp. 799-805

[4] R. HEINRICHS, T. DASEY, M. MATTHEWS, S. CAMPBELL, R. FREEHART, G. PERRAS, and P. SALAMITOU - *Measurements of Aircraft Wake Vortices at Memphis International Airport with a cw CO_2 Coherent Laser Radar.* Proc. SPIE 2737, 122 (1996)

[5] M. HARRIS, R. I. YOUNG, F. KÖPP, A. DOLFI, JP. CARIOU - *Wake Vortex Detection and Monitoring*. Aerospace Science and Technology, Volume 6, Issue 5, September 2002, Pages 325-331.

[6] K. ASAKA, S. KAMEYAMA, T. ANDO, Y. HIRANO, H. INOKUCHI, and T. INAGAKI - *A 1.5µm all-Fiber Pulsed Airborne Doppler Lidar System*. JAXA IS17-06, (2003).

[7] J.-P CARIOU, B. AUGÈRE, D. GOULAR, J.-P. SCHLOTTERBECK and X. LACONDAMINE - *All-Fiber 1.5 µm CW Coherent Laser Anemometer DALHEC. Helicopter Flight Test Analysis.* 13th Coherent Laser Radar conference (CLRC), Kamakura (2005).

[8] F. KÖPP, I. SMALIKHO, S. RAHM, A. DOLFI, J.-P. CARIOU, M. HARRIS, R. I. YOUNG, K. WEEKES and N. GORDON - *Characterization of Aircraft Wake Vortices by Multiple-Lidar Triangulation.* AIAA Journal, vol. 41, no. 6 (June 2003), pp. 1081-1088.

[9] G. CANAT, L. LOMBARD, S. JETSCHKE et al. - *Er-Yb-Doped LMA Fiber Structures for High Energy Amplification of Narrowlinewidth Pulses at 1.5 µm*. Talk CtuBB, Conf. on Lasers and Electro-Optics (CLEO), Baltimore (2007).

[10] S. M. HANNON and J. ALEX THOMSON - *Real Time Wake Vortex Detection, Tracking and Strength Estimation with Pulsed Coherent Lidar*. Proceedings of the 9th Conference on Coherent Laser Radar, June 23-27, 1997, Linköping, Sweden.

[11] F. KÖPP, S. RAHM and I. N. SMALIKHO - *Characterization of Aircraft Wake Vortices by 2-µm Pulsed Doppler Lidar.* Journal of Atmospheric and Oceanic Technology, vol. 21 (2004), pp. 194-206.

[12] D. DOUXCHAMPS, Y. VERSCHUEREN, S. LUGAN, L MUTUEL, B. MACQ and K. CHIHARA - *On-Board Axial Detection of Wake Vortices Using a 2µm Lidar*. IEEE Trans. on Aerospace and Electronic Systems, vol. 44, No. 4 (2008).

[13] A. DOLFI-BOUTEYRE, G. CANAT, M. VALLA, B. AUGÈRE, C. BESSON, D. GOULAR, L. LOMBARD, J.-P. CARIOU, A. DURECU, D. FLEURY, L. BRICTEUX, S. BROUSMICHE, S. LUGAN and B. MACQ - IEEE jstqe, vol. 15, no 2, march/april 2009.

[14] E. COUSTOLS, E. STUMPF, L. JACQUIN, F. MOENS, H. VOLLMERS and T. GERZ - *Minimised Wake: a Collaborative Research Programme on Aircraft Wake Vortices*.AIAA Paper 2003-0938, 41st Aerospace Sciences Meeting & Exhibit, Reno, NV, USA, 6-9 January 2003.

[15] E. COUSTOLS, L. JACQUIN, F. MOENS and P. MOLTON - *Status of Onera Research on Wake Vortex in the Framework of National Activities and European Collaboration*. European Congress on Computational Methods in Applied Sciences and Engineering, ECCOMAS 2004 Conference, Jyväskylä, Finland, 24-28 July 2004 (P. Neittaanmäki, T. Rossi, S. Korotov, E. Oñate, J. Périaux and D. Knörzer, eds).

[16] E. COUSTOLS, L. JACQUIN and G. SCHRAUF - *Status of Wake Vortex Alleviation in the Framework of European Collaboration: Validation Attempts Using Tests and CFD Results*. European Conference on Computational Fluid Dynamics, ECCOMAS CFD 2006 (P. Wesseling, E. Oñate and J. Périaux, eds).

[17] L. JACQUIN - *Scales in Turbulent Motions*. AerospaceLab N°1, December 2009.

Acronyms

MOPA (Master Oscillator Power Amplifier)
LIDAR (Light Detection And Ranging)
CW (Continuous-Wave)
PIV (Particle Imaging Velocimetry)
MOPFA (Master Oscillator Power Fiber Amplifier)
HMI (Human-Machine Interface)
SBS (Stimulated Brillouin Scattering)
LMA (Large-Mode-Area)
ASE (Amplified Spontaneous Emission)

Agnès Dolfi-Bouteyre graduated from the «Ecole Supérieure d'Optique», Orsay, (1986) and received a PhD degree in Physics from University Paris XI Orsay (1990). She joined Onera in 1990 where she has been involved in the development of lidar systems for defense and aerospace.

Béatrice Augere has a PhD in non-linear optics (1988). She has been working at Onera since 1989 and is a research scientist in the ''Lasers and Optoelectronics'' research Unit. Her major research interests are lidars, laser propagation in turbulent flows and coherent detection.

Matthieu Valla received engineering and PhD degrees from Telecom Paristech (Paris, France) in 2001 and 2005. He has been working as a research engineer at Onera since 2002.

Didier Goular received a degree in electrical engineering from CNAM in 1990. Since 1985 he has been with the Onera Lidar team working on optimization of electronic and informatics processing of coherent optical systems.

Didier Fleury received an engineering degree in Physics and Metrology from DPE. He is currently working with the Onera Lidar team in SLS Unit.

Guillaume Canat graduated from the Ecole Polytechnique, Palaiseau (2000). He did his PhD thesis at the Ecole Nationale Supérieure de l'Aéronautique et de l'Espace in 2006. He has been a research scientist at Onera since 2002. His research interests include high-power fiber laser sources, non-linear effects in fibers and coherent combining.

Christophe Planchat has been working at Onera, on the optimization of electronics and informatics processing of coherent optical systems in the Optics Department, since 1991.

Thierry Gaudo has obtained his engineering degree from the «Conservatoire National des Arts et Métiers» (CNAM) in 1991. He has been involved in various LIDAR projects for defense or aerospace.

Claudine Besson obtained her PhD in Physics in 1989 at Optics Graduate School. She is a senior scientist and SLS group leader at Onera. Her current fields of interest are Fiber lasers and Lidars.

Anne Gilliot received the VKI Diploma in 1990 and her doctorate in Mechanics in 1997 from the University of Lille. Since 1991 she has been employed as a scientist by Onera and has taught Fluid Mechanics and Turbomachinery in engineering schools. She started with experimental work on problems of Fundamental Fluid Mechanics. Now she is working mainly on the development of Particle Image Velocimetry (PIV) and its use in aerodynamic applications and in large industrial scale wind tunnels in the PIV team of Applied Aerodynamics Department.

Jean-Pierre Cariou received an engineering degree in Optics from the "Ecole Superieure d'Optique" in Orsay and a PhD in Astronomy and Spatial Techniques in 1983. At Onera, he has been involved in coherent lidars and laser imagers. He led the Laser and Optoelectronics research group for 10 years and was then special adviser for laser applications in the Optics Department. He joined the Leosphere company in 2007 as Technical Director, developing commercial wind and aerosol lidars for atmospheric applications.

Olivier Petilon graduated from 'ENSEA (Ecole Nationale Supérieure de l'Electronique et de ses Applications) (1992). From 1994 to 2001, he was Research and Development engineer for Electrocardiograms Analysis at Novacor, and from 2001 to 2002 Project Manager for Image processing at Poséidon-Technologie / Vision-IQ. He is currently Software Team Manager for Lidar Analysis at Leosphere. He is also the developer of Midizen software for music analysis (detection and recognition of pitches by fft algorithms).

Julius Lawson Daku received a M.Sc. degree in Physics («Magistère de Physique») from Université Paris 7 in 1993 and a M.Sc. degree in matter-radiation interaction («DEA Lasers et matière») from Université Paris 11 the same year. He received a PhD degree in Atom Optics from Université Paris 13 in 1997 and an M.Sc. degree in Computer Science from the CNAM in 2003. He is the technical director of the optoPartner company and a senior consultant for the company's partners and customers.

Sebastien Brousmiche received an Electrical Engineering degree from the ECAM in 2002 and a DEA degree in electrical engineering from the Université Catholique de Louvain in January 2005. Since 2004, He has been a research engineer at the Communication and Remote Sensing Laboratory at the UCL. He is now working towards a PhD.

Sébastien Lugan received his master's degree and DEA in 2003 at the Ecole Supérieure d'Ingénieurs en Électronique et Électrotechnique (ESIEE), and the Gaspard-Monge Institute of Electronics and Computer Science, respectively. Since then, he joined the Communications and Remote Sensing Laboratory of the Université catholique de Louvain, where he is preparing a PhD thesis. His research interests include medical imaging, mega-image navigation and LiDAR detection of wake vortices.

Laurent Bricteux received his degree in mechanical engineering from the Université catholique de Louvain in 2000. Then, he worked for three years at LMS international as engineer in the field of numerical simulation of vibro-acoustic and aero-acoustic phenomena. In 2004 he joined the research group in Turbulence & Vortical flows held by Prof. G. Winckelmans. He received his ph.D degree from the Université catholique de Louvain in 2008. He is currently working on research projects in aeronautics and energetics.

Benoit Macq is currently a Professor at the University Catholique de Louvain in the Communication and Remote Sensing Laboratory.

A.K. Mohamed, J. Bonnet
S. Larigaldie, T. Pot
J. Soutadé, B. Diop
(Onera)

E-mail: ajmal_khan.mohamed@onera.fr

Electron Beam Fluorescence in Hypersonic Facilities

The Electron Beam Fluorescence (EBF) technique is well-suited to providing local measurements in low-density high-speed flows for atmospheric reentry studies. High fluorescence yields are obtained from the excitation of the molecules or atoms of a gas flow with high energy electrons, which makes this technique advantageous for studying very low density gases. The most common measurement is flow field visualization with a sweeping electron beam (or sheet of electrons) from which shock structures of the flow can be observed and in certain cases a density map of the flow field can be obtained. Spectroscopic analysis of fluorescence leads to species detection as well as rotational or vibrational temperature measurements. This is particularly useful for characterizing the shock layer chemistry at non–equilibrium which usually occurs with high speed flows or in studying boundary gas-surface interactions. Velocity measurements are also possible using the Doppler shift principle or with a time of flight method with a pulsed electron beam.

Introduction

Characterization of high enthalpy flows is of paramount importance for improving our understanding of the various tests and experiments carried out in supersonic facilities to simulate the dynamics and the energy exchanges which take place during the re-entry of vehicles through the upper atmosphere. In addition to classical probes, new approaches based on electron beam fluorescence, X-ray scattering and laser diagnostics have been developed to improve our knowledge of hypersonic flows. These new techniques are attractive because they allow for non-intrusive measurement of density, velocity, and translational and vibrational temperatures within the flow field.

The Electron beam fluorescence (EBF) technique is particularly well-suited to low density hypersonic flows (< 10^{16} molecules/cm^3) because high fluorescence yields are obtained from excitation of the molecules or atoms of gas flows with high energy electrons, making this technique advantageous for studying very low density gases. Since its first application in 1953, it has been used in numerous facilities to perform local and non-intrusive measurements of density, vibrational and rotational temperatures Tv, Tr and velocity on different species such as N_2, NO, CO, CO_2 and He (References [1] to [15]). The technique has also been applied on several occasions for in-flight measurements on rockets to probe the shock layer or the upper atmosphere ([12] to [16]).

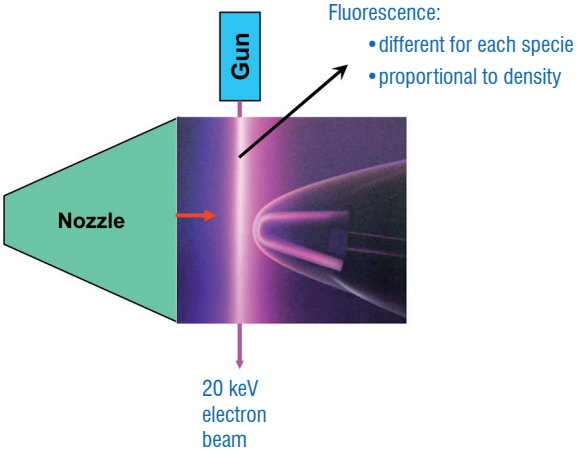

a) Typical EBF setup in a wind tunnel - Visualization of the electron beam and use of its afterglow to visualize a Mach 10 flow around the ESA EXPERT atmospheric re-entry vehicle

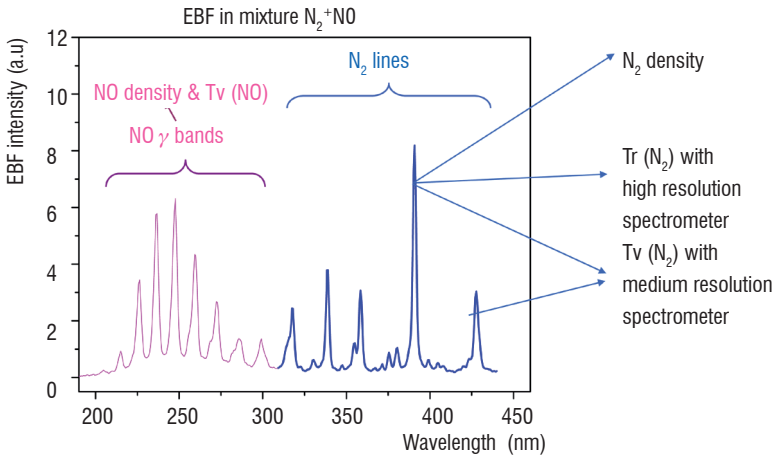

b) EBF spectra of N_2 and NO

Figure 1 - Typical features of the EBF technique

The EBF technique is based on the excitation (and related broadband fluorescence) induced by an electron beam on gas atoms and molecules along the electron beam's path. Figure 1a presents a typical EBF setup in a wind tunnel application. In a low-density gas flow, the use of an energetic electron beam (typically 25 keV) induces a complicated set of excitations in the gas all along the beam. These excitations produce broadband fluorescence ranging from X-rays to infrared. Each molecular or atomic species has its characteristic EBF signature in the form of characteristic vibrational bands or rotational emission lines from which measurements specific to that species can be performed.

For molecular Nitrogen, the main emissions in the UV and visible spectrum (Figure 1b) are mainly the first negative system N_2^+(1N) and the second positive system N_2(2P) from which most of the measurements are made. For NO, the most prominent bands are the gamma bands in the UV between 200 and 300 nm.

For a given species, the spectral analysis of its fluorescence provides the vibrational temperature and even the rotational temperature if high spectral resolution is possible for that species. The density of that species in the flow can be measured from the intensity of one or several of its fluorescence lines. Velocity measurements can also be made by Doppler shift of the radiative emission or with the time of flight method [2][3].

These measurements can be useful in the following applications:

- Validation of aerodynamic simulation codes from wind tunnels or in-flight testing
- Gas-surface accommodation
- Atmospheres of other planets

Parameters	Range
Flow Density	10^{13} -10^{16} molecules/cm^3
Flow visualization	10^{13} -10^{17} molecules/cm^3
Temperatures - of rotation Tr - of vibration Tv	from a few Kelvins to more than 1000 K
Velocity by Doppler shift Velocity by Time of flight	1000 m/s (for density range 10^{18} – 10^{13} molecules/cm^3

Table 1 presents the various parameters which can be measured on nitrogen based flows.

The measurements are:

- non-intrusive
- local (spatial resolution depends mainly on the optical imaging of the fluorescence from the beam which usually has a diameter of 1 mm: we can easily have a resolution of 1 mm^3).

This technique has also been used on other species such as NO, O_2, O and N, mainly to study gas discharges and in Helium flows for high Mach number studies. There is also a renewal of interest in extending the technique to higher densities and to studying CO/CO_2 flows (Mars atmosphere studies)[17].

Measurement principle

Electron impacts on atoms or molecules induce transitions among the energy levels of the atoms or molecules as depicted in Figure 2. The interactions follow dipolar rules for electrons of energy higher than 800 V. For lower energies, quadrupolar excitations are substantial and provide higher fluorescence rates, but these are difficult to use because of the excessive non-linearity between the fluorescence intensity and the electron beam intensity or gas number density. For this reason, and also for sufficient propagation of the beam in a low density gas, the technique is usually applied with electron energies of a few keV. It is then comparable to laser-induced fluorescence (LIF): from knowledge of the radiative emission and excitation coefficients, one traces the intensity of a fluorescence line to the population number density of a fundamental energy level. In fact, in EBF there is broadband excitation of many fundamental levels due to the high energy of the electrons, thereby allowing for measurement of population distributions on many fundamental levels simultaneously.

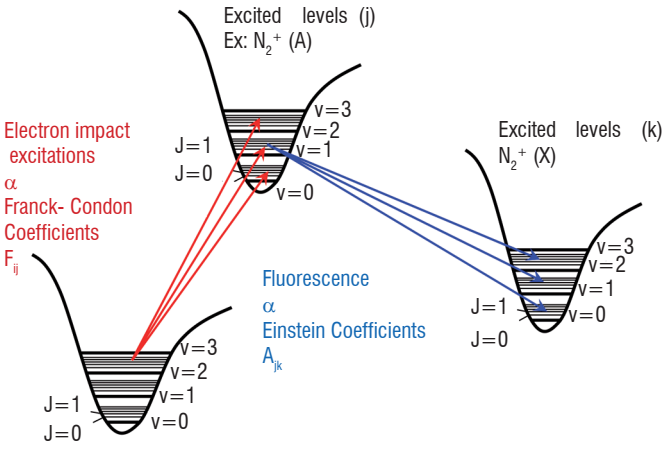

Intensity of a fluorescence line:

$$I_{jk} = n_j A_{jk} h\nu_{jk} = h\nu_{jk} \frac{\sum_i n_p v_p \sigma_{ij}(E_p) n_i}{\sum_e A_{js} / A_{jk}} \propto n_0$$

- n_p, n_j : populations on levels *i,j*; both are proportional to the total density n_0 of the gas
- n_p : density of primary electrons,
- v_p : velocity of primary electrons
- E_p : energy of primary electrons, $E_p = \frac{1}{2} m_e v_p^2$, m_e being the electron mass
- $\sigma ij(E_p)$: cross section of the excitation by electron impact, where A_{jk} is the probability of radiative transition in s^{-1}, h is the Planck constant, ν_{jk} the frequency of the transition *j-k*

Figure 2 - Electron Beam excitation-fluorescence principle.

The intensity of a fluorescence line is therefore proportional to the total density of the gas n_0 as n_i is proportional to n_0. This linear depen-

dence is valid up to density levels of 10^{16} cm^{-3}. Above that value there are two phenomena which cause deviations from linearity:

- Fluorescence quenching (collisional non-radiative deexcitation)
- Supplementary excitations by secondary electrons (created through ionization from the electrons of the beam, and which have sufficient energy to cause excitation (mainly quadrupolar).

Beam dispersion also becomes important for electron density in excess of 10^{16} cm^{-3}.

Secondary effects	Criteria	Upper density limit n_g in molecules.cm^{-3}
Beam dispersion	Beam propagation length for at least 100 mm	$\leq 10^{16}$
Quenching	Linear relation between intensity of fluorescence and gas density: $I = \alpha n_g$	$\leq 3.\ 10^{16}$
Secondary electrons	Excitations by e_s are less than excitations by e_p	$\leq 10^{16}$

Table 2 – Main causes for EBF limitation to high densities

Measurements examples

Figure 3 recalls the typical setup in a wind tunnel as well as the potential measurements of the EBF technique matched against the appropriate optical detectors.

Density and flow visualization

Density measurements are quite straightforward in a low-density gas (up to 10^{15} molecules/cm^3) where the intensity of fluorescence is directly proportional to the density as shown, see § Measurement principle, page 2. As mentioned above, for higher densities, collisional non radiative deexcitation (quenching) established a non-linear relationship between fluorescence intensity and density when other parameters such as temperature are involved. Nevertheless, qualitative density variation can still be extracted from visible fluorescence for better understanding of flow structure, highlighting shock waves for example. This is usually done by sweeping the beam to illuminate a sheet of the flow, which provides spectacular images of visualization. Figure 4a shows an example of interaction of shock waves between two models placed in a Mach 10 flow (Onera R5 wind tunnel). Figure 4b shows a visualization of the flow structure around a 25/65 sharp double cone obtained by post luminescence from a fixed electron beam. The densities are too high here ($> 10^{16}$ molecules/cm^3) to allow for accurate density measurements with visible fluorescence, but this kind of visualization can help in configuring the models and choosing the right type of interaction for more accurate measurements by other techniques (CARS for instance).

Ways to overcome quenching and other non-linear effects at high densities include accurate modeling of these effects or measurements using X-ray radiation which are not subject to quenching and to spectral broadening. An example of a density profile with the latter method is presented in Figure 5.

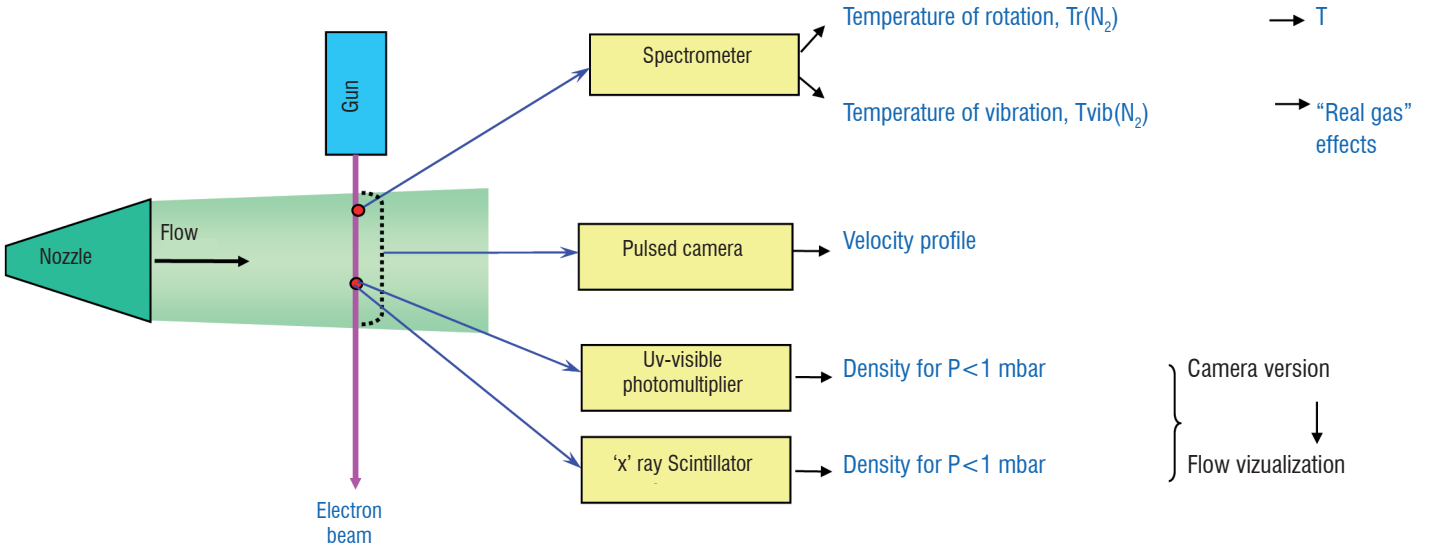

Figure 3 - EBF potential measurements and setups in wind tunnels.

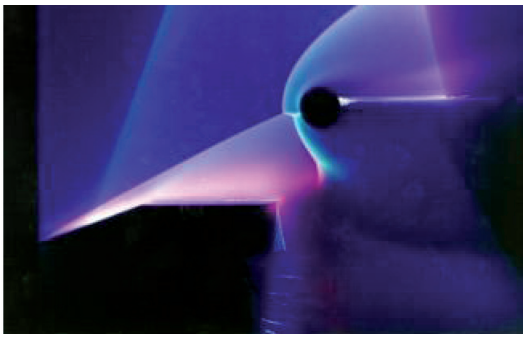

a) Visualization by a sweeping electron beam to study the interaction of shock waves.

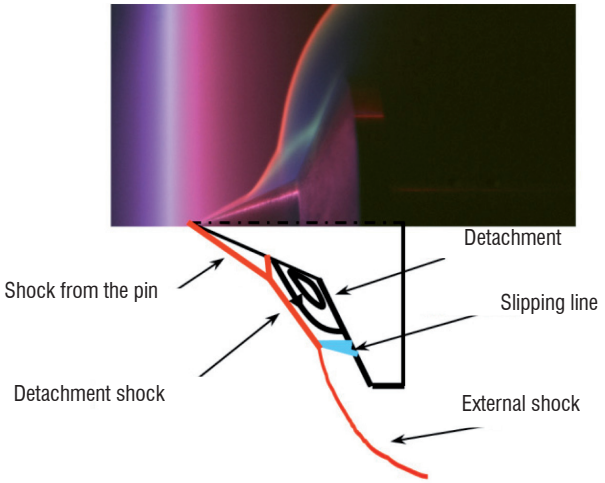

b) Visualization by post-luminescence to study flow structure around a 25/65 sharp double cone.

Figure 4 – EBF visualization in a Mach 10 flow.

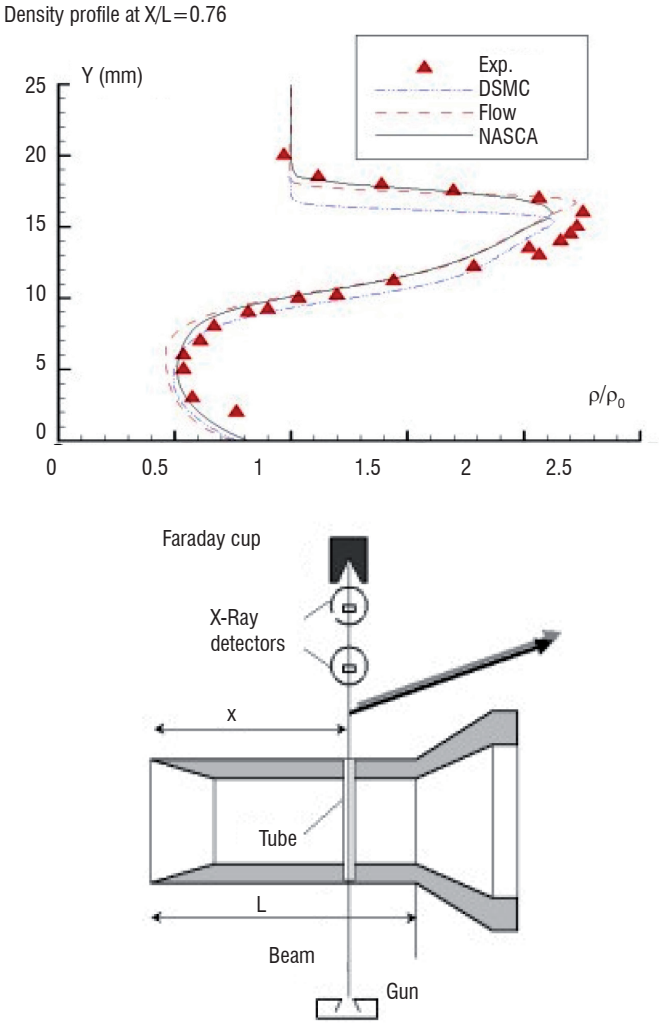

Figure 5 - Flow density profile measurements using electron beam-induced X-ray radiation and comparison to CFD.

Vibrational and rotational temperatures

Measurement of the intensities of the rotational or vibrational lines and the use of the expression in Figure 2 allow for determination of the corresponding temperatures of a molecular species in the gas being studied.

To illustrate rotational temperature measurement capabilities at low and high temperatures, we present here an application which allowed for the characterization of a gas containing two groups of molecules, each one having a different rotational temperature (transient phase). The objective was to measure the rotational temperature of nitrogen molecules reflected from a 5 mm-diameter disc placed in a hypersonic flow.

The experiments were carried out in cooperation with the DLR at the V2G wind tunnel in Göttingen [10] [11]. The Knudsen number (λ/L where λ is the mean free path and L is a representative physical length scale) is set very high by using a low-density flow and a small surface in order to prevent a shock wave being formed in front of the surface: the molecules are just reflected from the surface. Measuring the rotational temperature of these reflected molecules allows us to study how these molecules accommodate to the surface temperature, which can be varied from room temperature up to 1200 K. The effect of the velocity of the incoming molecules has also been studied through variation of the stagnation temperature of the flow from 300 K to 1200 K.

The beam is set to cross the flow vertically at a distance of 1 mm from the disc surface. A simple lens conjugates about 1 mm of the beam on the entrance slit of a high resolution spectrometer. Figure 6a shows the rotational spectrum of only the free flow when the model is away. The rotational temperature in this case is 32 K for stagnation conditions of 1020 K and 5 bar. In front of the disc surface, the rotational structure of the fluorescence (Figure 6.b and c) is more complex as it is a superposition of fluorescence from two groups of molecules: the free flow molecules and those reflected from the surface (here found to be at 1000 K). The density of the reflected molecules can also be deduced from spectrum inversion: it is here seen to be about three times higher than the free flow in the probe volume. The data interpretation is given in reference [11].

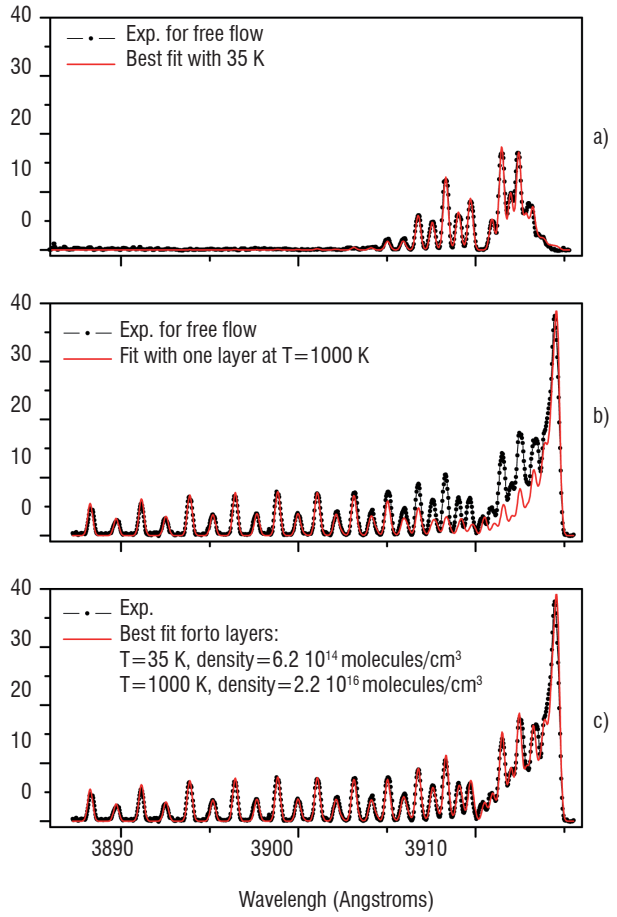

Figure 6 - EBF rotational spectra of reflected molecules by a disc placed in an N2 hypersonic flow { a) spectrum in the free stream at 35 K; b) and c) present the same spectra in the flow at 1 mm in front of the disc but with different simulated spectra to show that there are two groups of molecules: incoming flow at 35K and reflected molecules at 1000K }.

Velocity

Velocity measurements by EBF can be performed using the following methods:

- Doppler shift technique
- Time of flight technique
  - Electrical detection with Langmuir probes
  - Optical detection of afterglow

The Doppler shift technique is quite straightforward and involves simply analyzing the Doppler shift induced in the fluorescence lines observed by a high resolution spectrometer at an angle which is the smallest possible with respect to the flow axis [2]. We will describe more thoroughly here the time of flight method and particularly when it involves optical detection of afterglow.

Velocity Measurements using a classical pulsed electron beam

Gas ionization is an important process among excitations due to electron beams. This phenomenon can be used with a pulsing electron beam to induce columns of plasma which are convected by the flow. The plasma columns contain mainly N_2^+ ions and low energy secondary electrons es produced during the ionization process.
After tagging the flow with these columns of plasma, local velocity measurements can be done by measuring the time of flight of the plasma columns between two chosen points through electrical detection of the N_2^+ ions (or the secondary electrons) with Langmuir probes [3].
The movement of the plasma columns can also be traced by the radiative emissions (afterglow) produced from secondary electron excitations in the columns. Some of the secondary electrons have sufficient energy to excite molecules of the gas producing fluorescence (N_2^+1N and $N_2$2P emissions) similar to the ones due to the excitations by the primary electrons of the beam. These secondary excitations can occur over a relatively long distance downstream from the electron beam depending of the flow velocity and the relaxation time of the secondary electrons. The radiative lifetime τ of the excited molecules is very short ($\tau \sim 60$ ns), which means that the fluorescence can be considered to be emitted at the point of excitation in the columns for flow velocity V less than 10000 m/s.
Velocity measurements can be made here by measuring the distance of flight of the luminous plasma columns during a known time interval. For a single column, a streak and/or intensified camera for example can be used to take snapshot pictures at different known times to follow the column displacement. The opening time must be very short (a few hundreds of nanoseconds for velocities less than 10000 m/s) to freeze the movement of the column at each opening. Usually, the light collected is quite low and image accumulation must be used to enhance detection, but this is possible only if the flow velocity is constant. A further improvement is to use a train of columns induced at regular intervals of time by a pulsed electron beam and perform stroboscopic detection by a camera whose openings are pulsed at the same frequency of the electron gun. Chemiluminescent reactions of N_2(A) metastables (created by the electron beam) with species like NO or OH can also be used to enhance optical detection of the plasma columns [6].
Figure 7 presents an image of acceptable contrast for measuring the free stream velocity in a Mach 10 flow using a frequency of 100 kHz for both the electron gun (see box 1) and the camera pulses. Application inside a shock layer is more difficult as we must first know the local direction of the velocity or the stream line structure.

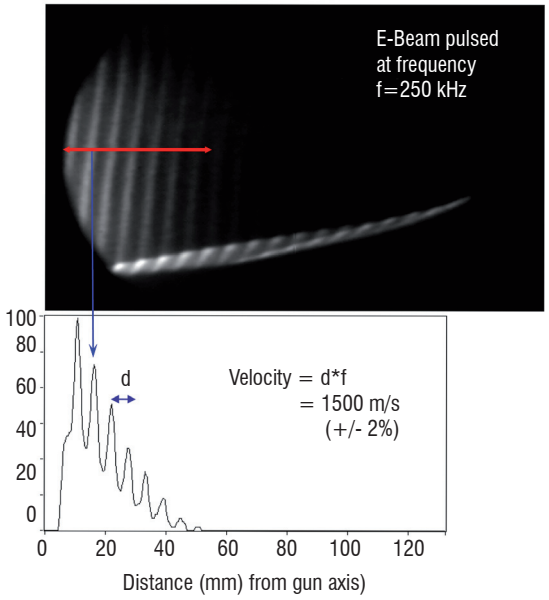

Figure 7 - Velocity measurements using pulsed afterglow. An electron beam pulsed at frequency f (pulse duration of a few hundred ns) induces a train of luminous plasma columns convected by the flow. Flow velocity is proportional to the distance between two successive columns.

Box 1 - Electron guns

The electron gun is a key element in the EBF technique, which requires a thin monoenergetic electron beam of a diameter around 1 mm (for adequate spatial resolution), energy of about 20 keV (for propagation length of a few hundred mm in a gas at pressures of 100 Pa) and current of about 1 mA (for a sufficient fluorescence signal).
At Onera we have developed three types of guns:

- hot filament [1] [2] [3],
- secondary emission (beam or sheet emission) [4],
- pseudo spark [8] [18] [19],

Their main characteristics are presented in Figure B1- 01 and Table B1 - T1.

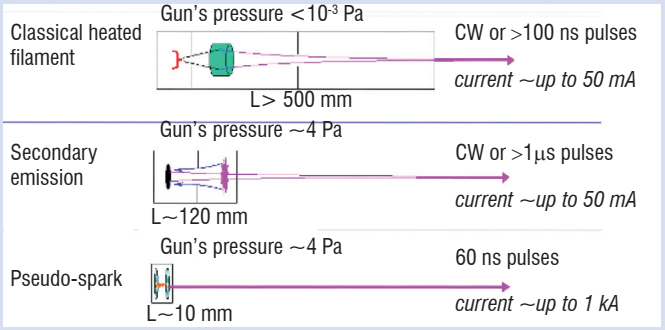

Figure B1 - 01 - The three main types of electron guns

Gun	Measurement duration	Repepition rate	Measurements
Classical gun (Hot filament) (beam 30 kV, 1 m A, diam 1, 0.1 mm)	100 ns to CW	CW or pulsed up to 10 MHz	All EBF measurements in low enthalpy conditons (Hi/RTa <10)
Pseudo-spark (beam 60 kV, 100 A,diam 1 mm)	30 ns to 5 μs	Pulsed up to 1 kHz	Velocity in all conditions; sufficiently miniature to be placed inside a body in the flow
Secondary emission (25kV, 10 mA, diam 1 mm)	1 μs to CW	CW or pulsed up to few kHz	All EBF measurements

Table B1 - T1 Main properties and performances of different types of electron gun

Usually heated filament electron guns (and pseudo-spark in a few experiments) are used to generate the electron beam in wind tunnels. But these devices are quite difficult to use in flight experiments because of their relatively large weight and energy consumption as well as secondary vacuum requirements for their operation.

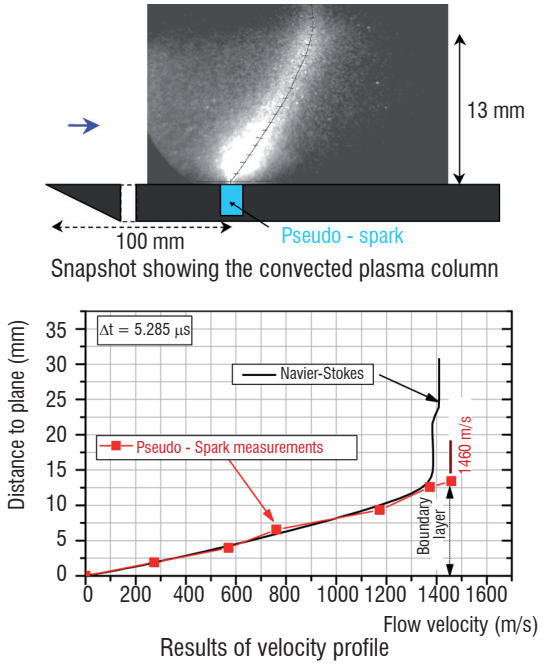

Figure 8 - Velocity profile measured by a pseudo spark electron from within a flat plate model in the Onera R5 Mach 10 wind tunnel.

Velocity measurements across the boundary layer in hypersonic flows using a pseudo spark electron-beam-assisted glow discharge

Instead of image accumulation, one can try to increase the afterglow by using a more intense electron beam or some technique to increase the number of excitations in the plasma column. One such method is to use a so-called "pseudo spark" type electron gun which by principle of operation delivers a pulsed beam of some tens of nanoseconds (see box 1). However, the high current intensity (a few amps) remains insufficient for single-shot detection with an intensified CCD. One way to further increase the afterglow is to create and maintain a glow discharge in the plasma column created by the pseudo spark beam through proper electrical ground connections [8].
This pseudo spark technique offers the further advantage of being quite small in dimensions so that it can be placed inside a model to measure the velocity profile in a shock layer of simple geometry. We present in Figure 8 an example of a velocity profile across a boundary layer obtained with an electron gun inside a model in the Mach 10 low-density hypersonic R5 wind tunnel at Onera. In these experiments, an intense pulsed electron beam is emitted by a very small

Box 2 - EBF for in - flight measurements

Based on the advent of a new compact electron gun designed from the secondary emission principle, Onera is studying a laboratory prototype to demonstrate the feasibility of obtaining a compact EBF instrument for in-flight measurements onboard an atmospheric re-entry vehicle as shown in Figure B2 - 01.
The perimeter of development for the in-flight EBF system will have at least the following measurement objectives:

- Species density: ρ/ρ_∞ profile across a shock layer. The species is N_2 and possibly NO in the event of atmospheric re-entry or CO and CO_2 in the case of a Martian re-entry.
- Temperature of vibration T_{vib} and/or temperature of rotation $T_{rotation}$ of one of the above mentioned species;

The measurements are to be made with a spatial resolution on the order of a few mm^3 along a line perpendicular to the wall of the vehicle. The segment of the line to be measured is of a minimum length of 100 mm with the center at about 300 mm from wall of a vehicle. The measurements are to be provided at a minimum repetition rate of 10 Hz in the altitude range of 50 km to 70 km.
Measurements at higher altitudes are possible with this technique but at the expense of a lower signal to noise ratio which can partly be compensated for by a longer integration time (~1 s) and lower repetition rate (~1 Hz). Measurements are less likely below 50 km due to non-linearity in the fluorescence signal as well as high beam dispersion and attenuation.

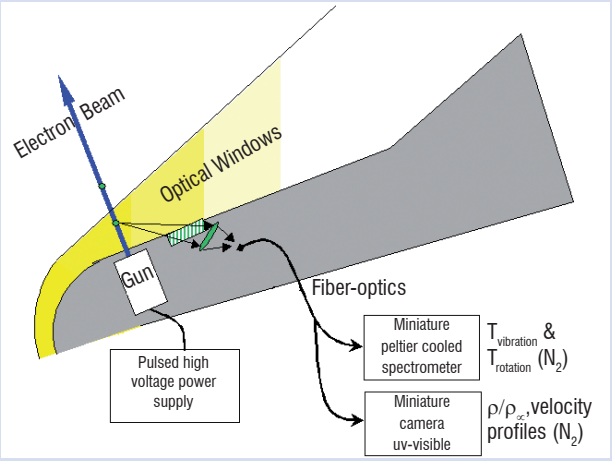

Figure B2 - 01 - Electron beam fluorescence measurements on board a re-entry demonstrator

The EBF prototype will use an electron gun to produce a pulsed (around 10 Hz) electron beam of about 20 keV energy, about 1 mA intensity and 2 mm diameter which will be emitted through a small diameter (few mm) opening on the vehicle wall. A turbo-molecular pump and high-voltage power converters operating from 24 V are needed for the beam emission. Two optical detectors (one camera and one spectrometer) will be used to observe, through specific optical windows on the vehicle wall, the fluorescence induced by the electron beam. The data collected will be transmitted to the vehicle controller for recording and/or tele-transmission. The processing of the data will be done during the post-flight analysis.

The design studies leading to the final configuration presented in figure B2 - 02 used many off-the-shelf components selected for their potential to be easily upgraded for space applications. The obtained prototype is quite compact, occupying a volume of 370 x 300 x 250 with few interfaces for data communications and a low-voltage power supply. The mass of the instrument is around 11 kg but there are still ways to reduce the mass through further optimization of the design.
One of the validation tests of the final laboratory prototype was done in a small transparent vacuum chamber. This chamber is a cylinder of 300 mm diameter and of 400 mm length with the cylindrical part made of 8 mm thick glass. There are metallic plates on the top and bottom of this cylinder. The EBF assembly base plate has been adapted to the top plate where appropriate holes have been drilled for the prism windows and the electron beam exit. The bottom plate is equipped with the necessary feed-throughs for pumping and pressure monitoring. Figure B2 - 03 shows the setup disposed on an office table. Alongside the cylinder there is an electronic box which was specially manufactured to manually control the operation of the EBF assembly. This electronic box also includes a converter to provide 24 V power to the EBF prototype from a standard 220 V power supply.

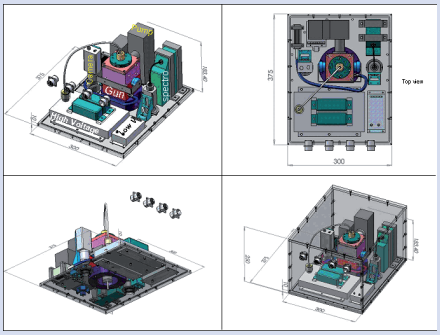

Figure B2- 02 - EBF final assembly design for the laboratory prototype

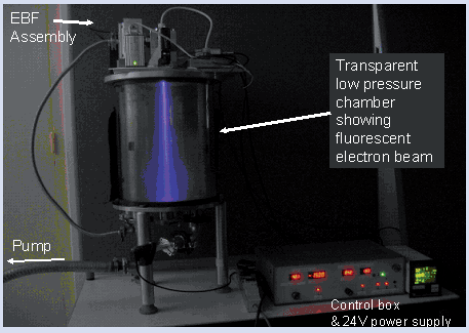

Figure B2- 03 - Tests of the laboratory prototype for an inflight EBF instrument

(2cm x 3 cm) pseudo-spark [18] [19] electron gun located inside the model (2D grounded metallic plate).
It penetrates the flow from a 0.3 mm hole across the surface, and traces the path of a high-voltage glow discharge in some ten nanoseconds. The filamentary discharge is instantaneously connected to a high voltage capacitor via a thin, high-voltage metallic rod placed parallel to the flow axis and 100 mm away from the gun exit. This maintains the gaseous filament very bright for a few microseconds. The initial linear pattern of the discharge then closely follows the streamlines which are known in this case. It is verified that no distortion occurs when the discharge is triggered within the same gas at static pressure.
At a precise time delay (5 μs) after the electron gun actuation, a CCD camera is opened briefly (250 ns) to image the position of the luminous column convected by the flow (Figure 8). The local velocity of the stream versus the distance above the plane is simply deduced from the horizontal displacement of a given point during the selected delay time.

The observation field extends 20 mm above the model. As a calibrated grid is used to determine the magnification of the optics, the global accuracy of this method can be estimated to 50-100 m/s. For identical aerodynamic conditions, the measured velocity profile compares correctly to the results of a numerical Navier-Stokes calculation.

Conclusion

Onera has further developed the EBF technique through new methods and electron guns and extended the application to high enthalpy flows together while rendering it less complex for routine use in wind tunnels. The challenge now is to use this technique for in-flight measurements in the flow around a reentry vehicle for Earth reentry studies or probing of the atmospheres of other planets, and Onera has already taken steps in this direction through the development of a prototype described in box 2 ■

References

[1] A. E. GRUN, E. SHOPPER, B. SCHUMACHER - *Electron Shadowgraph and Afterglow Pictures of Gas Jets at Low Densities*. J. Appl. Phys., 24, p1527, 1953.
[2] E. P. MUNTZ - *The Electron Beam Fluorescence Technique.* AGARDograph 132, 1968.
[3] A. MOHAMED - *EBF in Blow-Down HypersonicWind Tunnels.* Phd Dissertation, Paris XI, 1991.
[4] R. COLOMBA, J. BONNET - *Canon à électrons pour technique FFE en nappe.* Onera RT 46/3409 PN, 1994.
[5] D. P. WEAVER, D.C. WADSWORTH, D. CAMPELL, E.P. MUNTZ (DSMC) - *Comparison with Electron Beam Measurements of Sonic Orifice Expansion Flow of Nitrogen.* Proceedings of the 18th International Symposium on Rarefied Gas Dynamics, Vancouver, Canada, AIAA, Washington, DC, Vol.158, pp.1314 (1994).
[6] A.K. MOHAMED, T. POT, B. CHANETZ - *Diagnostics by Electron Beam Fluorescence in Hypersonics*. ICIASF'95 Record 95-CH3482-7,14.1, International Congress on Instrumentation in Aerospace Simulation Facilities, Wright-Patterson AFB, Ohio, USA, July 1995.
[7] L. A. GOCHBERG - *Electron Beam Fluorescence Methods in Hypersonic Aerothermodynamics.* Prog. Aerospace Sci., Vol. 33, 1997, pp. 431-480.
[8] S. LARIGALDIE, D. BIZE, A. K. MOHAMED, M. ORY, J. SOUTADÉ, and J. P. TARAN - *Velocity Measurement in High Enthalpy, Hypersonic Flows Using an Electron-Beam-Assisted Glow Discharge*. AIAA Journal, Vol 36, N° 6, (1998).
[9] J-C. LENGRAND - *Mesure des températures de rotation dans l'azote à basse densité par la sonde à faisceau électronique. Application à l'étude d'écoulements.* Thèse de Doctorat en Sciences Physiques, Université Paris VI, 1974.
[10] G. GUNDLACH, C. DANKERT - *Rotational Accommodation of NO on a Hot SiC-Surface in a Rarefied Flow, Proceedings of the 18th International Symposium on Rarefied Gas Dynamics*. Vancouver, Canada, AIAA, Washington, DC, Vol.158, pp.976 (1994).
[11] S. NOVOPASHIN, C. DANKERT, K. LEHMKÖSTER, A. MOHAMED, T. POT - *Rotational Temperatures of N2-molecules Reflected from a Wall, Rarefied Gas Dynamics,* Proceedings of the 20th International Symposium, 19-23 August 1996, Beijing/China, Ed. Ching Shen, Peking University Press, Beijing, China, 1997.
[12] J.H. DE LEEUW, W.E.R. DAVIES - *Measurement of Temperature and Density in the Upper Atmosphere Using an Electron Beam*. Can. j. Phys, 50(10), 1044 (1972).
[13] R. R. O'NEIL, W.R. PENDELTON, A.M. HART, A.T. STAIR - *Vibrational Temperature and Molecular Density of Nitrogen Measured by Rocket-Borne Electron Beam Induced Luminescence*. J. Geophy. Res., 79(13), 1942, (1974).
[14] R.J. CATTOLICA, R.J. SCHMITT, R.E. PALMER - *Feasibility of Non-Intrusive Optical Diagnostic Measurements in Hypersonic Boundary Layers for Flight Experiments.* AIAA paper 90-0627 (1990).
[15] T. KAWASHIMA, K. OYAMA AND K. SUZUKI - *A Measurement of Vibrational-Rotational Temperature and Density of Molecular Nitrogen in the Upper Atmosphere by Rocket-Borne Electron Beam Induced Luminescence*. The Institute of Space and Astronautical Science(Japan), report n° 672, 1999.
[16] C. DANKERT, R.J. CATTOLICA, W. SELLERS - *Local Measurements of Temperatures and Concentrations: A Review for Hypersonic Flows, in New Trends in Instrumentation for Hypersonic Research*. Ed. A. Boutier,, Kluver Academic Press, ISBN 0-7923-2024-7, 1993.
[17] D. R. FARLEY, R. J. CATTOLICA - *Electron-Beam Fluorescence from the A2Πu→X2Πg and B2Σu+→X2Πg Transitions of CO_2^+.* J. Quant. Spectrosc. Radiat. Transfer, Vol. 56, N° 1, p. 83 - 96, 1996.
[18] J.CHRISTIANSEN and C. SCHULTHEISS - *Production of High Current Particle Beams by Low Pressure Spark Discharges*. Z. Physik, Vol. A290, pp. 35-41 (1979).
[19] S. LARIGALDIE - *Study of the Breakdown Phase in a Pseudospark Switch: Part I-Basis Experiments and Crude Model, Part II-Ultrafast CCD Cameragrams Using HE+ Spectral Line Emission*. IEEE Trans. on Plasma Science, Special Issue on Physics and Application of Pseudospark Discharges,Vol. 23, N° 3, pp 362-374 (1995).
[20] S. LARIGALDIE, D. BIZE, A. K. MOHAMED, M. ORY, J. SOUTADÉ and J. P. TARAN - *Velocity Measurement in High Enthalpy, Hypersonic Flows Using an Electron-Beam-Assisted Glow Discharge.* AIAA Journal, Vol 36, N° 6, (1998).
[21] A. MOHAMED, J. BONNET, J.-P. FALÉNI, U. KOCH, B. ESSER, A. GHULAN, R. JANOVSKY, P. VAHLENKAMP - *ESA ITI project- Demonstration of Electron Beam Fluorescence (EBF) Feasibility for Flight Application in the DLR LBK wind tunnel.* Onera report RF 1/10453 DMPH - April 2007.
[22] L. WALPOT, H. OTTENS - *FESART/EXPERT Aerodynamic and Aerothermodynamic Analysis of the REV and KHEOPS Configurations.* TOS-MPA/2718/LW, 16 September 2002.

Ajmal Khan Mohamed obtained his Ph.D. in Molecular Physics from the University of PARIS XI in 1991. He then joined the Physics Department of Onera to continue the development of several optical diagnostics (Infrared Diode Laser Absorption Spectroscopy, Electron Beam Fluorescence, Emission Spectroscopy) to probe high enthalpy hypersonic flows in arcjets and shock tubes. He has also been involved in solid state laser development for Laser Induced Fluorescence and in cavity enhanced spectroscopy for trace species detection. He managed several internal or European projects on these techniques for in-flight measurements as well as for environmental applications and is still active in the field of optical diagnostics.

Jean Bonnet after a Ph D in Plasma Physics obtained in 1975 at Paris Sud University, he worked on High Power gas lasers and electron beams. In 1990 he began to work on plasma propulsion and associated diagnostics, mainly thrust balance and Laser Induced Fluorescence (LIF). In the same time he uses his knowledge of secondary emission electron guns developed at Onera to improve the EBF technology for wind tunnel.

Serge Larigaldie graduated from the University of Paris XI, Orsay, France, in 1968, and received the Doctorat de Spécialité in plasma physics in 1970. In 1985, he received a State Doctorate Thesis from the University of Paris XI. Since 1971, he has been with Onera where he has been involved in studying the physics of lightning, high-voltage commutation, plasma mirrors, and plasma assisted combustion. Dr. Larigaldie was awarded Senior Scientist in 1988 and is a Senior Member of the French Société des Ingénieurs et Electroniciens. He is presently retired.

Thierry Pot entered at Onera in 1983, he has been in charge of the R5Ch facility and participate actively to the improvement of the electron gun techniques and diagnostics.

Jacques Soutadé obtained his CNAM engineering degree in 1991 with a mémoire on «Système d'acquisition et de traitement des images des diagrammes de diffraction d'électrons obtenus en expitaxie par jets moléculaires». He joined Onera windtunnel facilities at Le Fauga in 1983. In 1991 he switched to the F4 hypersonic arcjet facitity as an instrumentation and optical engineer and is now the head of this facility since 2002.

Babacar Diop obtained his R&D engineering degree on Micro-nanoélectronics and instrumentation from the University of Strasbourg I in 2007. Since then he is doing a PhD work at Onera on the Electron Beam fluorescence technique for reentry aerothermodynamics characterization.

J.M. Desse, R. Deron
(Onera)

E-mail: Jean-Michel.Desse@onera.fr

Shadow, Schlieren and Color Interferometry

This article describes the three main methods for visualization of a gas in motion based on local refractive index variations: shadowgraph, schlieren and interferometric techniques. These non-invasive methods have been used by Onera for visualizing and measuring the gas density fields of two-dimensional and axisymmetric flows, varied examples of which are presented here. The originality of this paper lies, on the one hand, in recent developments in polychromatic holographic interferometry using transmission and reflection panchromatic plates and, on the other hand, the results obtained in digital color holographic interferometry. Although the CCD resolution and size are not as good as that of holographic plates, digital three-wavelength holographic interferometry appears, for the near future, to be the best candidate to characterize future complex flows.

Introduction

Fine characterization of complex flows has become an recognized, specific approach since the 1950's. The need to develop measurement tools adapted to the study of aerodynamic flows was already a major concern at the time and, for this reason, specific shadow, schlieren and interferometric optical benches were built in various Onera wind tunnels. Among the optical methods used in fluid mechanics, those based on variations of the refractive index of media have the advantage of being non-invasive, as only luminous phenomena occur. Some of these processes, such as shadow or schlieren techniques, provide information that is most often qualitative, while others, such as interferometry, give access to a property of the fluid, the gas density, if the flow is two-dimensional or axisymmetric.

Shadow technique

Changes in the refractive index of a gas can be made sensitive by using the deviation produced by the light rays through this gas [1]. It is assumed that the refractive index n is independent of z, the z axis being perpendicular to the flow axis. The gas thickness e, the refractive index n and the optical thickness E are functions of x and y. The Malus theorem determines that the deviations θ_x or θ_y produced by the gas are respectively equal to $\delta E / \delta x$ or $\delta E / \delta y$. Light deviations are caused by variations in the refractive index which are directly related to variations in gas density. The visualization methods based on this principle are shadow or schlieren techniques: they are called «methods of deviation.»

In the shadow technique, the test section is crossed mostly by a beam of parallel light. It uses a small source located at the focal length of a converging lens or a spherical concave mirror. After crossing the test section, the beam illuminates a screen placed beyond the test section at a distance b. A beam undergoing a deviation θ will be visualized on the screen at a nearby point where it would be visualized without flow. This deviation depends on the gradient of the gas density. For a uniform gas density gradient, this shift is constant and the screen is evenly lit. However, if the gas density gradient is variable, displacements vary from one point to another and light and dark areas can be observed on the screen. The contrast on the screen is measured by the relative variation of the illumination I and we have:

$$\frac{dI}{I} = -b\frac{dE^2}{dx^2} \quad (1)$$

The shadow technique indicates the second derivative of the optical thickness of the test section, and thus the gas density if the thickness e is constant. The visualization of shock waves gives particularly good results, because the second derivative of the density changes sign. The situation is illustrated in Figure 1 where one can see the flow around a circular cylinder at Mach 0.75 [2] and the phenomenon of the incoming blast wave of a small rifle [3]. In the first case, high speed visualizations synchronized with unsteady pressure measurements show a strong coupling between the flow over the cylinder and the vortex street formed in the near wake. In the second case, the effects produced by the firing of guns are visualized by high-speed shadow technique and a certain number of parameters have been identified to establish the rules of similarity for this phenomenon. Here, the exposure time of each frame is 300 nanoseconds.

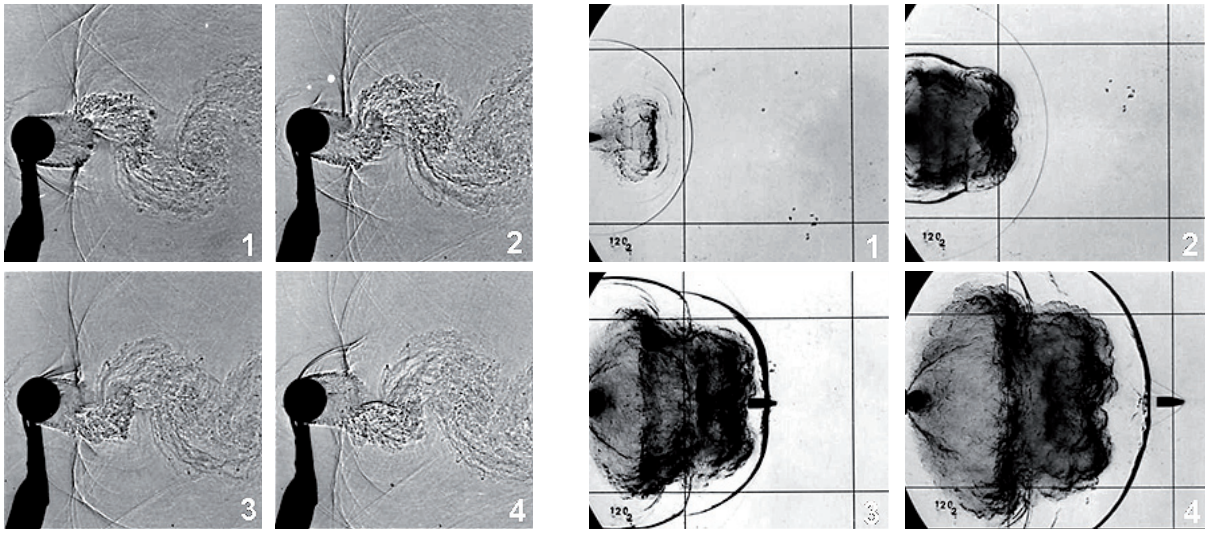

Figure 1 - Visualizations recorded with high-speed shadow technique
Video - http://aerospacelab.onera.org
http://aerospacelab.onera.fr/al1/Shadow-Schlieren-and-Color-Interferometry

Schlieren technique

The schlieren method devised by Foucault and developed by Töpler involves intercepting, with a knife, some of the light rays which are deflected in the test section [4]. In practice, a condenser forms from a source S an image S' which is cut with a knife. A lens located between the screen and S' gives an image of the test section. A part of the light rays passing through S at one point in the test section is intercepted by the knife while the other part A converges on the screen (see Box 1). If the brightness of the source is constant, the irradiance I is proportional to the beam of light that is stopped by the knife. When the rays are not deflected, section A does not change regardless of the point of the screen. The illumination is uniform and I proportional to S' which emerges from the knife. When the optical thickness of the test section varies, section A varies as a result of deviations of the light beams. The variation dI depends on θ_x, because the illumination I is proportional to part A. If b is the distance from the knife to the section and h the height of section A in the absence of variation, it is shown that:

$$\frac{dI}{I} = \frac{dA}{A} = \frac{b}{h}\theta_x = \frac{b}{h}\frac{dE}{dx} \qquad (2)$$

We see that the schlieren method shows the first derivative of the gas density if the flow is two-dimensional and if the test section walls are parallel. Two examples are given in Figure 2. First, a comparison of the shadow and schlieren techniques shows the flow instabilities on the upper side of an airfoil at Mach 0.76 (8° attack angle). Schlieren pictures reveal fine structures, especially downstream from the shock wave and in the separated flow. The schlieren technique can be also applied in a water tunnel. The picture in Figure 2 shows the wake flow around a circular cylinder in a hydrodynamic tunnel. Natural temperature gradients existing in the water are sufficient to induce variations in the refractive index exhibited by the wake flow downstream from the cylinder and it is possible to increase the schlieren observations by thermally marking large-scale structures [5].

Box 1 - Schlieren technique

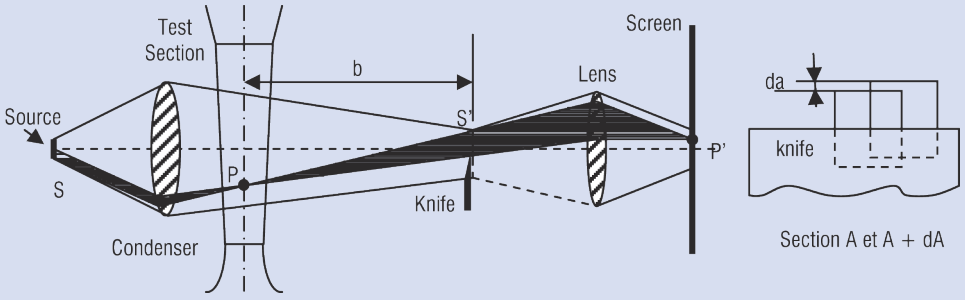

Methods of light deviation : $\theta_x = dE/dx$ or $\theta_y = dE/dy$
Optical thickness : $E = (n-1).e$ e: test section width
Gladstone-Dale relation : $(n-1)/(\rho/\rho_s) = K$ $K = 296.10^{-6}$ (air) and ρ_s : standard gas density
Shadow technique : dI/I // to dn^2/dx^2 or dn^2/dy^2
Schlieren technique: dI/I // to dn/dx or dn/dy

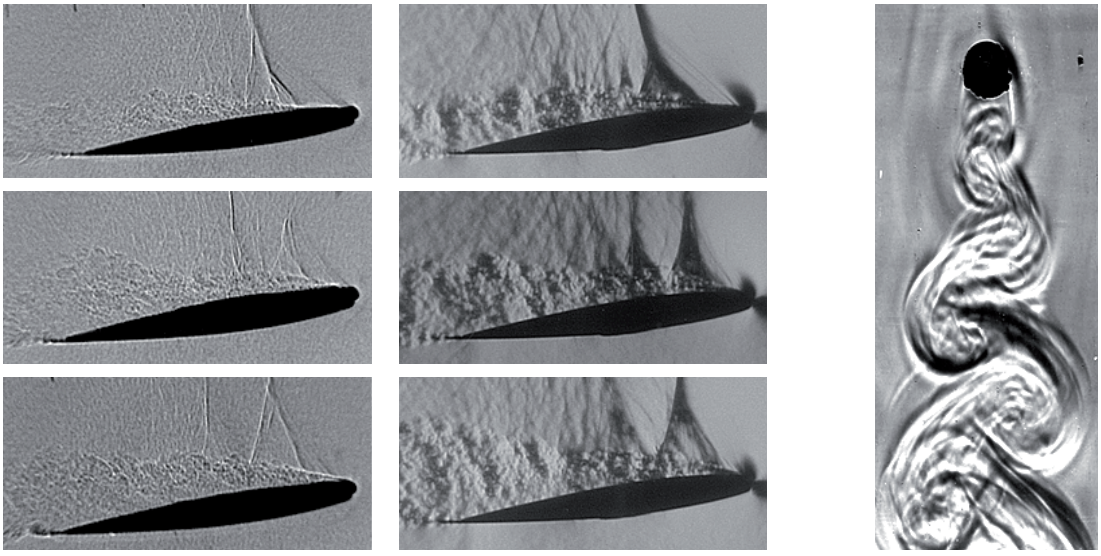

Shadow technique | Schlieren technique | Water tunnel

Figure 2 - Schlieren technique applied to aerodynamic and hydrodynamic flow.

Background Oriented Schlieren technique : a simple quantitative schlieren method

The Background Oriented Schlieren (BOS) technique [6] is one of the most recent schlieren techniques. This method likewise takes advantage of a very simple phenomenon: the mirage effect. The basic principle of the BOS thus consists of imaging a structured scene, preferably a dot-pattern, observed through the flow of interest. The refractive index variations in the flow make the images of the dotted points move. The displacement d of each individual image corresponds to a light deflection angle ε in two spatial directions (Figure 3). The deflection angle is given by:

$$\varepsilon = -\frac{d \times p}{D} \qquad (3)$$

where p is the physical dimension of a pixel in the dot-pattern background and D the distance between the background pattern and the intersection point between the undisturbed and disturbed light rays. This technique is thus sensitive to the density gradient vector field. In contrast to the classical schlieren methods, digital image processing replaces the optical processing to compare the schlieren distorted and undistorted image of the pattern background. The image correlation PIV technique is used to derive the projected mass density gradients in the observing direction.
The main value of the technique is that it can be applied to visualize large fields of interest in wind tunnels but also in outdoor experiments with simplified experimental equipment, eliminating the need for high-quality optics and windows, knife-edges, and laser sources. In its simplest form, this low-cost method requires a structured, randomly-generated background pattern, a high-speed camera and a high-intensity light source to illuminate the scene (Figure 4).

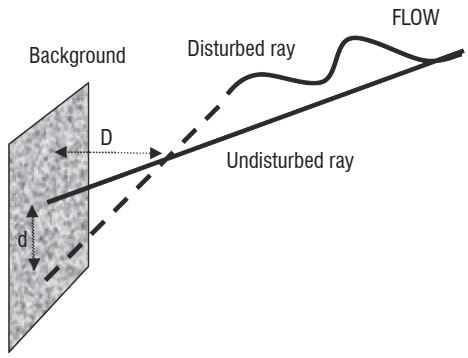

Figure 3 - Schematic of the BOS principle

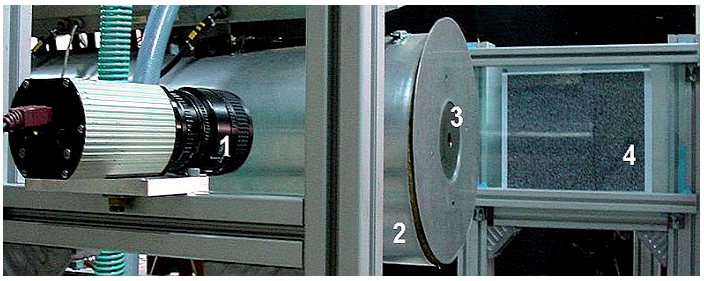

Figure 4 - BOS set-up with camera and dot-pattern background for studying supersonic jets.
1: Camera sensor, 2: Supersonic jet nozzle, 3: Duct , 4: Dot-pattern scene

Further quantitative density measurements can be obtained in the same manner by using another schlieren technique. The BOS technique was implemented at Onera to study the aerothermal effects of hot supersonic jets [7]. Quantification of the jet turbulence was derived from BOS measurements using the Abel transform under the assumption of an axisymmetric jet (Figure 5).

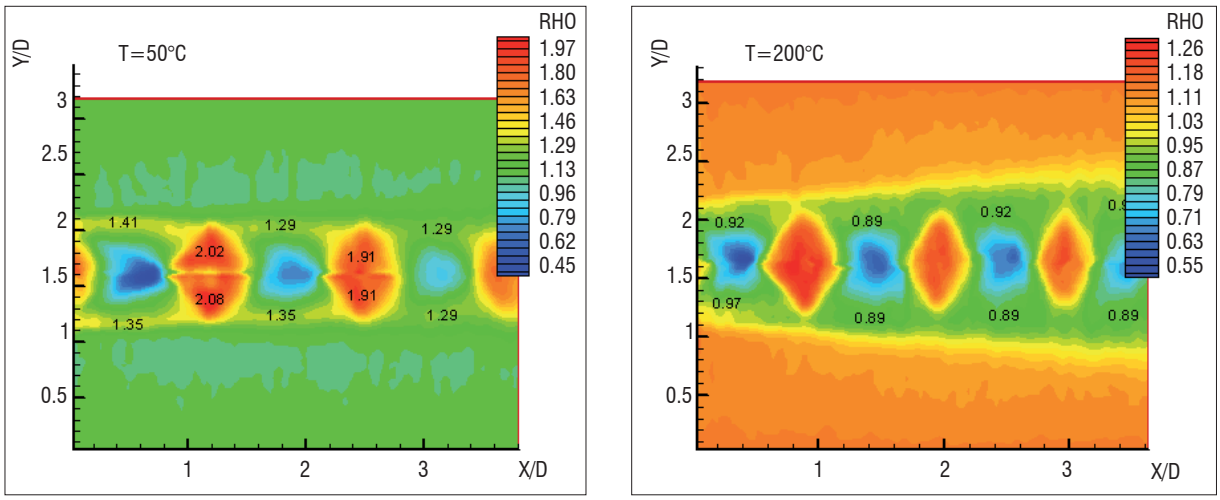

Figure 5 - Mass-density fields of the mixing zone in a hot supersonic jet at T=50°C and at T= 200°C

The size of the turbulent mixing zone dramatically increases downstream at high temperature. The application of the BOS technique was also successfully demonstrated by the DLR through investigations on compressible vortex formations from the blade tips of two different helicopters in flight [8].

Differential interferometry or color schlieren technique

In the observation and analysis of high-speed flows, monochromatic interferometry has been developed to obtain quantitative information about gas density in large fields [9]. When density gradients are relatively weak, differential interferometry in polarized white light is very well suited [10], [11]. Briefly, a Wollaston prism decomposes a light wave polarized in a given direction into two orthogonal vibrations of approximately equal amplitudes separated by a small birefringence angle ε. The prism is placed at the center of curvature of a spherical mirror placed behind the test section. After crossing it, the beam is focused back towards the source, thus crossing it a second time, so that the sensitivity is increased. This is a compensating device, as the initial path difference between the two rays can have an arbitrary value, thus yielding a uniform color on the screen, simply by translation of the prism. It is also self-compensating because, the prism being fixed, any deviation of the light rays produces optical path lengths in the air and prism which compensate for each other. In white light, a colored fringe pattern can be observed in a sequence approximately matching Newton's color scale. The prism used is of the wide-field type (see Box 2), which yields a uniform background tint in a convergent light beam. The apparatus is easy to set up and it has a high sensitivity and is much smaller and less subject to vibrations than the conventional separated-beam interferometers such as the Mach-Zehnder interferometer.

Application to 2D-unsteady wake flows

In this example, the unsteady wake flow is analyzed behind schematic turbine blades at Mach 0.4 [12]. The unsteady pressure signals are simultaneously recorded around the trailing edge in order to be able to synchronize pictures and pressure variations. Two successive interferograms and the gas density field are given in Figure 6. The gas density ρ is referenced to the upstream gas density ρ_∞. With this model, the trailing edge is circular and 15 mm in diameter and the boundary layer state is quasi-laminar. In fact, because of the shifting of the two interfering rays, the interferograms cannot be analyzed down to the model wall. For example, an analysis conducted following a vertical line is only possible until one of two interfering rays is blocked by the model. In the conditions of the optical setup, the analysis is made down to 1.57 mm from the model wall and the gas density at the wall is obtained through extrapolation of the data. The density fields of Figure 6 show the vortices as concentric rings, with density decreasing toward the center. These vortices pass through a formation phase where the density decreases in the vortex center and a dissipation phase where the density and the size of the vortex increase.

Box 2 - Large-field Wollaston prism

n_e : extraordinary refractive index
n_0 : ordinary refractive index
α : pasted prism angle
ε : birefringence angle

$\varepsilon = 2.(n_e - n_0).\tan\alpha$
Measurement sensitivity depends on the birefringence angle

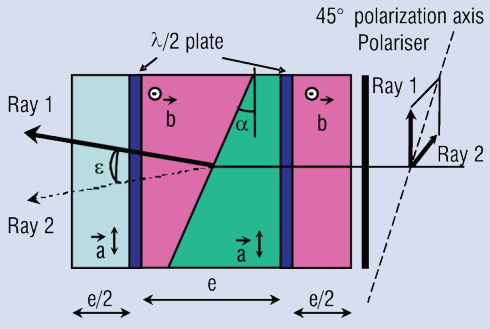

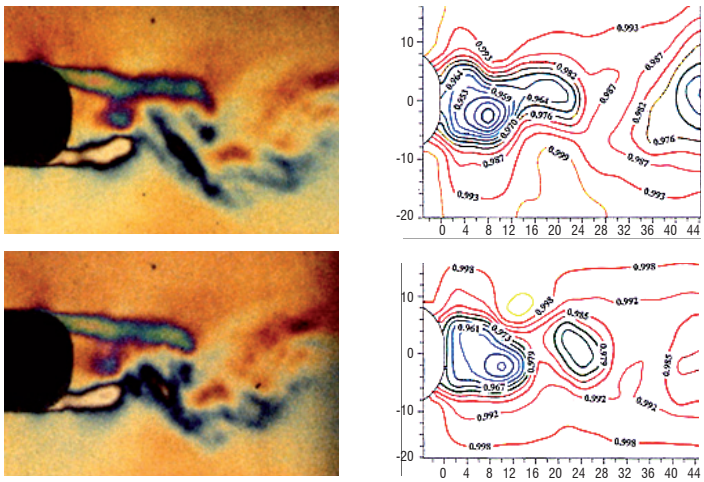

Figure 6 - High speed interferograms and gas density field reconstruction $\Delta t = 50\ \mu s$, M = 0.4

Application to axisymmetric wake flows

Differential interferometry is a non-intrusive technique that is particularly well-suited to investigation of phenomena related to compressibility and high temperatures. In the case of axisymmetric wake flows, it has been used to analyze the structure of a hot supersonic jet at Mach 1.8 injected into a coaxial supersonic flow at Mach 1.5. The method is sufficiently sensitive for a quantitative analysis to reconstruct the local density field. This operation is possible from a single interferogram provided the flow is two-dimensional or axisymmetric. The flow structure was assumed axisymmetric [13] and the interferograms were recorded with horizontal fringes, so that vertical gradients of the refractive index are detected. The radial density distribution was determined by spectrum analysis of the colors in the upper half-plane. Wherever possible, a similar analysis was made for the lower half-plane to see whether the flow was effectively axisymmetric. The axisymmetric flow was reconstructed from the undisturbed flow starting as close as possible to the axis of revolution.

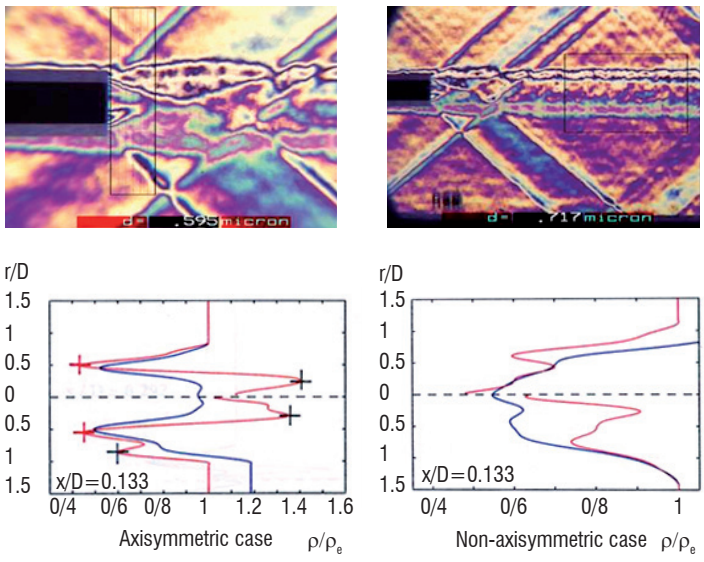

Figure 7 - Interferograms of the jet and radial distribution of the gas density.

Figure 7 shows two interferograms recorded for two different pressure ratios of 2.74 and 3.38 at the same temperature ratio of 1.67. In the analysis of the interferograms, the density distributions were computed along vertical lines. Whenever the vertical line, where the analysis is performed, completely crosses the jet, a density profile can be determined by integration in the upper half-plane and in the lower-plane. If the flow is strictly axisymmetric, the two profiles should be identical. In Figure 7 and for the axisymmetric case, the profiles of the optical thickness (blue line) and the gas density (red line) obtained near the nozzle exit section are relatively symmetric around the flow axis. In the non-axisymmetric case, the analysis made far downstream provides relatively contrasted density profiles which reflect the presence of local turbulences in the flow.

Application to hypersonic wake flows

In a hypersonic wind tunnel, the difficulty in measuring gas density is due to the fact that the index variations to be measured in the test section are very small. There are two reasons for this. Firstly, the light deviations are produced by beams that are passing through a phenomenon that is axisymmetric, and not two-dimensional. The integration paths traveled by the beams are therefore shorter, especially in the close vicinity of the shock. Secondly, since the free stream mass density is low (on the order of 2.10^{-2} kg/m^3), the index variations caused by the mass density gradients in the passage through the shock waves will induce index variations that remain very small (Box 3). The example presented consists of analyzing hypersonic flows around slender axisymmetrical bodies in order to compare the gas density distributions obtained in the shock layers with the analytical solutions [14]. Here, the Wollaston prism used separates the partial beams very widely. The prism angle itself is about 18° so that the distance between the two partial beams is 14.60 mm at the level of the spherical mirror, and it is therefore greater than the domain to be measured. This is equivalent to an ordinary interferometry arrangement with a separate reference, because the interferogram is directly interpretable in a two-dimensional flow but the setup is still differential because one of the beams, used as a reference, is placed in the undisturbed flow, either upstream from the model or, as in the present case, on the side of the model, outside of the shock layers. The interference fringes are placed horizontally so that the separation between the two beams will be vertical. The radial distribution of the mass density shown in Figure 8 has been obtained in the shock layer that develops around a cone of length $L = 300$ mm and apex semi-angle $\theta_c = 11.5°$. Results show that they are in good agreement with the analytical solutions on slender ogives following Merlen and Andriamanalina's power law and Jones' tabulated data for an inviscid flow of ideal gas around a cone.

Box 3 - Optical limit of differential interferometry

Minimum phase difference δ_{min} detected : 30.10^{-9}m
(from Gontier [10])

Optical thickness difference : $\Delta E = \delta_{min} / 2$
(double crossing of test section e)

For e = 40 mm (width of the test section) : $\Delta\rho_{min} = 1.64.10^{-3}$ kg/m^3

For e = 150 mm (width of the test section): $\Delta\rho_{min} = 4.4.10^{-4}$ kg/m^3

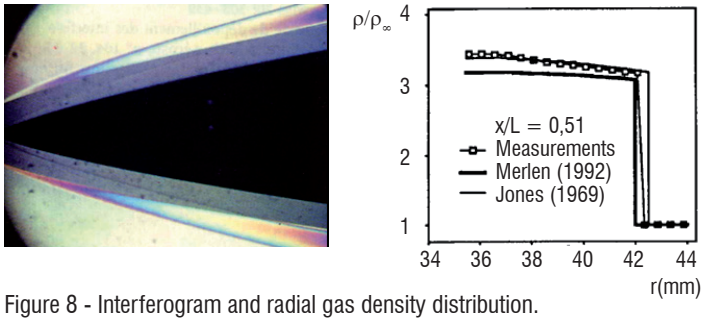

Figure 8 - Interferogram and radial gas density distribution.

Application to gaseous mixture

Differential interferometry has also been used to analyze the stability of the interface separating two fluids of highly different densities when it is impacted by an incoming shock wave [15]. The shock tube is vertical in order to keep the interface stable before the arrival of the shock wave. In this test, two diagnostic techniques are compared: X-ray densitometry and differential interferometry. For the X-ray technique, the partial gas density profile of one of the two gases can be obtained with careful calibration if the gas pair is air/xenon. In the case of SF6/air, both gases are transparent to X-rays and radiography cannot be used. Only differential interferometry can yield a measurement of SF6 distribution in air. The optical setup requires two Wollaston prisms (0.5° pasted angle) installed head to foot and two "Clairaut" achromatic lenses, 800 mm in focal length and 120 mm in diameter.

In the case of two-gas mixtures, Merzkirch has shown that the Gladstone-Dale relation can be extended if the Gladstone-Dale constants of each gas are known [11]. Then, the analysis of the interferogram yields the partial density profile of one of the two gases across the interface. Figure 9 shows three interferograms recorded at different times. On the interferogram (a), the shock wave has already crossed the interface, has been reflected from the tube end wall and is about to again impact on the modified interface. Picture (b) was taken shortly after this second impact and the wave is seen to have been partly transmitted into SF6 and partly reflected into the air. On picture (c) the transmitted wave can be seen close to the bottom of the picture while the reflected part has again been reflected from the end wall and is about to impact on the interface.

The SF6 partial density profiles were obtained through the interface by averaging a dozen interferograms. For the xenon/air gas pair, the xenon partial density profiles were compared to those obtained by the X-ray technique. The two techniques yield very similar results (Box 4).

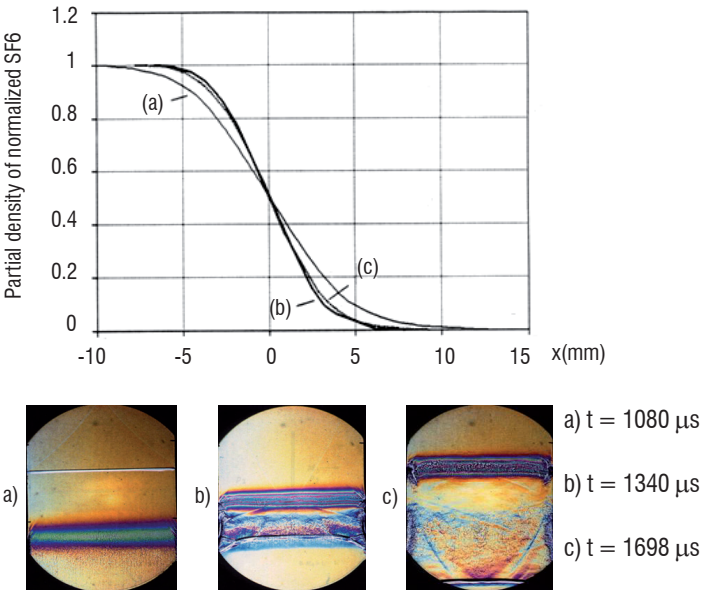

Figure 9 - Gas density profiles of SF6 6 - Interface: SF6-Air, Ms = 1.45.

Box 4 - Galdstone-Dale relation in gas mixture

If ρ_1 and ρ_2 are partial gas densities:

$$n-1=K\rho=K_1\rho_1+K_2\rho_2$$

Interferogram analysis yields:

$$n(y)-n_L=(n(y)-1)-(n_L-1)=\frac{\int\theta_y.dy}{L}$$

L : test section width
n_L : refractive index of reference gas
$n_1(y)$ through the interface :

$$n_1(y)-1=\left[1-\frac{(n(y)-1)-(n_L-1)}{(n-1)_{\max}-(n_L-1)}\right](n_L-1)$$

and then the partial gas density profile:

$$\rho_1(y)=\frac{(n_1(y)-1)}{K_1}$$

Real-time true-color holographic interferometry

The use of differential interferometry implies data integration to get the full gas density and this integration results in a certain measurement inaccuracy. To obtain absolute data, Onera developed real-time true color holographic interferometry using a three-color laser source [16]. As shown in Figure10, the interference fringe patterns versus the optical path difference are compared for three different sources. With a xenon light source (a), the central white fringe visualizes the zero order deformation and small path differences are correctly measured but above several micrometers, the tints are no longer distinguishable and large path differences cannot be measured. With a monochromatic laser source (b), the central white fringe (zero order) can never be identified and it is not possible to follow the displacement of the fringes through a shock wave. But, when it is possible to count the fringe number, large path differences can be measured. With a three-laser source (c), the zero order is always identifiable (white fringe) and the colors always remain identifiable for small and large path differences.

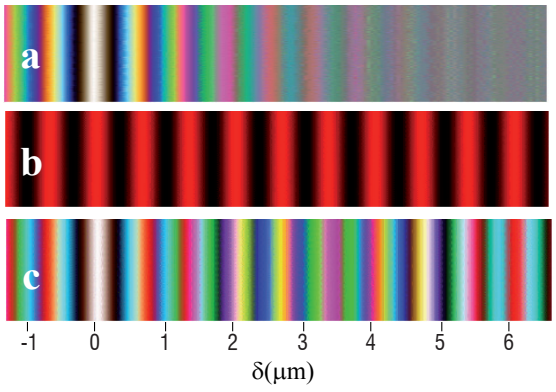

Figure 10 - Color of interference fringes.

Transmission hologram

The feasibility of this technique was confirmed with the Research Institute of Saint-Louis (ISL) and applied in several Onera wind tunnels. Figure 11 shows the optical setup using single-layer panchromatic holograms recorded by transmission. A reference hologram made without flow records the interferences between the three reference waves and the three measurement waves. It is then developed and is replaced on the setup. If a change in optical path is created in the test section, color variations representing the phenomenon will be visualized in real time behind the hologram. The flow studied was the unsteady flow downstream from a cylinder of 20 mm in diameter placed crosswise in the test section at Mach 0.37. High speed interferograms were recorded with a rotating-drum camera at high frame rate (30,000 f/s) and the exposure time of each interferogram was 750 nanoseconds. On the interferogram of Figure 11 we see that each vortex is defined by concentric rings where each color visualizes an isochore line. These colors were analyzed using proprietary software [17] to find the vortex position and velocity and the evolution over time of the gas density field.

Reflection hologram

To increase the diffraction efficiency of a hologram, which is about a few percent in transmission, Onera created an optical bench that uses reflection holograms. In transmission however, the interference fringes are set down perpendicular to the plate and a small variation in gelatin thickness caused by the chemical treatment of the hologram does not modify the three interfringes. In reflection on the other hand, the interference fringes are recorded parallel to the plate surface and the interfringes are very sensitive to small variations of gelatin thickness. Solutions were proposed to control the gelatin shrinkage. Very good results were obtained with narrowed fringes and a uniform background at Mach 0.45 around the same circular cylinder [18]. In the setup in Figure 12, the holographic plate is set in the front of the test section and, at the first exposure without flow, it records the interferences between the incoming rays and the rays reflected by the flat mirror located just behind the test section. As the hologram simultaneously records the interferences of the three wavelengths, the diffraction efficiency of the three gratings becomes close to 50%. This value is very important because, at the second exposure, as the diffraction efficiency is close to 50%, 50% of the light is reflected by the hologram and constitutes the three reference waves. The other 50 % crosses the test section twice and interferes in real-time with the three reference waves. Interference fringes are not localized because they can be observed from the holographic plate to the camera. If no disturbances exist in the test section, a uniform background color is obtained in the camera. If variation in the refractive index exists in the test section, it will be seen on the screen. This original arrangement constitutes the first real-time, three-color holographic interferometer using reflection holograms and the holograms obtained exhibit well-saturated and more contrasted colors than those obtained in previous experiments performed with transmission holograms. That makes the quasi-automatic analysis of interferograms easier.

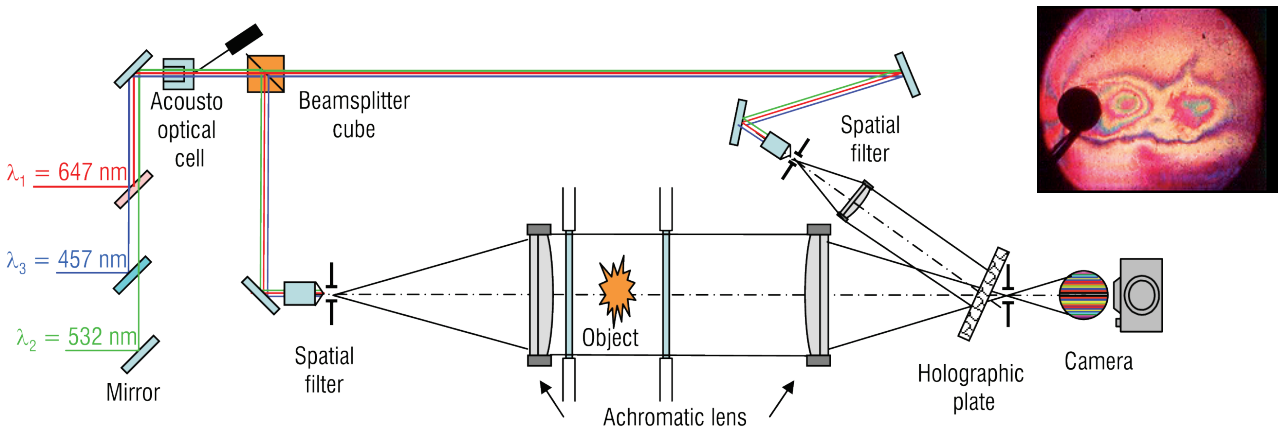

Figure 11 - Real-time three-wavelength transmission holographic interferometry
Video - http://aerospacelab.onera.org

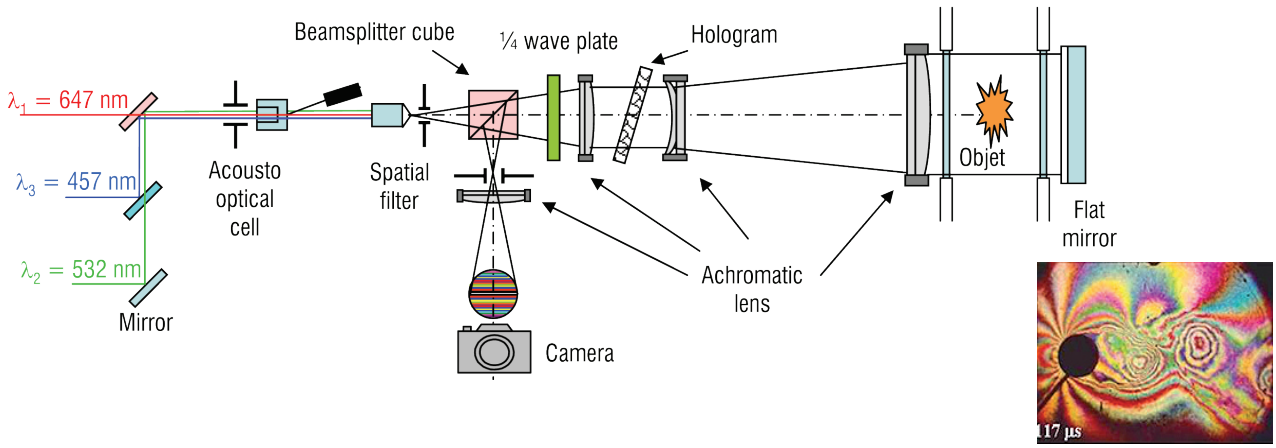

Figure 12 - Real-time three-wavelength reflection holographic interferometry
Video - http://aerospacelab.onera.org

Digital color holographic interferometry

One possibility for avoiding holographic plates and chemical processing is related to digital three-color holographic interferometry. Technological improvements in the field of matrix sensors offer new possibilities for holography. Hologram recordings can be done using CCD matrices with increased resolution and greater digital gain. For this reason, the feasibility of the digital three-color holographic interferometer was designed to analyze the variations in refractive index induced by a candle flame [19]. Color holograms are generated and recorded with a three-layer photodiode stack sensor allowing for simultaneous recording with high spatial resolution. Phase maps are calculated using a Fourier transform and spectral filtering are applied to eliminate parasitic diffraction orders (see Box 5). From the phase differences, it is possible to calculate the intensities of interferences induced by the flame in the RGB colors calculated. The optical bench used and the results in the case of the candle flame are presented in Figure 13. Zero order fringe (white fringe), meaning zero optical path difference, can be easily extracted from the experimental data by considering the wrapped phases along the three wavelengths. The use of three colors is of great value if one looks at precisely the background tint observed outside the flame. In normal experimental conditions, the synthesized background color should be represented in white ($\delta = 0$) if there has been no disturbance between the reference and the probe recordings. In Figure 13, it can be seen that the white fringe is shifted and located inside the flame (see zoom of flame). This means that the background pattern has moved slightly between the reference and probe recording. This feature was not observed in experiments based on single wavelength interference and shows the value of using color in digital holographic interferometry.

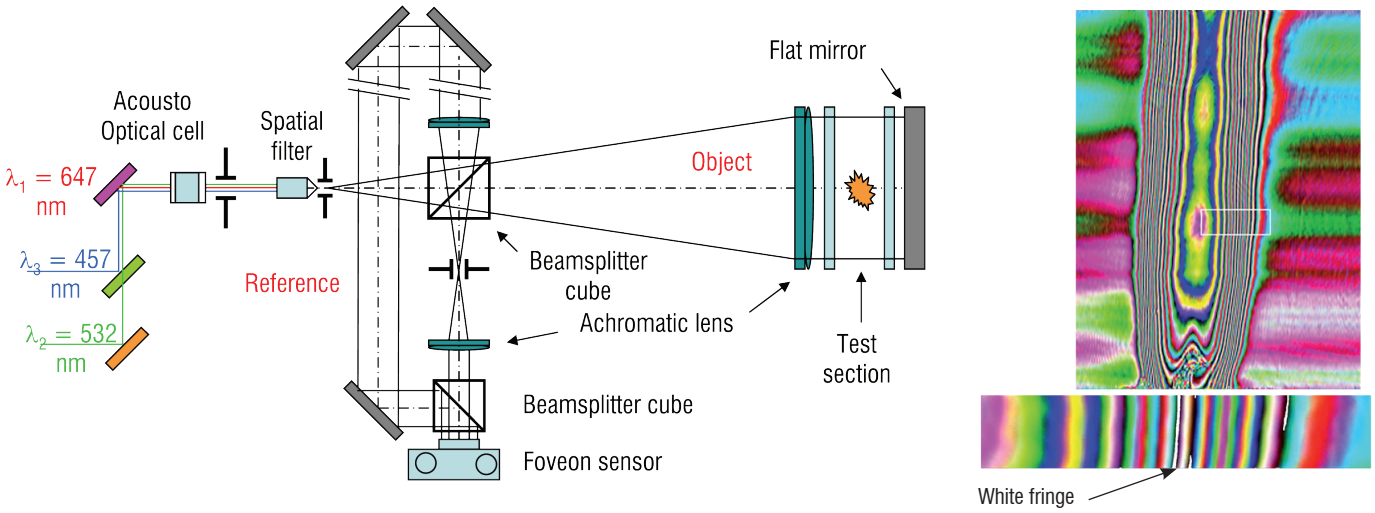

Figure 13 - Digital three-color holographic interferometer and application to flame.

Box 5 - Off-axis hologram analysis by direct and inverse 2D FFT algorithms

- Image plane hologram can be expressed: $H_\lambda(x,y) = O_0(x,y) + b_\lambda(x,y)\exp\left[i\phi_\lambda(x,y)\right]\exp\left[2i\pi\left(u_\lambda x + v_\lambda y\right)\right] + b_\lambda(x,y)\exp\left[-i\phi_\lambda(x,y)\right]\exp\left[-2i\pi\left(u_\lambda x + v_\lambda y\right)\right]$

where $2\pi(u_\lambda x + v_\lambda y)$ is the spatial carrier modulation along xy.

- Fourier transform gives: $\tilde{H}_\lambda(u,v) = A_\lambda(u,v) + C_\lambda(u - u_\lambda, v - v_\lambda) + C_\lambda^*(u + u_\lambda, v + v_\lambda)$

where $C_\lambda(u,v)$ and $A_\lambda(u,v)$ are the Fourier transform of $b_\lambda(x,y)\exp\left[\mathrm{i}\phi_\lambda(x,y)\right]$ and $O_o(x,y)$.

- Inverse Fourier transform gives: $\hat{c}_\lambda(x,y) \cong \left\{b_\lambda(x,y)\exp\left[i\phi_\lambda(x,y)\right]\exp\left[2i\pi\left(u_\lambda x + v_\lambda y\right)\right]\right\} * h(x,y)$

where * means convolution and h(x,y) the impulse response.

- At any wavelength λ, the phase is given by: $\xi_\lambda^P(x,y) = \phi_\lambda(x,y) + \Delta\phi_\lambda(x,y) + 2\pi u_\lambda x + 2\pi v_\lambda y$

- The phase change between the two states of the object is simply obtained by computing

$\Delta\phi_\lambda(x,y) = \xi_\lambda^P(x,y) - \xi_\lambda^R(x,y)$ and the optical path difference is given by: $\delta = \frac{\lambda}{4\pi}\Delta\phi_\lambda$

A comparison can be made between digital and image color holographic interferometry for the previously obtained results [18-19]. In image color holographic interferometry, a panchromatic holographic plate (7,000 to 10,000 l/mm in spatial resolution) must be illuminated with a total energy of 600 μJ and the coherence length of the three lasers must be more than 2 m. Each interferogram has to be digitized and processed. It is important to obtain a reference hologram of about 50% diffraction efficiency for the three lines and the implementation of the optical setup is not very easy. In digital color holographic interferometry, an energy of 1μJ is sufficient to illuminate the Foveon sensor (200 l/mm in resolution). The laser length coherence can be reduced to several centimeters and some problems can be encountered with the RGB filters overlapping. The implementation is easy enough and the phase difference is entirely estimated with a computer.

Conclusion

Computational fluid dynamics need to be validated by fine measurements in a smaller space or shorter time, or both at once. That is why Onera has devoted much time to developing optical methods based on differential or color interferometry. For shadow and schlieren measurements, these techniques are very easy to implement and they will always yield qualitative data and help with the understanding of unsteady and complex flows. But, if quantitative data are required, color interferometry or color holographic interferometry will continue to be used due to the high resolution of holographic plates. In near future, digital three-wavelength holographic interferometry seems the best candidate to characterize the future complex flows. Although CCD resolution and size are not as good as that of holographic plates, the digital approach is more accessible and versatile since the time for the hologram processing is greatly reduced and the processing is purely numerical.

On the other hand, the value of using color has been demonstrated as the zero order fringe can be easily determined and the variation in the background color due to disturbances can be quantified. The limitations of the method lie in the wide spectral sensitivity of the sensor which produces light diffusion in each monochromatic hologram. Work is currently in progress for removing the color diffusion using a segmentation approach. Success in this strategy will allow for wide spatial filtering, increasing the spatial resolution in the reconstructed object.

Future work will focus on the extension of the proposed technique for analyzing 3D unsteady wake flows. At present, a specific setup of digital holographic interferometry has been defined in a single sight direction, and the aim will be to reproduce the same optical setup along several sight directions, each shifted by a given angle. It is obvious that the optical setup can be reproduced no more than three or four times. But the lake of sight directions should be compensated by high tomographic interferogram resolution for the reconstruction of the 3D gas density field ■

References

[1] G. S. SETTLES - *Schlieren and Shadowgraph Techniques, Visualizing Phenomena in Transparent Media.* Ed. Springer, 2001.

[2] O. RODRIGUEZ - *The Circular Cylinder in Subsonic and Transonic Flow.* AIAA Journal, vol. 22, n° 12, pp. 1713-1718, 1984.

[3] J.M. DESSE - *Influence of Flight Parameters on Air Intake Internal Flow Distortions due to Gun Blast-Air Interaction.* La Recherche Aérospatiale, n° 4, pp. 1-10, 1991.

[4] H. SCHARDIN - *Schlieren Methods and their Applications.* Report TT-F-12731, NASA, Washington, DC, 1970.

[5] O. RODRIGUEZ - *Base Drag Reduction by Control of the Three-Dimensional Unsteady Vortical Structures.* Experiments in Fluids, n° 11, pp. 218-226, 1991.

[6] G.E.A. MEIER - *Hintergrund Schlierenmessverfahren, Deutsche Patentmeldung.* DE 199 42 856 A1, 1999.

[7] C. BARTHE, F. MICHELI, P. MILLAN - *Etude aérothermique de jets supersoniques chauds.* Congrès francophone de techniques laser, CFTL, Toulouse, 2006.

[8] M. RAFFEL, C. TUNG, H. RICHARD, Y. Yu and G.E.A. MEIER - *Background Oriented Stereoscopic Schlieren Helicopter Vortex Characterization*. Proc. 9th Int. Symposium on Flow visualization, Edinburgh, 2000.

[9] C.M. WEST - *Holographic Interferometry.* Ed. Wiley-Interscience, New-York, 1978.

[10] G. GONTIER - *Contribution à l'étude de l'interférométrie différentielle à biprisme de Wollaston.* Publication Scientifique et Technique du Ministère de l'Air, n° 338, 1957.

[11] W. MERZKIRCH - *Flow Visualization*. New-York, Academic Press, 1974.

[12] C.H. SIEVERDING, G. CICATELLI, J.M. DESSE, M. MEINKE and P. ZUNINO - *Experimental and Numerical Investigation of Time-Varying Wakes Behind Turbine Blades.* Notes on Numerical Fluid Mechanics, Vol. 67, Community Research in Aeronautics, 1999.

[13] O. RODRIGUEZ, J.M. DESSE, J. PRUVOST - *Interaction between a Supersonic Hot Jet and a Coaxial Supersonic Flow.* Aerospace Science and Technology, n° 6, pp. 369-379, 1997.

[14] J.M. DESSE, E. FABRE - *Differential Interferometry for Studying Hypersonic Flows.* Experiments in Fluids, n° 20, pp. 273-278, 1996.

[15] I. GALAMETZ - *Visualisation et mesure de masse volumique dans un mélange gazeux en tube à choc.* Thèse de doctorat, Université de Lille, 1994.

[16] J.M. DESSE, F. ALBE, J.L. TRIBILLON - *Real Time Color Holographic Interferometry.* Applied Optics: Vol. 41, n° 25, pp. 5326-5333, 2002.

[17] J.M. DESSE - *Recording and Processing of Interferograms by Spectral Characterization of the Interferometric Setup.* Experiments in Fluids, vol. 23, pp. 265-271, 1997.

[18] J.M. DESSE, J.L. TRIBILLON - *Real-Time Colour Denisyuk Setup for Analyzing High Speed Flows.* Speckle Metrology 2006, Nimes, September 13-15, 2006.

[19] J.M. DESSE, P. PICART, P. TANKAM - *Digital Three-Color Holographic Interferometry for Flow Analysis.* Optics Express, Vol. 16, n° 8, pp. 5471-5480, 2008.

Acronyms

BOS (Background Oriented Schlieren)

Jean-Michel Desse, doctor/engineer, is working at Onera from 1979 in the Applied Aerodynamic Department. His research interests the development of high speed non invasive optical methods based on the refractive index variations in wake flows. Specialist of color interferometry in polarized white light and polychromatic light, his work are now oriented on digital holographic interferometry using three different wavelengths for studying unsteady wake flows.

Ruy Deron received the PhD degree in Automatic and Signal Processing from the University of Nice in 1983. He joined the French National Establishment for Aerospace Research (Onera) in 1984. Since 1990, he has managed experiments dealing with propagation through atmospheric turbulence: laser guide star and ground-based satellite observation, airborne IR imagery. In 2001, he became project manager for an Onera 4 year funded project on aero-optical effects (wind-tunnel experiments and LES simulations). In 2004, he became involved in multi-code development and validation in an aero-thermo-optical 3 year DGA funded project, which he took over for the last year. He is also working in a European working group on optical plume effects.

F. Dupoirieux
(Onera)

E-mail: francis.dupoirieux@onera.fr

Optical Diagnostics Used at Onera to Characterize Turbulent Reactive Flows and to Validate Aero- and Rocket Engine Combustor Modeling

The reactive flows encountered in combustion systems are very complex and varied. Optical diagnostics have been a great help in improving our understanding of the physics of combustion because they can give information on the core of the flow without perturbing it. Optical measurements are essential for validating the CFD codes for reactive flows. These techniques have undergone continuous improvement so that we can now obtain 2D visualizations and simultaneous measurements of different quantities with high resolution on combustor systems operating in tough conditions of pressure and temperature. Examples of such measurements are given in this article; they concern industrial combustors as well as burners dedicated to basic research. The article also compares numerical simulations to these measurements. Optical diagnostics still need further improvements, for instance, so that they can operate in dense sprays or characterize soot particles accurately. Higher data acquisition frequency is also needed in order to better understand and remove combustion instabilities.

Introduction

In many cases, the production of heat or mechanical energy depends on combustion devices. In order to prevent energy waste and to limit pollutant emission, it is therefore essential to improve the control of turbulent reactive flows in which heat release is produced by exothermic reactions between a fuel and an oxidizer. The physics involved in such a reactive flow are not simple because they are highly multi-scale and result from the interaction of many basic phenomena. For instance, as shown in figure 1, the interaction between turbulence and chemistry gives rise to different combustion regimes according to the ratio between their characteristic length or time scales. The Borghi-Peters diagram, [1], [2] aims to characterize these combustion regimes as a function of an integral turbulent scale (L in abscissa) and the turbulence intensity (u' in ordinate). For the sake of simplicity, the diagram shown here applies to premixed flames but the conclusions drawn from this diagram concerning the variety of the combustion regimes can be extended to flames that are not perfectly premixed.

Figure 1 demonstrates that very different situations are encountered in combustion systems. Moreover, physical phenomena are not limited to turbulence and chemistry. For sub-critical pressures, the fuel or the oxidizer is often introduced in the shape of a liquid phase and, for super-critical pressure, in the shape of a dense phase. If a liquid phase is present, the corresponding species must evaporate; sometimes oxidizer and fuel are premixed before introduction in the combustion chamber but, most of time, they have to mix or at least to meet each other before burning. The next step is the ignition, which is obtained by a temperature rise resulting from a heat exchange between burnt and fresh gases. Lastly, the combustion reactions must propagate to the rest of the reactants before the burnt gases leave the combustion chamber.

The physical phenomena involved in this set of events are the following:

- atomization of the injected liquid fuel or oxidizer,
- turbulent dispersion of the liquid droplets,
- vaporization of the liquid droplets,
- turbulent mixing on a small and large scale,
- complex chemistry,
- turbulent heat transfer in the core of the reactor and near the walls,
- radiative transfer between the different parts of the fluid and between the fluid and the walls.

All of these phenomena are in interaction with each other. Most of the time the pressure can be considered spatially constant in the combustion chamber from the point of view of the thermodynamic phenomena such as vaporization and chemical reactions but an exception is the supersonic combustion envisioned for very high speed propulsion, which involves shock waves and expanding fans.

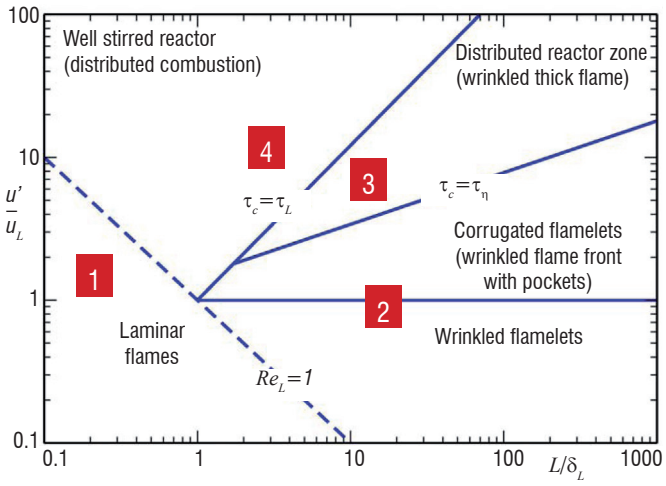

L = integral length scale of turbulence
δ_L = laminar flame thickness
u' = turbulent velocity fluctuation
u_L = laminar flame velocity
τ_c = characteristic chemical time
τ_L = integral turbulent time
τ_η = Kolomogorov turbulent time

The different combustion regimes can be illustrated by the following examples:

1 Miniature combustion chamber (< 1 cm³): laminar distributed combustion

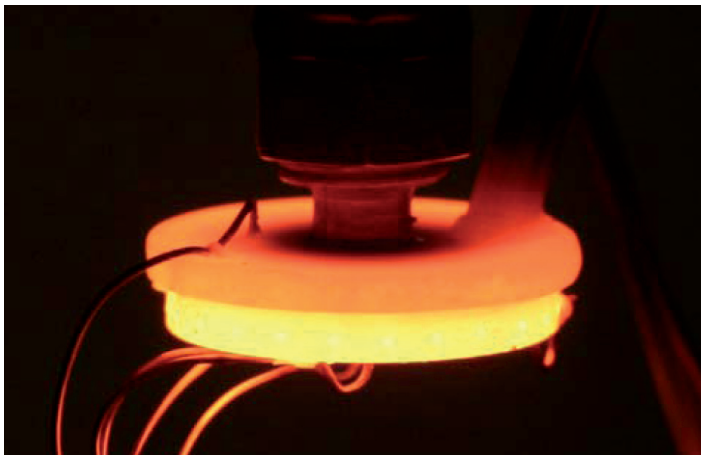

2 Bunsen flame: corrugated flame (corrugated in instantaneous pictures)

3 Ramjet combustion chamber: wrinkled thick flame in the combustion chamber downstream from the air inlets (below temperature field obtained by numerical simulation in the combustion chamber of a ramjet engine)

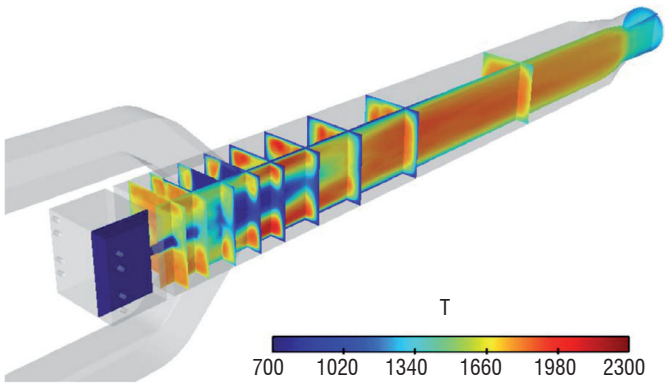

4 Gas turbine combustor using gaseous or prevaporized fuel: distributed turbulent combustion in the recirculations taking place in the primary zone (below the temperature field obtained by numerical simulation in a dual annular combustion chamber of a gas turbine; distributed combustion is expected behind the upper row of prevaporized fuel injectors)

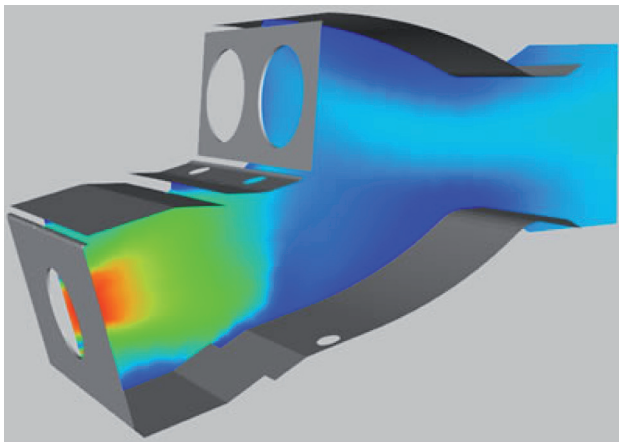

Figure 1 - Combustion regimes proposed by Borghi and Peters in terms of turbulence-combustion scales and turbulence intensity.

Despite rapid technical evolution, some improvements have still to be realized. They involve combustion efficiency, especially at transient regimes for devices with changing operating conditions, the control of combustion instabilities, the limiting of hot points on walls, the reduction of pollutant emissions to comply with more and more stringent standards for aircraft emissions, the decrease in combustor volume, maintaining a satisfactory possibility of re-ignition in the case of aeronautic gas turbines, the efficiency of thermal transfer in the case of devices producing heat, the homogeneity of the outlet temperature profile for gas turbine combustors, etc. All of these objectives can be achieved by different means. Short-term improvements are empirically obtained using global measurement techniques such as gas sampling and ex-situ analysis, applied to experiments on industrial or semi-industrial scales. To go beyond the limitations of an empirical approach, some more fundamental experiments including accurate, non-intrusive measurement techniques resolved in time and space are required. These experiments, associated with numerical simulations, are needed to understand the physics of combustion and to find intelligent and efficient solutions to combustion problems. The experiments must reproduce all the characteristic time ratios of the physical phenomena occurring in real combustors, but the geometry can be simplified in order to make possible large optical access for observation and measurements. For example, an annular chamber can be replaced by a parallelipipedic sector including a reduced number of injectors. There is an expectation for the measurement of many physical quantities, such as droplet size and velocity, gas velocity, gas temperature, concentration of major and minor species. However, the measurement of a given quantity in one given point at a given instant is not very valuable for understanding the organization of a turbulent reactive flow if this measurement is not connected to other information. A major improvement in our understanding of turbulent combustion will require instantaneous 2D visualizations, simultaneous measurements of different physical quantities and, if possible, high frequency measurements. Simultaneous measurements give access to important turbulent quantities such as the Reynolds stress tensor appearing in the Navier-Stokes equations for turbulent reactive flows. They also facilitate the understanding of the interaction between various physical phenomena, such as fuel vaporization and chemical reactions. High frequency measurements are useful to obtain the dissipation rates of velocity and concentration fluctuations. These dissipation rates have a great influence on the organization of the flow and on the consumption rate of the fuel. They can also be used to reveal instability cycles. Such time-resolved information is more and more sought after to validate unsteady simulations, such as Large Eddy Simulation (LES) or Delayed Detached Eddy Simulation (DDES). 3D or quasi 3D measurements, made possible by high frequency laser pulses, can give interesting information on the size of the structures found in the reactive flows.

Progressive improvement of optical measurement techniques leads to the possibility of obtaining more and more advanced experimental results of this type. At Onera, research teams of the “Physics, Instrumentation and Sensing” Department, on one hand, and the “Fundamental and Applied Energetics” Department, on the other hand, work together to apply these techniques to different types of combustion devices. This paper gives some examples of measurement campaigns done by advanced optical diagnostics in Onera combustion facilities, with an outline of the conclusions drawn from these measurements and the associated numerical simulations. The experiments involve combustion with air on a laboratory scale, semi-industrial or industrial scale and combustion with liquid oxygen (LOx combustion). They apply directly to aeronautics and space propulsion, except for the first one on the laboratory scale which is only for fundamental research purposes.

Optical diagnostics applied to air breathing combustion: fundamental work

Manufacturers of aeronautic jet engines are nowadays able to make combustion chambers that take up little space and that are easier to integrate in the engine than older combustors. At full power, the combustion in these chambers is stable and the combustion efficiency is over 98 %, so no gain can be expected on this side. However, in order to reduce the fuel consumption and CO_2 emission, the thermodynamic efficiency of these gas turbines can be improved by increasing the pressure and the inlet gas temperature in the combustor. With the usual combustion chambers, this unavoidably leads to higher NOx emission. Indeed, NOx formation is strongly influenced by the gas temperature, the gas residence time in the zone of high temperature and the chamber pressure (see box 1). NOx formation in flames is therefore an important issue for the development of new environmentally-friendly aircraft engines. In contrast with ground combustion devices, the problem of NOx formation in aircraft gas turbines cannot be solved by post-treatment but only with new combustion chamber concepts. These NOx concerns imply the need for broad activity ranging from fundamental research to applied action.

Unsteady H_2-air diffusion flame

Initially, some fundamental work was carried out at Onera in the framework of cooperation between the “Physics, Instrumentation and Sensing” Department of Onera and the Air Force Research Laboratory (Wright Patterson AFRL) concerning NO formation in an unsteady axisymmetric H_2-air diffusion flame [3],[4]. This flame was carefully characterized in terms of temperature by Coherent Antistokes Raman Spectroscopy (CARS) and in terms of H_2, O, OH, H and NO concentration by Laser Induced Fluorescence (LIF) and Degenerate Four Wave Mixing (DFWM) [20]. Thanks to the synchronization of the measurements with the movement of the periodic aerodynamic structures, it was possible to obtain the time evolution of the temperature and of the various species concentrations. Figure 2 gives the results of these measurements as well as the results of a Direct Numerical Simulation (DNS) of the flame performed by AFRL[5],[6]. This figure clearly shows that high NO concentrations do not coincide exactly with high temperature. High NO concentrations can be found in the vortices resulting from the unsteady behavior of the flame, because the residence time of the hot gases in these structures is high, while the NO concentration in the thin part of the flame is much lower due to a shorter residence time for the hot gases. One can deduce from these NO measurements that thermal NO is the major contributor to NO formation in this type of flame and that flamelet models, assuming that all the chemical reactions take place in a thin wrinkled interface, are not adequate to predict NO formation in that case. The DNS of the flame is in good agreement with the measurements overall and this combustion experiment validates the DNS technique applied to H_2-air chemistry. DNS of this flame was successfully carried out at Onera as well [7].

Box 1 - NOx formation in gas turbine combustors

NOx is the designation for the nitrogen oxides, NO, NO_2, N_2O, that can be found in the atmosphere and that are created directly or indirectly by combustion devices. In practice, mainly NO is produced in gas turbine combustors, even if NO_2 can be found during a transient phase of combustion. Two types of mechanisms are involved in NO formation: the prompt NO and the thermal NO mechanisms [18], [19]. The effect of these mechanisms is illustrated in the following figure, taken from [18], which gives the evolution of the NO concentration in a combusting gas pocket as a function of the time spent by this gas pocket in a premixed flame (Phi is the stoichiometry of the flame):

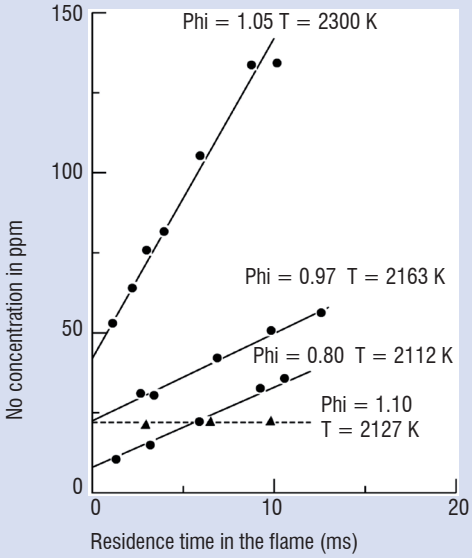

Figure B1 - 01 - Concentration of NO as function of the residence time in a premixed flame for different mixture ratio conditions; the time needed to cross the zone where the main fuel oxidation reactions take place is less than 1 ms.

The prompt NO appears quasi instantaneously when the gas pocket starts crossing the flame, i.e. it leads to non-zero concentrations of NO when the residence time is approximately zero. It can be seen that a higher Fuel-Air Ratio (FAR) results in a larger prompt NO concentration. The chemical path which leads to prompt NO is complex and includes very fast reactions involving amines and cyano compounds.

After the prompt NO has been created, i.e. as soon as the residence time becomes significant, some additional NO appears continuously during the progress of the gas mixing behind the flame. This slowly created NO is called “thermal NO”. The rate of thermal NO formation is proportional to the slope of the plotted lines of the above figure, which depends on the conditions of premixed combustion. The slope is maximal for slightly over-stoichiometric FAR (Phi=1.05) because higher temperatures, which are obtained near or just above stoichiometry, lead to larger NO concentration as long as a small amount of O radicals is available. For higher FAR, i.e. Phi=1.1, all the O radicals are consumed by other oxidation reactions and no more thermal NO is created. The thermal NO mechanism, also called the Zeldovich mechanism, is simple and is composed of the following reactions, the kinetics of which are well known:

$$O + N_2 \leftrightarrow NO + N$$
$$O + O_2 \leftrightarrow NO + O$$
$$N + OH \leftrightarrow NO + H$$

In gas turbine combustors, the residence time of the burnt gases ranges from 10 to 30 ms so that thermal NO formation is preponderant.

Optical diagnostics such as LDV or PIV are required to experimentally obtain a good estimation of the mean residence time of the burning gas and optical techniques such as CARS or Rayleigh give information on the temperature and its fluctuations which is very useful for understanding the NO formation process.

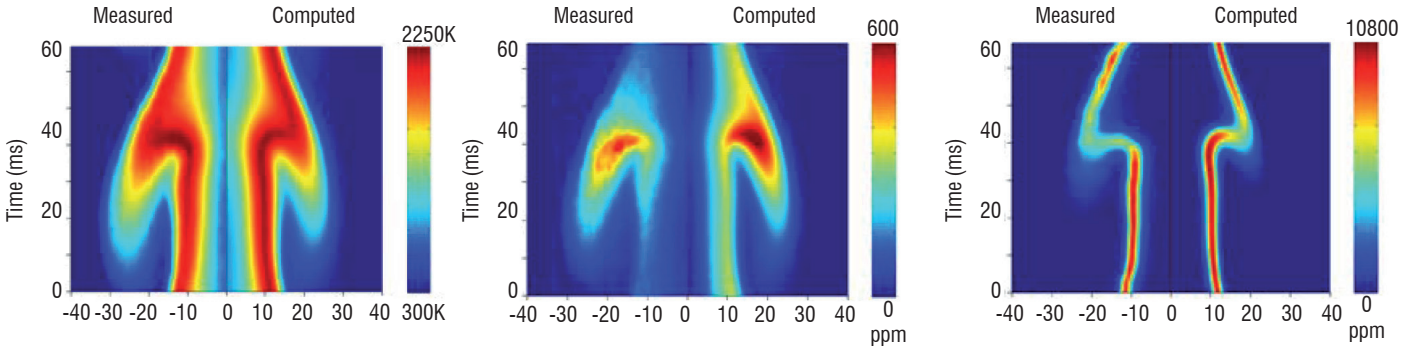

Figure 2 - Comparison of experimental and numerical time evolution at a given flame height for temperature, NO concentration and OH concentration in an unsteady H_2-air diffusion flame

Turbulent premixed flame

In parallel, new combustor concepts must be developed to solve the problem of NOx emission (see box 2). Premixed combustion is a good candidate for low NOx emission but is prone to instabilities and flame flash-back. This type of combustion has been studied in the LAERTE facility of Onera [8, 9].Although the geometry of the combustor is relatively simple, the quantitative determination of the reactive flow organization requires accurate measurements provided by optical diagnostics because the size of the recirculation zone, which acts as a flame stabilizer, and the angle the flame, which influences the length of the combustor, are not imposed by the combustor geometry but are dependent on the operating conditions. The fields of temperature and velocity including averaged values and turbulent fluctuations have been obtained by Laser Doppler Velocimetry (LDV), and CARS. As shown in Figure 3, they have been used to validate an unsteady simulation of the LAERTE combustor by the DDES technique [10]. The main features of the reactive flow are well reproduced by the numerical simulations despite local discrepancies.

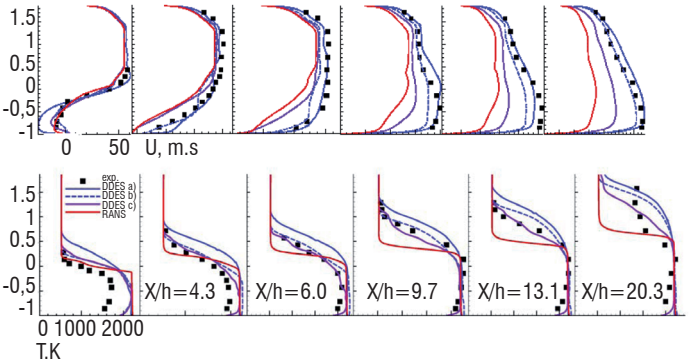

Figure 3 - Comparison of the velocity (lengthwise component) and temperature profiles obtained, on one hand, experimentally by LDV and CARS and, on the other hand, numerically by RANS and by three different types of DDES simulations.

Instantaneous 2D pictures of the flow are required to characterize the tendency of the reactive flow to instabilities and flashback. Planar LIF (PLIF) on the OH radical has been achieved to give such pictures for different operating conditions. Large OH concentrations are correlated with high combustion rates. Figure 4 exhibits snapshots of OH concentration obtained at different instants for a stoichiometry equal to 0.82 and a pressure equal to 1.35 bar resulting from a partial closing of the outlet section. The sequence of pictures reveals instabilities and intense flashback phenomena because OH radicals can be found upstream from the step corner in pictures (4) to (9). We note that some pockets of OH are disconnected from the main combustion zone. These pockets are more visible on visualizations, not shown here, performed in the cross section of the combustor. For a stoichiometry of 0.8, very close to the previous one, but with a smaller outlet obturation giving a pressure of 1.12 bar and some different acoustic impedance, the instabilities and the tendency to flashback disappear, so that instantaneous PLIF visualizations lead to pictures similar to picture (1) of Figure 4 whatever the time of the snapshot. Visualizations based on the chemiluminescence of the excited OH* radical, shown in Figure 5, could be done simultaneously with measurement of the pressure on the upper wall of the combustor at the location of the step. The PIV technique, requiring seeding of the flow with small particles [21], was also used to obtain instantaneous 2D pictures of the reactive flow velocity field. An example of the velocity field is given in Figure 5. The sequence of OH* visualizations indicates that flame flashback, which can be seen in the 2nd, 3rd and 4th snapshots from the top, starts just after a pressure drop. This tendency to flashback can be reproduced by DDES, as shown by Figure 6 displaying two instantaneous simulated temperature fields with flashback visible on the first one.

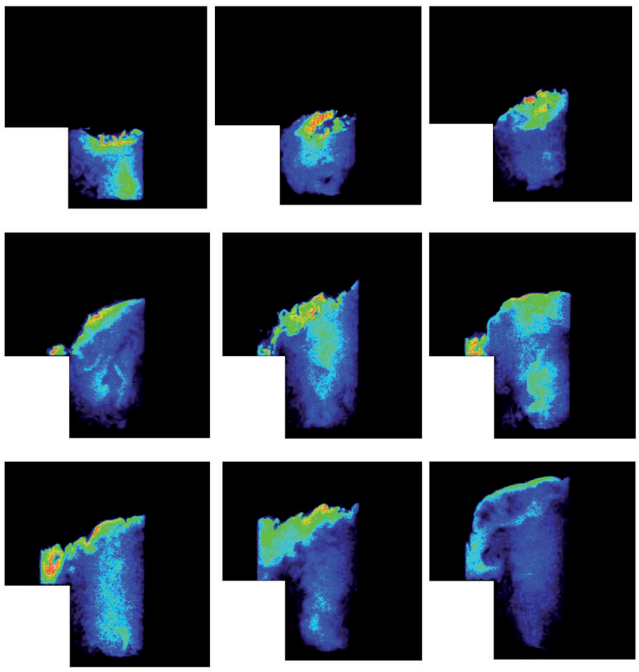

Figure 4 - Reconstructed cycle of instability from samples of OH radical visualizations by PLIF.

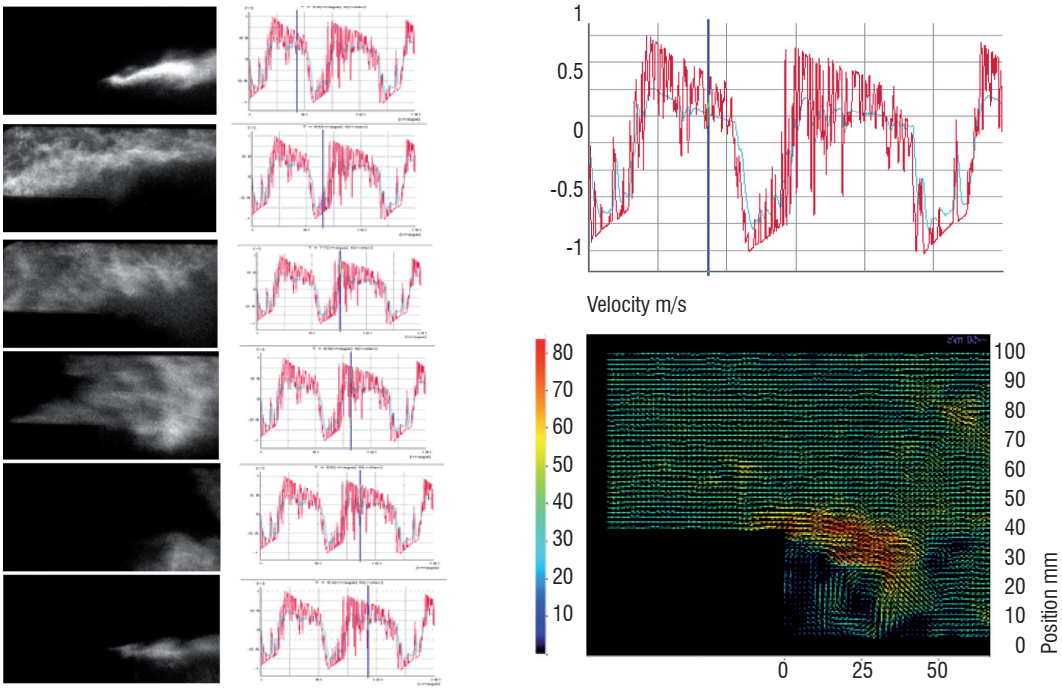

Figure 5 - Sequence of visualizations by OH* chemiluminescence around the step corner and corresponding time (blue bar) during pressure evolution (left); evolution of the pressure measured on the upper wall displayed on a larger scale (upper right); Flow visualization around the step corner by PIV (lower right).

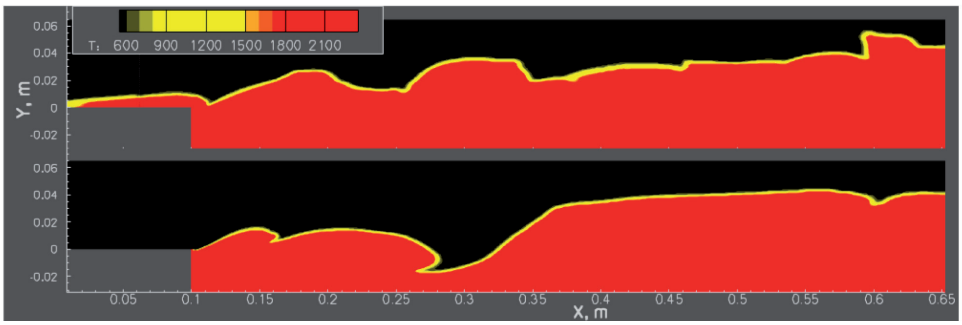

Figure 6 - Temperature fields obtained by DDES numerical simulation at two different instants.

Optical diagnostics applied to air breathing combustion in industrial burners

Soot measurements

Another candidate for lowering NOx emissions is the RQL concept (see box 2). In this type of combustor, the existence of an extended zone with a high Fuel Air Ratio (FAR) unavoidably leads to high soot production. For efficiency and environmental reasons, the soot must be oxidized before the burning gases leave the chamber. The soot formation is the result of a very complex process which includes different steps occurring partly successively, partly in parallel (see box 3). Non-intrusive measurements of the concentration of soot particles are not easy. Emission or absorption techniques applied to axisymmetric flames require spatial deconvolution which must be very carefully carried out and are misleading in the case of turbulent flames, since emission is integrated along the direction of the view and absorption along the laser beam [11]. The technique of Laser Induced Incandescence (LII) [22] however allow us to obtain instantaneous measurements of soot concentration. Within the framework of cooperation between Onera and DLR, this technique was applied to a turbulent ethylene-air jet flame, as shown in Figure 7, and to a semi-industrial burner equipped with a multi-point fuel injector, as shown in Figure 8. In the first case the measurements were used to validate a numerical model described in [12]. In the second case, the objective was to check that the pilot flame is not producing a large quantity of soot particles and, if any are produced, that they are oxidized within the combustor [13]. Figure 8 clearly indicates that the concentration of soot is very low and that the soot particles are correctly oxidized before the outlet section of the combustor.

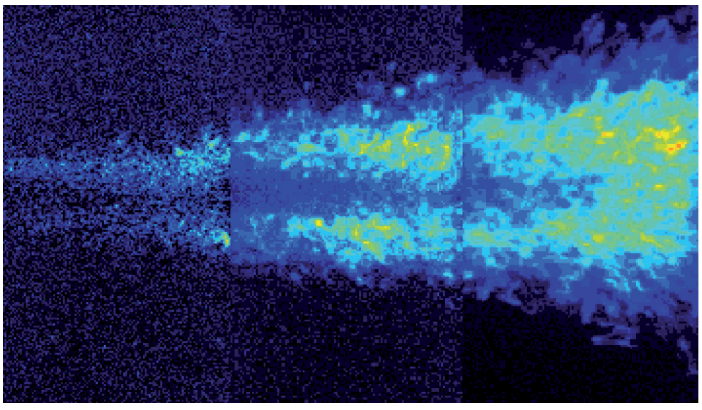

Figure 7 - Field of soot concentration in a turbulent ethylene-air jet flame obtained by LII (arbitrary scaling).

Box 2 - Low NOx combustor technology

Conventional combustors, see Figure B2 - 01, include a primary zone with gas recirculation where the fuel-air ratio is large and the temperature is high. This primary zone acts as a flame stabilizer and allows the reactive flow ignition in high altitude conditions when the pressure and the gas inlet temperature are low. After the primary zone, the reactive flow receives some additional air in the secondary and dilution zones to complete the combustion and to lower by dilution the burnt gas temperature to a level acceptable for the turbine.

The combustor NOx reduction technology is based on the fact that (see box 1):

- NOx production requires high temperatures (> 1800 K)
- thermal NO is the largest part of the NO produced in gas turbine combustors and thermal NO is produced when the gas residence time is high,
- thermal NO production requires the presence of O (oxygen) radicals, i.e. fuel-air stoichiometry not larger than 1.1.

A decrease in the residence time can be obtained in two-head combustors in which a part of the chamber of relatively small volume is dedicated to combustion in full power operating conditions. This type of combustor is currently used in aircraft engines of the CFM 56 and GE 90 types but is not totally satisfactory.

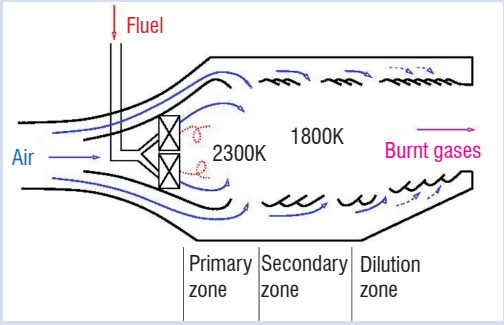

Figure B2 - 01 - Schematic view of the lengthwise section of a conventional gas turbine combustor.

Limitation of the temperature resulting in low NO production can be obtained in Lean Premixed Prevaporized combustors (LPP combustors) in which the uniform fuel-air ratio prevents the reactive flow from temperature peaks. Combustion instabilities and flame flash-back are possible in this type of combustor however. Optical diagnostics are of great help to characterize the unsteady behavior of these combustors.

NOx production can also be limited by the use of Rich-Quick quench-Lean combustors (RQL combustors). In the first part of the combustor, the fuel-air ratio is very high so that no oxygen radical is available for NO production. Downstream from this zone of high fuel-air ratio, sudden dilution by air occurs in such a way that the rest of the oxidation takes place at a relatively low temperature. Optical diagnostics are used to check the complete oxidation of the reactants in the exit section of the combustor.

An example of a two-head combustor including both LPP and RQL heads is given in Figure B2 - 02.

A new concept that is now being explored consists of creating in the same volume behind the same fuel injector a small zone with high stoichiometry acting as a pilot flame and located in the axis of the combustor, and, around this pilot flame, a larger zone with a low stoichiometry, relatively homogeneous in fuel-air ratio. Good mixing between air and fuel in the low stoichiometry zone is obtained by a multi-point fuel injection device, as shown in Figure B2 - 03. Optical diagnostics are very useful for finding the best compromise between homogeneity of the reactive mixing and stability of the combustion.

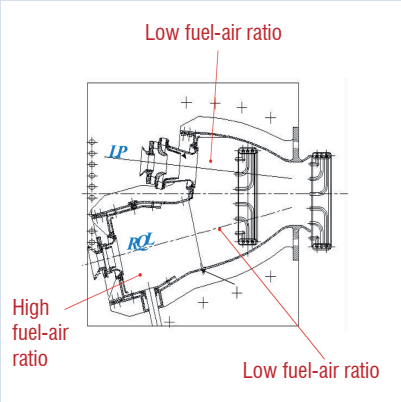

Figure B2 - 02 - Lengthwise section of a two-head LPP-RQL combustor

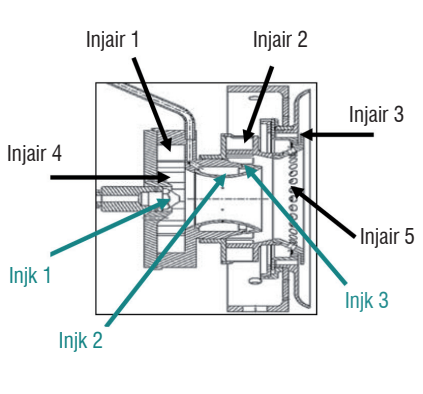

Figure B2 - 03 - Lengthwise section of a multi-point fuel injector (injk1: pilot fuel injection, injki, i=2,3: multi-point fuel injection, injairi, i=1-5: air injection)

Box 3 - Soot formation

The formation of soot particles includes the following steps:

• The starting point is the reaction between small aromatic molecules (molecules including carbon rings with electron loops) which gives rise to bigger aromatics. The agglomeration of big aromatic species leads to small solid particles (size of a few nm) of approximately spherical shape containing a large amount of carbon. This is the nucleation step.

• From this point, the increase of the mass of soot mainly results from surface growth with the HACA process while agglomeration by collision between soot particles, i.e. coalescence, tends to increase the size of the particles and to decrease their number. If AnH is a soot particle with n carbon atoms and a H atom on its surface, the HACA reaction sequence is:

$$A_nH + H \leftrightarrow A_n^{\bullet} + H_2$$
$$A_n^{\bullet} + H \leftrightarrow A_nH$$
$$A_n^{\bullet} + C_2H_2 \rightarrow A_{n+2} + H$$

If the residence time in the reactor is large enough, the spherical particles agglomerate to form much bigger particles (a few hundred nm) of very irregular shape, as shown by this picture.

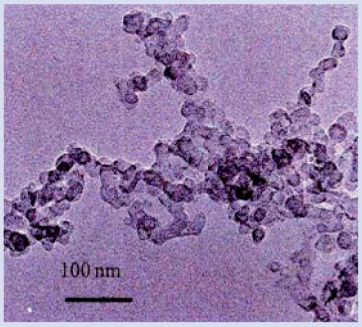

• Lastly, oxidation by O_2 and the OH radical tends to decrease the mass and the size of the soot particles if oxidizing species are available and if the temperature is still high enough.

The soot particles greatly influence the heat transfer by enhancing the radiative transfer in flames. For that reason, they have to be characterized experimentally. Non-intrusive optical techniques are the most convenient tools for that. However, reliable characterization of soot particles in a reactive flow is a challenge because the interpretation of the detected signals in terms of concentration or particle size depends on the optical properties of the soot particles which are not well known. Indeed the interpretation of the optical measurements requires the knowledge of the complex refractive index of the soot particles which is known with a large uncertainty. Numerical simulation of soot formation is possible: It is based on the resolution of equations giving the evolution of the soot volume fraction and soot particle number [12]. These equations include source terms taking into account the above mentioned phenomena of nucleation, surface growth, coalescence and oxidation. These simulations are difficult because they require the calculation of the concentration of the soot precursors which are minor species resulting from a complex chemistry.

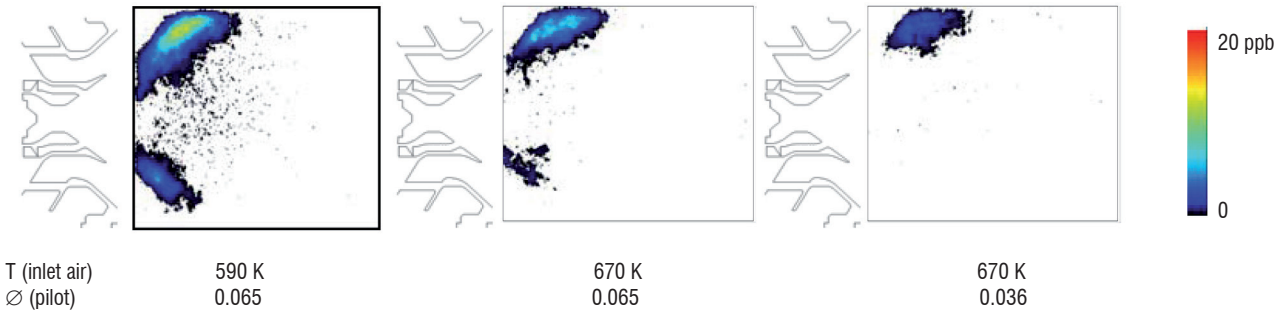

Figure 8 - Field of soot volume fraction obtained by LII downstream from a multi-point injector; pressure: 16.5 bar; global (stoichiometry): 0.36.

Other measurements in combustor equipped with multi-point injector

Nowadays, a large share of the work on low NOx concepts involves multi-point injection. Thanks to pilot fuel injection, the reactive flow is kept alighted even at low power operating conditions which are not favorable to combustion. In these low power conditions, the combustor is prone to CO emission and to combustion instabilities. In order to correct such possible dysfunctions, knowledge of the flow features downstream from the injector is required. The distribution of the fuel droplet size and velocity is important, especially if the experimental analysis of the combustor is completed by a numerical simulation which requires known intake conditions for the liquid fuel and fresh air. The information on fuel droplets can be obtained from Phase Doppler Particle Analyzer (PDPA) measurements, an example of which is given in Figure 9 [23]. The measurement by PDPA is similar to LDV for the particle velocity and uses the information on the phase difference between signals obtained on different detectors for the size of the particle.

This technique gives simultaneously the size and the velocity of the fuel droplets in a small probe volume but, until now, the measurements for droplets could not be done in real pressure and temperature conditions. These experimental results therefore could not be used directly in numerical simulations made in real operating conditions. However, with the PLIF technique, it was possible to achieve, in real conditions, simultaneous visualizations of the kerosene vapor and the OH radical. Kerosene vapor is detected through the fluorescence of monoaromatic and diaromatic species selected by an appropriate laser wavelength (266 nm). These visualizations show that combustion takes place in a widely open region slightly shifted downstream with regard to the vaporization zone, as shown in Figure 10. Information deduced from PLIF visualizations was used to adjust the inlet conditions concerning fuel droplets in numerical simulations. The left part of Figure 11 exhibits the experimental OH concentration field obtained just downstream from the injector and the right part exhibits the temperature field obtained by a 3D numerical simulation. The opening of the combustion region downstream from the injector is similar in the experiment and in the calculation. The correct numerical result can be obtained only after adjusting the initial diameter of the injected fuel droplets. It should be noted that visualizations can be achieved at pressures as high as 22 bar [14].

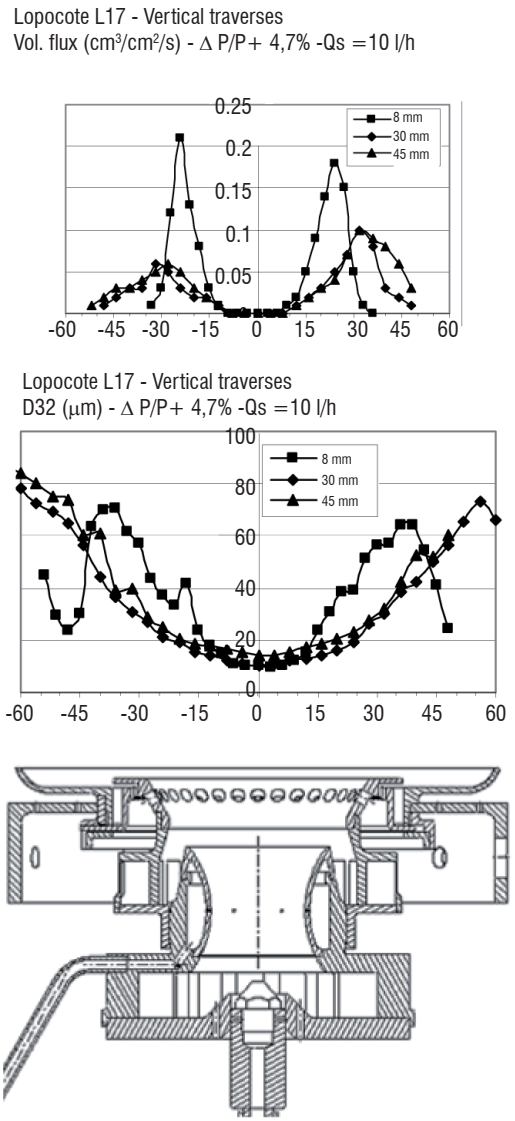

Figure 9 - Profiles of mean Sauter diameter (D32) of droplets and liquid flow rate behind a multi-point injector (profiles obtained by PDPA).

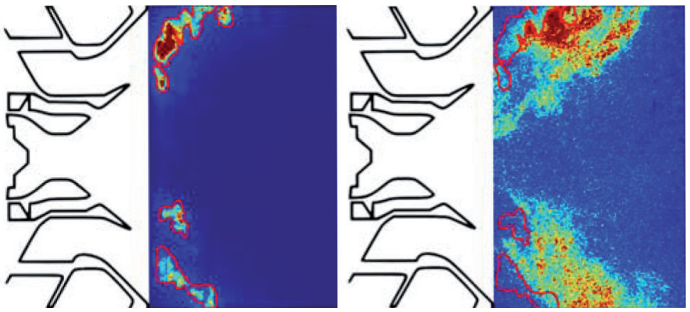

Figure 10 - Simultaneous PLIF visualization of the kerosene vapor (left) and of the OH radical (right); the OH visualization is completed by the contour indicating the presence of kerosene vapor; inlet temperature: 590 K, operating pressure: 9.5 bar.

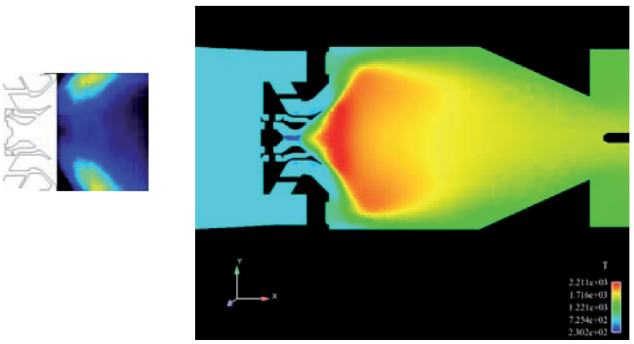

Figure 11 - PLIF visualization of the averaged OH concentration (left) and temperature field obtained by numerical simulation (right).

Combustion with liquid oxygen

Liquid oxygen (LOx) associated with a liquid or gaseous fuel such as hydrogen, methane or kerosene is often used in rocket engines to obtain a good specific impulse. In fact, if the LOx is really liquid during the short transient phase of the engine ignition, the pressure

increases rapidly to frequently reach a level much higher than the critical pressure of oxygen. For example, the operating pressure of the Vulcain 2 engine is 115 bar while the critical pressure of oxygen is 50.4 bar. 2D optical visualizations are of primary importance for characterizing the mixing between the dense oxidizer generally injected in the center of a co-axial injector and the fuel injected in the periphery of the oxidizer jet. As can be seen in Figure 12, shadowgraph visualizations [24] of such flows [15], although they are not spatially resolved in the observation direction, show the difference of behavior between sub-critical and trans-critical conditions (trans-critical in the sense that the pressure is higher than the critical pressure but the LOx injection temperature is lower than the critical temperature, equal to 154.6 K for oxygen).

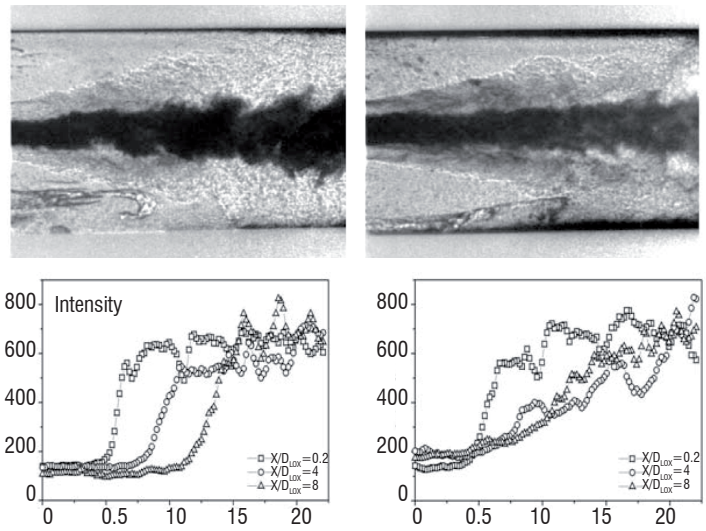

Figure 12 - Flow visualization by shadowgraphy and corresponding radial profiles of light intensity, (left) P=30 bar, (right) P=60 bar.

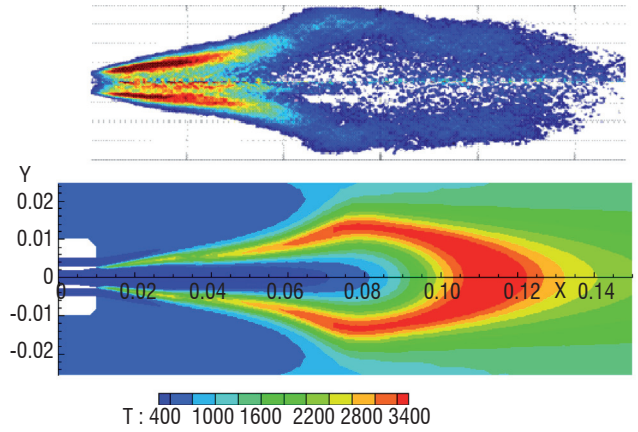

Figure 13 - Flow visualization by emission of OH* obtained after Abel transform in transcritical conditions (top); temperature field obtained by RANS numerical simulation (bottom) in the same conditions.

In the sub-critical case the region located around the injector axis and occupied by oxygen is totally dark without any gradient of light intensity while, in the trans-critical case, a zone of smooth gradient separates the dark region occupied by oxygen and the bright region occupied by hydrogen. That means that, at 60 bar, density gradients are present in the core of the oxygen jet. Moreover, the structures appearing at the periphery of the oxygen jet indicate the development of a usual liquid-gas shear layer at 30 bar but of a one-phase like mixing layer at 60 bar. These observations suggest that, in sub-critical conditions, the combustion rate is limited by the vaporization rate which depends directly on the size of the liquid droplets created by atomization of the liquid oxygen, whereas, in sub-critical conditions, it is limited by the oxygen-fuel mixing, which seems relatively intense on a large scale but can be much slower on a small scale. As for air breathing combustion, useful visualizations can also be obtained by LIF or from spontaneous emissions of excited radicals [16]. Figure 13 gives an example of visualization by spontaneous emission of the OH* radical and the temperature field obtained by numerical simulation in the same operating conditions [17] (case A60 of MASCOTTE [15] experiment). It appears that the structure of the flame is correctly reproduced by the calculation.

Conclusion

Continuous improvement is necessary to adapt optical diagnostics to the demands of the scientific community for combustion, i.e. more and more stringent requirements concerning the quality of the information provided by the diagnostics as well as adaptability to the tougher operating conditions of combustors, such as higher pressures and stiffer temperature and concentration gradients. It is not even enough that the measurements are resolved in space and time; in addition, understanding the complex physics of turbulent reactive flows requires 2D visualizations and simultaneous measurements of several physical quantities. The use of 2D lasers associated with different synchronized detection devices gives us the possibility of highlighting correlations existing between various physical phenomena in reactive flows. For example, simultaneous kerosene-OH LIF measurements have shown that, in a multi-point combustor, a large opening of the flame zone was the consequence of the particular location of the vaporizing kerosene region. The fact that these measurements are now possible under high pressure conditions greatly enhances the benefit of the experiments. However, some additional improvements of optical diagnostics are expected. They involve measurement of sprays, soot particles and other minor pollutant species in the real operating conditions of industrial combustors. In dense sprays, the absorption of the laser beam or sheet, higher than in a pure gas, is problematic. With regard to soot particles, the reliability of the results must be improved through better knowledge of the optical properties of the particles. Also, the possibility of higher frequency measurements could help to analyze instabilities which may appear in combustion devices, especially when new concepts for low NOx emission are tested ■

Acknowledgements
We thank our colleagues of the DMPH and the DEFA for their help and for providing documentation.

References

[1] R. BORGHI - *On the Structure and Morphology of Premixed Flames, Recent Advances in the Aerospace Sciences*. Plenum Press, New York, 117-138, 1985.

[2] N. PETERS - *Laminar Flamelet Concepts in Turbulent Combustion.* 21st Symposium (International) on Combustion, The Combustion Institute, Pittsburgh, 1986, 1231-1256.

[3] W. M. ROQUEMORE, V. R. KATTA - *Role of flow visualization in the development of UNICORN*. Journal of visualization, 2(3-4) pp. 257-272, 2000

[4] F. GRISCH, B. ATTAL-TRETOUT, A. BRESSON, P. BOUCHARDY, V. R. KATTA AND W. M. ROQUEMORE - *Investigation of a dynamic diffusion flame of H2 in air with laser diagnostics and numerical modelling.* Combustion and Flame, 139, pp. 28-38, 2004.

[5] V. R. KATTA, L. P. GOSS AND W. M. ROQUEMORE - *Effect of Non unity Lewis Number and Finite-Rate Chemistry on the Dynamics of a Hydrogen-Air Jet Diffusion Flame*. Combustion and Flame, 96(1-2), pp. 60-74, 1994.

[6] V. R. KATTA AND W. M. ROQUEMORE - *On the Structure of a Stretched/Compressed Laminar Flamelet - Influence of Preferential Diffusion*. Combustion and Flame, 100(1-2), pp. 61-70, 1995.

[7] J. DE CHARENTENAY - *Simulation numérique d'écoulements réactifs instationnaire à faibles nombres de Mach.* Thèse de l'Ecole Centrale Paris soutenue en 2002.

[8] P. MOREAU, J. LABBE, F. DUPOIRIEUX AND R. BORGHI - *Experimental and numerical study of a turbulent recirculation zone with combustion*. 5th Symposium on turbulent shear flow, Ithaca, NY, USA, 1985.

[9] V. SABELNIKOV, C. BROSSARD, M. ORAIN, F. GRISCH, M. BARAT, A. RISTORI AND P. GICQUEL - *Thermo-acoustic instabilities in a backward-facing step stabilized lean-premixed flame in high turbulence flow*. 12th French congress on visualization in fluid mechanics, Nice, July 1-4, 2008.

[10] B. SAINTE-ROSE, N. BERTIER, S. DECK AND F. DUPOIRIEUX - *Delayed detached eddy simulation of a premixed methane air flame behind a backward facing step*. 44th AIAA/ASME/SAE/ASEE Joint Propulsion Conference & Exhibit, Hartford, Connecticut, 21-23 July 2008.

[11] S.J. BROOKES, J.B. MOSS - *Measurements of Soot Production and Thermal Radiation from Confined Turbulent Jet Diffusion Flames of Methane.* Combustion and Flame, Vol. 116, pp. 49-61, 1999.

[12] B. ZAMUNER, F. DUPOIRIEUX - *Numerical simulation of soot formation in a turbulent flame with a Monte Carlo PDF approach and detailed chemistry.* Combustion, Science and Technology, Vol. 158, pp. 407-438, 2000.

[13] K.P. GEIGLE, J. ZERBS AND C. GUIN - *Laser-induced incandescence for soot measurement in technical flames at increased pressure at the Onera M1 test rig.* 9th Onera-DLR Symposium, Châtillon sous Bagneux, 22-24 October 2008.

http://www.onera.fr/odas2008/sites/www.onera.fr.odas2008/_files/docs/29-Geigle.pdf

[14] F. GRISCH, M. ORAIN, B. ROSSOW, E. JOURDANNEAU AND C. GUIN - *Simultaneous Equivalence Ratio and Flame Structure Measurements in Multipoint Injector using PLIF.* AIAA 2008-4868, 44th AIAA/ASME/SAE/ASEE Joint Propulsion Conference & Exhibit, Hartford, Connecticut, 21-23 July 2008.

[15] M. HABIBALLAH, M. ORAIN, F. GRISCH, L. VINGERT AND P. GICQUEL - *Experimental studies of high pressure cryogenic flames on the MASCOTTE facility.* Combustion, Science and Technology, Vol. 178, pp. 101-128, 2006.

[16] S. CANDEL, G. HERDING, R. SNYDER, P. SCOUFLAIRE, J.-C. ROLON, L. VINGERT, M. HABIBALLAH, F. GRISCH, M. PEALAT, P. BOUCHARDY, D. STEPOWSKI, A. CESSOU AND P. COLIN - *Experimental investigation of shear-coaxial jet flame. J. Propulsion Power,* 14(5), pp. 826–834, 1998.

[17] L. MATUSZEWSKI, F. DUPOIRIEUX AND V. GIOVANGIGLI - *Combustion supercritique LOx-H_2.* Second colloque INCA 23-24 Octobre 2008.

[18] C. P. FENIMORE - *Formation of nitric oxide in premixed hydrocarbon flames.* 13th Symposium (Int.) on Combustion, pp. 373-379, The Combustion Institute, Pittsburgh 1971.

[19] J. A. MILLER, C. T. BOWMAN - *Mechanism and modelling of nitrogen chemistry in combustion.* Progress in Energy and Combustion Science, 1989, Vol. 15, pp. 287-338.

[20] F. GRISCH, M. ORAIN - *Role of Planar Laser-Induced Fluorescence in combustion research.* Aerospace Lab n°1, December 2009.

[21] C. BROSSARD, J.-C. MONNIER, PH. BARRICAU, F.-X. VANDERNOOT, Y. LE SANT, F. CHAMPAGNAT, G. LE BESNERAIS - *Principles and Applications of Particle Image Velocimetry.* Aerospace Lab n°1, December 2009.

[22] F. GRISCH, M. ORAIN - *Role of Planar Laser-Induced Fluorescence in combustion research.* Aerospace Lab n°1, December 2009.

[23] G.LAVERGNE, Y. BISCOS, C. LAURENT, V. BODOC - *Advanced Measurement Techniques for Spray Investigations.* Aerospace Lab n°1, December 2009.

[24] J.M. DESSE, R. DERON - *Shadow, Schlieren and Color Interferometry.* Aerospace Lab n°1, December 2009.

Acronyms

CARS (Coherent Antistokes Raman Spectroscopy)

LIF (Laser Induced Fluorescence)

DFWM (Degenerate Four Wave Mixing)

DNS (Direct Numerical Simulation)

LAERTE (LAboratoire des Ecoulements et de leurs Techniques d'Etude - Reactive flows and their research techniques laboratory)

LDV (Laser Doppler Velocimetry)

DDES (Delayed Detached Eddy Simulation)

PLIF (Planar LIF)

FAR (Fuel Air Ratio)

LII (Laser Induced Incandescence)

DLR (Deustches Zentrum fur Luft und Raumfahrt (German Aerospace Center))

PDPA (Phase Doppler Particle Analyzer)

RQL (Rich-Quick quench-Lean)

PIV (Particle Image Velocimetry)

LES (Large Eddy Simulation)

AUTHOR

Francis Dupoirieux is deputy head of the Energetics department of Onera, in charge of the scientific management of the activity. He created 3D CFD tools for the numerical simulation of turbulent reactive flows that have been widely used by research laboratories and industrial partners of Onera. He also developed physical models of pollutant formation in flames. He is now involved in the development of the CEDRE code dedicated to multi-physic problems in reactive flows. This task includes the definition of experiments for validating the models implemented in CEDRE and the global validation of this code.

Frédéric Grisch,
Mikaël Orain
(Onera)

E-mail: frederic.grisch@onera.fr

Role of Planar Laser-Induced Fluorescence in Combustion Research

Laser diagnostics are now considered an indispensable tool in fluid dynamics research. Such measurements provide a deeper understanding of the inner physical and chemical processes, which is required to validate and improve computer-based simulations and to assist applied research in practical combustors. This paper presents an overview of the potential of planar laser-induced fluorescence (PLIF), which currently allows for the imaging of scalar properties such as species concentration, temperature, velocity, pressure and density over wide pressure and temperature ranges with high temporal and spatial resolution. Although a complete picture of the present research and PLIF applications to fluid mechanics is beyond the scope of this article, this overview focuses rather on the basic concepts underlying the technique and its application to various flowfields at Onera. These examples cover applications to primarily gas flows like mixing experiments under isothermal and isobaric conditions, fuel/air mixing and temperature measurements in heated jet flows, subsonic and supersonic flame structures and improvement of combustion processes using nanosecond pulsed discharges. Several examples of measurements of fuel concentration in multiphase flows, flame structure around isolated droplets and fuel/air mixing processes in kerosene/air combustion at high pressure are presented. The paper concludes with a section that addresses key issues that remain as challenges for continued research towards the improvement of quantitative PLIF measurements.

Introduction

Knowledge of the physics and modeling of turbulent gaseous and reacting flows is constantly progressing. Detailed information is vital to demonstrate the reliability of the various numerical models already developed and to further improve their prediction capabilities in order to increase combustor performances. Since the advent of the laser in the early 60's, various laser-based spectroscopic techniques have been developed for diagnostic purposes. These methods are extremely valuable for probing harsh environments such as turbulent flames, where non-intrusive optical techniques with high spatial and temporal resolution are very useful. Among the various laser-based diagnostics currently employed, imaging techniques including planar laser-induced fluorescence (PLIF), Raman, Rayleigh, and Mie scattering have proven useful in a wide variety of flows [1-3]. The resolved image can reveal important information about the structure of the flow and/or the combustion processes that influence combustor design. Spatially-resolved measurements are obtained over a large number of points included in the laser sheet, thereby providing an instantaneous image of the flowfield properties. A detailed study of large- and small-scale structures within the image is possible in both reacting and non-reacting flows, as well as fundamental studies dealing with the validation of turbulent flow modeling.

PLIF imaging is one of the most promising of these techniques because it is species- and quantum state-specific, and is therefore sensitive to species composition, temperature, number density and velocity. The other advantage of PLIF is its ability to provide instantaneous information over the whole plane of the flowfield, without the light-of-sight averaging inherent to the Schlieren and Shadowgraph techniques. Signals are higher than those of Rayleigh and Raman scattering, while the use of atomic or molecular fluorescent species generally ensures that the tracer is a suitable marker of the flow. Since its initial development in the late 70's and early 80's [4, 5], the potential of PLIF has been demonstrated in a wide variety of environments [6-8]. Achieving quantitative PLIF measurements can be very challenging, primarily because the effects of collisional quenching must be considered in the signal analysis. However, several strategies have been developed to either account for or to minimize the effects of collisional quenching. For instance, quantitative time-averaged imaging

of concentration, temperature, pressure and velocity has been demonstrated in compressible flows [2]. Temporally-resolved imaging of concentration and temperature has also been demonstrated in a non-reacting jet and flame, respectively, but detailed instantaneous two-dimensional property measurements in complex mixing and turbulent combustion flows were limited. While time-averaged measurements are useful for validation of computational models, there is a clear need for instantaneous imaging measurements in realistic mixing and combustion flowfields. For instance, temporally-resolved measurements are needed for a better understanding of the flow physics, leading to improved modeling of turbulent mixing mechanisms and the interaction between turbulence and combustion [55] Instantaneous measurements are also particularly relevant in light of the importance of large-scale structures in turbulent mixing and combustion [9]. Therefore, the need to better understand the instantaneous structure of a given flow, which ultimately governs combustion processes, provides a strong motivation for the continued development and application of temporally-resolved PLIF techniques.

This paper first provides a brief general background for the PLIF technique and references to relevant literature. Practical considerations and a selection of fluorescent tracers are then discussed in the second part of the article. In the third part, examples covering PLIF applications in mono- and two-phase reactive flowfields are presented. Finally, the paper concludes with a section that addresses key issues that remain as challenges for continued research towards the improvement of quantitative PLIF measurements.

Fundamentals

Theory

Fluorescence denotes the radiation emitted by an atom or a molecule when it relaxes by spontaneous emission of a photon from a higher to a lower energy level. In laser-induced fluorescence (LIF) processes, the upper energy level is populated using laser excitation with a wavelength tuned to a resonance between the excited state and a discrete lower state. Typically, the lower state is in the ground electronic level, as the other electronic states may be negligibly populated at combustion temperatures. For more detailed information about LIF, see [3,7,8].

After excitation, the laser-populated upper state may undergo a number of subsequent processes. First, the molecule can return to the ground state by laser-induced, stimulated emission. Second, absorption of an additional photon can excite higher molecular states, including ionized levels. Third, the internal energy of the system can be altered via inelastic collisions with other molecules, producing rotational and vibrational energy transfer, together with electronic energy transfer; the latter is often referred to as quenching. Fourth, interactions between the separate atoms of the molecule, known as “internal” or “half” collisions, produce internal energy transfer and dissociation of the molecule. When the dissociation is produced by a change between a stable and a repulsive electronic arrangement in the molecule, it is called predissociation. Finally, the originally populated state, and nearby upper states, are indirectly populated through collisions and fluoresce, producing the LIF signal.

LIF signals can be related to specific properties (concentration and temperature) of the absorbing species through modeling of these state-to-state transfer processes. As fluorescence is a function of the upper state’s population, such modeling requires solving the state-dependent population dynamics. While quantum-mechanical density-matrix descriptions of the interactions involved in LIF are available [10-11], most treatments of LIF are based on a semi-classical rate equation analysis [12]. Generally, a simplified treatment of this rate equation is used. It consists of a two-level molecular system, where the two levels are those probed by the laser radiation.

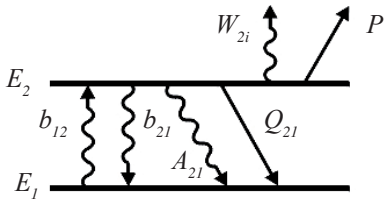

Figure 1 - Energy level diagram for a two-level fluorescence model

Figure 1 displays the rate constants for the different optical and collisional processes connecting the upper and lower energy levels, E_1 and E_2. b_{12} corresponds to absorption and b_{21} to stimulated emission, b_{12} and b_{21} are related to the Einstein coefficients for stimulated emission and absorption, B, through $b = BI_\nu / c$, where I_ν is the incident laser spectral irradiance. A_{21} (given by the Einstein A coefficient) is the rate constant for spontaneous emission, which represents the fluorescence signal. P corresponds to predissociation and W_{2i} to photo-ionization. These processes are generally negligible and they are not considered here. Q_{21} corresponds to the collisional quenching. This term represents the de-excitation that the molecule undergoes based on inelastic collisions with other molecules. It is described by:

$$Q_{21} = N\sum_i \chi_i \sigma_i v_i \tag{1}$$

In this expression, N represents the total number density, χ_i the collider species mole fraction, σ_i the collision cross section (species dependent) and v_i the mean molecular speed between the absorbing species and colliding species.

The rate equations for the population densities of the two energy levels, N_1 and N_2 are then expressed by:

$$\frac{dN_1}{dt} = -N_1 b_{12} + N_2(b_{21} + A_{21} + Q_{21}) \tag{2}$$

$$\frac{dN_2}{dt} = N_1 b_{12} - N_2(b_{21} + A_{21} + Q_{21}) \tag{3}$$

As commonly suggested, the upper level has a negligible population prior to the laser excitation, so the initial condition, $N_2(t=0)=0$. Additionally,

$$N_1 + N_2 = N = N_1^0 \tag{4}$$

where N_1^0 represents the initial population of N_1. Resolution of Eqs. 2 and 3 yields the following expression for N_2:

$$N_2(t) = \frac{b_{12} N_1^0}{(b_{12} + b_{21} + A_{21} + Q_{21})}(1 - e^{-\tau t}) \tag{5}$$

Where the time constant τ is equal to $1/(b_{12} + b_{21} + A_{21} + Q_{21})$. For laser pulses that are long compared to τ (10 ns vs. ~ 1 ns), the system reaches steady state with N_2 equal to:

$$N_2 = N_1^0 \frac{b_{12}}{(b_{12}+b_{21})} \frac{1}{1+\dfrac{A_{21}+Q_{21}}{b_{12}+b_{21}}} = N_1^0 \frac{B_{12}}{B_{12}+B_{21}} \frac{1}{1+\dfrac{I_\nu^{sat}}{I_\nu}} \quad (6)$$

where I_ν^{sat}, is the saturation irradiance defined as:

$$I_\nu^{sat} = \frac{(A_{12}+Q_{12})}{B_{12}+B_{21}} \quad (7)$$

The fluorescence rate is finally converted to a total fluorescence signal by temporal integration over the laser pulse duration and by taking into account the collection efficiency of the detection optics. Assuming the fluorescence is emitted equally over 4π steradians, the total number of photons N_p detected by a photo-detector from the collection volume V is:

$$N_p = \eta \frac{\Omega}{4\pi} f_1(T) \chi_m n V B_{12} E_\nu \frac{A_{21}}{A_{21}+Q_{21}} \quad (8)$$

η is the transmission efficiency of the collection optics, Ω is the solid angle of collection, $f_1(T)$ is the fractional population of the lower-coupled state, χ_m is the mole fraction of the absorbing state, n is the total gas number density and E_ν is the spectral fluence of the laser. The term $A_{21}/(A_{21}+Q_{21})$ is called the Stern-Volmer factor or fluorescence yield. It is generally much smaller than 1 as $A_{21} << Q_{21}$. In order to perform quantitative measurements of species concentrations in the linear regime, the quenching rate constant must be evaluated. The quenching rates can be calculated in various flames using available data for the specific quenching cross sections and weighting by the mole fractions of species in the gas mixture. For some cases, the fluorescence signal can be independent of quenching, which allows for quantitative LIF measurements. If the laser irradiance is increased until $I_\nu >> I_\nu^{sat}$, the fluorescence signal also becomes independent of both laser irradiance and quenching. However, these conditions are difficult to obtain in the spatial, temporal, and spectral wings of the laser pulse, which precludes the use of this approach in most situations.

Planar imaging: practical considerations

Several requirements must be satisfied in order to perform quantitative measurements on a given species. First, the molecule needs to have a known absorption and emission spectrum. Second, the rate of radiative decay of the excited state, which directly influences the fluorescence signal, must be known. Third, all the excited state losses, mainly coming from collisions, photo-ionization and predissociation, must be taken into account. Several measurement strategies including one and two-wavelength excitation techniques have been specifically developed to measure species concentration and temperature. When mole fraction has to be measured, a single-wavelength excitation scheme can be used [6]. A quantum state is selected to minimize the overall temperature dependence of the fluorescence signal in the temperature range of the experiment, leading then to a direct proportionality between the number density and the fluorescence intensity. Using suitable calibration techniques, the proportionality factor can be evaluated. It depends on the experimental parameters such as observation volume, solid angle, the spectral and spatial efficiencies of filters and cameras, the power density of the laser, spectroscopic constants such as transition probability, absorption lineshape and fluorescence quantum yield, which are usually known. However, the knowledge of the fluorescence quantum yield may be problematic. Pressure, temperature and species composition at the observation volume govern the local collisional-quenching rate and are thus determinant for the fluorescence quantum yield. In flames, when steep gradients of temperature and mixture composition take place, the fluorescence quantum yield can change drastically with position, making quantitative LIF measurements difficult to perform.

Temperature measurements require consideration of several factors including (i) the reduction of the fluorescence signal to a function of temperature only; (ii) a large variation of fluorescence yield with temperature; (iii) the capability of accurate prediction of the fluorescence signal; (iv) high signal levels compatible with the dynamic range of the detection system. A two-line excitation scheme is then selected based on preliminary studies such as [13-14]. In our case, the fluorescence ratio obtained by the sequential excitation of two different initial states of the absorbing molecule was used. The ratio of the fluorescence intensities is then proportional to the relative populations of the corresponding absorbing states and hence is a function of temperature through Boltzmann statistics, assuming a thermodynamic equilibrium. The change of the number density, mole fraction and collisional quenching with temperature can be minimized if the same upper state is selected for both excitations. The technique can be therefore used in a wide range of flowfields, including those that are compressible and/or varying in composition.

The typical arrangement for PLIF measurements is schematized in Figure 2. In the single-line approach, the UV laser beam is tuned to excite a molecular transition. A system of cylindrical and spherical lenses is used to focus the laser beam into a thin sheet. Fluorescence from part of the laser sheet interacting with the flow is collected by an imaging lens at a right angle, and imaged on a gated, intensified CCD camera. A spectral band-pass filter is placed in front of the imaging lens to reject the scattered light and to select the suitable fluorescence. The spatial resolution achievable depends on the pixel size of the detector array, the depth-of-field of the collection optics, the image magnification factor, and the size of the beam waist at the probe volume. A diode array may be used to measure the distribution of laser irradiance over the height of the laser sheet in order to correct the spatial non-uniform laser excitation (flat fielding procedure) as well as to account for drift and fluctuation of the laser energy. A trigger system is required to drive the pulsed laser and the synchronous amplification of the CCD camera over a suitable gate duration. This temporal discrimination improves the rejection of flame luminosity that is partly made by spectral filtering. For the two-line temperature measurements, two lasers are used to excite two different transitions offering the best sensitivity to temperature. The two laser pulses are fired sequentially, with a delay as low as 100 ns to temporally separate the fluorescence decays of each transition. The two Intensified Charge-Coupled Device (ICCD) cameras are gated to integrate the fluorescence signal accordingly.

While two-dimensional images yield a wealth of structural information and give good insight into the physical processes governing the fluid dynamics, in many cases more information is desirable. Multi-species measurements are then of major interest to fully describe the thermodynamic parameters of the observed volume element and to understand correlations between different species concentration and potentially their local variations. The PLIF technique offers the advantage to easily combine with other two-dimensional imaging techniques based on incoherent scattering processes (Raman, Rayleigh,

Mie, LII, etc.). For instance, a Sequential PLIF imaging setup can be used with 2D or 3D (stereoscopic) PIV, with Rayleigh scattering and also with another PLIF system [2]. For these measurements, separate laser sheets were produced from different lasers and these were overlapped in the observed region. Separate detectors were then used to collect the respective signals.

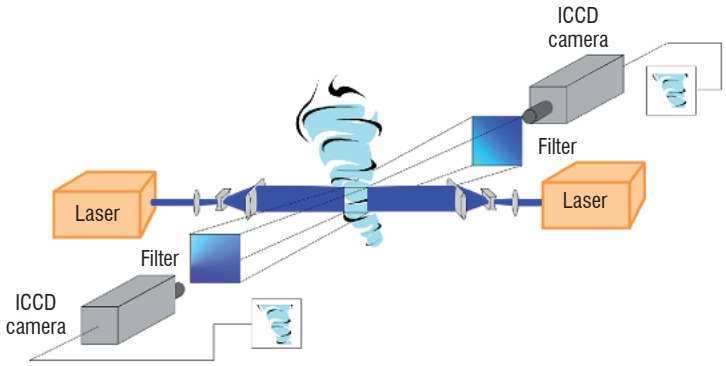

Figure 2 - Schematic representation of a typical experimental set-up for PLIF imaging

Molecular tracers for fluid systems

PLIF diagnostics require the use of fluorescent molecules with well-understood physical and spectral behavior that allows for remote measurements of scalar quantities of interest. Typically, these molecules need to be selected with regard to the physical processes investigated in the flowfield. The following section does not intend to review all fluorescent species detectable in reactive flowfields, but focuses on the main molecules used for the experiments carried out at Onera to yield temporal and spatial information on scalars. In particular, two classes of fluorescent tracers are selected to gain deeper insights into the immensely complex processes prevailing in aeronautic engines such as flow generation, fuel injection and spray formation, mixing, ignition and combustion.

Flame front tracers

The flame front, or reaction zone, is the thin region in a flame where most of the chemical reactions which convert fuel and oxidizer to combustion products take place. These reactions also deliver high local heat release rates which can be also indicators of the flame front. In a non-premixed flame, the flame front separates fuel and oxidizer and in a premixed flame it separates burned and unburned gases. Information about the flame front is essential because it is in the flame region that most of the energy is released, and the total flame front area determines the total amount of energy released in the flame. Assumptions about the properties and structures of flame fronts are part of all turbulent combustion models, e.g. the flamelet approach in RANS modeling or the G-equation approach in LES. The OH radical is the most commonly used flame front indicator. However, other flame front markers such as CH, HCO and the product CH_2O x OH are suitable.

The OH radical is one of the most important intermediate species present in combustors involving air as the oxidizer. OH is formed by fast two-body reactions, such as the attack of H radicals on O_2 molecules, and appears as an intermediate species in many reaction pathways of both hydrogen and hydrocarbon combustion. The OH radical is then consumed by slower three-body recombination reactions [15]. The OH lifetime is particularly long compared to typical fluid-mechanical timescales and, therefore, OH can be convected away from its production location by the local flowfield. OH concentrations are large in the lean regions of the flame front, where chemical reactions involved in the combustion process are completed. In a premixed flame, OH produced in the flame front is slowly consumed in burnt gases, and thus remains present in the burnt gas region at equilibrium concentrations. In a non-premixed flame, OH marks a wider region of the flame front than for instance the CH radical. From studies of flame-vortex interactions, it is also found that the peak of OH concentrations can nevertheless be used as a reliable indicator of heat release and flame front position. However, care has to be taken in situations of large unsteady flame curvature, conditions for which this is no longer valid [16].

CH is produced during the initial reaction of hydrocarbons and air and then rapidly decays as the products of these fast reactions are converted into other species. The CH profile is therefore relatively thin and represents the fuel rich side of the flame where fuel consumption is initiated [15]. Chemical kinetic computations and experiments have also shown that the HCO radical concentration closely matches the distribution of heat release, making it an ideal tracer of the flame front [16]. HCO is an important radical for the oxidation of hydrocarbons in combustion processes. It is formed by CH_2O, and reacts with almost every other molecule in the flame to yield CO and other radicals. The place of HCO in combustion mechanisms makes it a direct link to the overall rate of fuel consumption, and it is also a fast dissociating species which makes its concentration approximately equal to its production rate. These two factors correlate well with the heat release. However, single-shot HCO-PLIF measurements are difficult due to the low concentration of this molecule and its fast predissociation. The product of OH and CH_2O can also be a good alternative because it correlates well with the local heat release rate, and the measured heat release allows for determination of the position of the flame front. It can be shown that the product of OH and CH_2O concentrations is proportional to the reaction rate of the reaction $CH_2O+OH \rightarrow H_2O+HCO$, over a limited temperature range. The rate of this reaction reveals a strong correlation with the global heat release rate as for the HCO concentration [17].

Fuel tracers

Fuel concentration distribution is one of the most important parameters to measure in industrial combustors, e.g. gas turbines or IC engines. In general, most gaseous fuels do not fluoresce as opposed to commercial liquid fuels (kerosene, gasoline, etc.), which fluoresce when excited by UV radiation. However, as commercial liquid fuel is a mixture of a large number of hydrocarbons, the fluorescence dependence on pressure and temperature, and the quenching behavior are generally unknown. Furthermore, the absorption and fluorescence properties vary with the composition from batch to batch. For these reasons, the preferred fuel visualization approach consists of using a single-component reference fuel for optical studies in combustors. The use of a pure fuel is also advantageous for comparisons between experiments and numerical simulations which become intractable for complex fuel mixtures. Fuel visualization is then performed using fluorescence from tracer molecules added to a non-fluorescing fuel. These tracers should meet several criteria. The tracer has to be soluble with the liquid fuel and it must behave like the fuel from the liquid phase to the gas phase, so the evaporation characteristics must be similar. In addition, the diffusion behavior of the fuel and tracer molecules must be equivalent. In most imaging experiments, it is not possible to resolve the regions of diffusive mixing. However, the effect of differential diffusion on the composition of the combustion products

can be important in flows where mixing timescales are longer than chemical timescales (high Damköhler number). In a combustion environment, the reaction characteristics such as the pyrolysis rate or auto-ignition temperature of the tracer must not differ much from the fuel. Finally, the tracer must not have a significant influence on the combustion process.

The fluorescent tracers commonly used in these experiments are aliphatic molecules [18]. Species containing chromophores that allow excitation into stable energy states that subsequently fluorescence are selected. This class of molecules includes ketones (R_2CO), aldehydes (R-CHO) and amines (R_3N), where R is a saturated aliphatic hydrocarbon chain. Ketones are most frequently used. Their spectroscopic properties have been thoroughly investigated and they have been applied to various practical systems. Due to their high vapor pressure, acetone (CH_3COCH_3) or 3-pentanone (diethyl-ketone, $[CH_3CH_2]_2CO$) are ideal tracers for gaseous flows. These tracers have transitions which can be easily excited with commercial lasers and the fluorescence, which is shifted to the red, is spectrally well-separated from the absorption spectrum. These species absorb in the near ultraviolet spectral region, with a maximum absorbance around 280 nm. Their fluorescence spectrum is broadband, extending from 330 nm to 600 nm, with a peak around 430 nm. 3-pentanone has been widely used to trace iso-octane in spark-ignition (SI) engines [19], as the evaporation characteristics of the two compounds match very well. Acetone has also been used to trace iso-octane in SI engines [20] or in practical combustors as a tracer of unburned fuel. Nonetheless, at temperatures above 1000 K, acetone starts pyrolyzing and reacts with radicals such as H, O and OH [21-22]. Therefore, differences of chemical behavior between acetone and the fuel must then be considered. Indeed, the pyrolysis rate of acetone is found to be higher than that of hydrogen and methane, but comparable with that of heavier hydrocarbons, e.g. ethane and propane. This limitation prevents the use of acetone in high-temperature, long residence time hydrogen or methane flows, but presents no drawbacks with heavier hydrocarbon fuels. When combustion takes place, the overall rate of destruction of acetone, hydrogen and hydrocarbons by radical attacks are similar. Differential diffusion also represents a limitation when light fuels such as hydrogen or methane are used, but for heavier hydrocarbon fuels, with molar weights closer to acetone, the effects are not significant.
Aromatics are the second family of attractive fluorescent tracers because of their natural presence in commercial fuels. These species exhibit interesting features such as a strong absorption in the UV and thus large fluorescence emission. For instance, single-ring aromatics like 1,2,4-trimethylbenzene and two-ring aromatics like naphthalene and its derivatives can be used to trace kerosene vapor. They typically have high fluorescence quantum yields and their absorption and emission spectra shift towards the red with increasing size of the aromatic structure. The wide variety of molecular sizes and, therefore, boiling points, makes this class of molecules attractive as tracers that can be adjusted to the evaporation behavior of the fuel or that are representative for vaporization classes in multi-component fuels. Another feature of these aromatics is the strong quenching of fluorescence with oxygen. The fluorescence signal intensities do not only depend on the tracer concentration but also on the oxygen molar fraction. As a result, fluorescence from aromatics is found to be proportional to the fuel/air ratio, which is a parameter of major interest to industrials [23].

Gas-phase applications

Mixture fraction / temperature imaging

Improving the extent of the mixing between fuel and air is of great importance in order to increase the combustion efficiency of aircraft engines:
• in terms of pollutant emissions (NOx, COx, soot), which can be greatly reduced if the spatial distribution of the air/fuel mixture in the combustor is homogeneous with a lean equivalence ratio,
• in terms of combustion instabilities, which are known to partly depend on temporal and spatial inhomogeneities of the air/fuel mixture in the combustion chamber.
Quantifying the mixing between fuel and air can be realized by measuring the local mixture fraction or the equivalence ratio in a flow using quantitative PLIF measurements [24]. These parameters characterize the spatial distribution of fuel and air all over the flowfield. Although realistic combustors do not operate at isothermal conditions, studies of mixing processes under such conditions are valuable to assess the validity of computational fluid dynamics (CFD) simulations in specific geometries, thus adding credibility to predictions under non-isothermal conditions.

Figure 3 represents typical instantaneous images of local mixture fractions measured by acetone-PLIF, recorded in an isothermal micro-channel for various Reynolds numbers. This micro-channel is used as a premixing duct and it is placed upstream from a micro-combustion chamber where the fuel/air mixture from the micro-channel is injected and burnt. The aim of the experiment is to better understand mixing and combustion in small volumes ($\sim$ 2 cm^3). The micro-channel is 1.2 mm high and 30 mm long. The airflow comes from the left hand side and a propane airflow seeded with acetone vapor is injected from the top through a 0.5 mm diameter hole. The air flow rate is between 0.3 and 1.5 g/s. In the present case, acetone is used as a fuel tracer to characterize the mixing of fuel with air. High-magnification optics is used in this experiment and the challenge here is to be able to visualize flow structures at the smallest turbulence length scales. With this set-up, the image size is 8x1.2 mm^2 and the spatial resolution of the technique is 14 μm. It is measured on a target of known size where lines with known thickness are drawn, which allows us to estimate the spread function due to the intensifier.

As the Reynolds number (Re) increases, the flow exhibits a transition from laminar to turbulent cases. For Re=100, the flow is laminar and the fuel spatial distribution shows little fluctuation with time and the morphology of the fuel jet remains constant. As can be seen, the fuel/air mixing is very poor and this indicates that combustion using a fuel/air mixture from this micro-channel would have low efficiency. The laminar/turbulent transition is observed for Re=250, where coherent structures start appearing, which influences the fuel jet and the subsequent fuel spatial distribution. For Re=500, strong vortices are observed, which leads to reduction of the mixing length in the micro-channel, hence to improved fuel/air mixing. Such a configuration leads to more homogeneous fuel/air mixing and subsequent combustion would exhibit high efficiency. Images such as those in figure 3 are used to validate micro-mixing models implemented in Onera's proprietary CFD code.

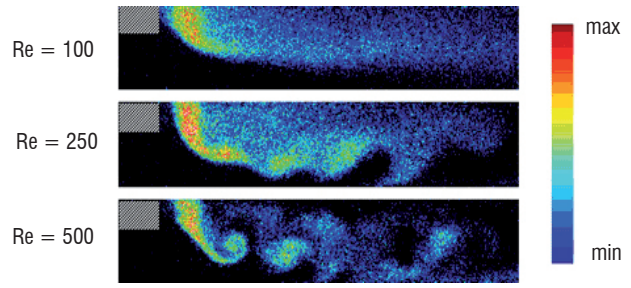

Figure 3 - Single-shot acetone-PLIF images of mixture fraction in a micro-mixing channel for various Reynolds numbers. The air flowrate is between 0.3 and 1.5 g/s, and the size of the image is 8x1.2 mm^2 [24]

A second application of acetone-PLIF is dedicated to temperature measurements in gaseous flowfields. The investigation of a heated turbulent jet is chosen to provide a good test case, which requires the optical diagnostic to have the ability to capture instantaneous temperature and concentration structure on small turbulence length scales. The specific flow considered is a 40 ms^{-1} turbulent jet of acetone-seeded air emanating from the 10 mm diameter nozzle of an electrical air heater with outlet temperature up to 1000 K. The jet is seeded with 3 % acetone, by bubbling part of the cold air stream through liquid acetone and adding it to the heated air immediately downstream from the electrical heater, preventing any acetone pyrolysis. The 266/308 nm dual excitation scheme was chosen because of its good temperature sensitivity within the range of temperature under investigation [22, 25]. Laser sheets at 266 nm and 308 nm, from a quadrupled frequency Nd:YAG and a XeCl excimer laser respectively, are located on the jet centerline just above the nozzle; the excimer laser pulse is delayed by 500 ns relative to the Nd:YAG pulse. Each laser sheet is focused down to a 0.3 mm thickness with a 50 mm height. In order to allow independent control of each sheet, separate focusing sets of lenses are employed in the optical layout. Acetone fluorescence excited by each laser sheet is collected on two separate intensified CCD cameras with a 100 ns temporal gate and the size of the image is 50x50 mm^2. Figure 4 shows typical instantaneous images of acetone molar fraction and temperature results for the heated jet obtained with acetone-PLIF. The turbulence structure of the flow is well captured. In particular, the instantaneous flow structures in the concentration field and temperature images are well correlated with each other.

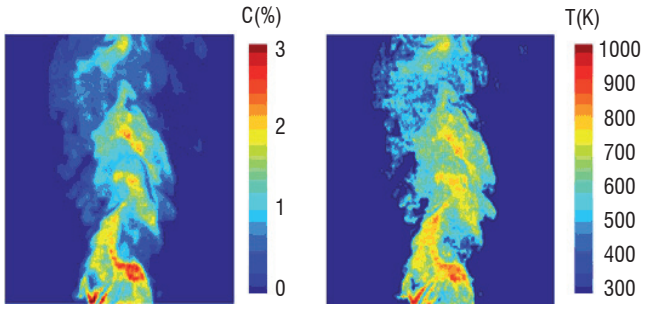

Figure 4 - Instantaneous acetone-PLIF images of acetone molar fraction and temperature in heated turbulent air jet seeded with acetone vapor. The size of the image is 50x50 mm^2

Thermocouple measurements are compared to mean temperatures obtained with 300 frame-averaged acetone-PLIF images and the results are plotted in Figure 5. The radial temperature profiles displayed for different locations downstream from the nozzle show good agreement. Though this flow is not reactive, these results allow for application of acetone-PLIF to reactive flows. In particular, the temperature/mole fraction PLIF described here would be ideal for imaging instantaneous structures in reacting mixing layers, where temperature significantly varies and acetone molar fraction changes because of pyrolysis and radical attack. It could also be useful to image spray flowfields in mixing and/or preheating regions [26].

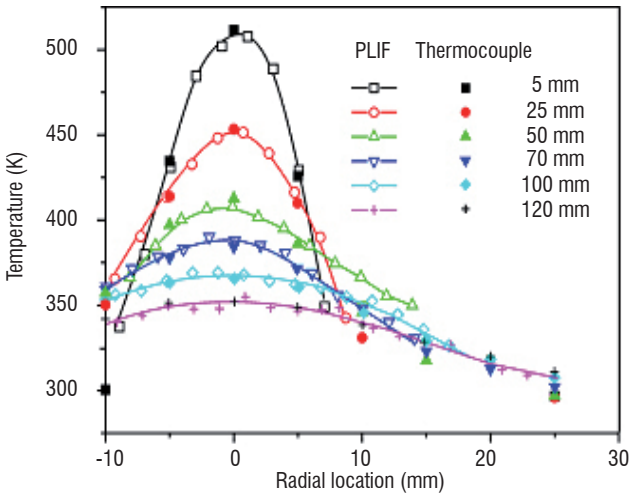

Figure 5 - Radial temperature profiles measured at six axial locations above the nozzle exit: comparison between frame-averaged acetone-PLIF temperature images (open symbols), and thermocouple data (solid symbols)

Subsonic and supersonic combustion

Species concentration measurements are required to study chemically-reacting systems such as flames. Radical number densities can be used to locate reaction zones, or to determine reaction rates. As mentioned before, the hydroxyl radical OH has received considerable attention in the past. For example, the instantaneous spatial distribution of OH is particularly attractive for analyzing the primary reaction zone of a flame. OH-PLIF images can be used to localize regions with high strain where the OH layer becomes thinner and the fluorescence signal is reduced. A useful application of OH-PLIF concerns the investigation of ethylene/air diffusion flames in the pressure range 0.1–0.5 MPa to study the formation of pollutants such as soot and NOx. The flame facility consists of a coflow ethylene/air jet with a concentric premixed ethylene/air pilot flame burner. An example of OH-PLIF images at 0.2 MPa is shown in Figure 6. The whole flame image (300 mm long) is reconstructed from six uncorrelated images (50x50 mm^2) recorded at different axial distances downstream from the injection location. Individual images are obtained using a single pulse with 4 mJ energy and 6 ns duration. The Nd:YAG-pumped dye laser is tuned to excite the Q1(5) line of OH radical at $\lambda = 282.75$ nm in the (1, 0) vibrational band of the $A^2\Pi^+ \leftarrow X^2\Sigma$ system to minimize the temperature dependence. The laser sheet is oriented vertically on the centerline and the size of the region imaged is 50x50x0.2 mm^3. The measurements are performed with jet velocities of 20 and 40 ms^{-1}, corresponding to a Reynolds number between 13000 and 26000. The results shown in Figure 6 provide information on the instantaneous distribution of OH in the central plane of the flame. In particular, it can be shown that the heat release due to the pilot flame stabilizes the shear layer, and the wake region acts as a flame holder providing a source of heat and radicals. Once stabilized, the reaction zone is a continuous filamentary structure where the filaments are often

connected by broader zones. Further downstream from the injector, the presence of broader diffusing OH zones is noticed. Although the OH molar fraction is not precisely known in the present case, the PLIF images can be calibrated by using a well-known reference flame where all parameters are calculated.

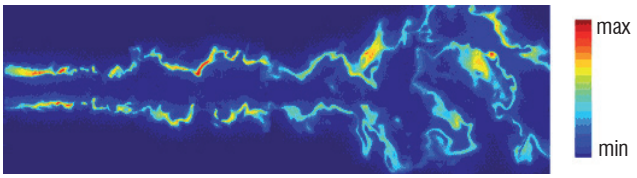

Figure 6 - PLIF images of the instantaneous OH distribution in an ethylene/air flame operating at 0.2 Mpa. The size of the image is 300x50 mm^2

An example of quantitative OH-PLIF is performed in a supersonic flame and results are displayed in Figure 7. The prime purpose is the experimental investigation of combustion in a turbulent reacting mixing layer where finite-rate chemistry effects take place. In the present case, the reactive mixing layer consists of a hydrogen flow at Mach 2 and ambient temperature injected through a cylindrical nozzle (diameter D = 6 mm), and a concentric preheated supersonic air stream at Mach 2 [26]. The probed section is constant over a length of 370 mm and then slightly diverges over 500 mm. The test facility is operated in a blow-down mode because most of its parts are used as a heat sink. Only the main nozzle and the hydrogen injector are water-cooled. The supersonic combustion runs are stabilized for 15 s. The experiments are performed at equivalence ratio (Φ), i.e. the ratio of the fuel-to-oxidizer ratio to the stochiometric fuel-to-oxidizer ratio, of about 0.29. The nominal stagnation air temperature (1800 K) is obtained by an auxiliary hydrogen burner, with oxygen replenishment in order to keep an oxygen molar fraction of 21 % at the inlet of the burner. In order to quantify the fluorescence signals, the raw images are corrected for the dark background and flat field non-uniform response of the camera and the energy and spatial distribution of the laser beam. LIF signals are temperature-dependent and, therefore, the absolute number density of OH needs to be calibrated in a laminar premixed hydrogen/air flame with an equivalence ratio of 0.9, where OH concentration, temperature and pressure are well-known. The reference profile is obtained by recording the fluorescence intensity as a function of the height above the porous burner. Measurements are performed under similar experimental conditions (optical beam path, pulse energy, distance laser/probe volume, ICCD gain, etc.) as for the supersonic combustion experiment. The absolute concentration is retrieved by rescaling the experimental and one-dimensional theoretical profile calculated using the CHEMKIN and PREMIX codes [27, 28]. This procedure gives a relative accuracy of about 10 %.

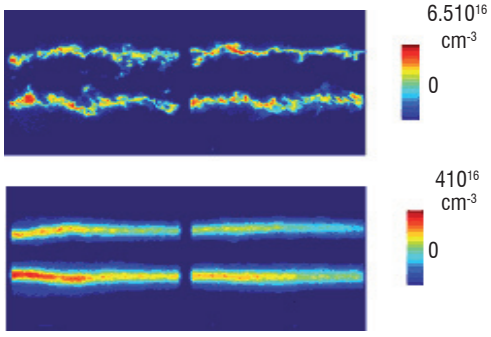

Figure 7 - Instantaneous (a) and averaged (b) PLIF images of OH concentration in a supersonic H_2/air flame at Mach 2. The size of the image is 100x50 mm^2

An example of instantaneous OH distribution recorded in the reactive mixing layer is shown in Figure 7a. The flow goes from left to right; the hydrogen core flow is surrounded by a coaxial air stream. The OH radical, and therefore the reaction zone, is confined in a narrow region along the shear layer on both sides of the hydrogen jet. As the flowfield develops downstream, the reaction zone widens up slightly. Small turbulence length scales of the combustion flow together with large coherent structures are clearly visible on the single-shot images. The structure of the instantaneous flame front consists of thin filaments tightened to the OH-concentrated pockets. The dimensions of these structures are on the order of the diameter of the injection nozzle. In Figure 7b, images averaged over 60 instantaneous frames show a small expansion of the reaction zone with axial distance. It mainly results from the unsteady nature of the flame. The average thickness of the flame is relatively constant and of the order of 6 mm, which is consistent with the size of the structures observed in the instantaneous images. The average reaction zone also presents a wavy shape with a typical spatial period of 50 mm, which can be explained by the presence of compression and expansion waves related to small discontinuities at the combustor walls. The average OH concentration decreases along the flow, confirming weak combustion efficiency related to poor mixing between hydrogen and air. Different fuel injection systems are also tested in order to evaluate their effect on the flame structure and location inside the combustion chamber. For instance, illustrations of the time evolution of the flame structure are displayed with axial fuel injection (movie-axial injection supersonic combustor) and wall fuel injection (movie-wall injection supersonic combustor). Note that the OH-PLIF images are recorded at a frequency rate of 4 Hz. Wall fuel injection exhibits better combustion efficiency due to improved mixing between fuel and air.

Plasma-assisted ignition and combustion

The control of ignition and combustion processes in aircraft jet engines is of significant importance for their performance and reliability. Reduction in ignition delay time, high altitude flame-holding, flame stability improvement and extension of blow-off limits are some of the key factors that are commonly controlled, with limited success, by systems based on conventional thermal ignition mechanisms (arc discharge, etc.). Alternative mechanisms can also trigger a better ignition on modifying the chemical reaction kinetics generated by large electron number densities. Better efficiency of population transfer within electronic and vibrational states can also be obtained using pulsed nanosecond discharges which handle weak reduced electric fields [29-31]. Relevant examples, in this regard, are the experimental studies focused on the influence of nanosecond pulse duration discharges on various phenomena such as reduction in ignition time [32], flame stabilization [33-34], ignition and flame holding [35-36]. However, the mechanisms of energy transfer between the plasma and the gas medium are still not fully understood. Experimental data characterizing the thermodynamic and kinetic processes governing this energy transfer are required for this. More specifically, the population distributions of neutral molecules and species composition are key scalar parameters which need to be used as input parameters for the simulation of these mechanisms. The analysis of the thermodynamic and kinetic mechanisms of fuel oxidation and ignition by a nanosecond pulsed discharge is presented here.

The probing of the pulsed discharge of a high voltage, nanosecond pulse duration, sustained in atmospheric premixed methane-air flows, was performed using laser diagnostics which allows for locally and temporally resolved measurements of temperature and species concentration. Among these diagnostics, coherent anti-Stokes Raman scattering (CARS), laser Thomson scattering (LTS) and planar laser-induced fluorescence (PLIF) were specifically developed and applied to characterize this discharge. CARS [56] was initially used to measure, within the plasma produced in various methane/air mixtures, the population distribution of N_2 in its electronic ground state [37]. Temporal evolution of the rovibrational populations was recorded by delaying the laser shots relative to the discharge pulse (from 10 ns to 1 ms). Experiments were carried out in premixed CH_4/Air flames to study the effect of the nanosecond discharge on ignition and stabilization of combustion at atmospheric pressure. These results were used to assess the feasibility of single-shot CARS measurements of temperature in order to highlight the thermodynamic and kinetic mechanisms of nanosecond discharges in hydrocarbon/air premixed mixtures. Results show that energy transfer induced by collisions of N_2 with the fuel or its decomposition products considerably increases the thermal heating of neutral molecules at temperatures up to 2500 K. The effect of the discharge on the local temperature then leads to the ignition of the CH_4/air mixture for equivalence ratios between 0.7 and 1.3. This work was completed by probing the conversion of the hydrocarbon fuel as well as the kinetic mechanism of recombination of radicals and atoms into neutral molecules such as H_2 and C_2H_2 in situations where no ignition occurs ($\Phi < 0.7$ and $\Phi > 1.3$). Laser Thomson scattering has been implemented to characterize the electric properties of the discharge such as electron density and electron temperature [38]. Results demonstrate that this nanosecond discharge can be classified in the range of weakly ionized plasmas with a reduced electric field of about 250, indicating a small production of ionized molecules. It is also known that nanosecond discharges can trigger a much more effective non-thermal ignition mechanism. This non-thermal ignition mechanism implies that specific plasma-generated active species - radicals, excited atoms and molecules, charged particles, and so on - stimulate the chain reactions of fuel oxidation leading to the ignition of the fuel-oxidizer mixture. In order to evaluate these effects, the temporal distributions of OH and CH within the discharge were measured using PLIF.

The laser system consists of a Nd:YAG laser (YG780, Quantel) combined with a dye laser (TDL 70, Quantel). For OH-PLIF measurements, Rhodamine 590 dye diluted in ethanol solvent is pumped by the Nd:YAG laser. The laser is tuned to the Q1(5) transition of the (1,0) band of the $A^2\Pi^+ - X^2\Sigma$ system of OH at 282.75 nm. Fluorescence from the A-X(1,0) and (0,0) bands is collected with an UV-Nikkor 105 mm/F=4.5 lens and imaged onto an intensified CCD camera (PIMAX, 1024x1024 pixels). Dichroic and WG295 optical glass filters are used to detect the fluorescence of the OH radical in the 306–312 nm spectral range and to reject plasma emission and incident light. For CH-PLIF measurements, the P1(10) transition of the $C^2\Sigma^+ - A^2\Pi(0,0)$ located at 317.30 nm is excited. This excitation wavelength is obtained using Rhodamine 610 diluted in ethanol solvent. Collection of fluorescence from the C-X(0,0) band located between 313 and 318 nm is obtained by using a dichroic filter centered at 313 nm and presenting a HWHM of 5 nm. For both measurements, the laser beam is shaped into a 150 μm vertical sheet with 3 mm height, corresponding to the distance between the two electrodes. Therefore, spatial resolution is limited to 20 μm x 20 μm x 150 μm. Optimization of the filtering of the fluorescence signals is performed with an image intensifier gate of 20 ns. As for the CARS measurements, the measurements are performed for various equivalence ratios surrounding the limits of ignition in order to well isolate the chemical mechanisms produced by the discharge from those induced by combustion.

Plasma-generated OH radicals were confirmed throughout the discharge volume between the electrodes. Figure 8 shows a typical instantaneous OH distribution recorded over a cross section in the middle of the streamer 20 μs after the high-voltage pulse. It is noted that OH production is quite homogeneous within the discharge. Observation of the OH spatial structures shows local disturbances close to the electrodes which probably arise from additional electrically-enhanced surface catalytic reactions and/or local joule heating of the electrode enhancing the heat release. This last effect is highlighted in the (movie-OHPLIF) presenting the time evolution of OH for delay times ranging from 0 to 300 μs.

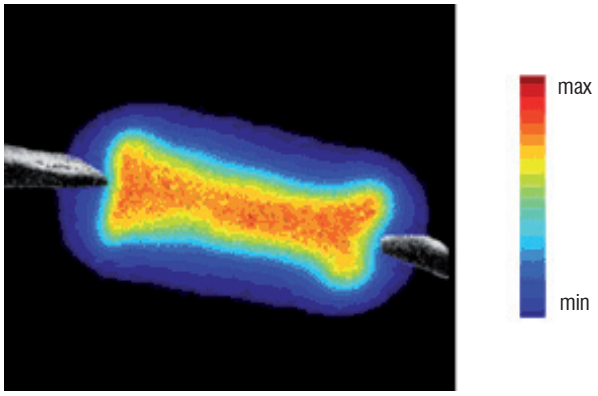

Figure 8 - Example of OH laser-induced fluorescence spatial distribution recorded between the electrodes 20 μs after the discharge

From the fluorescence images recorded at various times, the temporal evolution of OH fluorescence has been deduced for four equivalence ratios and the results are presented in Figure 9. First of all, OH production is observable at a time less than 10 ns in a very lean gas mixture (Φ=0.05). This species subsists at similar concentrations up to a time of 1 μs. After this time period, significant production of OH is observed with a peak located at 20-30 μs. Then, the OH fluorescence decreases and totally disappears after ~200-300 μs. In the lean-regime condition (i.e. equivalence ratio ranging from 0.5 to 0.65), a considerable increase of OH fluorescence is now observed when adding CH_4 into the gas mixture. The OH fluorescence continuously increases between 500 ns and 1μs, then OH distributions exhibit a flat profile over a period not exceeding 30 μs. The simultaneous presence of peaks of OH and temperature at a delay of 500 ns also represents favorable conditions of ignition of the gas mixture when increasing the equivalence ratio to 0.7 [37]. The relaxation of the OH population to the ground state is also noted. The maximum amount of OH is multiplied by a factor of 10-12, demonstrating the effectiveness of the plasma to produce large amounts of OH radicals compared with the case of Φ=0.05. For a rich CH_4/air mixture, fast production of OH is still observed up to a period of 20 ns. Then, OH fluorescence exhibits a flat profile over a period of 800 ns and finally decreases continuously to a time of ~20-30 μs. Comparison of these temporal distributions with temperature measurements recorded in the same conditions [37] also shows a strong correlation. In a very lean regime, the common increase of OH and rotational temperature arising from exothermic recombination reactions with transient species like O or H atoms, is observed. In the lean

regime ($0.5<\Phi<0.65$), similar correlations between temperature and production of OH radicals are also noted, indicating the existence of exothermic chemical fuel oxidation mechanisms triggered by plasma-generated radicals and leading to flow heating at temperatures up to 2500 K. Finally, the fast decrease of OH in the rich mixture is piloted by the efficient relaxation of energy into the plasma.

Figure 9 - Temporal Evolution of OH laser-induced fluorescence for various equivalence ratios

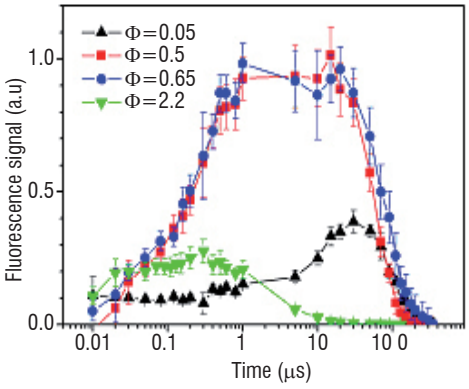

Preliminary experiments for CH detection using PLIF were also carried out in the same conditions as for OH. CH production is also observed within the discharge, indicating an efficient decomposition of the fuel by the plasma. For example, Figure 10 shows a typical instantaneous CH distribution recorded in a cross section in the middle of the discharge. This measurement was recorded 500 ns after the high-voltage pulse. Contrary to OH, the spatial distribution of CH fluorescence between the electrodes is not homogeneous. CH is observed along two thin regions located at the periphery of the plasma sheath. Analyzing the CH fluorescence images with the same method as for OH allows for measurement of the temporal behavior of the CH fluorescence.

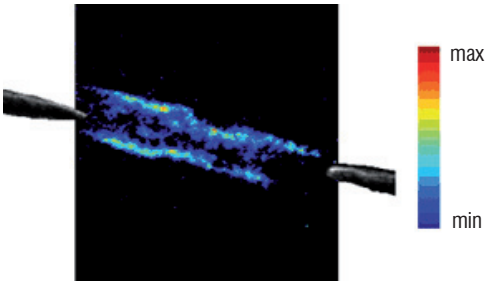

Figure 10 - Instantaneous CH laser-induced fluorescence distribution recorded between the electrodes 500 ns after the discharge

Figure 11 shows the temporal evolution for a rich CH_4/air mixture. After a large production of CH at a time less than 10 ns, the CH fluorescence signal decreases progressively until 100 ns. A flat profile with a small rising of CH at ~500-600 ns is then observed. CH radicals then continue to decrease before totally disappearing after ~10-20 μs. The temporal behavior of CH production, with a reduction of its total intensity, is found to be similar when using equivalence ratio close to the upper limit of ignition ($\Phi=1.3$). The amount of CH radical measured at very short durations yields a drastic enhancement of the initiation chemical mechanisms and subsequently the chain chemical reactions inside the gaseous flowfield. This effect, combined with the fast increase of temperature, exhibits a significant reduction in ignition time (~500 ns) and increases lean burn capability relative to conventional spark ignition [38]. For instance, the sequence of ignition and development of the flame downstream from the electrodes is displayed on the (movie-ignition OH) which presents the temporal evolution of the flame structure (represented by the OH* radical chemiluminescence) over a discharge cycle ($\Delta T=10$ ms) recorded in an atmospheric CH_4/air mixture with an equivalence ratio of 0.95. These results also confirm the numerical analysis of plasma simulation by Campbell and Egolfopoulos (2005) who investigated the kinetic paths to radical-induced ignition of CH_4/air mixtures [39]. In particular, the analysis of the kinetic mechanism evolution to the ignition by adding CH_3, CH_2, CH, and C (up to a few percent) demonstrates the key role of CH radicals, which rapidly oxidized to HCO, as the most effective in stimulating ignition through a chain mechanism.

Figure 11 - Temporal Evolution of CH laser-induced fluorescence for an equivalence ratio of 2.2

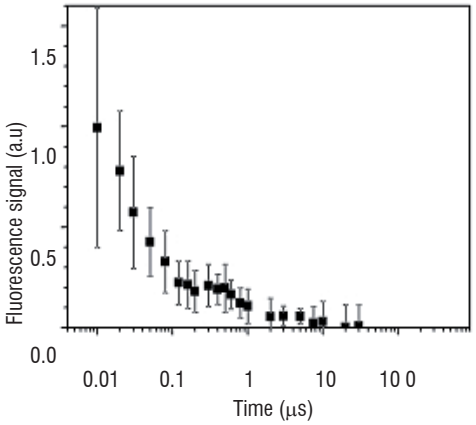

Multiphase chemistry and dynamics applications

Measurement in multiphase flows

By contrast with PLIF using ketone added to pure fuels for temperature and species concentration measurements in basic experiments, the probing of natural fluorescent tracers already present in commercial fuels will now be discussed. This concerns for example aeronautic fuel (kerosene or Jet A1) in which aromatics are naturally present in the species composition. From the pioneering work of Baranger et al. [23], it has been demonstrated that a kerosene vapor fluorescence spectrum excited with a 266 nm wavelength is composed of two fluorescence bands which vary differently with temperature, pressure and oxygen quenching. Identification of the fluorescent species has been performed and the two bands have been respectively attributed to the single-ring aromatics (1,2,4-trimethylbenzene) and the two-ring aromatics like naphthalene and its derivatives. Detection of fluorescence from aromatics with a single excitation wavelength over two specific spectral ranges can then provide dual-parameter imaging, yielding for example equivalence ratio in addition to temperature. Collection of mono-aromatic and di-aromatic fluorescence signals on two separate ICCD cameras with appropriate spectral filters may be one of the possibilities thanks to their different temperature and oxygen dependencies. Using experimentally-determined behavior of both fluorescence bands, along with a calibration point in a reference flow where thermodynamic parameters are well known, an iterative processing routine of both instantaneous fluorescence signals, combined with the closure relation for species composition is then used to determine the desired quantities. Note that this data reduction implies that the

ratio between mono-aromatics and di-aromatics remains constant during the experiments. This assumption remains valid for temperatures up to 1100-1300 K, where kerosene pyrolysis is observed.

Figure 12 - (a) Fluorescence raw image of the liquid and vapor phases of kerosene, (b) equivalence ratio at the outlet of a LPP injector (air inlet temperature: 580 K, overall equivalence ratio: 0.44, atmospheric pressure). The size of the image is 35x50 mm^2

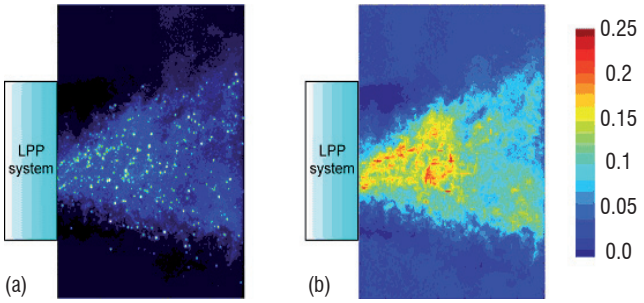

Figure 12a represents a typical single-shot image of fluorescence from kerosene droplets and vapor by kerosene-PLIF, recorded at the outlet of a lean premixed pre-vaporized (LPP) injector. This new type of injector is used in helicopter engines in order to improve the atomization and evaporation of liquid kerosene and to increase mixing between kerosene vapor and the surrounding air prior to combustion [40]. The idea underlying this concept is to burn a fuel/air mixture as lean as possible in order to reduce pollutant emissions. The goal of the experiment is to quantify the ability of the injector to provide a homogeneous fuel/air mixture with a low equivalence ratio. The experiments are carried out for evaporating conditions, without combustion. The picture size is 35x50 mm^2, the kerosene/air flow comes from the left hand side. Kerosene fuel is directly probed via the detection of aromatics, and therefore the current experiment does not require any added tracers. The bright dots, representing large intensities, correspond to droplets, while fuel vapor is displayed with a false blue-to-green color scale. Due to the difference of density between the liquid and vapor phases of kerosene, fluorescence signals are significantly larger for the liquid phase. As a result, there is a strong intensity gradient between a droplet and its surrounding vapor. Therefore, it is possible to take advantage of this feature to discriminate the liquid and gas phases and to identify the location of the droplets. Data processing using a calibration point in a reference flow allows us to obtain instantaneous two-dimensional maps of the equivalence ratio at the outlet of the injector, Figure 12b. As can be seen, the kerosene/air jet is fairly directional and exhibits some radial expansion with axial distance. In addition, kerosene vapor remains mainly located along the combustor centerline, which may be due to swirl effects which create a "shield" that prevents kerosene vapor from reaching a large radial location.

Combustion of isolated droplets

Spray vaporization and combustion are very complex topics which require an understanding of physical processes such as spray atomization and transport, turbulence and chemistry. Nonetheless, in an industrial-type burner, all these parameters interact with each other, which prevents determination of their separate influences. As a result, experiments are often carried out on idealized sprays in order to minimize the coupling between the different effects and to provide parametric results. The simplest geometry consists of studying the evaporation or combustion of suspended hydrocarbon droplets [41-44]. Another possibility is to consider porous spheres [45-46], which are particularly used for temperature measurements and determination of chemical species during droplet combustion. However, both of the aforementioned types of experiments make use of large droplets, of the order of few millimeters, which are not representative of real sprays. Streams or arrays of mono-dispersed droplets have also been frequently used in basic studies on sprays, for example to determine the influence of the spacing parameter on droplet combustion [47-49]. This simple geometry is particularly attractive because it generates a temporally and spatially repeatable stream of droplets with well-controlled injection frequency, droplet size and velocity and droplet spacing, which allows us to study the individual influence of each of these parameters on droplet vaporization. Physical models can be derived from such experiments and can be subsequently implemented in simulation codes in order to run more complex situations.

Figure 13 - Spatial distribution of OH radical laser-induced fluorescence around a burning droplet for different droplet combustion regimes: stationary envelope flame (a), envelope flame around a moving droplet (b-d), wake flame (e) and boundary-layer flame (f). Size of the image is 2x2 mm^2 [50]

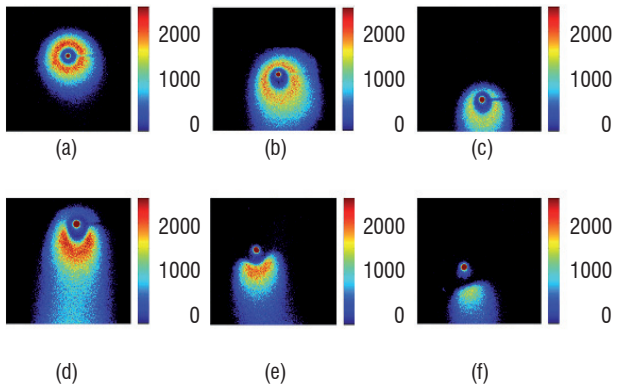

OH-PLIF imaging with high spatial resolution is used in a laminar diffusion counterflow burner fuelled with methane to provide information on isolated droplet combustion [50]. Measurements are performed on the oxidizer side at 10 mm above the flame front on the burner axis. The resulting images are presented with a false colorscale to display areas of fuel vapor phase and OH radical around droplets on the most suitable range. As a consequence, fluorescence signals from liquid acetone droplets, which are typically two orders of magnitude higher than the vapor one, appear to be uniform and at the maximum value of the colorscale. Figure 13 shows the OH distributions recorded with the magnification ratio of 1:1.2 and illustrates the effect of the droplet Reynolds number on isolated droplet combustion. Different burning regimes, from the configuration of the envelope flame to that of the boundary-layer flame, are obtained for droplet Reynolds numbers between 10 and 40. Typical envelope flames around the droplet are illustrated in Figures 13a-13c. In particular, the perfectly spherical shape of the flame around the droplet in Figure 13a indicates the combustion regime of a stagnant droplet. This regime is observed when the droplet, after its ignition through the flame front, reaches the top of its ballistic trajectory (i.e. when the droplet has an axial velocity equal to ≈0). By contrast, in Figures 13b and 13c, a stretching of the flame behind the droplet is observed, which suggests that fuel vapor is not distributed in a spherical manner around the droplet, hence that these droplets are moving. Comparison between Figures. 13b and 13c also shows that the OH concentration peak is first located ahead of the

droplet and then gradually switches to the region behind the droplet. This transition characterizes the evolution of the flame reaction rate around a burning droplet injected in an airflow with bulk direction opposed to droplet motion. A noticeable reduction of the flame front thickness ahead of the droplet is also observed, which suggests that fast cooling occurs on the top of the flame due to the counterflowing air stream. In Figure 13d, the flame is extinguished ahead of the droplet and in Figure 13e, the transition has occurred and the envelope flame is now replaced by a wake flame. Due to flame front extinction ahead of the droplet, the counterflowing air stream penetrates the recirculation zone behind the droplet and mixes with fuel vapor present in that region. An increase in OH intensity behind the droplet is also observed in Figures 13d and 13e, which suggests that the droplet burning rate may be enhanced by the change of combustion regime from envelope to wake flame. In Figures 13f, a boundary-layer flame replaces the wake flame and combustion only takes place in the droplet puff. In this situation, flame stability is strongly reduced and extinction occurs very easily. Compared with the previous wake flame, OH fluorescence intensity and flame thickness strongly decrease while the distance between droplet surface and the flame front increases by roughly 60 %. It is noteworthy that the current study presents good agreement with the numerical results from Jiang et al. [51] and Liu et al. [52] which were obtained with 100 and 200 μm n-octane droplets respectively. In particular, the occurrence of various droplet combustion regimes is clearly identified in the present experiments for droplet Reynolds number of the same order as that from Liu et al. [52]. Experimental evidence of the different combustion regimes has been reported in the literature for large droplets [46-47] or porous spheres [53] with diameters of several millimeters. However, to the best of our knowledge, this is the first time that the phenomena have been observed with OH-PLIF for droplets that are representative of real sprays.

The influence of droplet dynamics on the counterflow flame front also shows that the flame front can be strongly distorted by the droplet crossing. For instance, the different steps of the local extinction mechanism of the CH4/air flame by a droplet are presented in the (movie-droplet without flame). Note that the images of this sequence are not recorded in real-time because of the limited acquisition rate of the ICCD camera (3 Hz) compared to the duration of the event (few ms). This sequence is reconstructed by selecting OH images recorded from different series of measurements. The velocity of a droplet entering the flame front is estimated from Figure 13f which corresponds to the case where a boundary-layer flame is present behind the droplet. This physical process, considered as the limit case before the droplet extinguishes, occurs for a droplet velocity of about 2 m/s. Consequently, droplets crossing the flame front have velocities higher than this value. As seen in the movie, droplets with high velocity lead to local extinction of the flame front. By contrast, droplets with lower velocity can ignite within the flame front and burn on the oxidizer side (movie-droplet with flame).

Kerosene spray combustion in practical combustion systems

This application highlights the potential of PLIF to simultaneously measure several scalar quantities in practical combustors at high pressure. The goal of the present experiments is to combine kerosene-PLIF and OH-PLIF described previously in order to simultaneously measure the local equivalence ratio and flame front structure in a fired high-pressure combustor operating with Jet A1 fuel. The spatial and temporal correlation between fuel vapor distribution and flame structure are measured to evaluate the influence of fuel concentration on the local flame reaction rate. The techniques are successfully applied at pressures of up to 2.2 MPa [54].

The combustor used in the experiments is the so-called “M1 test bench”, which is the high temperature-high pressure combustion facility at Onera dedicated to the investigation of aircraft and helicopter injectors under real operating conditions. This bench can preheat air up to 900 K for flowrates up to 4 kg/s. Preheated air is injected into the combustor together with liquid kerosene via a new multipoint injector designed by the French company SAFRAN: a single pilot injector is located on the combustor axis and it is used to stabilise the flame whereas a multipoint main injector is located at a larger radial distance. The fuel flowrate is split between both injectors and the ratio between equivalence ratios from the pilot and the main injector (Φ_{pilot}/Φ_{main}) lies between 0.1 and 1, except for a condition where only the pilot injector is used. The combustor comprises a water-cooled visualization sector which is equipped with optical accesses for laser measurements. The outlet of the combustor is equipped with a sonic throttle which can be partly obstructed by a water-cooled needle in order to control the pressure inside the combustor. The air inlet temperature varies between 480 and 730 K and the pressure inside the combustor is in the range of 0.45–2.2 MPa.

Two laser systems are used to perform OH and kerosene vapor PLIF measurements simultaneously. Measurements for the OH radical are performed by exciting the Q1(5) line of the (1, 0) band of the OH ($X^2\Pi$ - $A^2\Sigma^+$) system. Measurements of kerosene fluorescence use a single-excitation scheme which comprises a frequency-quadrupled Nd:YAG laser generating 8 ns, 50 mJ pulses at 266 nm. The time delay between the two laser beams is set at 200 ns in order to avoid cross-talk between fluorescence signals from the OH radical and the kerosene. This duration is found to be much shorter than the typical flow timescales, ensuring that images of OH and kerosene fluorescence are representative of the same phenomenon at the time of recording. Both laser beams are transported via optical mirrors around the combustor facility and superimposed with a combination of dichroic mirrors. They are then transformed into two superimposed collimated sheets using a unique set of cylindrical and spherical lenses. The fluorescence from the OH radicals is recorded with a 16-bit ICCD camera while the fluorescence from the kerosene vapor and liquid phases is simultaneously recorded by two 16-bit ICCD cameras. The camera used for OH visualization has a CCD array of 1024x1024 pixels, a temporal gate of 40 ns, with a framing rate of 4 Hz and it is equipped with a 105 mm, f/4.5 UV-NIKKOR lens. The cameras used for kerosene detection have a CCD array of 512x512 pixels, a temporal gate of 40 ns, with a framing rate of 4 Hz, and each camera is equipped with an achromatic UV lens. For OH measurements, the camera has a combination of glass filters (WG 295 and UG 5) and an interferential filter centered at 310 nm. For kerosene measurements, the first camera is equipped with a combination of glass filters to collect the whole fluorescence from mono- and di-aromatics, whereas the second camera uses a combination of glass filters to collect fluorescence from di-aromatics only.

Figure 14 shows typical radial single-shot images of kerosene and OH fluorescence for the condition where the pilot and the main injectors are operated at 0.95 MPa with the same equivalence ratio. The laser sheet propagates across the combustor, perpendicular to the injection system. Images are corrected for distortion due to the angle of observation ($\sim 30°$) between the laser sheet and the ICCD cameras. It is noticed that the flame front exhibits a double structure:

one is close to the combustor axis and comes from the pilot injector, whereas the peripheral flame front can be attributed to the main injector. Comparison of Figures 14a and 14b shows that kerosene is located at a larger axial distance than the OH radical, which indicates that combustion occurs on the inner side of the cone delimiting the kerosene. Finally, the spatial distribution of both kerosene and the OH radical are axisymmetric, which confirms another result of the axial measurements. This suggests that such a multi-point injector can provide a fairly homogeneous distribution of kerosene in the combustor. Regions with large gradients of fuel concentration should therefore be limited, which may help to achieve stable combustion and low levels of pollutant emissions.

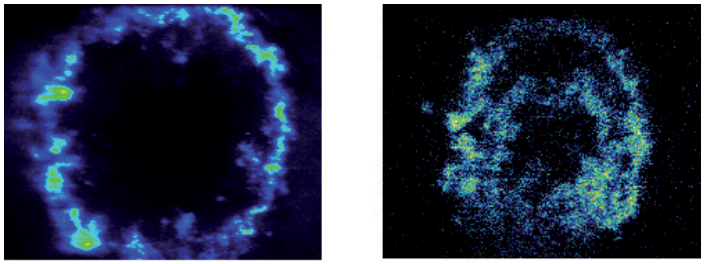

(a) (b)

Figure 14 - Radial instantaneous fluorescence images of (a) kerosene and (b) OH radical at the outlet of a multipoint injector (Air inlet temperature: 590 K, pressure: 0.95 MPa, $\Phi_{pilot}/\Phi_{main}=1$). The size of the image is 50x50 mm^2 [54]

Conclusion, future outlook

PLIF imaging diagnostic is a powerful tool for the understanding of fluid dynamics and combustion physics which can enhance the research and development process. There has been a remarkable increase in PLIF diagnostic capability over the last two decades, and the field continues to develop at a fast pace. Its capabilities go far beyond the mere observation of two-dimensional signal intensities. The development status of PLIF has now passed the threshold between qualitative and quantitative images. Nowadays, both in laboratory research and practical combustion, PLIF is well-suited to a wide variety of applications performed at high pressures and temperatures relevant to real engines and gas turbines.

In the near future, the availability of new laser sources operating at high frequency rates, detectors, and data processing schemes will allow for the acquisition of more accurate data, and measurements that could be more specifically tailored to the needs of the modeling community. One orientation, which is already underway in different research laboratories, will involve the development of 2D and 3D time-resolved planar imaging and simultaneous measurements of multiple scalars. The data collected will help to uncover yet undetected physical processes in turbulent combustion for which new models can be elaborated. For example, time-sequenced imaging of combustion instabilities in Internal Combustion (IC) engines, ultra-lean gas turbines, new aircraft injection systems and re-ignition at high altitude with laser and plasma igniters will provide significant insight into the immensely complex flows prevailing in these combustors. In a similar way, multi-scalar diagnostics will provide significant contributions to our understanding of turbulent combustion and, in particular, the effects of turbulent mixing on flame chemistry. Multi-scalar data, combined with velocity measurements, will constitute a quantitative database for testing advanced models of multiphase turbulent combustion. The scalars of interest include temperature, fuel molecules, key intermediate combustion species, pollutant precursors (PAH) and pollutants like aldehydes, NOx and CO. Successful implementation of PLIF is expected to provide high quality experimental data for traditional and emerging fuels (biofuels), which can be used as a benchmark for developing and validating the predictive capability of combustion models in engines and gas turbines ■

Acknowledgements

The authors are greatly indebted to their former co-workers A. Bresson, P. Baranger, B. Rossow, D. Messina and G.A. Grandin as well as the Direction Générale de l'Armement (DGA) and the French industrialist SAFRAN for financial support of many projects providing important input to combustion analysis by PLIF.

References

[1] R.K. HANSON - *Combustion Diagnostics: Planar Imaging Techniques.* Proc. Combust. Inst., (1986) 1677-1691.
[2] R MILES - *Flow-field Diagnostics, Applied Combustion Diagnostics.* Edited by Katharina Kohse-Höinghaus & Jay Jeffries, Taylor and Francis Publishers (2002).
[3] A.C ECKBRETH - *Laser Diagnostics for Combustion Temperature and Species.* 2nd edition, Gordon and Breach Publishers, Amsterdam (1996).
[4] A.H. EPSTEIN - *Quantitative Density Visualization in a Transonic Compressor Rotor.* J. Energ. Power 99 (1977) 460-475.
[5] G. KYCHAKOFF, R.D. HOWE, R.K. HANSON - *Quantitative Flow Visualization Technique for Measurements in Combustion Gases.* Appl. Opt. 23 (1982) 704-712.
[6] R.K. HANSON, J.M. SEITZMAN, P.H. PAUL - *Planar Laser Fluorescence Imaging of Combustion Gases.* Appl. Phys. B50 (1990) 441-454.
[7] K. KOHSE-HOÏNGHAUS - *Laser Techniques for the Quantitative Detection of Reactive Intermediates in Combustion Systems.* Prog. Energ. Combust. 20 (1994) 1-203.
[8] J.W. DAILY - *Laser Induced Fluorescence Spectroscopy in Flames.* Prog. Energy Combust. Sci. 23 (1997) 133-199.
[9] J.E. BROADWELL, P.E. DIMOTAKIS - *Implications of Recent Experimental Results for Modelling Reactions in Turbulent Flows.* AIAA Journal, 24 (1986) 885-889.
[10] A. YARIV - *Quantum Electronics.* Wiley, New York (1975).
[11] W. DEMTRÖDER - *Laser Spectroscopy.* Springer, Berlin Heidelberg, (1982).
[12] E.H. PIEPMEIER - Spectros. Chimi. Acta 27b (1972) 431-443.

[13] N.M. LAURENDEAU - Prog. Energy Combust. Sci. 14 (1988) 147-170.
[14] B.K. MCMILLIN, J.L. PALMER, R.K. HANSON - *Temporally Resolved, Two-line Fluorescence Imaging of NO Temperature in a Transverse Jet in a Supersonic Crossflow.* Appl. Opt. 32 (1993) 7532-7545.
[15] K.A. WATSON, K.M. LYONS, J.M. DONBAR, C.D. CARTER - *Scalar and Velocity Field Measurements in a Lifted CH4-air Diffusion Flame.* Comb Flame, 117 (1999) 257-271.
[16] H.B. NAJM, P.H. PAUL, C.J. MUELLER, P.S. WYCKOFF - *On the Adequacy of Certain Experimental Observables as Measurements of Flame Burning Rate.* Comb. Flame, 113 (1998) 312-332.
[17] P.H. PAUL, H.B. NAJM - *Planar Laser Induced Fluorescence Imaging of Flame Heat Release Rate.* Proc. Comb. Inst. (1998) 43-50.
[18] C. SCHULZ, V. SICK, *Tracer LIF Diagnostics: Quantitative Measurements of Fuel Concentration, Temperature and Fuel/air Ratio in Practical Combustion Systems.* Prog. Energy Combust. Sci. 31 (2005) 75-121.
[19] H. NEIJ - *Development and Demonstration of 2D-LIF for Studies in SI Engines.* Comb. Flame 99 (1994) 449-457.
[20] D. WOLFF, H. SCHLÜTER, V. BEUSHAUSEN, P. ANDRESEN - *Quantitative Determination of Fuel Air Mixture Distributions in an Internal Combustion Engine using PLIF of Acetone Ber. Buns.* Phys. Chem. 97 (1993) 1738-1741.
[21] F. GRISCH, M.C. THURBER, R.K. HANSON - *Mesure de température par fluorescence induite par laser sur la molécule d'acétone.* Revue Scientifique et Technique de la Défense, 4 (1997) 51-60.
[22] M.C. THURBER, F. GRISCH, R.K. HANSON - *Temperature Imaging with Single and Dual-Wavelength Acetone Planar Laser-Induced Fluorescence.* Opt. Lett. 22 (1997) 251-253.
[23] P. BARANGER, M. ORAIN, F. GRISCH - *Fluorescence Spectroscopy of Kerosene Vapor: Application to Gas Turbines.* AIAA Paper 2005-828, 43rd AIAA Aerospace Sciences Meeting and Exhibit, Reno, Nevada, (2005).
[24] J. GUIDEZ, C. DUMAND, T. COURVOISIER, M. ORAIN - *Specific Problems of Micro Gas Turbine for Micro Drones Application.* ISABE Paper 2005-1273, ISABE Conference, Munich (2005).
[25] M.C. THURBER, F. GRISCH, B. J. KIRBY, M. VOTSMEIER, R.K. HANSON - *Measurements and Modeling of Acetone Laser Induced Fluorescence with Implications for Temperature-imaging Diagnostics".* Appl. Optics, 37 (1998) 4693-4978.
[26] A. BRESSON, P. BOUCHARDY, P. MAGRE, F. GRISCH - *OH/acetone PLIF and CARS Thermometry in a Supersonic Reactive Layer.* AIAA paper 2001-1759, 10th AIAA/NAL/NASDA/ISAS International Space planes and hypersonic Systems and technologies conference, Kyoto, Japan, 2001.
[27] R.J. KEE, F.M. RUPLEY, J.A. MILLER - Sandia National Lab. Rep. SAND89-8009, 1989.
[28] R.J. KEE, J.F. GREAR, M.D. SMOOKE, J.A. MILLER - Sandia National Lab. Rep. SAND85-8240, 1985.
[29] A. BOGAERTS, E. NEYTS, R. GIJBELS, J. VAN DER MEULEN - *Gas Discharge Plasmas and their Applications.* Spectrochemica Acta Part B 57 (2002) 609-658.
[30] C. H. KRUGER, C. LAUX, L. YU, D. PACKAN, L. PIERROT - *Nonequilibrium Discharges in Air and Nitrogen Plasmas at Atmospheric Pressure.* Pure Appl. Chem. 74 (2002) 337-347.
[31] S.M. STARIKOVSKAYA, J. PHYS - D: Appl. Phys. 39 (2006) 265-299.
[32] A.M. STARIK, N.S. TITOVA, L.V. BEZGIN, V.I. KOPCHENOV - *Initiation of Diffusion Combustion in a Supersonic Flow of H2-air Mixture by Electrical-Discharge-Excited Oxygen Molecules.* J. Phys. D: Appl. Phys. 41 (2008) 125210 (12pp).
[33] E.I. MINTOUSSOV, S.V. PANCHESHNYI, A.YU. STARIKOVSKII - AIAA Paper 2004-1013, 42nd AIAA Aerospace Sciences Meeting and Exhibit, Reno, NV, January 2004.
[34] W. KIM, H. DO, M.G. MUNGAL, M.A. CAPPELLI - Proc. Combust. Inst..(2007) 3319-3326.
[35] S. PANCHESHNYI, D.A. LACOSTE, A. BOURDON, C. LAUX - AIAA Paper 2006-3769, 37th AIAA Plasmadynamics and Lasers Conference, San Francisco, CA, June 2006.
[36] G. LOU, A. BAO, M. NISHIHARA - Proc. Combust. Inst. (2007) 3327-3334.
[37] D. MESSINA, B. ATTAL-TRÉTOUT, F. GRISCH - *Analysis of a Non-Equilibrium Pulsed Nanosecond Discharge at Atmospheric Pressure using Coherent anti-Stokes Raman Scattering.* Proc. Combust. Inst. (2007) 825-832.
[38] D. MESSINA, G.A. GRANDIN, B. ATTAL-TRÉTOUT, F. GRISCH - *Laser-Based Measurements of Gas-Phase Chemistry in Non-Equilibrium Pulsed Nanosecond Discharges.* 2nd Colloque INCA, CORIA, Rouen (France), 2008.
[39] C.S. CAMPBELL, F.N. EGOLFOPOULOS - *Kinetics Paths to Radical-induced Ignition of Methane/air Mixtures.* Combustion Science and Technology, 177 (2005) 2275-2298.
[40] M. ORAIN, F. GRISCH - *Equivalence Ratio Measurements in Kerosene-Fuelled Combustors Using Planar Laser-Induced Fluorescence: Comparison between LP and LPP Injectors.* Paper 136, 2nd European Conference for Aero-Space Science (EUCASS), Brussels (Belgium), July 2007.
[41] G.A.E. GODSAVE - *Burning of Fuel Droplets.* 4th Int. Symp. on Comb. (1952) 818-830.
[42] S. OKAJIMA, S. KUMAGAI - *Further Investigations of Combustion of Free Droplets in a Freely Chamber Including Moving Droplets.* Proc. Combust. Inst. (1976) 401-407.
[43] J.J. WHANG, C.Y. YUKAO, J.T. HO, S.C. WONG - *Experimental Study of the Ignition of Single Droplets under Forced Convection.* Comb. and Flame, 110 (1997) 366-376.
[44] T. SUEKANE, K. YASUTOMI, S. HIRAI - *Experimental Observation of Effects of Convection on Flame Shape and Extinction on N-Heptane Single Droplets.* Comb. and Flame, 126 (2001) 1599-1601.
[45] D.B. SPALDING - *The Combustion of Liquid Fuels.* Proc. Combust. Inst. (1952) 847-864.
[46] S. R. GOLLAHALLI, T.A. BRZUSTOWSKI - *Experimental Studies on the Flame Structure in the Wake of a Burning Droplet.* Proc. Combust. Inst. (1974) 1333-1344.
[47] J.P. GORE, W.H. MENG, J.H. JANG - *Droplet Flames in Reactive Environments.* Comb. and Flame, 82 (1990) 126-141.
[48] J.J. SANGIOVANNI, M. LABOWSKY - *Burning Times of Linear Fuel Droplets Arrays: A Comparison of Experiment and Theory.* Comb. and Flame, 47, (1982) 15-30.
[49] M. ORAIN, X. MERCIER, F. GRISCH - *PLIF Imaging of Fuel Vapor Distribution around a Monodispersed Stream of Acetone Droplets, Comparison with Modelling.* Combustion Science and Technology, 177 (2005)1-30.
[50] X. MERCIER, M. ORAIN, F. GRISCH - *Investigation of Droplet Combustion in Strained Counterflow Diffusion Flames using Planar Laser-Induced Fluorescence.*

Applied Physics B, 88, (2007) 151-160.
[51] T.L. JIANG, W.H. CHEN, M.J. TSAI, H.H. CHIU - *A Numerical Investigation of Multiple Flame Configurations in Convective Droplet Gasification Flame, Comb. and Flame, 103 (1995) 221-238.*
[52] C.C. LIU, W.H. CHEN, T.L. JIANG - *Model of Unsteady N-Octane Droplet Burning in High-Temperature Streams, Combust.* Sci. and Tech. 176 (2004) 183-213.
[53] V. RAGHAVAN, V. BABU, T. SUNDARARAJAN, R. NATARAJAN - *Flame Shapes and Burning Rates of Spherical Fuel Particles in a Mixed Convective Environment.* Int. J. Heat Mass Transf. 48 (2005) 5354-5370.
[54] F. GRISCH, M. ORAIN, B. ROSSOW, E. JOURDANNEAU, C. GUIN - *Simultaneous Equivalence Ratio and Flame Structure Measurements in Multipoint Injector Using PLIF.* AIAA Paper 2008-4868, 44th AIAA/ASME/SAE/ASEE Joint Propulsion Conference & Exhibit, Hartford, CT (USA), July 2008.
[55] F. DUPOIRIEUX - *Optical Diagnotics Used at Onera to Characterize Turbulent Reactive Flows and to Validate Aero and Rocket Engine Combustor Modeling*. AerospaceLab N°1, October 2009.
[56] B. ATTAL-TRETOUT - *Laser Spectroscopy for in situ Diagnostics.* AerospaceLab N°1, October 2009.

Acronyms
PLIF (Planar Laser-Induced Fluorescence)
LIF (Laser-Induced Fluorescence)
CCD (Charged-Coupled Device)
ICCD (Intensified Charged-Coupled Device)
RANS (Reynold Average Navier Stokes)
LES (Large Eddy Simulation)
CARS (Coherent Anti-Stokes Raman Scattering)
LTS (Laser Thomson Scattering)
LPP (Lean Premixed Pre-vaporized)

AUTHORS

Frédéric GRISCH, Masters degree in fluid mechanics in 1982, PhD in Energetics in 1988 and HDR in 2008 from the University of Rouen (France). Senior scientist at Onera in charge of the development and application of laser diagnostics (CARS, PLIF, Raman scattering, Rayleigh scattering, Thomson scattering, etc.) for gaseous, liquid and solid propellant combustion, plasmas and nonreactive flow fields. Head of an Onera/CNRS research project on optical techniques for the investigation of multicomponent spray evaporation.

Mikael ORAIN, Masters degree in fluid mechanics in 1996, PhD in Mechanical Engineering in 2001 at Imperial College London (UK). Research scientist at Onera in charge of developing PLIF for the measurement of temperature and species concentration in reacting and non-reacting two-phase flows.

B. Attal-Trétout
F. Grisch
D. Packan
I. Ribet-Mohamed
M. Lefebvre
(Onera)

E-mail: brigitte.attal-tretout@onera.fr

Laser Spectroscopy for in Situ Diagnostics

Laser spectroscopy based on nonlinear processes such as four wave mixing and laser-induced gratings or based on spontaneous Raman and Thomson scattering is widely used, from near IR to near UV, to probe reactive media. The bulk of this monograph is devoted to the application of these techniques to the specific area of plasma, combustion and hypersonic flow field. For each technique a brief description of the signal amplitude is given from which spectral and/or temporal evolution can be predicted as a function of temperature and pressure. Experimentally, the dependence of the signal on parameters such as temperature, pressure, gas composition, or the energy of pump and probe laser pulses have been investigated. Comparison of the experimental results with theoretical predictions allows us to accurately measure these parameters in situ. Therefore, temperature, velocity or number density of important species (major or minor) can be derived from the spectral or temporal content. The synchronization of pulsed laser with particular physical phenomena provides time evolution of the sample over a μs or ms duration, depending on the probed events, thanks to the time resolution (ns) of the lasers. Several examples are given. CARS is applied to a buoyant H_2/air flame, a monodisperse droplet stream in combustion and a pulsed plasma in a methane/air flow. In each case, time and space evolution of temperature is recorded. DFWM has proved particularly useful for probing NO, especially when spectral interference is overwhelming the LIF signal; LIF is used otherwise. Laser induced gratings are also valuable tools in some typical cases. Examples are given to illustrate their potential in measuring NO_2 molecules in a flame and in measuring the temperature and velocity of a high speed flow. Finally, electron density can be inferred using Thomson scattering and an application in the pulsed plasma is presented.

Introduction

Over the past decades a great deal of researches were devoted to the development of diagnostic methods for environments that are particularly difficult to analyze, like turbulent flames, hypersonic flows or plasmas. Indeed, only non invasive techniques that are able to measure simultaneously temperature, density and velocity are suitable to fully characterise combustion reactive flows or non-equilibrium flows. At Onera, non-equilibrium flows are produced in high enthalpy wind tunnels. We have dedicated the paper to typical cases such as the processes of energy transfer between a plasma and gas medium, between flame and vortices and also inside two-phase combustion. They yet represent a key issue to improve the understanding of the main mechanisms taking place in a discharge-flame or flame-vortex or flame-droplet interaction. The main objective of the present work is to investigate the thermodynamics and kinetic properties of these reactive media through optical diagnostics, on a fundamental basis as well as for application to practical systems [26].
In this context, experimental values of the population distributions of neutral molecules are important quantities which can be used as input parameters for the simulation of these interactions. Due to the specifications of the pulsed events such as limited spatial dimensions and short duration, only laser-based methods have the potential to provide information without disturbing the media. The development of pulsed laser of large power initiated the research in diagnostic techniques which are today always providing more data in shorter duration and on larger scale. The more elaborate are the technology of lasers and detectors and the more efficient are the measurements. Laser techniques have high spatial and temporal resolution, enabling locally and temporally resolved measurements of temperature and species concentration. Among the various diagnostics techniques, non linear techniques provide stronger and collimated signals allowing highly luminous media at high temperature and pressure to be studied in situ [1,2]. Among other, coherent anti-Stokes Raman scattering (CARS) was developed at Onera and extensively used for temperature measurements in hostile reactive environments presenting interest in the aeronautic field. The basic principle of temperature measurements by CARS is to probe relative population of the molecular levels from

which the thermodynamic temperature of the molecular system is drawn. Then, a peculiar objective of our work was to combine techniques to retrieve more data simultaneously.

First, we discuss the principle of the CARS and DFWM laser techniques and give some examples of measurements targeting the temporal sampling of repetitive events. The thermal gratings are then presented; they are applied to the probing of NO_2 in ambient air and flames. In that section, electrostrictive gratings are also combined with CARS to obtain the speed of the flow and the temperature respectively, in a wind tunnel. Thomson scattering, applied to a pulsed plasma investigation is presented in Box 1.

Laser-based techniques

Four wave mixing processes: CARS, DFWM

Third order processes are the strongest non linear processes in centrosymetric media and form the basis for Doppler free polarization spectroscopy, Doppler free two photon absorption, Stimulated Raman gain spectroscopy (SRS), inverse Raman scattering (IRS), Coherent stokes Raman scattering (CSRS), Degenerate four wave mixing (DFWM) and Coherent anti-Stokes Raman Scattering (CARS). CARS, which was first observed by Maker and Terhune [3] is but one of many well-known third order processes. CARS offers many advantages over conventional Raman techniques since very intense signals can be detected in most of the major species. These advantages are inherent to its coherent nature, leading to collimated emission and efficient detection of the anti-Stokes signal. It has been used successfully for single point, single shot temperature measurement in a variety of combustion, low pressures gases, discharges and plasmas. The "resonance enhanced" CARS technique (RECARS) applies more particularly to the probing of trace species and a degenerate version of the four wave mixing process called DFWM [4] offer a simpler alternative to RECARS offering similar detectivity [5,6]. In the resonant process, the incident laser frequencies are tuned to reach one photon transitions of the molecules.

Model description

CARS takes place in media with a Raman active vibrational modes (ω_v). It is observed when two collinear beams of frequencies ω_1 (laser) and ω_2 (Stokes) such that $\omega_1 - \omega_2 = \omega_v$ are passed through the sample (Figure 1). A new wave is generated at the anti-stokes frequency $\omega_3 = 2\omega_1 - \omega_2$ in the forward direction and collinear with the exciting beams (Figure 2a). The new wave is often described as resulting from the inelastic scattering of the wave "ω_1" by the molecular vibrations (coherently driven by the incident waves at ω_1 and ω_2). We note that the same mechanism creates, in the degenerate case (DFWM), a similar wave at $\omega = \omega_4 = \omega_1 = \omega_2 = \omega_3$ (Figure 2b). If the incident beams have different polarizations, these states of polarization are changed by the interaction and this property is also used to improve the nonlinear background rejection in CARS and to improve the laser light rejection in DFWM [7, 8] (Figure 2c). CARS spectroscopy is performed with a fixed ω_1 frequency and by tuning the frequency ω_2 in order to scan the Raman resonance. Broadband multiplex CARS is an interesting excitation scheme using a broad width Stokes (60 to 80 cm^{-1}) from which temperature can be measured instantaneously, since the whole anti-Stokes spectra is recorded in a single shot on a ICCD camera (Figure 1 b).

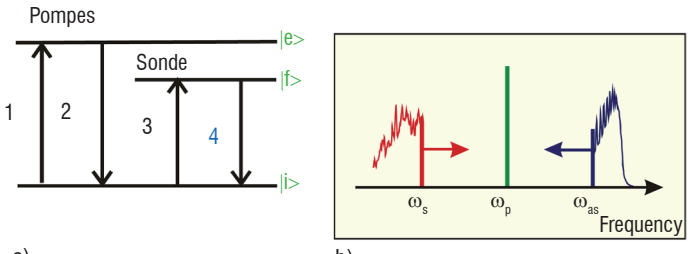

a) b)

Figure 1 - (a): Energy level scheme of a four wave mixing process; 1,2,3,and 4 are the four steps of the process; (b): excitation scheme of the multiplex CARS; ω_p, ω_s and ω_{as} are the frequencies of the laser, Stokes and anti-Stokes beams. $\omega_1 = \omega_3 = \omega_p$; $\omega_s = \omega_2$; $\omega_4 = \omega_{as}$

The intensity variation of the new wave created at ω_3 (or ω) is driven by the induced third order non linear polarization ω (ω_3). The spectral features are representative of the squared modulus of the third order non linear susceptibility ω_3 (ω_3) according to the following formulae:

$$P(\omega_3) = 4\omega_3^4 / c^4 \left| X^{(3)}(-\omega_3, \omega_1, \omega_1, -\omega_2) \right|^2 P_1^2 P_2 \text{ in CARS,}$$

$$P(\omega) = 4\omega^4 / c^4 \left| X^{(3)}(-\omega, \omega, \omega, -\omega) \right|^2 P^3 \text{ in DFWM,}$$

where P_1 (P) and P_2 are the power of the incident beam at ω_1 (ω) and ω_2 respectively.

This expression is valid assuming that the signal is generated using focused laser beams, in a small cylindrical volume around the focus of the beams. Its length is equal to the confocal parameter 1 of the

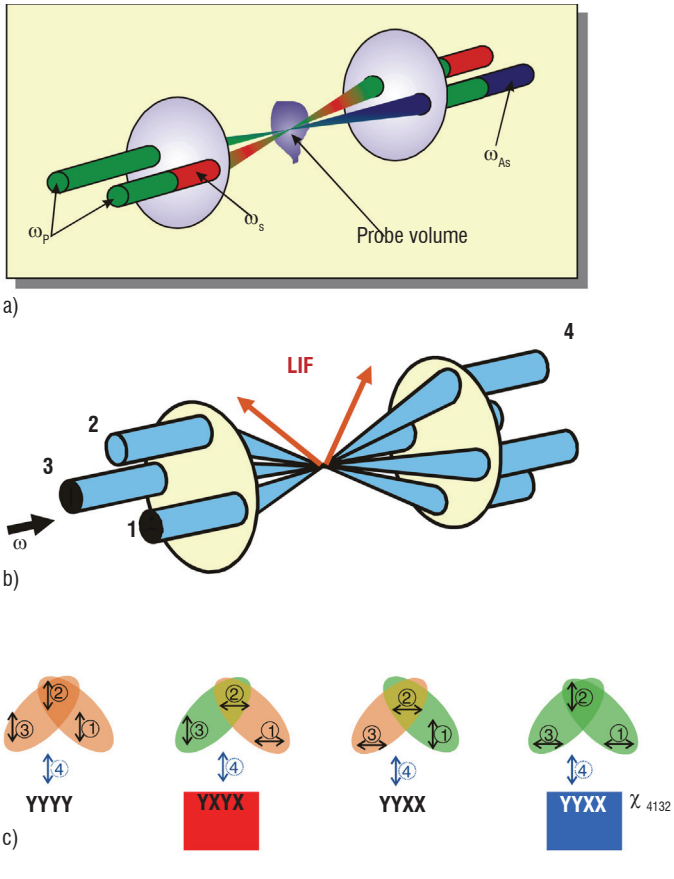

Figure 2: (a): BOXCARS geometry of the CARS excitation; (b): folded BOX-CARS geometry applied to DFWM; (c): polarisation arrangement used in four wave mixing processes with the corresponding susceptibility χ_{4132}; laser induced fluorescence (LIF) signal, which is incoherent, is emitted in 4π steradian.

beams with $1 = \pi\Phi^2 / 2\lambda$ and for Gaussian beam the waist at the focus is $\Phi = 4\lambda f / \pi d$ where f is the focal length of the lens and d the incident laser beam diameter in the plane of the lens.

At triple resonance, a strong increase of the nonlinear susceptibility is observed relatively to the non resonant background which greatly improves the contrast of the lines since all transitions become resonant together (see equation (1)). Thanks to that property, resonance CARS (RECARS) and DFWM were successfully applied to most of the radicals of interest in physical chemistry using tunable dye lasers. Detectivity threshold can reach 10^{11} cm^{-3} at one bar total pressure on resonance [5,9] whereas conventional CARS is usually detected on major species (typically $>10^{16}$ cm^{-3}) [2].
Using density matrix formalism, the resonant susceptibility of CARS is derived using a perturbative treatment of the field interaction which gives [9]:

$$e_4 X^{(3)}\left(-\omega_3,\omega_1,\omega_1,-\omega_2\right)e_1 e_3 e_2 = N/\hbar^3 \sum_{a,b,n,n'} \mu_{an'}^{(4)} \mu_{n'b}^{(3)} \mu_{bn}^{(2)} \mu_{na}^{(1)}$$
$$\int \left(A_1 - B_1 + B_2 - B_3\right) F\left(v_z\right) dv_z \qquad (1)$$

with :

$$A_1 = \rho_{aa}^{(0)}\left[\left(\omega_{na} - \omega_1 + k_1.v_z - i\Gamma_{na}\right)\times \left(\omega_{ba} - \omega_1 + \omega_2 + \left(k_1 - k_2\right)v_z - i\Gamma_{ba}\right)\times \left(\omega_{n'a} - \omega_4 + k_4.v_z - i\Gamma_{n'a}\right)\right]^{-1}$$

$$B_1 = \rho_{bb}^{(0)}\left[\left(\omega_{nb} - \omega_2 + k_2.v_z + i\Gamma_{nb}\right)\times \left(\omega_{ba} - \omega_1 + \omega_2 + \left(k_1 - k_2\right)v_z - i\Gamma_{ba}\right)\times \left(\omega_{n'a} - \omega_4 + k_4.v_z - i\Gamma_{n'a}\right)\right]^{-1}$$

$$B_2 = \rho_{bb}^{(0)}\left[\left(\omega_{n'b} - \omega_3 + k_3.v_z - i\Gamma_{n'b}\right)\times \left(\omega_{n'n} - \omega_3 + \omega_2 + \left(k_3 - k_2\right)v_z - i\Gamma_{n'n}\right)\times \left(\omega_{n'a} - \omega_4 + k_4.v_z - i\Gamma_{n'a}\right)\right]^{-1}$$

$$B_3 = \rho_{bb}^{(0)}\left[\left(\omega_{nb} - \omega_2 + k_2.v_z + i\Gamma_{nb}\right)\times \left(\omega_{n'n} - \omega_3 + \omega_2 + \left(k_3 - k_2\right)v_z - i\Gamma_{n'n}\right)\times \left(\omega_{n'a} - \omega_4 + k_4.v_z - i\Gamma_{n'a}\right)\right]^{-1}$$

where $\mu_{\alpha\beta}^{(i)} = -\mu_{\alpha\beta}.e_i$ and $\alpha\beta = a,b,n,n'$; $N\rho_{\alpha\alpha}^{(0)}$ is the population of the molecular level $|\alpha>$ and N is the total number density.
One has in forward DFWM [4,6,7]:

$$X^{(3)}\left(-\omega,\omega,\omega,-\omega\right) = N B_{an}^2\left[\rho_{aa}^{(0)} - \rho_{nn}^{(0)}\left(2J_a + 1/2J_n + 1\right)\right]$$
$$L\left(\omega\right)G_F^T\left(e_4,e_1,e_3,e_2,J_a,J_n,\omega\right) \qquad (2)$$

with $L(\omega) = L_{12}^a\left(\omega\right) + L_{32}^a\left(\omega\right) + L_{12}^n\left(\omega\right) + L_{32}^n\left(\omega\right)$ where $L_{j2}^{\alpha}(\omega)$ is a complex line shape function defined by :

$$L_{j2}^{\alpha}(\omega) = \int\left[\left(\omega_{na} - \omega + k_j.v_z - i\Gamma_{na}\right)^{-1} - \left(\omega_{na} - \omega + k_2.v_z + i\Gamma_{na}\right)^{-1}\right]\times \left(\omega_{na} - \omega + k_4.v_z - i\Gamma_{na}\right)^{-1} F(v_z)\,dv_z \Big/ \left[\left(k_j - k_2\right)v_z - i\Gamma_{\alpha}\right]$$

and $(j = 1,3)$.
Also one has:

$$G_F^T\left(e_4,e_1,e_3,e_2,J_a,J_n,\omega\right) = W_{13}(\omega)\,G_F\left(e_4,e_1,e_3,e_2,J_a,J_n\right) + W_{31}(\omega)\,G_F\left(e_4,e_3,e_1,e_2,J_a,J_n\right)$$

$G_F\left(e_4,e_3,e_1,e_2,J_a,J_n\right)$ are the geometrical factors that depends solely on the polarisation unit vectors e_i and on the total angular momentum quantum numbers J_a and J_n [7,8]. W are weighting factors defined by

$$W_{13}(\omega) = \left[L_{12}^a(\omega) + L_{32}^n(\omega)\right] / L(\omega)$$
$$W_{31}(\omega) = \left[L_{32}^a(\omega) + L_{12}^n(\omega)\right] / L(\omega)$$

The strength of the electronic transition moment $\mu_{\alpha\beta}$ of the resonant step (or the Einstein coefficient $B_{\alpha\beta}$) is driving the electronic enhancement and the final intensity of the signal in RECARS and DFWM. As a matter of fact, much larger signals are observed in atomic species such as Iron or Cesium than in radicals such as OH or CH and signals are even smaller in tri atomic such as NH_2. Moreover, a precise set of spectroscopic data must be available to correctly interpret the CARS and DFWM spectral content [4,9]. Finally, to measure a concentration, signal dependence versus spectroscopic parameters and temperature must be known in order to retrieve the number density N from the signal amplitude. Optical diagnostics accurately provides relative concentration but absolute values are only measured through calibration of the signal at normal temperature and pressure.

Temporal resolution

CARS was also developed with femtosecond pulses to study reaction dynamics and to take advantage from the good stability of the laser power and the high repetition rates of these lasers [10]. However, spectroscopy of gases is straightforward and was first applied using spectral resolution in the 0,1 to 1 cm^{-1} range easily achieved with nanosecond laser sources. A disadvantage of the femtosecond regime in gases is the rise of the peak power density which produces much stronger saturation effects [8]. In nonlinear processes, the detectivity limit of diagnostic techniques is usually limited by these effects when laser power is increased in order to reach optimum sensitivity. The stationary regime is also changed since the stationary approximation is not valid anymore when the state lifetime becomes larger than the laser duration. Transient solutions of the system evolution have to be calculated.
At Onera, much of the effort was dedicated to the probing of atoms and molecules using nanosecond laser sources, some of which are presented in the following. The sampling of the reactive media using nanosecond pulses allow us to investigate the space and time evolution of temperature and concentrations during periodic events such as vortex flames or plasma generated by a periodic discharge. These experiments are presented in section 2-1-4. The sequence of event displayed in figure 3 is used thanks to a simple synchronization of the laser with the flame (or plasma) period and with the gate of the detector (ICCD camera or PM tube).

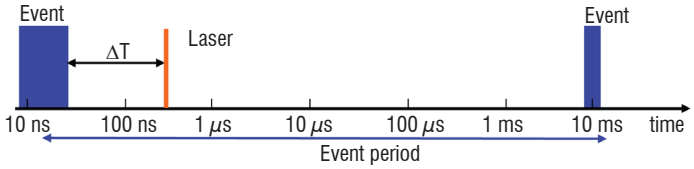

Figure 3 - Sequence of analysis of a short time event by a pulsed laser.

Figure 4 - CARS image of polystyrene balls of 3 μm in diameter.

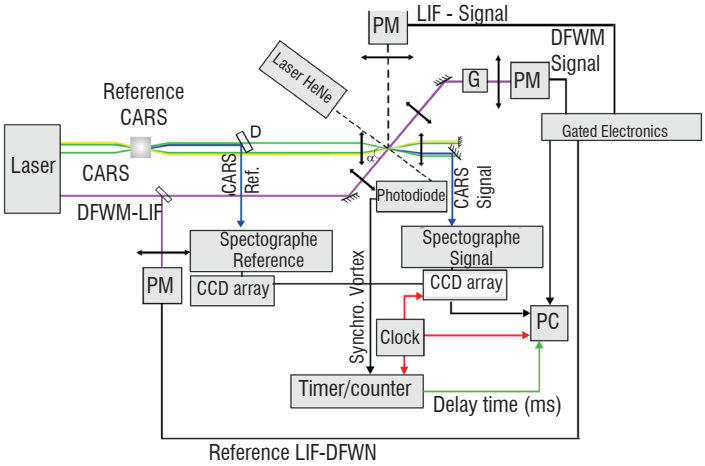

Figure 5 - Experimental set up combining CARS, DFWM and LIF techniques.

a)

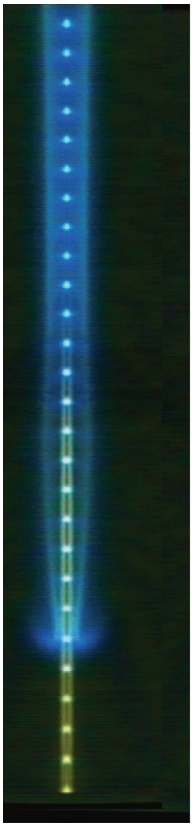

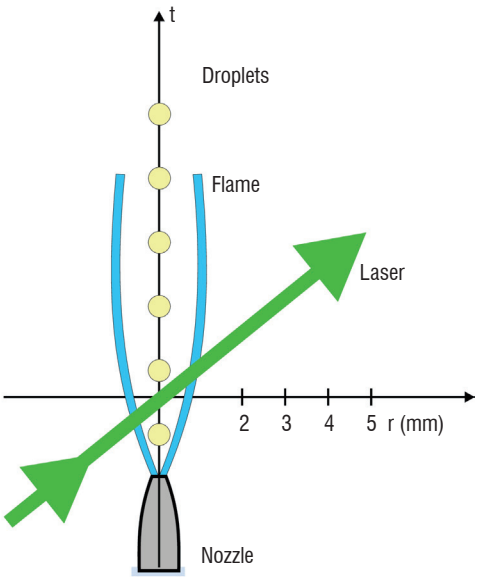

Figure 7 - View of the burning monodispersed droplet stream.

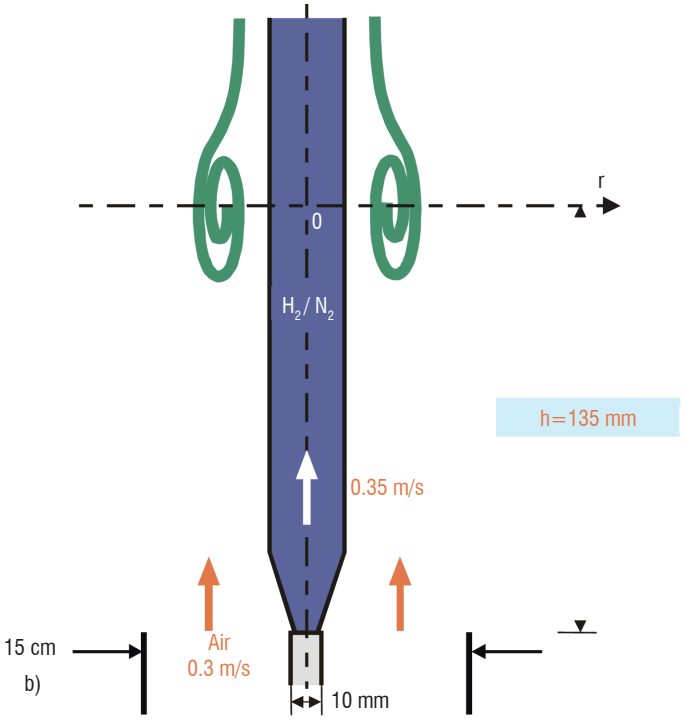

b)

Figure 6 - Buoyant H_2/air flame, producing vortices at a period of 15Hz, (a): flame; (b):scheme.

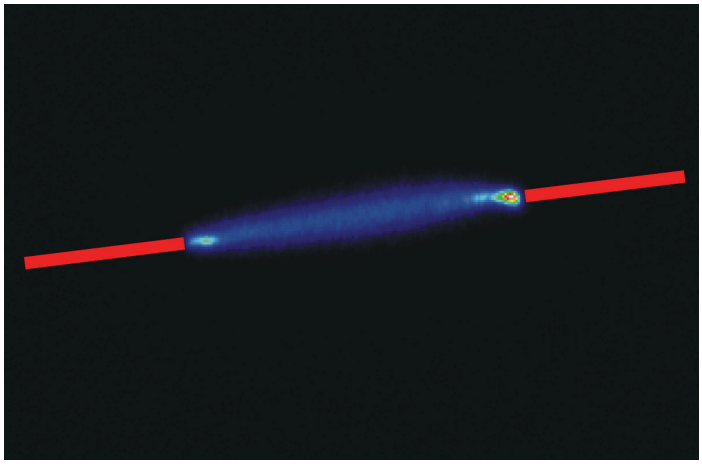

Figure 8 - Pulsed plasma generated by a 20 kV, 70 ns discharge.

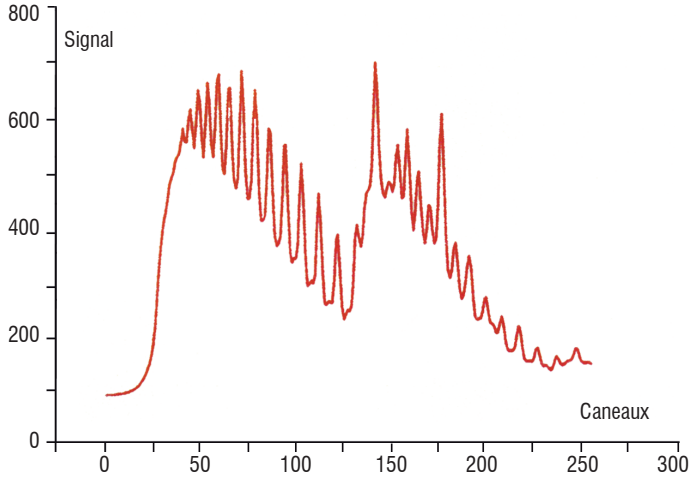

Figure 9 - N_2 CAR-S spectrum obtained in a flame using multiplex CARS , the Stokes is 100 cm^{-1} wide and the laser power is about 30 mJ for P1 and 5 mJ for P2.

Spatial resolution

It was shown that 75 % of the anti-Stokes power is generated within a length lr= 61 which is defined as the spatial resolution. The expression (1) is valid as long as lr is smaller than the coherence length lc. The coherence length depends of the dispersion of the media and is much shorter in liquids and solid than in gases. In gases, the spatial resolution lr is about 8 mm for d=3 mm and f=10 cm, therefore another arrangement is used providing a better resolution called BOXCARS geometry. By splitting the pump at ω_1 into two parallel beams, the signal is created in the focal volume common to all three incident beams, and can be reduced to less than 1 mm (figure 2) At macroscopic scale, the focusing geometry only allows nonlinear techniques to provide a single point, single shot information. The sample volume is a small cylinder of 100 μm in diameter and 1 mm in length. One main advantage of LIF is that imaging is simple to implement by using laser sheets whereas mainly single point measurements are presented in the following sections [27].
However, during the last decade, CARS has been also developed in near field microscopy thus providing images at the focus of the microscope which are usually few tens of μm in size (Figure 4) with a spatial resolution which can reach less than one μm [11].

The Probing of mixtures

The analysis of gas mixtures has motivated most of the work performed so far. Conventional CARS is then mainly used to measure the gas temperature while DFWM or LIF is used to measure transient species concentration. The coupling of CARS thermometry with DFWM and LIF method is achieved thanks to a set up built by SOPRA (Figure 5). The laser system was especially designed to allow simultaneous trace species analysis and conventional CARS thermometry. Determination of NO concentrations is presented in the flames experiments (Figure 6 and 7) whereas major species like H_2, CH_4 and C_2H_2 are sampled in the plasma experiment (Figure 8).
Two benches are mounted on a single table in order to deliver the pump and Stokes beams required for the multiplex CARS temperature measurement and the UV beam necessary to monitor the NO concentration. The first bench comprises a frequency doubled injection seeded Nd: YAG laser and a broad band dye laser that generates the CARS signal of nitrogen Raman Q branches (Figure 9). The second laser bench consists of a suitable narrow-band dye laser pumped by a multi mode Nd: YAG laser which is frequency doubled in a BBO crystal to generate the UV beam at 226 nm. The output energy is about 3 mJ per pulse with FWHM of 0.12 cm^{-1}. The laser repetition rate is 10 Hz width 10 ns and the two laser systems are synchronized within the temporal jitter (1 or 2 ns). The CARS and UV beams are focused co-linearly using respectively 300 mm and 900 mm focal length lens. The hole is drilled at the centre of the 300 mm lens in order to allow the UV beams to be focused at the same point on the CARS beams. A BOXCARS geometry is used for the CARS beams (Figure 2a): refocusing and non-resonant background cancellation is applied systematically. This geometry provides a 3 mm long, 80 μm diameter CARS probe volume superimposed on a 1 mm long, 150 μm diameter UV probe volume. The long UV focal length is used to prevent saturation of the NO transition in the $A^2\Sigma - X^2\pi\,(0-0)$ γ system (Figure 10). The superposition of the CARS and DFWM/LIF probe volume is performed using a pinhole mounted on three translation stage and positioned carefully to allow beam superposition with an accuracy of about ± 20 μm. Reference and sample CARS spectra are dispersed in separate spectrometers and detected by means of diode arrays. The DFWM and LIF signals are detected by Photo Multiplier Tubes (PMT). In LIF, spectral filtering of the NO line is used, namely the Q1(21,5) in the (0-0) band of the γ system.

Buoyant H_2/air flame

In order to illustrate the great potential of these non linear optical techniques, we show the results of the study of a buoyant H_2/air flame for which instantaneous measurements in a periodically oscillating jet diffusion flame (Figure 6) were obtained [12], [26]. The temporal and spatial evolutions of the vortex/flame interactions were investigated by phase-locking the measurements and using laser diagnostics in combination. CARS was used to measure temperature, and DFWM and LIF were used for the concentrations of NO and radicals. Synchronisation is achieved by using the following procedure: the frequency of the outer vortices was monitored by passing a He-Ne laser beam through the outer part of the flame and detecting the beam wandering using a PIN photodiode. The phase angles at which single-shot measurements were performed were obtained by measuring the delay between the laser pulses and the periodic signal generated by the PIN photodiode using a counter/timer (Hewlett-Packard). Point measurements were made in the flame by translating the burner to the specified axial (z) and radial (r) locations. The radial position was changed in coarse steps of 1 mm. For each location single-point measurements were recorded in real-time over several successive

cycles of the buoyant vortices. Typically, sequences of 500 laser shots were recorded with a laser repetition rate of 9.8 Hz to obtain a sampling time of ~ 1 ms.

Temperature (K)	NO_2 detectivity (ppm)
670	5
775	22
830	63

Table 1 - Estimated NO_2 detectivity in the CH_4/air flame.

Temperature (K)	NO_2 detectivity (ppm)
520	9
640	12
760	17

Table 2 - Estimated NO_2 detectivity in the H_2/air flame.

Variations in temperature and NO concentrations were recorded simultaneously as a function of time over a vortex-crossing period at different locations in the flame. For validating the theoretical model, a location with axial and radial distances of 135 and 15.5 mm, respectively, was chosen. As the vortices travel past this probe location, hot combustion products convect not only in the axial direction but also in the radial direction. Typical time-dependent profiles of measured temperature and [NO] at this location are shown in Figure 11 with solid circles and squares, respectively. These profiles represent the data in the bulge region during the vortex-flame interaction. The two peaks in temperature-time plot (Figure 11) are highly reproducible and represent stretched and compressed flamelets [12]. When the flame is bulged in the braid region of a vortex pair, the flame section (flamelet) that is being pulled outward by the lower vortex becomes compressed, and the flame section being pushed inward by the upper vortex becomes stretched. This means, with reference to time that the flame section crossing the probe location first (t ~ 13 ms) represents the stretched flame (due to the upper vortex) and the one crossing later (t ~ 30 ms) represents the compressed flame (due to the lower vortex).

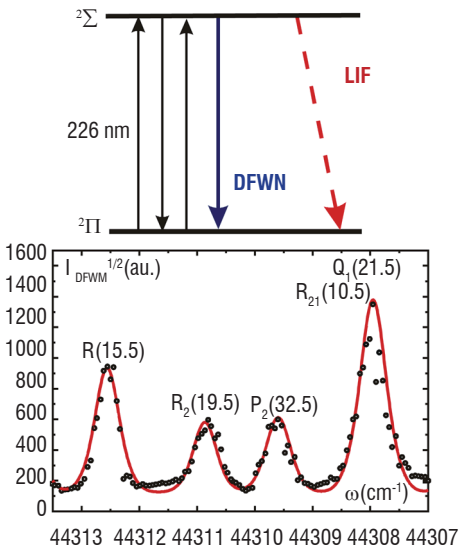

Figure 10 - NO excitation scheme in DFWM and corresponding spectrum recorded at resonance in the γ system in a flame at 2000K and 1bar.

Contour plots of the measured parameters in space and time were constructed from the individual time profiles recorded at several radial locations (Figure 12). About 10 single-shot measurements were averaged at each temporal (phase) and spatial position, i.e., at a specified height (135 mm from the burner) and a specified radius (1-mm intervals from the center), about 10 measurements were made every 1 ms during the flame-flicker period (~ 65 ms) and averaged to obtain one value in the contour map. Experimentally, it was observed that islands of high-temperature (Figure 12a) and high [NO] (Figure 12b) developed in the compressed region of the flame bulge (~ 40 ms). It is interesting to note that the location of the NO peak was shifted slightly by a few millimeters in the radial direction from that of the peak temperature. In the stretched region of the flame, measurements also showed a peak-temperature drop of ~ 100 K, which is consistent with the simulations (Figure 12c). [NO] followed the temperature, with the peak located in the bulge region, as predicted in the calculations (Figure 12 d). Finally, [NO] closely follows the temperature, with the peak in the former being located in the bulge region. The large [NO] in the compressed flame arises, in part, from the transport of the NO generated in other regions of the flame.

Monodisperse droplet stream in combustion

These techniques can also be applied to the study of multiphasic media, such as droplets combustion. We use a droplet injector which has a 50 μm internal diameter orifice to generate the ethanol droplet stream (Figure 7a) probed by the CARS and LIF laser beams. The laser beams are focussed at 20 mm above the injector (Figure 7b) and the droplet size is about 100 μm in the configuration under study [28].

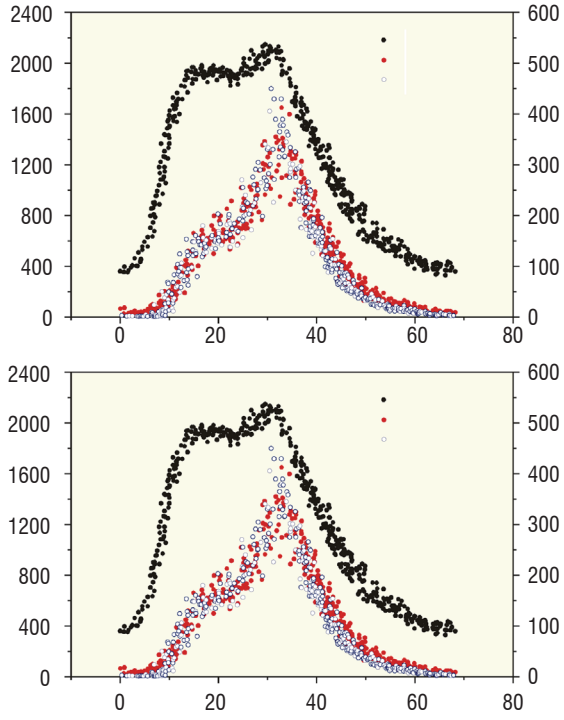

Figure 11 - Temporal evolution of the temperature and NO concentration obtained by CARS and by DFWM and LIF respectively ; (a): in the centre of the vortex, (b): on the edge of the vortex.

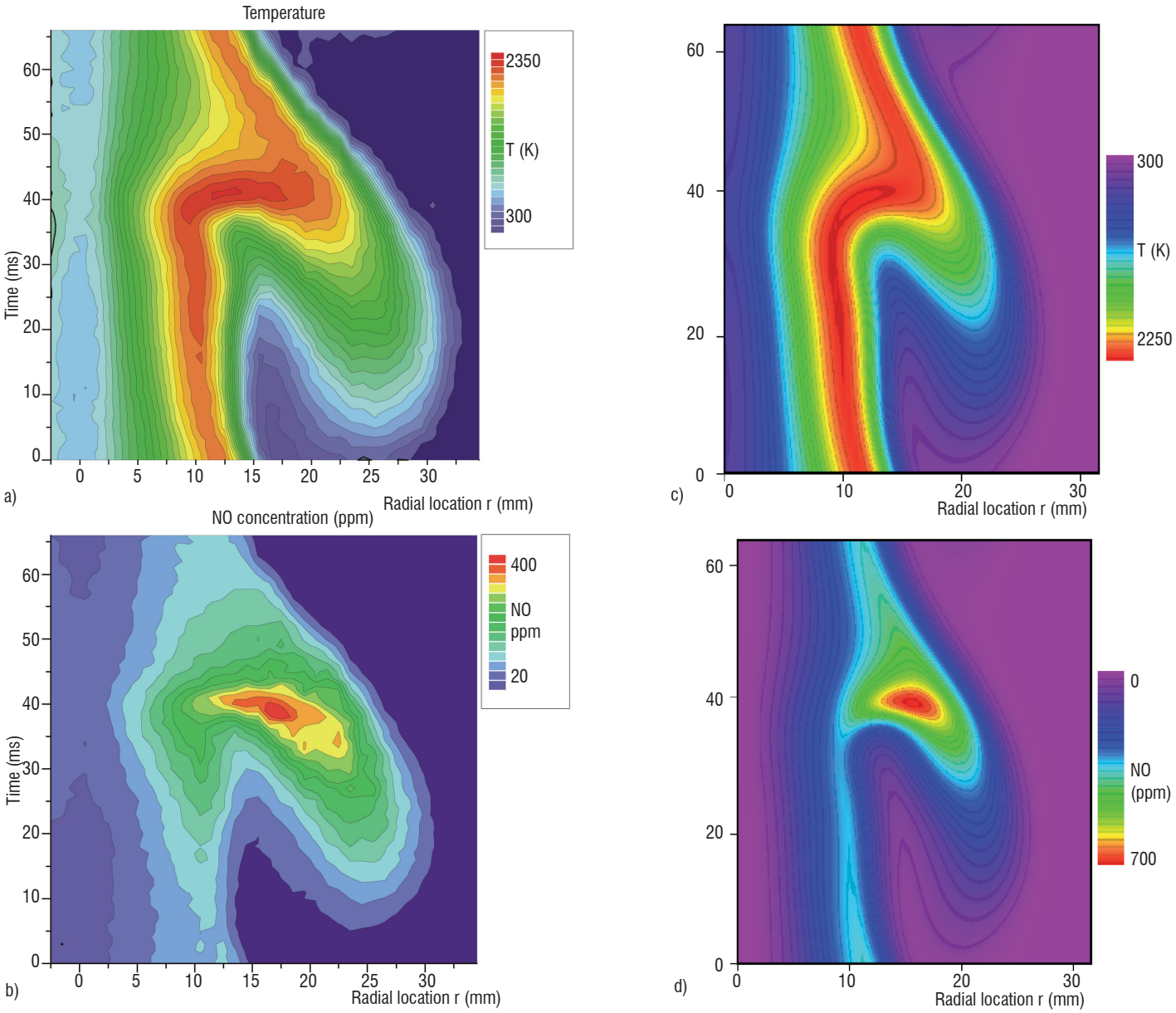

Figure 12 - Measured two dimensional map of temperature (a) and NO concentration (b) in the vortex flame and corresponding calculation of [12] for T (c) and NO (d).

Two excitation frequencies are used experimentally, 16700 and 33200 Hz, which correspond to a droplet spacing parameter C=6 and 3 respectively [13]. A careful check of the datation system is performed prior to the sequence of measurements. Sets of 400 single shots are acquired and plotted as a function of time over a period of 60 μs (30μs) for the 16700 Hz (33200 Hz) generator frequency. Instantaneous measurements are regularly spread over the period with about 6 points in each μs range. The flame radius is scanned over 20 successive positions to sweep the flame in which the reaction zone is located at about 1.6 mm from the droplet axis (Figure 7b). Time profiles are presented over a droplet period in figure 13. The region located between the droplet axis and the flame zone is displayed in figure 13a and the region located beyond the reaction zone is shown in figure 13b. The droplet is easily seen in figure 13a since optical breakdown occurs when the laser beams are focussed inside the droplets. In this case the acquisition routine automatically rejects the measurements. Averaged profiles further illustrate the temperature and NO concentration evolution along the flame radius (Figure 14).
On the logarithmic scale of figure 14, the UV signal rapidly change near the flame centre where the signal strength is already two orders of magnitude smaller than at the droplet axis. In the flame, NO signal becomes predominant and then smoothly decreases toward the burnt gas region. The slow decrease is suggesting that thermal NO is mainly produced according to the drop in temperature also measured in that region (Figure 14). The first observation is due to the laminar character of that kind of flame. However, the spatial resolution can degrades the temperature sampling within the accuracy of 50 K given by standard deviation and the steady state nature of the temperature profile may not be unambiguously demonstrated everywhere above the nozzle. The second observation is related to the strength of the UV signal on the droplet axis suggesting that other species may be at the origin of that signal. Consequently, the spectral discrimination of the NO signal was performed by setting the laser frequency to the top of the Q1(21.5) line whereas parasite UV contribution is measured by shifting the frequency in the wing of the NO line. In figure 15, the radial appearance of NO at the flame centre is demonstrated whereas important background is observed between 0 and 1.2 mm radial location.

The time behaviour of temperature and NO is found flat whatever the flame conditions investigated (16700 Hz and 33200 Hz). The steady state character of the temperature profile is representative of a laminar diffusion flame which is obtained at 20 mm above the nozzle. The steady state regime is probably not fully achieved near the nozzle orifice for the first droplets of the stream [13]. The temperature maximum is 2160K (within the 50 K accuracy) and corresponds to the equilibrium temperature of stoechiometric ethanol/air combustion. In the two flame investigated, that value does not versus height above the nozzle. The location of the flame front is constant, at r= 16 mm in the two flames. The NO concentration peaks in the flame zone and its concentration reaches 100 ppm at 33200Hz and 70 ppm at 16700Hz as shown in figure 14. The closer the droplets, the lower is the burning rate therefore leading to a higher NO concentration. It is known that the closer the droplets are, the less is the evaporating rate. Actually, the vapor liberated by a front droplet surrounds the following droplet because their spacing parameter is small. As a result, the following droplet has a lower evaporating rate due to the vapor saturated environment. The change in NO production is thus related to the flame condition through the change in spacing parameter.

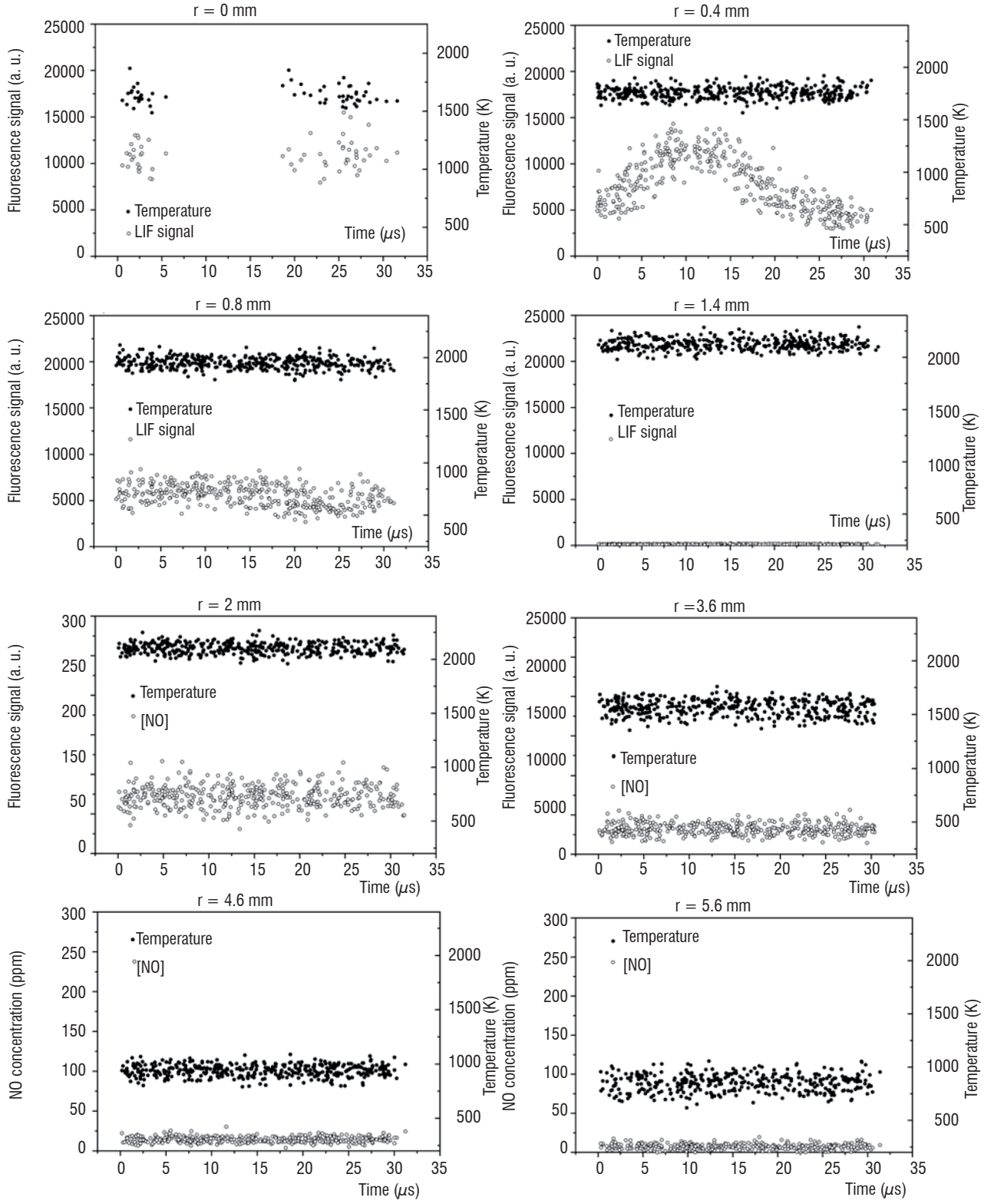

Figure 13 - Temporal evolution of the temperature and NO concentration inside the monodispersed droplet stream.

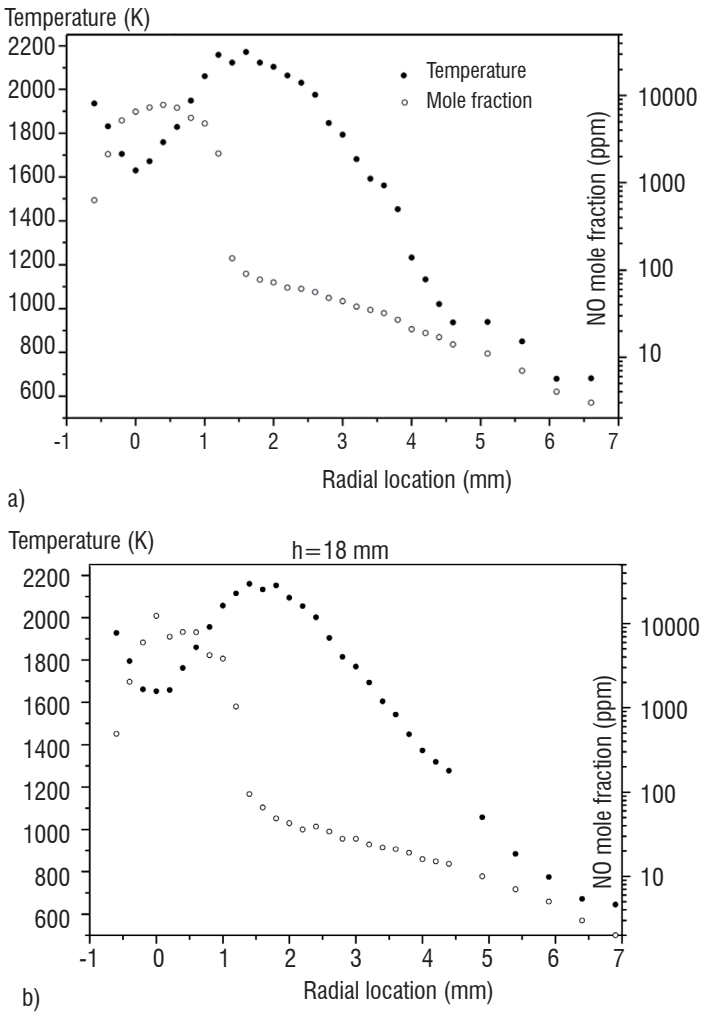

Figure 14 - Averaged profiles of temperature and NO mole fraction in the droplet stream injected at (a): 33200 Hz and (b): 16700 Hz.

The concentration of the parasite species is maximum on the droplet axis. Therefore, it seems to indicate that the signal originates from a reaction product appearing near the flame front, in the cooler region. Although the exact nature of the ethanol derivative is not known, it is probably C2H5O isomers resulting from decomposition of the fuel. Finally, the temporal evolution of these products can be compared to the change in vapour concentration which occurs near the droplet surface. In effect, the dynamic of the evaporation is influenced by the experimental burning rate between r=1 and 5 droplet diameters [13]. The radicals, which are produced through a transient process over the droplet period, reach a maximum concentration at r=5 dia. for C=6 and r=4dia. for C=3. The efficiency of that production is assumed to result from the aerodynamic drag effect.

Nanosecond discharge in CH_4/air flow

The time and spatial resolution of these techniques is now illustrated in the study of plasma-assisted combustion. Experimental investigation of a non-equilibrium nanosecond pulsed discharge at atmospheric pressure has been carried out [14]. The plasma is produced by a repetitive pulse generator and electric pulses of 10-40 kV in amplitude and 70 ns in duration with a pulse repetition frequency up to 200 Hz are produced. The high-voltage pulse generator is built using a hydrogen thyratron. Thanks to that system, triggering synchronization

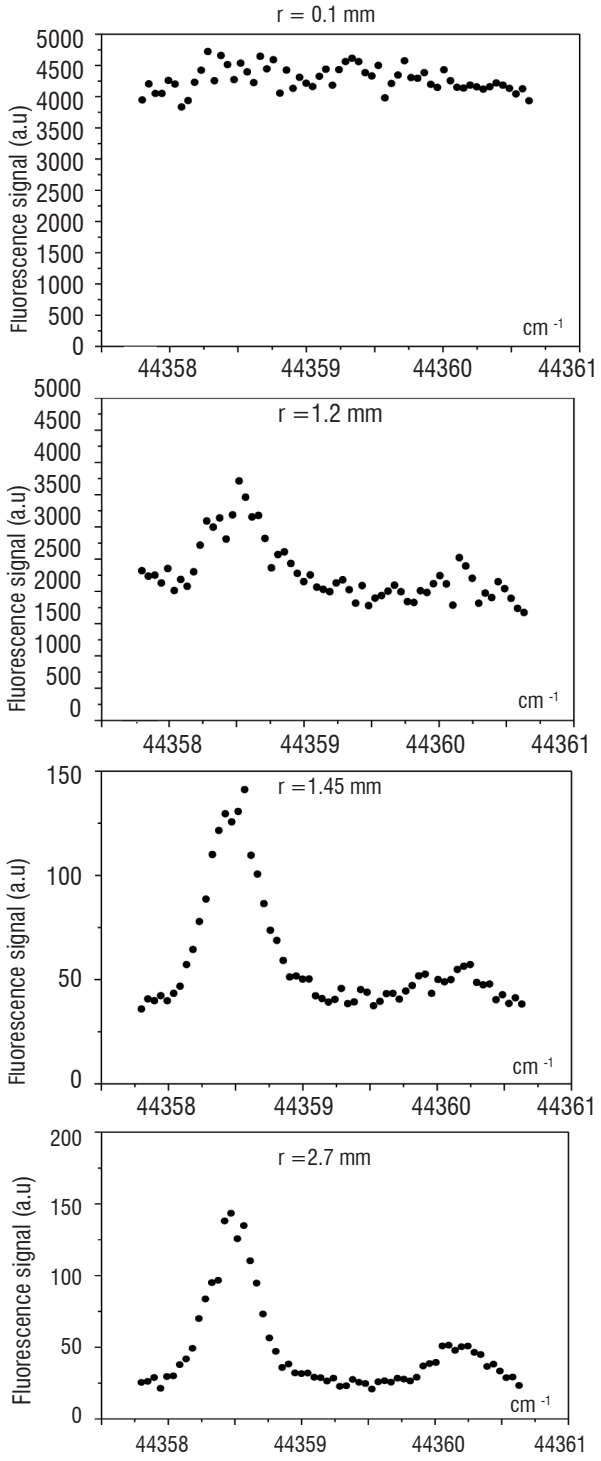

Figure 15 - Spectral evolution of the NO LIF signal versus radial location in the droplet stream in combustion.

is possible with a small jitter by using a pulse/delay generator. A jitter of about 10 ns is achieved, allowing good synchronization of the lasers with the pulsed discharge. Two stainless-steel needles, with a curvature radius at the tip of 0.1 mm are placed above the nozzle exit to produce the discharge (Figure 8). Positions of the needles with respect to the nozzle could be varied horizontally and vertically. Both electrodes are tilted vertically by 9° with respect to the propagation of the laser beams in the discharge. In this way, the laser beams can be focused at the centre of the discharge (Figure16).

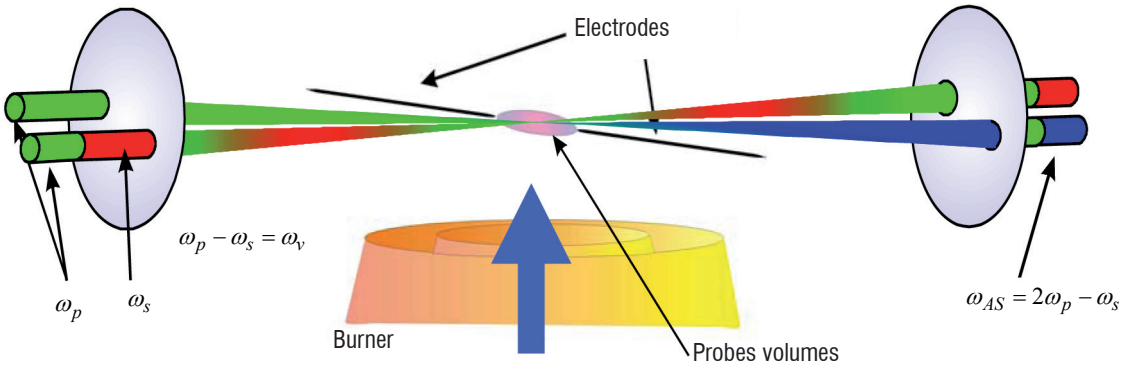

Figure 16 - Geometry of the excitation above the nozzle and between the electrodes.

Time-resolved CARS measurements are reported in the discharge. Experiment is performed in pure air and in mixture of methane and air. Spatial and temporal evolution of temperature and species distributions are recorded by delaying the probe lasers relative to the discharge pulse in the range 10 ns^{-1} ms.

The gases are flown from two concentric nozzles made of ceramics which is an electrically non-conductive material used to avoid electrical disturbances of the discharge. The inner injection nozzle is 10 mm diameter and is surrounded by an annular nozzle which is 20 mm in diameter. The inner nozzle operates with a methane/air mixture, while inert gas is injected through the surrounding nozzle to prevent chemical and hydrodynamical disturbances of the inner flow. Temperature measurements are performed using N_2 CARS thermometry. These measurements are intended to quantify the energy transfer in the gas mixture. It is demonstrated that energy transfer induced by collisions of N_2 with CH_4 considerably increases the thermal heating of neutral molecules at temperatures up to 2500 K (Figure 17). Effect of the discharge on the local temperature also allows to ignite the CH_4/air mixture for equivalence ratio ranging from 0.7 to 1.3 [15]. Fast development of a flame kernel was observed. The experiment also shows that the flame can be sustained above the discharge due the repetitive ignition of the flame at the plasma repetition rate. Then, the CARS investigation of major species such as CH_4, H_2 and C_2H_2 is performed as a function of time, (Figure 3). The evolution of the species is monitored over more than 1ms. The results are shown in figure 18 [15]. The CH_4 consumption and H_2 and C_2H_2 formation are localized and further calculations are under progress to identify that particular chemistry.

The experiments have demonstrated that a strong vibrational non-equilibrium can be sustained in N_2 at 1 bar. The effect of different colliding partners on the vibrational relaxation of N_2 is studied in CH_4/air mixtures with different equivalence ratio. The observed temperature distributions suggest that thermal equilibrium is not fully achieved.

Finally, the characterization of electron temperature and density was successfully performed using laser Thomson scattering (LTS) in the plasma (see Box 1).

Laser induced Gratings

Laser induced gratings consist in “printing” grating (index or coherence) into the flowing gas molecules. The time evolution of this printed gratings, determined by laser diffraction, gives access to a wealth of gas parameters such as speed or temperature.

Thermal

Laser-induced thermal gratings (LITG) have been described theoretically and we recall the derivation procedure of the main expressions driving the LIG signal temporal shape when the pump frequency is resonant with a one-photon transition of the probed molecules. The process is also described as the inelastic scattering of the wave “ ω_2 ” by the laser grating induced by the two waves at “ ω_1 ” (Figure 19).

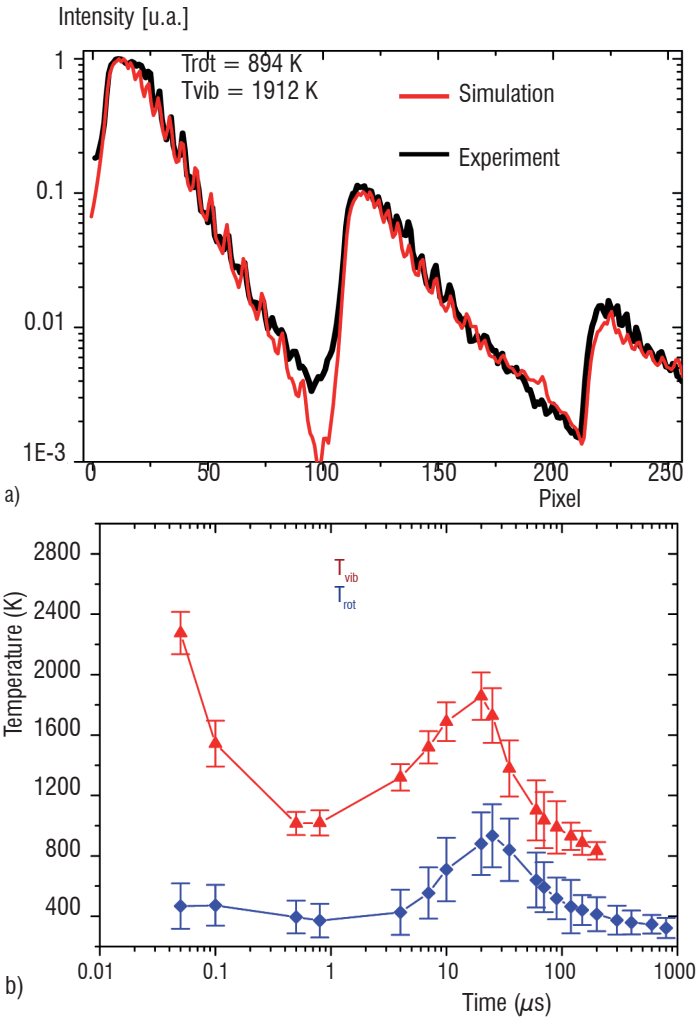

Figure 17 -(a): N_2 CARS spectra at a delay of 60 μs relative to the pulse discharge, spectral resolution of the multiplex CARS experiment is 0,25 cm^{-1}; (b): temporal evolution of the vibrational and rotational temperatures

Box 1 - Thomson Scattering

Laser Thomson scattering (LTS) is a powerful method for studying electron properties (electron density and temperature) in glow discharge plasmas occurring in gases having electron density in the range of 10^{15}-10^{20} m^{-3} [16]. LTS is the scattering of laser radiation by free electrons, when photon energy is small compared with the energy equivalent to the rest mass of the charged particles. The energy lost by the radiation is accounted for by the classical theory as a result of the radiation emitted by the charged particles when they are accelerated in the transverse electric field of the radiation. Because the electron mass is several orders of magnitude less than that of ions, the acceleration of electrons is larger for a fixed electric field. Therefore, we usually observe LTS only from electrons. The principle and general experimental arrangement of LTS is briefly presented. The Thomson scattering intensity $I_T(\Delta\lambda,\theta)$ is deduced from, $I_T(\delta\lambda,\theta)\,\Delta\Omega\,\delta\lambda = I_0 ne\,\Delta V\,d\sigma_T(\delta\lambda,\theta)\,\Delta\Omega\,\delta\lambda$ (A)
In this expression, the differential Thomson scattering cross section $d\sigma_T(\Delta\lambda,\theta)$ is given by :

$$d\sigma_T(\delta\lambda,\theta) = r_0^2(1-\sin^2\theta\cos^2\xi)\,S(\delta\lambda,\theta) \quad \text{(B)}$$

The scattering parameter α is defined by:
$\alpha = 4\pi/\lambda i \sin(\theta/2)$
When the scattering parameter α is $<< 1$, the radiation is incoherently scattered as in spontaneous Raman scattering. It consists in a simple summation of contributions from individual electrons. For the present experimental condition, the scattering is in this incoherent domain, e.g., $\alpha = 0.02$ from typical values of electron density (N_e=1 x 10^{18} m^{-3}) and electron temperature $(T_e = 3\ eV)$ with laser wavelength of 532 nm and a scattering angle of 90°. The electron velocity distribution $S(\Delta\lambda,\theta)$ is assumed to be Maxwellian. Electron temperature is measured from its half width at half maximum (HWHM). The electron density ne is obtained from Eq. A. By calibrating the detection system, the scattered light intensity measured by integrating over the spectrum gives the absolute electron density. Absolute calibration is performed in our case by using the spontaneous Raman scattering from N_2, with a known Raman cross section.

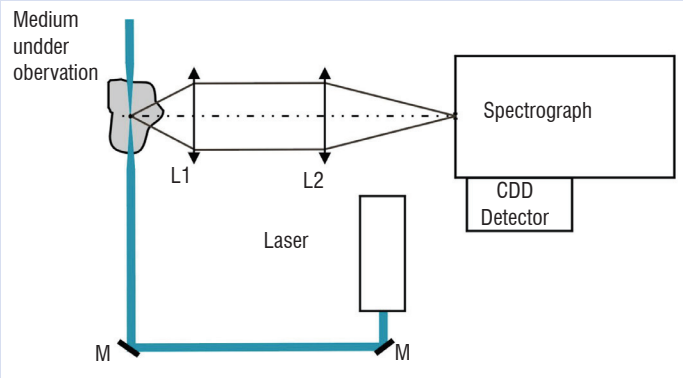

Figure B1 - 01 - Schematic diagram of the laser Thomson scattering apparatus

The experimental setup is presented in Figure B1 - 01 [17]. The laser beam at 532 nm (Nd: YAG) delivers 10 mJ per pulse at a repetition rate of 10 Hz. It is focused within the pulsed discharge using a 500 mm focal length lens. The Thomson scattered light is collected by an 80 mm focal length lens and imaged onto the spectrograph entrance slit using a 200 mm focal length lens. The Raman spectrograph (Jobin-Yvon T 64000) was especially designed to provide a good noise rejection. It has a 640 mm focal length and an f-number of 7.5. Its three 1800 grooves.mm^{-1} diffraction gratings allow good rejection of the light emitted at the excitation wavelength (Rayleigh, Mie and stray light). The spectrum is detected on a back-thinned liquid nitrogen cooled CCD-camera (800 × 2000 chip, Jobin-Yvon), providing quantum efficiency of 85 % at 500 nm. The dark current is lower than 3 e^-/pixel/hour and the readout noise is about 3 - 4 counts. The spectral resolution of the system is given by the spectrograph (0.003 nm/pixel). The whole optical system is mounted on a high precision three-axis remotely-controlled translation stages, allowing the displacement of the probe volume across the plasma.

The LTS setup is aligned and calibrated by recording the rotational Raman spectrum of air. The LTS spectrum is recorded over a spectral window of 200 cm^{-1} located at about 30 cm^{-1} from the excitation wavelength. The spectrum is integrated over a period of 1 min to improve the signal-to-noise ratio. In this case, the peak intensity of the Thomson signal is typically equal to 500 photoelectrons. No interference from the Rayleigh or from stray light has been observed, demonstrating the high noise rejection of the spectrograph. The procedure consists in recording the plasma emission without any laser beam before to record the LTS spectrum. The LTS light together with the plasma emission is then recorded after sending the laser beam in the plasma. The net Thomson scattering spectrum is obtained by subtracting the plasma emission from the raw Thomson spectrum. The absolute intensity is obtained from the Raman spectrum recorded before every measurement. The Thomson spectrum is then fitted using a Gaussian profile (electron velocity distribution function). The fit is obtained using a least-squared method. In the fitting procedure, only the wings of the profile are used. The electron density and the electron temperature are drawn from the fit.

In Figure B1 - 02, Thomson measurements are performed at different delays from the high-voltage pulse providing the temporal evolution of electron temperature and electron density during the discharge pulse. Measurements at $\Delta T = 20$ ns, show that electron temperature is about 2.6 eV and electron density is 10^{15} cm^{-3}. These values obtained at P = 1 bar and T = 300 K, allows to calculate the physical parameters characterizing the plasma; A Debye length of 3.7 10^{-7} m, a mean gap between electron of 10^{-7} m, a Landau radius of 5.7 10^{-10} m and an electron mean free path of 9.6 10^{-4} m. The ionization factor estimated to be 4 10^{-5} allows to conclude that this plasma is weakly ionized.

Measurements performed at larger delays (between 30 and 70 ns) show a fast decrease of electron temperature (from 2.6 to 1 eV) and a reduction of electron density by a factor of 10. This last value is in accordance with the reduction of electrical current by a factor of 8, demonstrating then the potential of LTS to measure the electron properties of these nanosecond pulsed discharges.

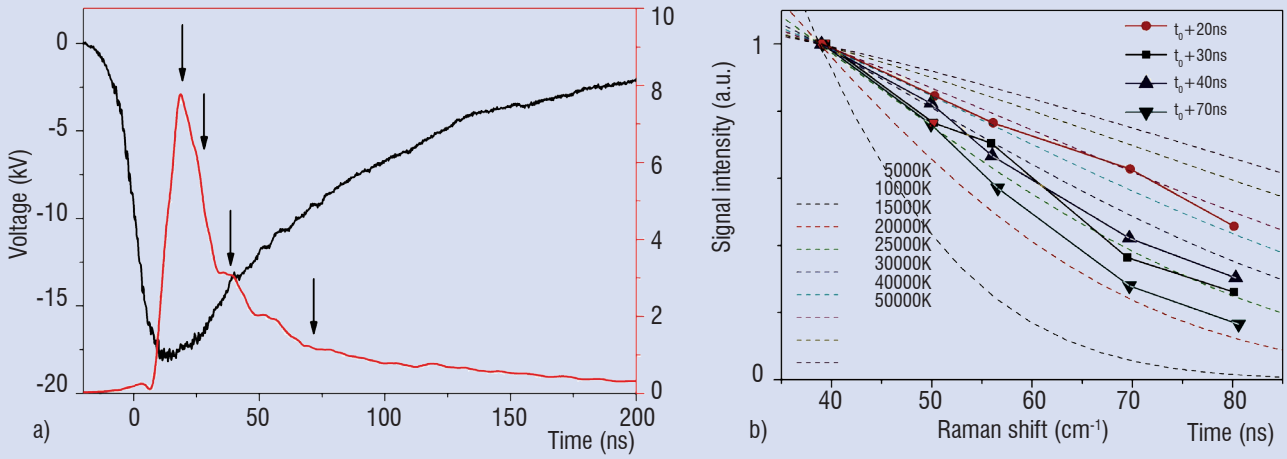

Figure B1 - 02 - (a): temporal delays relative to the discharge trig at which LTS measurements are performed; (b): experimental-theory comparison of LTS signals versus Raman shift with indication of electron temperatures.

Model description

The temporally overlapping crossed pump beams with parallel polarizations interfere and form an intensity grating. The fringe spacing Λ of the interference pattern is given by Bragg's law [18]:

$$\Lambda = \frac{\lambda_p}{2 \sin\theta} \qquad (3)$$

where λ_p is the wavelength of the pump beams and 2θ is their crossing angle. Pump beams energy resonantly absorbed by the molecules may be collisionally redistributed in the course of different non-radiative de-excitation processes, also referred to as quenching processes. They may take place even on the time scale of the coherent interaction characterizing standard four-wave mixing and represented in Figure 1. Collisional relaxation of spatially-periodic excitation may generate respective variations of temperature and density in the gas medium, which produce modulations of the complex refractive index; the phenomena is referred to as laser-induced gratings. The LIG signals are formed when the probe laser beam is diffracted by this regular modulation in the Bragg phase-matched direction, at the angle θ_B to the optical axis. The temporal evolution of the diffraction efficiency η is mainly determined by the time scale of the relaxation processes and can be recorded by using cw or long-pulse probe radiation, or by varying the delay between the probe laser pulse with respect to the pump laser one. The latter technique was used at Onera to probe NO_2 [19, 20].

Probing of mixtures

We present an application of the LITG technique to the detection of NO_2 molecules seeded in an atmospheric pressure flow [19] and flame [20]. The beams were focused in the geometry of figure 19. The temporally delayed short pulses of pump and probe radiation were used in the experiment.

The pump and probe beams have horizontal polarization. They are made collinear by means of a dichroïc mirror (D1). The three beams are aligned in a planar forward BOXCARS geometry (Figure 2a) and focused using an achromatic lens (L1) with a 500 mm focal length. The energy of each of the pump beams in the probe volume is typically about 1.5 mJ. In this case, a power density of about 1.6 GW/cm^2 is obtained at the focus with a beam diameter of about 100 μm. The crossing angle of about 1.9° provides a fringe spacing of $\Lambda = 12 \pm 0.5$ mm. A dichroïc mirror (D2) is installed into the path of the pump beam (1) in front of the focusing lens in order to suppress the stray light from the probe beam in the direction of the signal beam. It was found that filtering at this location is particularly efficient to suppress scattering by the nearby optics inserted into the probe beam (3), that is separated by only 22 mm from the pump beam (1). The recollimated LITG signal beam is filtered out by means of pinholes inserted into the detection path which is about 12 m long. A set of 6 mm OG570 (Schott glass) colored filters (CF) is positioned after the first pinhole to reduce the scattered light of the pump laser. The signal is registered by a photomultiplier tube (XP1017, Philips).

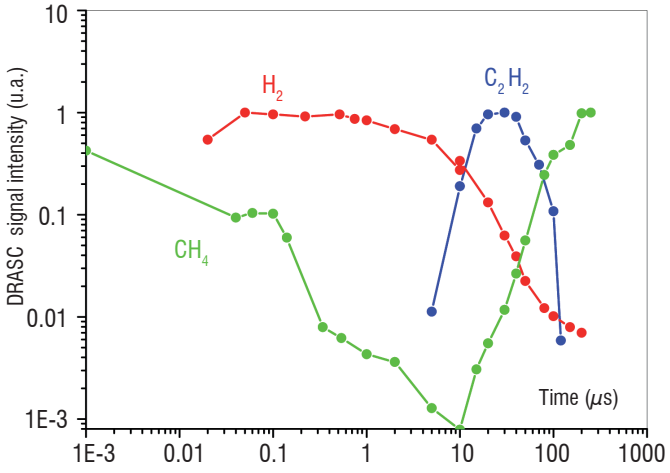

Figure 18 - Temporal evolution of H_2, CH_4 and C_2H_2 sampled by CARS over 1 ms after the discharge pulse.

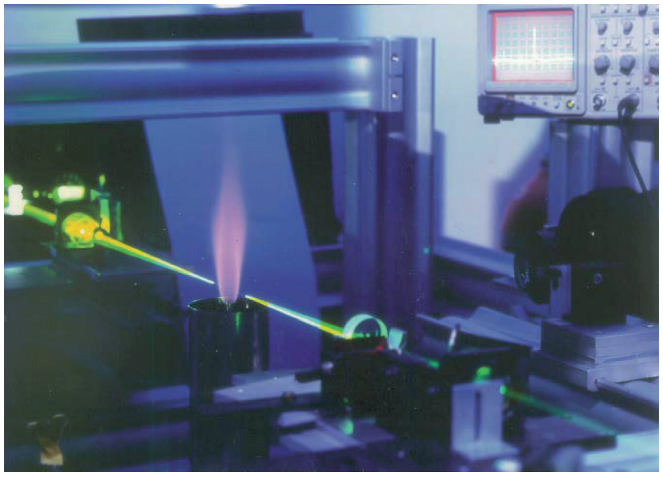

Figure 20 - View of the seeded flame and of the pump (green) and probe (yellow) lasers used for LITG experiment.

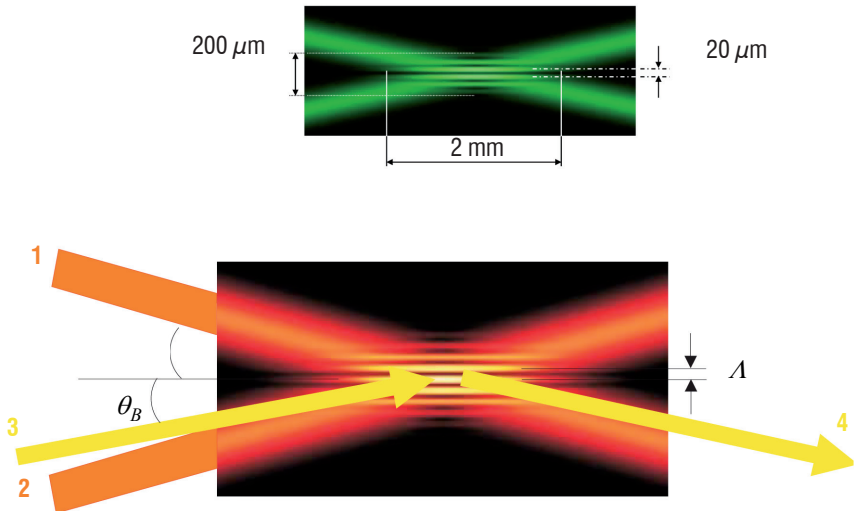

Figure 19 - Principle of the LITG excitation; the two strong pump beams (1) and (2) induce the grating on which the probe (3) is diffracted.

The signals from the detection channels are gated, integrated using an electronic unit (E) and processed by a computer (PC), using the acquisition routine. An average of 10 to 100 laser shots can be taken in each measurement condition.

The burner is presented in Figure 20. It is a coaxial jet assembly composed of a short tapered-contour fuel jet nozzle, of 10 mm inner diameter, located at the axis of an annular cylindrical cavity for air flow, with 80 mm external diameter. This cavity is filled inside with small glass balls providing conditions of laminar air flow around the central jet. The fuel is a mixture of hydrogen (or methane) with nitrogen.

To analyze the characteristics of the LITG signals, the transversal temperature profiles of these two flames should be known. We used N_2-CARS to perform these measurements at a height h = 2 mm above the plane of the nozzle orifice. The spatial resolution of CARS measurements employing a lens with a focal length of 300 mm was 3 mm. For CH_4/air flame the flowing gases in the burner were the following: 1.44 l/min of CH_4 and 0.55 l/min of N_2 seeded with 0.1 % of NO_2, that provided NO_2 concentration of 276 ppm, were being supplied to the nozzle, while 71.0 l/min of air were being delivered to the peripheral annular cavity. The radial temperature profile of this flame is shown in Figure 21(a). For H_2/air flame 5.9 l/min of H_2, 1.48 l/min of pure N_2 and 0.35 l/min of N_2 seeded with 1 % of NO_2, corresponding to NO_2 concentration of 453 ppm, were being supplied to the nozzle, while 60.3 l/min of air were flowing at the periphery. The corresponding radial temperature profile is shown in Figure 21(b). The reaction zone is slightly closer to the burner axis for CH_4 (r = 7.5 mm) than for H_2 (r = 8.0 mm). Temperature profile has a marked influence on the radial variation of the LITG signal in these two flames.

Temporal evolution of LITG signals was recorded by varying the delay between the pump and probe pulses to determine the dependence of the signal strength on NO_2 concentration, on type of a buffer gas (or fuel), and on temperature at various positions inside the flame. Thermal grating signals are generated through the thermalization of energy resonantly absorbed by NO_2 molecules. We have investigated the dependence of LITG signals on temperature and gas composition in figure 22 and 23. Theoretical description of the signal strength and temporal evolution was performed following the approach employed in [18-20]. Comparison of experimental results with theoretical predictions is shown. LITG signal in a cold CH_4 flow at 1 bar and 300 K is presented in Figure 22(a). The flow supply was the following: 1.67 l/min of CH_4 and 0.7 l/min of N_2 seeded with 0.1% of NO_2 (295 ppm of NO_2) - through the nozzle, and 12.5 l/min of air - through the annular cavity. In the CH_4/air flame, LITG signal was detected at two radial positions: r = 0 mm (Figure 22b) and r = 3.1 mm (Figure 22c). LITG signal in a cold H2 flow at 1 bar and 300 K is shown in Figure 23(a). The flow supply was 3.0 l/min of H_2 and 1.1 l/min of N_2 seeded with 0.1% of NO_2 (250 ppm of NO_2) -

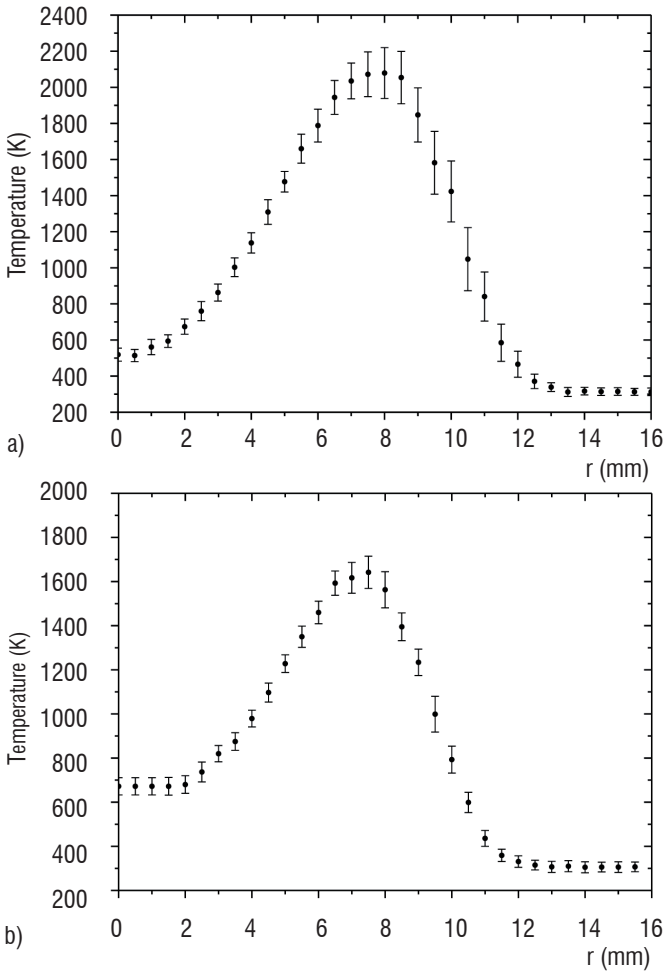

Figure 21 - CARS profiles of temperature measured on N_2 molecules in the two flames; (a): H_2/air and (b): CH_4/air.

through the nozzle, and 10 l/min of air - to the periphery. In the H_2/air flame, signal was detected at r = 0 mm (Figure 23b) and r = 2 mm (Figure 23c).A comparison of Figures 22 and 23 shows that in H_2 the lifetime of the thermal grating is relatively small, and hence the signal amplitude is damped over a shorter time scale, as opposed to CH_4. The dip between the two oscillation peaks is still visible at 300 K (Figure 22a), and vanishes at higher temperatures (Figures 22 b,c). The disappearance of the resolved oscillation peaks leads to lower accuracy in the non-linear fitting of signal shape that may provide less defined information in case of H_2 as compared to CH_4.

Finally, the sensitivity of the technique to NO_2 detection was measured under the flame conditions (Figure 24) and the estimated detectivities are given in tables I and II. It is seen that non linear techniques offer a quite good sensitivity level as compared to absorption on NO_2 [29] and offer an unique possibility to produce stronger signal when pressure increases.

Coherent and Electrostrictif

Here, we demonstrate that coherent Raman scattering is able to provide the velocity from the Doppler shift in low-pressure high speed flows while a more collective process like Brillouin scattering can be applied to measure the velocity in higher pressure conditions. These two techniques can be implemented either separately or in combination to measure simultaneously temperature, density and velocity over a large domain of flow fields. As shown below, the proposed approaches are based on the analysis of the time evolution of dynamic gratings (coherent or electrostrictif gratings [21]) produced by crossing two coherent pump beams, see Figure 19.

Time-domain coherent anti-Stokes Raman scattering

The CARS velocimetry technique is based on a single-shot time sequence where the anti-Stokes signal generation results from the application of a long pump (20 ns) and a short Stokes (1 ns) pulses, in the folded boxcars geometry. These two pulses are synchronised such that the Raman excitation which is coherently driven during the Stokes pulse application, is continuously probed by the long pump pulse (Figure 25). If the signal is produced in a low-pressure supersonic jet, the Raman coherence keeps oscillating freely after the Stokes interruption; during this free decay, the anti-Stokes shows a damped oscillation, which frequency gives the jet velocity. The anti-Stokes free decay oscillation can be readily explained by use of a grating picture. As previously introduced, crossing the two pump beams in the boxcars geometry leads to a periodic spatial modulation of the light intensity (Figure 19). This grating being illuminated by the short Stokes pulse, a spatially-modulated Raman excitation is printed within the gas leading to a coherence grating that is matched with the pump grating. When excitation stops, the coherence grating moves with the jet velocity; thus, the coherence and pump gratings are successively in an out of phase leading to a temporal modulation of the anti-Stokes response from which the velocity can be deduced. Furthermore, the translational temperature can be obtained from the time decay of the anti-Stokes signal which is imposed by the thermal motion of the molecules in the Doppler regime [22].
The performances of the Raman approach have been tested in a low-enthalpy Mach 10 wind tunnel delivering a uniform laminar flow in 90 s-long runs. The flow conditions are Vjet = 1382 ms^{-1}, static temperature = 48 K and static pressure = 5.5 Pa. The main objective of the experiment was the characterization of the thermodynamic behaviour of a laminar flow through a bow shock generated in front of a cylinder (16 mm diameter, 100 mm long). The axes of the CARS probe volume (14 mm long and 0.2 mm diameter) and the cylinder are aligned parallel to each others so that the velocity profile is recorded along the stagnation line (Figure 26). The optical CARS bench comprised two main parts:

- an injection-seeded Nd: YAG laser delivering 20 ns, 40 mJ pump beams at 532 nm
- a parametric source composed of a doubly resonant optical parametric oscillator followed by an optical parametric amplifier to deliver the 1.5 ns Stokes pulse around 535 nm [29].

The Stokes wavelength is adjusted to probe pure rotational Raman lines (S-branch) of nitrogen so as to take advantage of a long decay time of the Raman coherence [23]. Velocity measurements obtained by time domain CARS are reported in Figure 26. In addition, rotational temperature and density measurements obtained from dual-line CARS [24] are also reported in this figure. The different experimental profiles demonstrate the strong variations of the thermodynamic parameters through the shock:

- rotational temperature jumps from its static value (48 K) to the stagnation temperature (1058 K) as a result of the energy re-distribution between the different degrees of motion through the shock;
- gas density increases by a factor 6 as expected from a Navier-Stokes calculation;
- velocity variation is higher than 1 km s^{-1} within 0.3 mm through the shock, i.e. in the time duration of one or two collisions. These experiments illustrate the ability of CARS to capture strong velocity, temperature and density gradients.

In the collisional regime (several tens of hPa), the decay time of the Raman coherence is reduced to a few tens of picoseconds, precluding the potential use of time-domain CARS for velocity measurements. Hence, at high pressure, methods based on the time analysis of long persistent gratings such as thermal or electrostrictive gratings become more appropriate to get the flow velocity. As previously proposed [25], an elegant approach to get simultaneously temperature, velocity and density relies on the combination of two coherent techniques i.e. Raman and Brillouin scattering implemented with common pump lasers in the classical BOXCARS geometry (Figure 2a). Basically, temperature and density measurements are obtained from classical broadband CARS while the velocity is deduced from the temporal analysis of the two acoustic waves that are generated in opposite directions through electrostritive effect induced by the two crossing pump beams, see Figure 27 a).The experimental setup is depicted in Figure 27 b). A pulsed, injection seeded Nd: YAG laser, operating at 10 Hz, provides two excitation pump beams at 532 nm. The pulse duration is 15 ns (FWHM), the beam diameter is 4 mm and the total energy is 45 mJ per pulse. The excitation beams are focused by means of a 240 mm-focal length achromatic lens, with an angle of 2.9° ±0.1°. This results in a probe cylinder of approximately 2 mm in length and 30 μm in diameter; the corresponding grating wavelength is 10.56 μm. The read-out laser is a continuous wave argon ion laser, which delivers 400 mW in single-line operation at 458 nm. The probe beam intersects the grating at the Bragg angle θ_B. Figure 27 b) also shows the Stokes beam produced at a 607 nm central wavelength by a dye laser (energy per pulse = 2 mJ) for probing the Q-branch of nitrogen. After spectral separation of the Brillouin and CARS signals using a spectrometer, the time evolution of the Brillouin signal is recorded using a fast photomultiplier (Hamamatsu R2566U) while the CARS spectrum is dispersed on a CCD detector (Princeton ICCD - 512T).

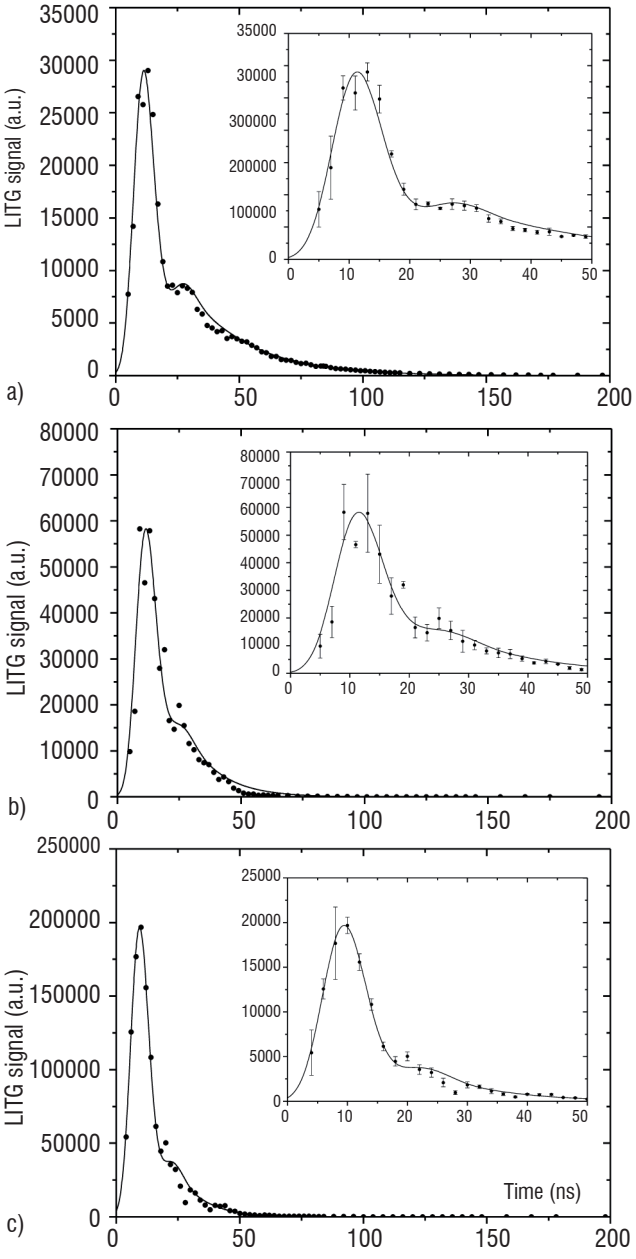

Figure 22 - LITG signal evolution measured (a) in the cold H_2/air mixture and in the H_2/air flame at two radial positions, (b): r = 0 mm and (c): r = 2 mm.

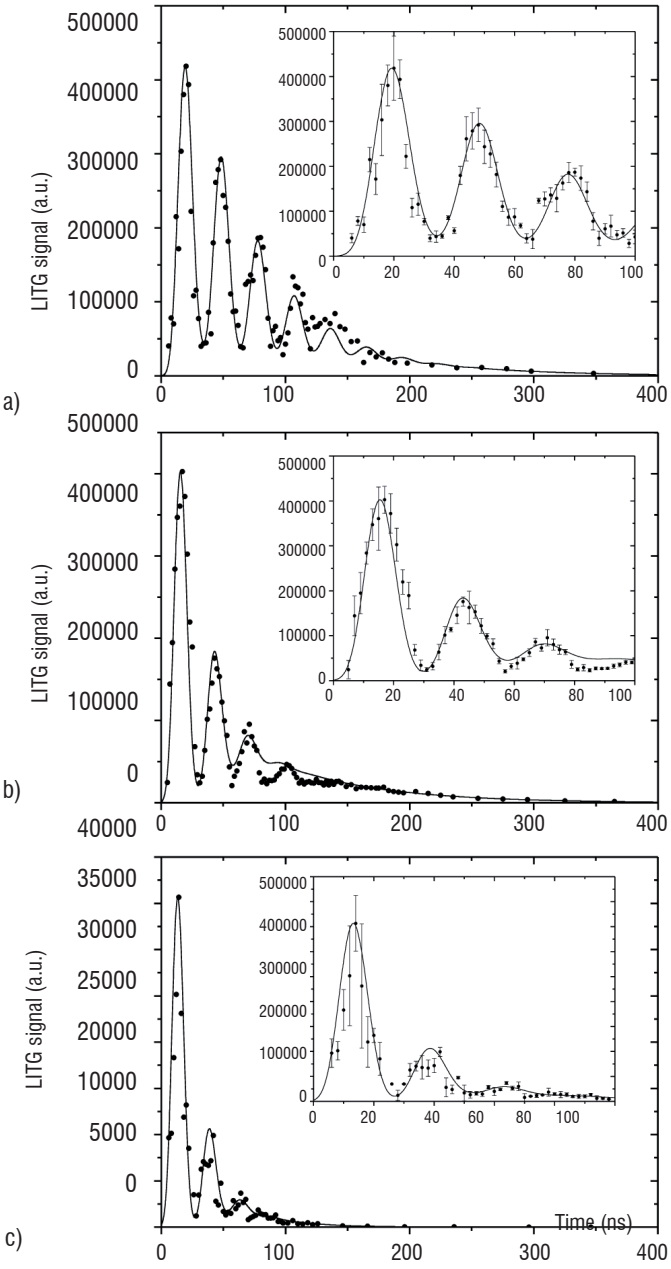

Figure 23 - LITG signal evolution measured (a) in the cold CH_4/air mixture and in the CH_4/air flame at two radial positions, (b): at r = 0 mm and (c) at r = 3.1 mm.

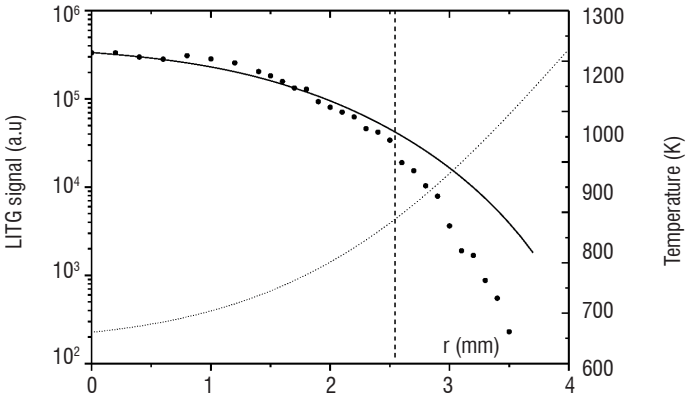

Figure 24 - NO_2 radial profile obtained by LITG in the CH_4 /air flame; the signal is decreasing toward the flame, located at r=8mm, because temperature is increasing and then because of NO_2 destruction beyond 3 m; measurements(••••), calculation (—) [18] and temperature (dotted). Dashed vertical line indicates the nozzle radius.

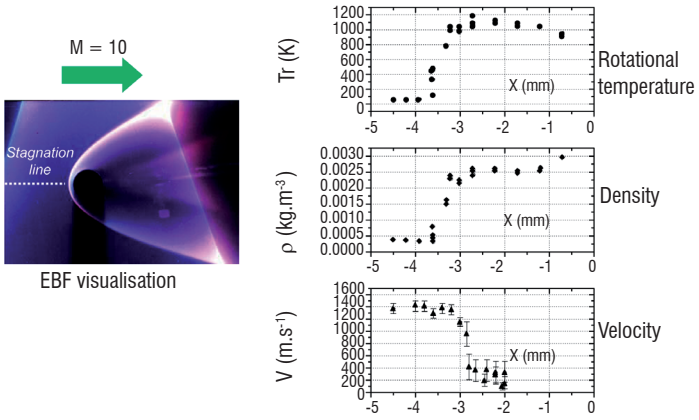

Figure 26 - CARS measurements through a bow shock ; Electron beam fluorescence (EBF) vizualisation of the shock (left) ; CARS measurements along the stagnation line (right).

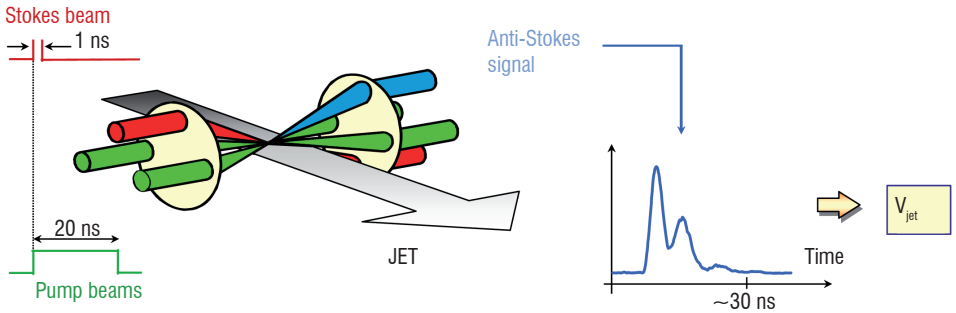

Figure 25 - Illustration of the time-domain CARS technique.

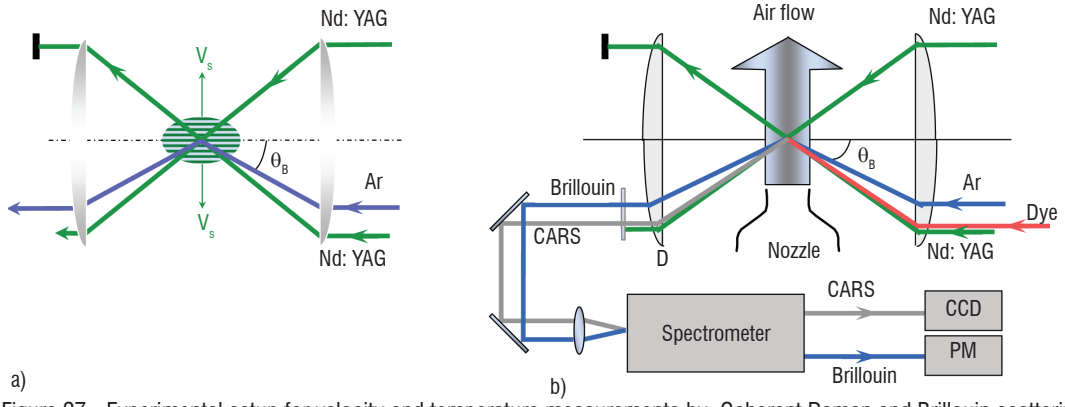

Figure 27 - Experimental setup for velocity and temperature measurements by Coherent Raman and Brillouin scattering.

The demonstration experiment has been carried out in a subsonic flow delivered by an étalon nozzle (Disa type 55D45, section = 60 mm^2). Two different beam configurations have been tested. In the first configuration, the argon spot beam was well superimposed with the pump grating whereas it was focused at a small distance ($\Delta x \approx 10\ \mu m$) apart from the pump gratings. The time-dependence of the Brillouin signals are reported in Figure 28 for both cases.

For well overlapping beams (Figure 28 a) in standing conditions (no flow), one obtains a damped oscillation which results from the interference of the two acoustic waves propagating in opposite directions within the probe volume. In presence of a 200 ms^{-1} flow velocity, the temporal dependence of the Brillouin signal changes significantly, one observes an oscillation with a tail which results from the different resident times of the two acoustic waves within the probe volume. For separated excitation and probe spots (Figure 28 b), the oscillating component disappears, and the signal is constituted of a hump. Only one sound wave meets the probe spot, after a time of flight $\Delta t1$. Figure 29 presents the results of simultaneous measurements of the CARS temperature (dots) and Brillouin velocity for the two beam configurations. These results are in good agreement with the expected values given by the Saint Venant formula, demonstrating the capability of the proposed approach.

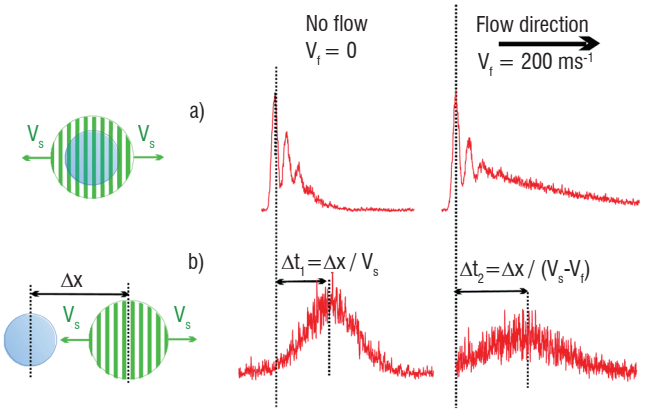

Figure 28 - Comparison of Brillouin signals obtained in a standing gas and a 200 ms^{-1} jet for two different beam configurations.

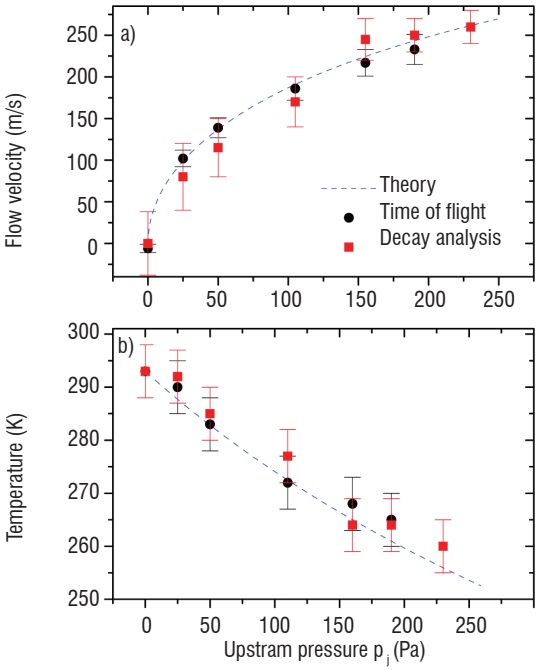

Figure 29 : Simultaneous velocity and temperature measurements obtained for different upstream pressures; experimental data have been obtained for the two beam configurations shown in Fig.28: 'decay analysis' is for the a) configuration while 'time of flight' is related to the b) configuration.

Conclusion

The experiments presented in the present paper have demonstrated the potential of non linear techniques and the interest in combining different techniques in situ. The choice of the techniques is relevant to the media under study namely, highly luminous, or high temperature (pressure) or strong non equilibrium. In effect, they are carefully handled not to perturb the evolution of the flow and to retrieve quantitative measurements.

In the buoyant flame it was shown that [NO] closely follows the temperature, with the peak in the former being located in the bulge region. The large [NO] in the compressed flame arises, in part, from the transport of the NO generated in other regions of the flame, which was not seen before. The contradictory behavior of temperature and [NO], which increase/decrease in the compressed/stretched flame location, respectively, was also quantified by time-resolved measurements. The techniques provide absolute concentrations of radicals and molecules during a vortex/flame interaction; they can be used to identify the important chemical pathways in diffusion flames. In the droplet study, we have probed a liquid/ gas media, less complex than realistic spray, by providing accurate data to improve the knowledge of droplet–flame interactions. To our knowledge, this is the first demonstration of time resolved measurements in a self sustained ethanol droplet stream flame. It was also shown that a pulsed plasma offer the possibility to improve combustion of a premixed CH4/ air flame. The transient plasma has consistently shown significant reductions in ignition delay and increased lean burn capability relative to conventional spark ignition. The demonstration of Thomson scattering to infer electron density in such a plasma was made possible thanks to a particular set up. Finally, CARS measurements were applied through a bow shock and temperature and velocity were obtained using a combination of CARS and Brillouin scattering. In all cases, the combination of pertinent laser diagnostics has proved their unique ability to identify the physical processes and diagnose the thermodynamic conditions without any disturbance of the media ■

References

[1] K. KOHSE-HÖINGHAUS AND J. B. JEFFRIES - *Applied Combustion Diagnostics.* Taylor and Francis, New York, 2002.

[2] S. DRUET, J.P. TARAN - *CARS Spectroscopy*. Prog.Quant. Electronics 7, 1 1981.

[3] P. D. MAKER AND R.W. TEHUNE, Phys. Rev, 137, A 801 (1965)

[4] T. A. WASSERMAN, P. H. VACCARO, B. R.JOHNSON - *Degenerate Four-Wave Mixing Spectroscopy as a Probe of Orientation and Alignment in Molecular systems.* J. Chem. Phys. 108 (1998) 7713-7738.

[5] H. BERVAS, B. ATTAL TRÉTOUT, L. LABRUNIE AND S. LE BOITEUX - Il nuovo cimento. vol 14D, n°10, pp1043-1050, 1992.

[6] H. BERVAS, S. LE BOITEUX, B. ATTAL-TRÉTOUT, J. P. TARAN - *OH Detection and spectroscopy by DFWM in Flames: Comparison with CARS*. J. Phys. B: At. Mol. Opt. Phys. 25 (1992) 949-969.

[7] S. WILLIAMS, R. N. ZARE, L. A. RAHN - *Reduction of Degenerate Four-Wave Mixing Spectra to Relative Populations 1.* Weak-field limit, J. Chem. Phys. 101 (1994) 1072-1092.

[8] V. KRÜGER, M. DUMONT, S. LE BOITEUX, Y. J. PICARD, F. CHAUSSARD, B. ATTAL-TRÉTOUT - *FDFWM spectra of NO in the Strong Field Limit Including Polarization, Line Coupling and Multipole Effects.* I. Theory, II. Experiments, Phys. Rev. A, 64, 012716-1 and 012717-1, 2001.

[9] B. ATTAL-TRÉTOUT, P. BERLEMONT, J.-P. TARAN - *Three-Colour CARS Spectroscopy of the OH Radical at Triple Resonance*. Mol. Phys. 70 (1990) 1-51.

[10] B. LAVOREL, H. TRAN, E. HERTZ, O. FAUCHER, P. JOUBERT, M. MOTZKUS, TIAGO BUCKUP, TOBIAS LANG, HRVOJE SKENDEROVI, GREGOR KNOPP, PAUL BEAUD, HANS M. FREY - F*emtosecond Raman time-resolved molecular spectroscopy.* Comptes Rendus Physique, Volume 5, Issue 2, March 2004, Pages 215-229.

[11] ZUMBUSCH, G.R. HOLTOM, X.S. XIE - *Three-Dimensional Imaging by Coherent anti-Stokes Raman Scattering*. Phys. Rev. Lett., Vol 82, N° 20, p 4142 1999.

[12] F. GRISCH, B. ATTAL-TRÉTOUT, A. BRESSON, P. BOUCHARDY, V. R. KATTA, W. M. ROQUEMORE - *Investigation of a Dynamic H2-Air Diffusion Flame With Advanced Optical Diagnostics And Numerical Modeling.* Combustion and Flame, 139,28-38 (2004).

[13] J.F. VIREPINTE, O. ADAM, G. LAVERGNE, Y. BISCOS - *Droplet spacing on drag measurement and burning rate for isothermal and reacting conditions. Journal of Propulsion and Power.* Vol. 15, pp 97-102, 1999.

[14] D. PACKAN, F GRISCH, AND B. ATTAL-TRÉTOUT - *Study of plasma enhanced combustion using optical diagnostics.* AIAA paper 2004-0983, 42nd AIAA AerospaceSciences Meeting and Exhibit (2004).

[15] D. MESSINA, B. ATTAL-TRÉTOUT, F. GRISCH - *Analysis of a Non-Equilibrium Pulsed Nanosecond Discharge at Atmospheric Pressure using Coherent anti-Stokes Raman Scattering.* Proceedings of the combustion institute, 31, pp 825-832 (2007).

[16] M. D. BOWDEN, Y. GOTO, H. YANAGA, P.J.A. HOWARTH, K. UCHINO, K. MURAOKA - Plasma Sources Science and technology 8 (1999), pp. 203-209.

[17] D. MESSINA, G.A. GRANDIN, B. ATTAL-TRÉTOUT, F. GRISCH. INCA meeting, Rouen (Coria), October 23-24, 2008.

[18] R. FANTONI, M. GIORGI, L. DE DOMINICIS, D. N. KOZLOV - *Collisional Relaxation and Internal Energy Redistribution in No_2 Investigated by Means of Laser-Induced Grating Technique.* Chem. Phys. Lett. 332 (2000) 375-380.

[19] E. LOUBIGNAC, B. ATTAL-TRÉTOUT, S. LE BOITEUX, D. KOZLOV - *Two-Color non-Linear Spectroscopy: Application to NO_2.* C.R. Acad. Sci. Paris, t. 2, série IV (2001) 1013-1027.

[20] E. LOUBIGNAC - *Etude du mélange à quatre ondes à deux couleurs dans les milieux en combustion : application aux composés azotés*. PhD thesis, Université de Bourgogne (2003).

[21] A. STAMPANONI-PANARIELLO, B. HEMMERLING, W. HUBSCHMID - *Temperature Measurements in Gases Using Laser-Induced Electrostrictive Gratings.* Appl. Phys. B 67 (1998) 125-130.

[22] M. LEFEBVRE, B. SCHERRER, P. BOUCHARDY, T. POT - *Transient Grating Iinduced by Single-Shot Time-Domain Coherent Anti-Stokes Raman Scattering : Application to Velocity Measurements in Supersonic flow.* J. Opt. Soc. Am., B13, n°3, 514 (1996).

[23] B. SCHERRER, A. GODARD, I. RIBET, P. BOUCHARDY, T. POT, M. LEFEBVRE - *Comparison of Dephasing Times for Vibrational and Rotational Coherent Anti-Stokes Raman Scattering : Implications for Velocimetry*. Appl. Phys., B71, 859 (2000).

[24] M. PÉALAT, M. LEFEBVRE - *Temperature Measurement by Single-Shot Dual-line CARS in Low-Pressure Flows.* Appl. Phys., B53, 23 (1991).

[25] M. RIBET - *Oscillateurs paramétriques optiques à cavités imbriquées pour l'étude des réseaux dynamiques créés par mélange à quatre ondes résolu en temps.* PhD Thesis Paris XI (2001).

[26] F. DUPOIRIEUX - *Optical Diagnostics Used at Onera to Characterize Turbulent ReactiveFlows and to Validate Aero- and Rocket Engine Combustor Modelling.* Aerospace Lab n°1, October 2009.

[27] F. GRISCH, M. ORAIN - *Role of Planar Laser-Induced Fluorescence in Combustion Research.* Aerospace Lab n°1, December 2009.

[28] G. LAVERGNE, Y. BISCOS, C. LAURENT, V. BODOC - *Advanced Measurement Techniques for Spray Investigations.* Aerospace Lab n°1, December 2009.

[29] A.K. MOHAMED, M. LEFEBVRE - *Laser Absorption Spectroscopy to Probe Chemically Reacting Flows.* Aerospace Lab n°1, December 2009.

Acronyms

SRS (Stimulated Raman gain Spectroscopy)
IRS (Inverse Raman Scattering)
CSRS (Coherent Stokes Raman Scattering)
RECARS (Resonance Enhanced)
LTS (Laser Thomson Scattering)
HWHM (Half Width at Half Maximum)
LITG (Laser-Induced Thermal Gratings)
CARS (Coherent Anti-Stokes Raman Scattering spectroscopy)

AUTHORS

Brigitte Attal-Trétout performed the first Coherent Anti-Stokes Raman Scattering spectroscopy (CARS) experiments at Onera. The so-called «resonant» version of CARS was created within this framework and used to record the first spectra of iodine. Since then, the Raman techniques and their degenerated version have been very widely applied to the measurement of low molecular concentrations. Brigitte Attal-Trétout has worked on the theme of optical metrology and non-linear spectroscopy applied to the diagnosis of reactive environments. She has directed a research unit and reoriented its work on diagnostics and plasmas. Brigitte Attal-Trétout is currently a director of research.

Frédéric Grisch, Masters degree in fluid mechanics in 1982, PhD in Energetics in 1988 and HDR in 2008 from the University of Rouen (France). Senior scientist at Onera/DMPH in charge of the development and application of laser diagnostics (CARS, PLIF, Raman scattering, Rayleigh scattering, Thomson scattering, etc.) for gaseous, liquid and solid propellant combustion, plasmas and nonreactive flow fields. Head of an Onera/CNRS research project on optical techniques for the investigation of multi-component spray evaporation.

Michel Lefebvre received his Ph.D. Degree from the University of Lille I and the Habilitation Degree in Optics from the University of Paris XI. He is currently senior scientist at Onera where he leads the 'Laser Sources and Sensing Physics' research unit in Palaiseau. He has conducted various studies in non linear optics and laser sources. He developed and applied the CARS technique to reactive flow and hypersonic wind tunnels. His current research covers parametric conversion processes and optical parametric laser sources.

Denis Packan received an Engineering Diploma from Ecole Centrale Paris (France) in 1996 and a PhD in Plasma Physics from Stanford University (USA) in 2002. He is currently a staff research scientist at Onera, Palaiseau, France where he is in charge of plasmas for aerospace applications, including space propulsion, combustion, aerodynamics, electromagnetic wave shielding and decontamination.

Isabelle Ribet-Mohamed received an Engineering Diploma from the Ecole Superieure d'Optique, Institut d'Optique, Orsay, France, in 1998 and the Ph.D degree from the University of Paris XI, France, in 2001. Since 2001, she has been a Research Scientist at Onera, Palaiseau, France. Her current research deals with infrared detectors.

A.K. Mohamed, M. Lefebvre
(Onera)

E-mail: ajmal_khan.mohamed@onera.fr

Laser Absorption Spectroscopy to Probe Chemically Reacting Flows

Laser absorption spectroscopy is now a well established tool to perform temperature, density and velocity measurements in a wide variety of aerodynamic and combustion flows. Measurements are usually performed on heterogeneous molecules like NO, CO, CO_2 and H_2O which present strong absorption line strengths in the infrared region due to their high dipole moments. In this paper, we present examples of applications using mid-infrared laser diodes in several hypersonic wind tunnels and combustion facilities of Onera and DLR followed by a review of actual developments in new OPO based laser sources providing better coverage of the infrared domain and opening new possibilities of ultra sensitive detection using cavity enhanced or photo-acoustic methods and stand-off distance measurements based on lidar schemes.

Introduction

Laser Absorption Spectroscopy for aerodynamics was developed in the mid 70's using infrared lead-salt diode lasers to probe combustion media [1][2] and has been used in hypersonic flows since the mid 90's [3][4] to probe the free stream in hypersonic facilities like the Onera-F4 hot shot facility [5], the DLR-HEG shock tube [6][7], or the Onera-S4 [6] and Astrium SIMOUN wind tunnels [8]. The technique is based on measuring the absorption intensity of a fast wavelength tuneable laser beam passing through the flow. Velocity, translational temperature and concentration measurements can be derived from the spectral features of molecular absorption lines acquired at high spectral resolution. Measurements are usually performed on heteronuclear molecules like CO, NO and H_2O which are naturally present as a result of real gas effects or as trace pollution species in air flows or on CO_2 in the case of Martian re-entry studies. All of these molecules have strong absorption line strengths due to their high dipole moments and usually the fundamental levels of absorption lines are located in the mid infrared region (wave number $> 4\ \mu$m), which is well covered by CW lead-salt diode lasers (Figure 1).

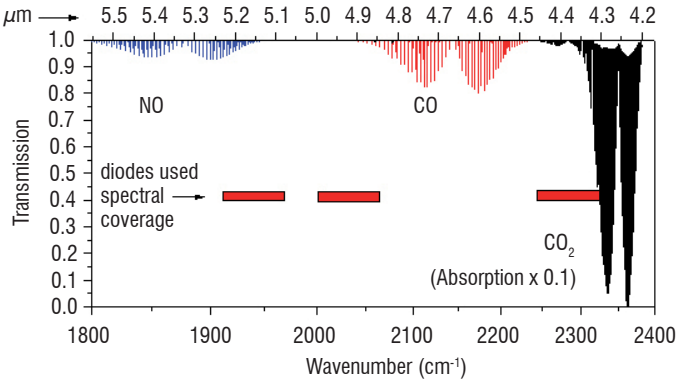

Figure 1- Absorption spectrum of some molecules of aerodynamic interest and spectral emission windows of some of the laser diodes used in wind tunnels and combustion applications.

These lead-salt diode lasers have very narrow line width emissions (around a few MHz or 10^{-3} cm^{-1}) and can be finely tuned (with a resolution close to 10^{-4} cm^{-1}) around absorption lines so that the temperature and pressure broadening can be visualized without any interference broadening from the laser line width itself. This high spectral resolution feature therefore allows temperature measurements from the Doppler line shape on trace molecules in low pressure (less than 1000 Pa) chemically reacting media such as in hypersonic flows where the lines are broadened mainly by temperature effects with typical Doppler line widths of 10^{-2} cm^{-1}. The gas velocity can also be determined from the Doppler shift induced in the line positions of the absorbing species when the beam is not perpendicular to the flow axis. The Doppler shift is of the order of 10^{-2} cm^{-1} at wavelengths around 5 μm for bulk velocities superior to 1000 m/s. Specie density measurements are possible from the integrated intensity of an absorption line if the gas is at Boltzmann equilibrium. Figure 2 illustrates the measurements that can be made from a spectrum presenting an NO absorption line with its Doppler-shifted component for flow conditions indicated in the figure. The unshifted line results from absorption of molecules at low velocities in the boundary layer of the flow or which are diffused outside of the flow.

Such measurements can be made at repetition rates up to 10 kHz which is fundamental to probe high enthalpy facilities with short duration flows (200 ms for Onera F4 and a few ms for DLR HEG) and where the aerodynamic conditions change quickly in the order of a few percent per ms. Lead-salt diode lasers are good at performing these high speed measurements as well as emitting in the mid-infrared to probe molecules of aerodynamic interest. However, one main drawback is that cryogenic technology (usually liquid nitrogen cooling) must be used to cool these diodes operating around 100K and as well as the HgCdTe detectors for optimal performance in the mid-infrared. Up to now, non-cryogenic instruments using visible or near infrared diodes have been limited to H_2O, or atomic species like Rubidium or Potassium which must be seeded beforehand in the flow [7].

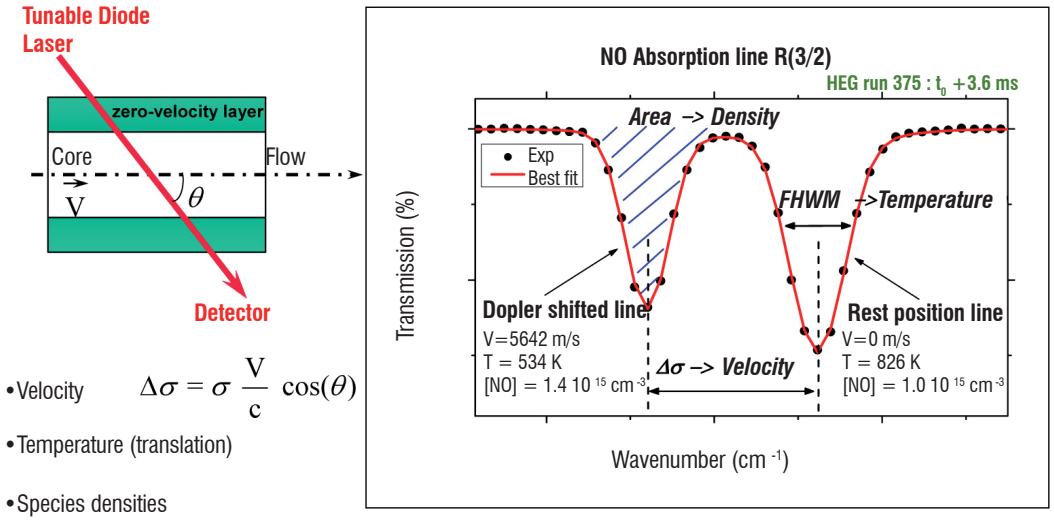

Figure 2 - The usual parameters which can be deduced from pressure-free absorption lines (Velocity is determined with an accuracy of about 5% whereas temperature and density have accuracies around 10%)

Fortunately, recent developments in new laser sources (Quantum Cascade Lasers [9], Interband Cascade Lasers [10], GaSb DFB laser diodes [11], OPO [12],…) now allow us to consider non-cryogenic setups (at least for the laser emission part) to probe the molecules of aerodynamic interest on their most absorbing lines in the infrared domain. Advances in cavity enhanced techniques [13](CRDS, ICOS,...) that improve the sensitivity of detection also offer new possibilities for probing some of these molecules in the visible or near infrared region with room temperature lasers.

Diode laser absorption spectroscopy in windtunnels

A typical diode laser absorption spectrometer (DLAS) is presented in Figure 3a. Such an instrument is composed of a laser emission head, photo-detectors and fast digitizers to convert and record the signals from the photo-detectors. For operations in the mid infrared domain, the diode laser emission head is in the form of a liquid nitrogen cooled cryostat containing one or two lead-salt diodes operating near 100 K. Nowadays Quantum Cascade lasers (QCL[9]) working in CW mode can also be used in the same cryostats. Stabilized current generators are used to control the diode temperature and current more finely for the required laser emission. A 500-mm focal length monochromator and optical collimating components are used to filter a single mode out of the emission spectrum of the diode and collimate the output laser light into a beam of about 15-mm diameter. About 30% of this beam is deviated for wavelength and intensity calibrations using a 0.00975 cm^{-1} free spectral range confocal spherical Fabry-Perot etalon and a reference cell filled with the gas to be probed at a few hundreds of Pascal. All these elements are grouped on an optical bench 1.5 m long and 0.8 m wide. The rest of the laser beam exiting this bench is then made to cross the gas medium to be studied with the help of mirrors before measurement of its intensity on a third photo-detector. Figure 3b presents a set of three absorption spectra (two for calibration and one for the medium being probed) which is typical when performing measurements with this instrument. The spectra are obtained through tuning the wavelength over about 1 cm^{-1} in a time interval of 1 ms. Figure 4 shows a typical experimental arrangement which is usually used in the Onera F4 wind tunnel.

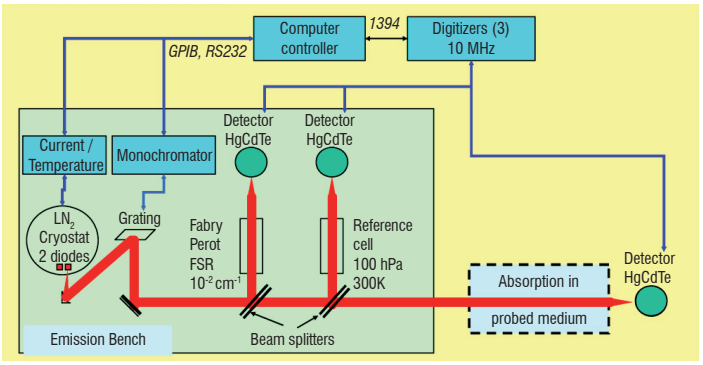

a) Spectrometer main features

TDLAS raw spectra exemple with a diode for CO probing
(CO line at 2055.6 cm^{-1} used to perform velocity measurements)
Three simultaneous channels (two for calibration : intensity and wavelenght)
Spectra acquired in 1 ms (at repetition rate 1 kHz)

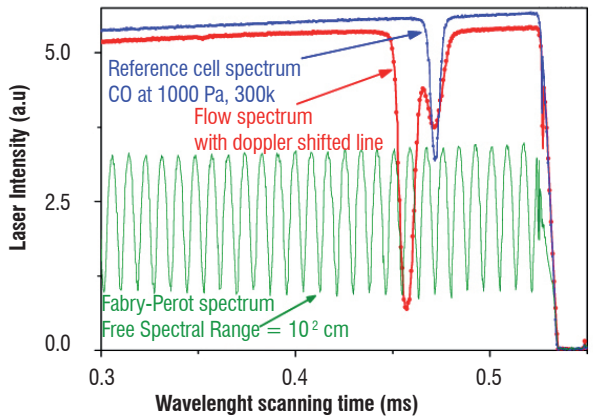

b) Examples of acquired spectra

Figure 3 : Typical DLAS spectrometer

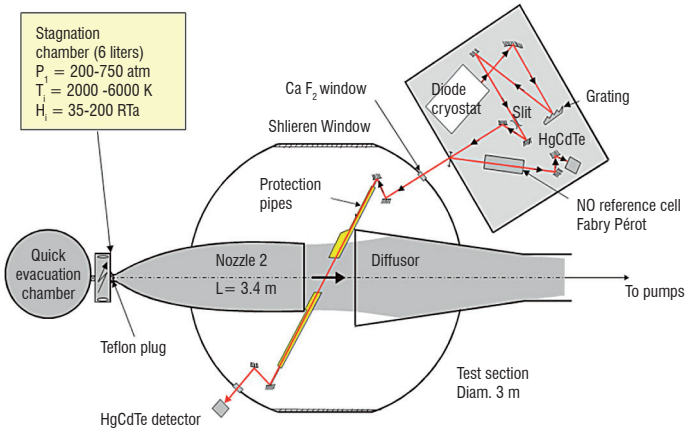

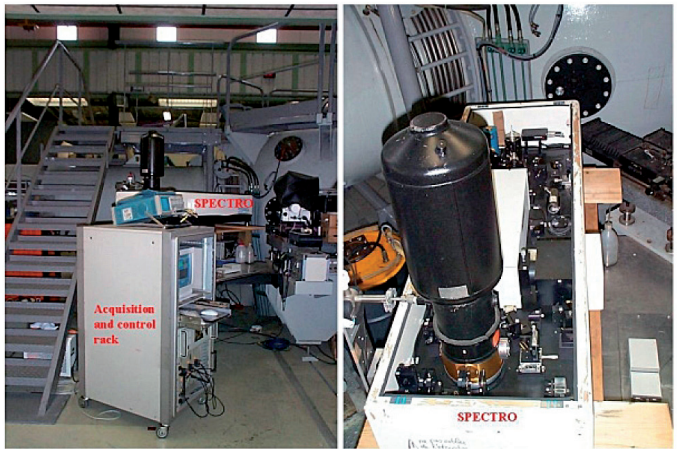

Figure 4 - Typical DLAS set up in the F4 wind tunnel The laser emission bench and the optical detection setup are outside the vacuum chamber. The laser beam enters the vacuum chamber through CaF_2 windows and crosses the flow at the smallest possible angle to the flow's axis, so as to induce the largest Doppler shift for velocity measurement purposes.

Data reduction

After wavelength and intensity calibration with the help of the calibration channels (Figure 3b), the useful segment of each corrected spectrum is matched to simulated spectra through an iterative non- linear least-squares fitting procedure [14] to retrieve the velocity, the kinetic temperature, and the concentrations of the absorbing species. The simulated spectrum is constructed from the classical Beer-Lambert absorption law. In a homogeneous medium, the attenuation of the beam intensity $I(\sigma)$ is thus described by:

$$I(\sigma) = I_0(\sigma)\exp\left[-S_x.f\left(\sigma,\sigma_x\right).N.L\right]$$

where $I_0(\sigma)$ is the initial intensity of the beam, N the density of the absorbing molecules, L the absorption path length, and S_x the absorption strength of the line centered at position σ_x. The function $f\left(\sigma,\sigma_x\right)$ is the normalized absorption line shape which takes into account all types of line broadening around the center wave number σ_x. Because of the high resolution achievable here, there is no line broadening due to the instrument used; the line profile is described solely by thermodynamic and molecular parameters of the medium. It is, in most cases, a Voigt function which is itself a convolution of a Doppler profile f_D with a Lorentz profile f_L. The Doppler profile describes broadening due to thermal motion of the molecules at the kinetic temperature, T :

$$f_D\left(\sigma-\sigma_x,T\right) = \frac{1}{\sqrt{\pi}\alpha_{xD}(T)}.\exp\left[-\left(\frac{\sigma-\sigma_x}{\alpha_{xD}(T)}\right)^2\right]$$

with the half-width at half maximum (HWHM) of the absorption expressed in cm^{-1} as :

$$\alpha_{xD}(T) = \sqrt{\ln(2)}\frac{\sigma_x}{c}\sqrt{\frac{2.k_B T}{m_{molécule}}} = 3.58.10^{-7}\sigma_x\sqrt{\frac{T}{M}}$$

where k_B is the Boltzman constant and M is the molar mass. The Lorentz profile represents line broadening due to collisions. It depends on the pressure P and the kinetic temperature of the medium:

$$f_L\left(\sigma-\sigma_x,P,T\right) = \frac{1}{\pi.\alpha_{xL}\left(P,T\right)}.\frac{1}{1+\frac{\left(\sigma-\sigma_x\right)^2}{\alpha_{xL}^2(P,T)}}$$

with HWHM given in cm^{-1} as :

$$\alpha_{xL}(P,T) = \alpha_{xL}^0\left(P_0,T_0\right)\frac{P}{P_0}\left[\frac{T_0}{T}\right]^{ylor}$$

The coefficients $\alpha_{xL}^0\left(P_0,T_0\right)$ and $ylor$ are derived either from quantum mechanics or through experiments. In our case, we use the values of $ylor$ (=1.5) and $\alpha_{xL}^0\left(P_0,T_0\right)$ from the HITRAN database [15], tabulated for a reference pressure $P_0 = 1$ atmosphere and temperature $T_0 = 296$ K.
In a flow with bulk velocity v, the center line wave number σ_x will be Doppler-shifted to $\sigma_x - \Delta\sigma_x$ with

$$\Delta\sigma_x = \sigma_x\frac{v}{c}\cos(\theta),$$

where θ is the angle between the laser beam and the flow axis, and c is the speed of light. In this case, the line shape has to be calculated from this shifted wave number $\sigma_x - \Delta\sigma_x$.
In a medium in thermodynamic equilibrium at T, the quantum mechanical expression of the line strength S_x is given as

$$S_x(T) = S_x(T_0).\frac{Q_x(T_0)}{Q_x(T)}.\frac{1-\exp\left[-hc\frac{\sigma_x}{k_B T}\right]}{1-\exp\left[-hc\frac{\sigma_x}{k_B T_0}\right]}.\exp\left[-\frac{E_x}{k_B}\left(\frac{1}{T}-\frac{1}{T_0}\right)\right]$$

where h is Planck's constant. $S_x(T_0)$ is determined experimentally or calculated at $T_0 = 296$ K [15]. $Q_x(T)$ is the partition function, E_x the molecular low-energy transition x absorbing at wave number σ_x.

Typical measurement results in high enthalpy wind tunnels

A simple two-layer model is usually assumed for the flow generated in high enthalpy wind tunnels. One layer corresponds to the flow core, with a constant free stream velocity V. The other layer (called the external layer) includes all of the gases outside the flow core with no bulk velocity that contribute to rest-position lines in the absorption spectrum. Figure 5a shows a series of spectra acquired at different times during a run together with the corresponding best fitted simulated spectra inferring the values for velocity, temperature and NO

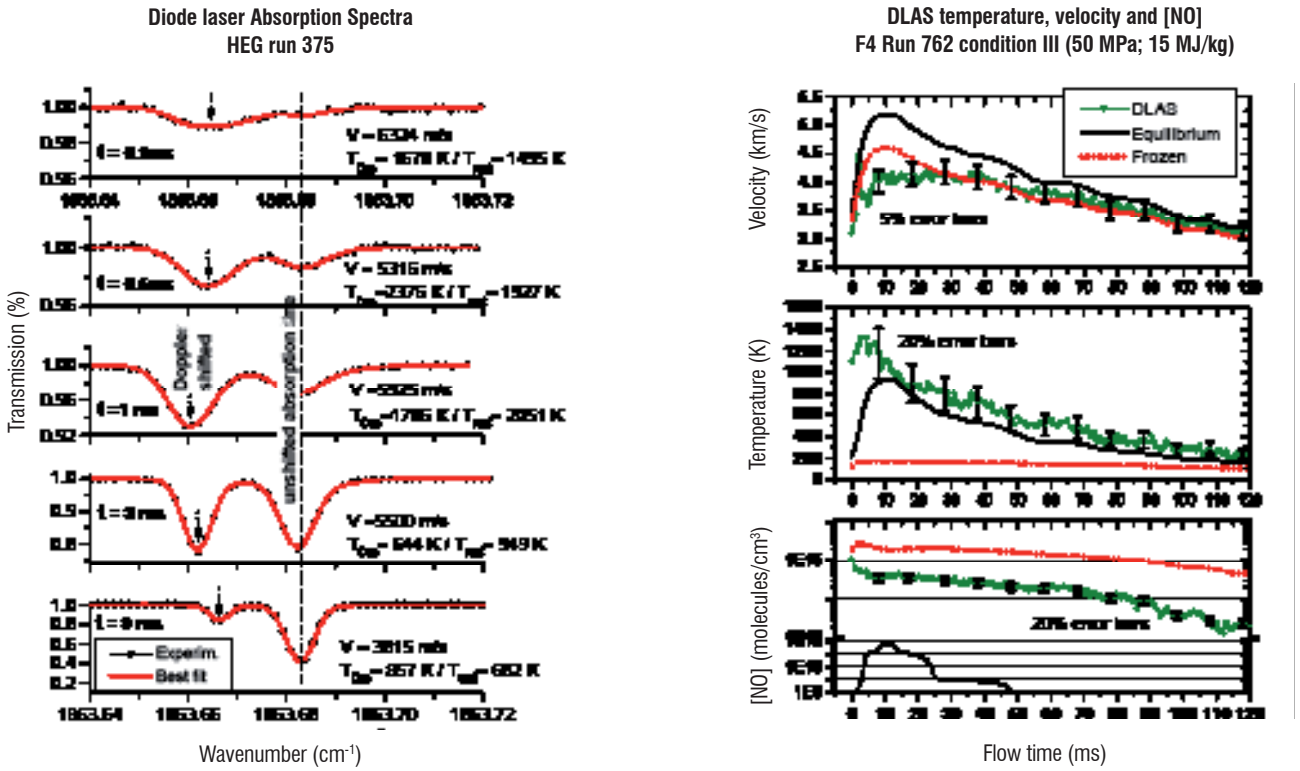

a) Typical flow absorption changes during a run at the DLR HEG shock tube monitored on the NO (R3/2) line [6]. The acquired spectra are matched to simulated ones to infer values for velocity, temperature and NO density

b) Changes over time in parameters deduced from acquired spectra for a run at the Onera F4 wind tunnel. The measured values are compared to two series of results from CFD calculations Equilibrium and Frozen hypothesis[16][17])

Figure 5 – Example of DLAS measurement results in high enthalpy wind tunnels

density. Only the spectral window around an NO line is presented. The parameter values derived from the processing of successive spectra are traced in Figure 5b and can be used to follow the time variations of such transient flows usually occurring in high enthalpy wind tunnels. In Figure 5b, the measured values are compared to two series of results from CFD calculations [16][17] assuming either 'equilibrium conditions' (where, using the temperature parameter example, vibrational temperature is equal to the kinetic temperature) or 'frozen conditions' (where the vibrational temperature remains at much higher values than the kinetic one and close to the temperature before expansion along the nozzle).

Measurements of aero engine effluents

We illustrate here the potential of laser absorption spectroscopy measurements on aero engine effluents through experiments performed in the framework of a European research project, MENELAS (Minority effluent measurements of aircraft Engine emissions by infrared Laser Spectroscopy [18]), carried out by a consortium of several aerospace institutes and laboratories led by Onera. The techniques which were under development were MIDROPO (Mid-infrared Doubly Resonant Optical Parametric Oscillator), Mid-infrared Pico-second LIDAR (MIRPL) and tunable diode laser absorption spectroscopy (DLAS). The latter was considered to be the technique with the highest maturity, which was ready to undergo field experiment demonstrations during the project's lifetime. The demonstrations were performed with a model gas turbine combustor in the DLR premises in Köln and on the exhaust gases of Cessna Citation II research aircraft at a test site at Amsterdam Airport Schiphol. An adapted version of the DLAS wind tunnel equipment already described above was deployed to probe CO, CO_2, NO and H_2O during these two demonstrations.

The experimental set up for the model combustor is presented in Figure 6. As the model combustor had optical access, the technique was not only used to measure at the outlet but inside the combustor as well. Fast fluctuations in the flow with a time scale of less than 1 ms were observed (Figure 7a) for the measurements. In order to reduce these effects on the spectra acquisition, the spectrometer was set to conduct measurements at a f=10 kHz repetition rate. This optical measuring technique provides integrated values along the line of sight of the laser beam.

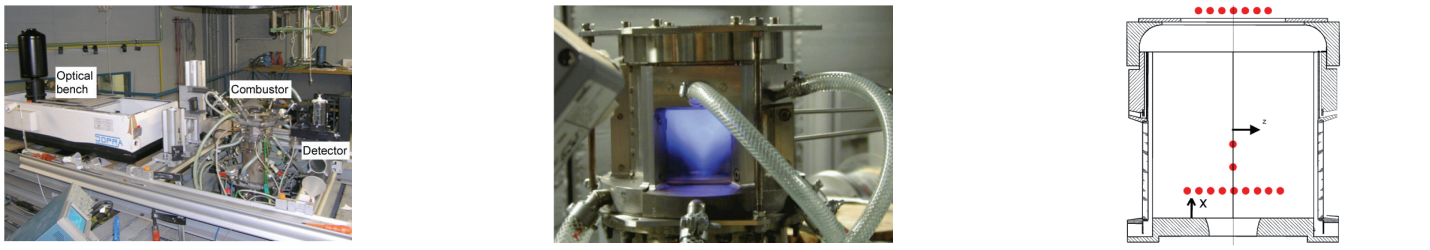

a) DLAS instrument at DLR testbed

b) Combustor in operation

c) Positions of optical measurements inside and at the outlet of the combustor

Figure 6 – DLAS experimental setup on a DLR combustor (Courtesy DLR Köln[19])

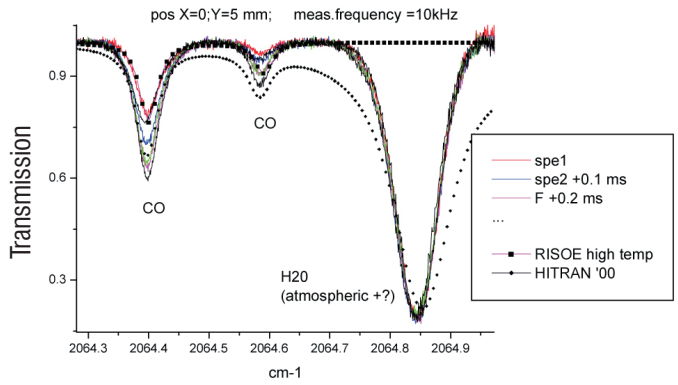

a) Examples of absorption spectra in the combustor

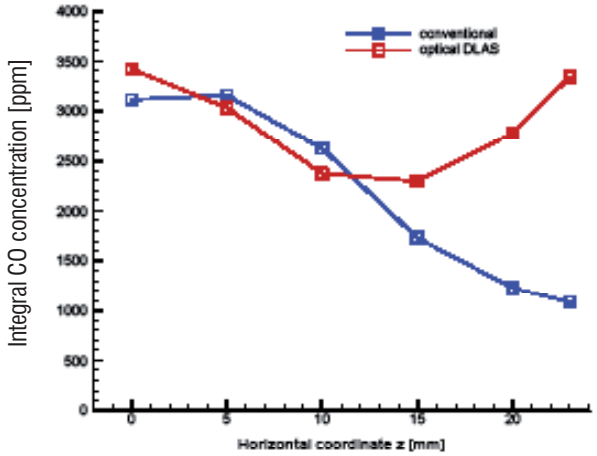

b) Horizontal profile of integral CO concentrations at x=10 mm inside the combustor at T_3=850 K and T_F=2000 K

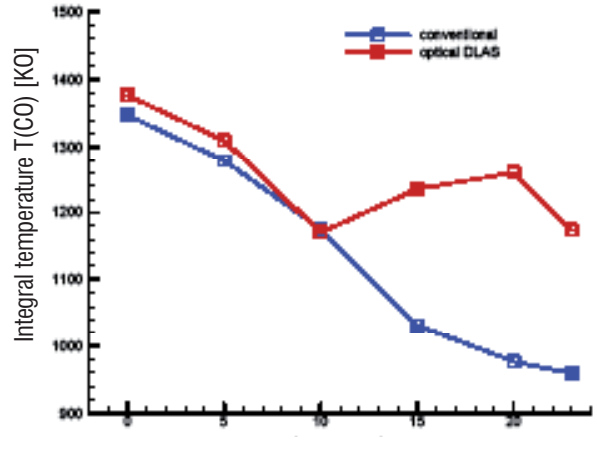

c) Horizontal profile of integral temperatures weighted with the CO concentration at x=10 mm inside the combustor at T_3=850 K and T_F=2000 K

Figure 7 – Examples of DLAS results for the DLR combustor (T_3= air preheat temperature; T_F: Flame temperature; detailed description is given in reference[19])

Therefore integral values had to be calculated [19] from the spatially resolved measurements with conventional techniques to allow a comparison with the optically measured data. Figure 7 (b,c) presents two comparative examples of temperature and CO concentration horizontal profiles. There is a good agreement with a deviation of about 10 % near to the flow axis whereas large differences, which are yet to be explained, appear close to the wall of the combustor.

The experimental setup for the second field experiment carried out during the MENELAS project is depicted in Figure 8a. The spectrometer was put in a van type vehicle placed at a distance of approximately 4 meters from the probed zone and mirrors mounted on poles near the engine were used to direct the laser beam so that it crossed the flow vertically at a distance of 80 cm downstream of the engine outlet. Only measurements on CO and H_2O were tried during the time window allowed for the experimental campaign. A few examples of results obtained are presented in Figure 8b for a set of successive spectra acquired at 10 kHz during 6 ms for engine thrust settings at 30% of maximum power (other details can be found in reference [20]).
These MENELAS experiments demonstrated that infrared laser absorption spectroscopy has the potential for fast and high spatial resolution measurements of combustion species. However, some future development work on more rugged equipment is still needed as the goal is to replace the gas analysis currently performed with intrusive probe measurements in order to fulfill ICAO standards for engine emission measurements and to help us understand the combustion processes in a gas turbine.

a) Set up at the NLR test site

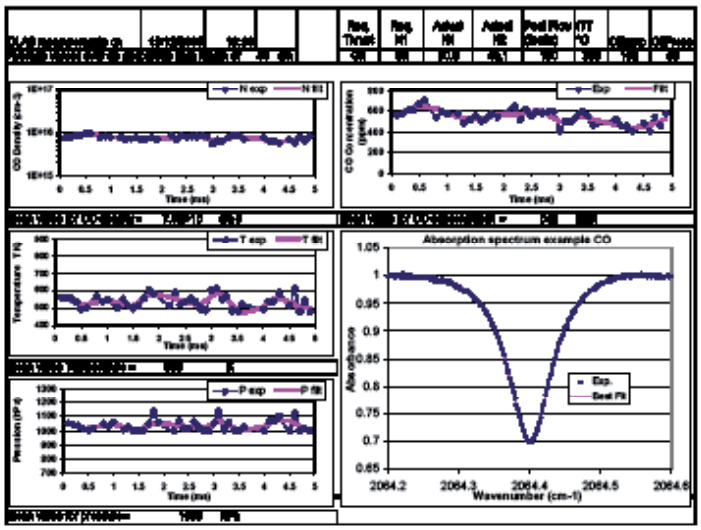

b) Examples of measurements

Figure 8 – DLAS measurements on the exhaust gases of the NLR's Cessna Citation II research aircraft at a test site at Schiphol Airport Amsterdam (Courtesy NLR)

Prospects

The use of mid-infrared diode lasers has been a great help in the development of absorption spectroscopy for applications in different flow media in aerodynamics and combustion. The trend now is to develop low cost setups with non-cryogenic semiconductor lasers

(QCL [9] in the mid IR, interband cascade lasers (ICLs [10]) and GaSb DFB diode lasers [11] in the 2-3 μm range) for less cumbersome and more routine use of this technique. Moreover, the beams from such lasers can be more easily collimated and open up new possibilities for fiber-optic coupling. This can help to protect the beam up to the edges of the flow thereby reducing the interference caused by diffused molecules outside of the flow. The fiber optic possibility also allows for the use of miniature probes which can be placed inside the flow for localized probing.

However, semiconductor lasers emit only on limited spectral windows and are of low power. Fortunately development in non linear optics now offers the possibilities of new laser sources (OPO [12]) with high brightness and wide spectral coverage in the mid-infrared spectrum. (see box 2).

Other improvements which may offer new possibilities for the laser absorption technique are:

- Use of several laser beams at different wavelengths for simultaneous measurements on several species
- Flow tomography coupled with Abel inversion through the use of several laser beams or quick spatial scanning of a single laser beam
- Use of multi-pass or CRDS methods to enhance sensitivity (see box 1): this can help with the probing of very weak absorption lines (like that for O_2) or can allow for short absorption lengths, with the aim of building miniature probes placed in a flow for more local measurements ■

Box 1 - High Speed Cavity Ring-Down Spectroscopy

CRDS is a laser-based absorption spectroscopy technique which directly deduces the absolute value of optical losses in a high finesse optical cavity from its photon lifetime [O'keefe]. The ring-down cavity is created by positioning two highly reflective mirrors (R>99.99) around the gas medium of interest. The light source is coupled to the ring-down cavity, resulting in a rapid buildup of the intensity of radiation trapped inside. After abruptly stopping the laser injection, the stored light propagates back and forth within the cavity and, at each pass, gradually leaks out through the mirrors. The transmitted intensity I(t) is an exponential decay of the initial intensity I0 given by the equation

$$I(t) = I_0 \exp\left(-t/\tau\right) \qquad (1)$$

where τ is the ring-down time of the cavity. The loss rate per distance is then given by

$$\frac{1}{c\tau} = \frac{1-R+A}{L} + \alpha \qquad (2)$$

with c the speed of light, L the cavity length, R the reflectivity of the mirrors, A the diffraction losses of the mirrors, and α the medium absorption coefficient. A plot of the loss rate α as a function of the laser frequency is a CRDS spectrum. The absorption loss profile is directly proportional to the chosen absorption line profile from which one can deduce the specie concentration, as well as the temperature, pressure and velocity in gas flows. CRDS has originally been developed with pulsed laser sources [O'keefe] but has since been proven to work with continuous-wave lasers as well [Romanini]. The basic principle of a cw-CRDS setup is illustrated in Fig. B1-01.

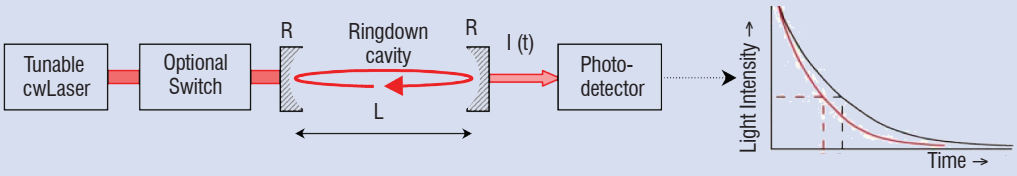

Figure B1-01. Diagram of a typical ring-down setup that produces an exponential decay of the transmitted light after termination of the laser coupling. An optional acousto- or electro-optic switch is generally used to interrupt injection by cw laser sources and prevent further entry of light. τ_0 and τ

Compared with traditional single or multi-pass absorption methods, CRDS exhibits the advantages of long effective absorption path lengths (many kilometers) combined with intrinsic insensitivity to source-intensity fluctuations, thus offering a great sensitivity which already been exploited in a wide variety of fields. But the measurements times using a standard scheme are usually relatively long in the order of seconds if not minutes due the laser wavelength positioning and optical switching for a clean exponential decay in the cavity.

Improvements in the measurement speed are therefore required to enable fast and sensitive analysis of transient flows such as those generated in blow-down hypersonic wind tunnels. Indeed, the flows we are targeting are generated during short gusts, typically lasting a few 100-ms, with aerodynamic conditions changing by a few % per ms. A scheme allowing the measurement of an absorption line within time period of a ms is therefore required (shorter times are sought to combat fluctuations in combustion flames). Another difficulty arises from the low pressure nature of the gas met in wind tunnels, usually of a few mbar presenting absorption line widths essentially due do Doppler broadening and which are at one tenth smaller than those at atmospheric pressure (Lorentz broadening).

It has already been demonstrated that, in conventional cw-CRDS, a rapid extinction of the laser beam, enabling a free exponential photon decay is possible without any optical switch using only a fast sweep either for the cavity length at fixed laser frequency [He1], or for the laser frequency over the motionless cavity modes [He2]. In both cases, a partial build-up of the intra-cavity energy rapidly occurs as soon as the resonance condition between the laser frequency and a cavity mode is satisfied. The subsequent light exponential decay is observed as the laser frequency and the cavity mode come out of resonance. However, to get a decent signal to noise ratio, averaging procedures have to be applied on the signals thus giving long integration times. At Onera, we further developed the fast laser sweep concept with low noise avalanche photo-detectors and were able to reduce the acquisition time of an exploitable absorption profile to 2 ms with a repetition rate of 250 Hz compatible with our wind tunnel application [Debecker].
In the case of a rapid laser frequency sweep on a static cavity of length L, the maximum achievable frequency resolution corresponds to the free spectral range (FSR), which is $FSR_{\text{static}} = 1/2nL$, in spectroscopic cm^{-1} units with n the refractive index approximated to one and henceforward discarded. As an example, for a 50-cm-long cavity, the separation between ring-down events is 0.01 cm^{-1} (0.3 GHz). In flows simulating reentry conditions at high altitudes, this resolution is insufficient to probe low pressure absorption line widths (or Doppler shifts for velocity measurements) which are of the order of 0.05 cm^{-1}. We present below two ways we investigate how to improve spectral resolution in high speed cw-CRDS designs.

CRDS spectral resolution enhancement by simultaneous laser and cavity tuning

One way to enhance spectral resolution involves simultaneous laser and cavity tuning. In order to increase the number of recorded ring-down events, the cavity resonance mode frequencies (V_{mode}) must be synchronously swept in the opposite direction to the laser mode (V_{λ}). This leads to an increased number of frequency-matched events between the laser and the cavity, giving ring down points separated by a spectral interval smaller than the FSR of the static cavity as shown in Figure B1-02. An experimental result on an O_2 line at high and low pressure is presented in Figure B1-03.

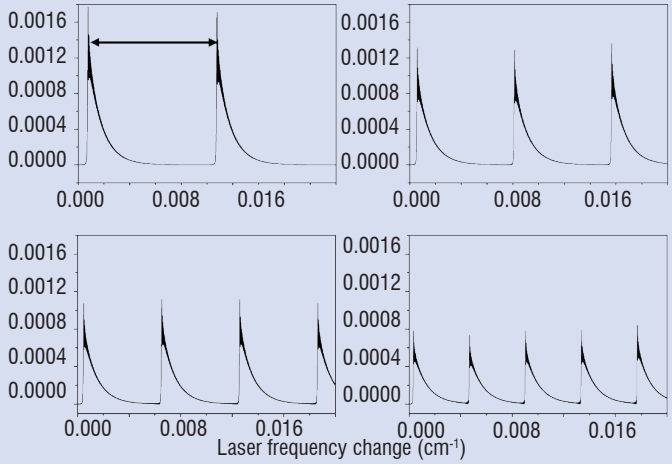

Figure B1-02 – Increased ring-down events for simultaneous cavity and wavelength tuning (0.4 cm^{-1} in 2 ms)

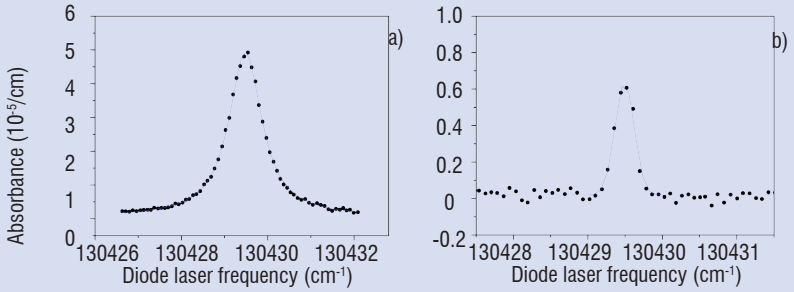

Figure B1-03. Absorption spectra for O_2 in air, recorded during a 280-Hz laser frequency-sweep and a synchronous 5-μm cavity modulation range. (a) At atmospheric pressure, a Lorentzian profile of 0.095-cm-1-FWHM is superposed to the experimental points. (b) At 20 mbar, a 0.025-cm-1-FWHM Gaussian profile provides a fit of the plotted points.

The spectral resolution enhancement factor can be derived from the expression of the dynamic FSR for a moving cavity [Debecker]:

$$FSR_{dynamic} = \frac{1}{2L - 2\lambda \frac{V_L}{V_\lambda}} \quad (3)$$

where V_{λ} and V_L are the linear scanning velocities respectively for laser wavelength and cavity length tuning. The velocity for a resonance mode of the cavity is expressed as $V_{\text{mode}} = -\lambda V_L / L$ and must therefore be of opposite sign to V_{λ} for spectral resolution enhancement.

The denominator in equation (3) presents all of the parameters to tune for resolution enhancement. Fig. B1-04a illustrates one of the possibilities, namely the influence of cavity length scanning velocity V_L while other parameters are fixed at the values $\lambda = 0.766\ \mu m$, L=0.5 m, $V_\lambda = 0.2$ cm-1/ms corresponding to one of our experimental setups described in reference [Debecker]. Fig. B1-04b shows that the resolution enhancement increases with shorter cavities, which is quite welcome in the task of miniaturizing a CRDS device.

a) Influence of velocity for cavity length tuning

b) Influence of cavity length

Figure B1-04- Dependence of the dynamic FSR and the enhancement factor of spectral resolution on the cavity length tuning speed.

CRDS spectral resolution enhancement using transverse modes

Another scheme we investigated for increasing spectral resolution during a rapid scan of the laser wavelength is based on the use of a cavity's transverse mode structure. But the straightforward use of the different mode orders leads to quite noisy absorption line profiles because of mode overlapping and also due to the fact that each transverse mode exhibits a distinct decaying coefficient. This is because each mode has a distinct spatial overlapping pattern with the mirrors' surfaces which are generally not homogeneous in reflectivity. However, these problems can be circumvented through off axis injection (Fig. A5). By choosing a proper ad hoc cavity length, called the "magic length", the continuum comb of the TEMmn cavity structure modes encountered by an incoming plane wave is converted into a fractionally degenerate mode structure. For a particular length, the "magic length", therefore is a finite number N of the family of degenerate modes within an FSR on-axis of the cavity. This factor N also defines the number of cavity round-trips before the spatial beam overlapping leading to an effective FSRoff-axis = FSR on-axis/N thereby increasing the spectral sampling by a factor of N. The cavity's length can be imagined as having been stretched by the factor N. There is no overlapping between individual transverse modes and the same surfaces of the mirrors are seen by all the groups of degenerate modes leading to absence of mode-to-mode fluctuations and hence quite smooth absorption profiles. Moreover, this injection scheme is also useful for attenuating the ringing effect usually observed with on-axis injection [Courtois].

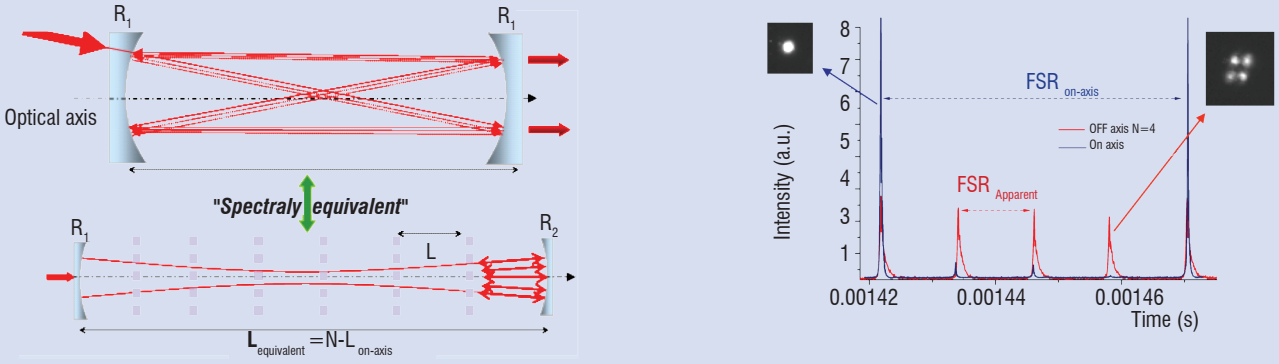

Figure B1- 05 - (Left side) Off-axis injection principle with below its on-axis spectral equivalence. (Right side) Comparison between TEM00 on-axis injection (Excitation of first transverses modes can be observed on the figure) and N=3,K=1 (i.e same cavity size) off-axis injection of the cavity. Because in off-axis (for discrete round trip Gouy phase value) light spatially overlaps on itself after N round trips (red ring down events), apparent FSR is divided by N. Since one resonance leads to one point on the profile, spectral resolution is increased by a factor N.

[O'Keefe] A. O'KEEFE AND D. A. DEACON - *Cavity ring-down optical spectrometer for absorption measurements using pulsed laser sources*. Rev. Sci. Instrum. 59, 2544-2551 (1988).

[Romanini] D. ROMANINI, A.A. KACHANOV, N. SADEGHI, AND F. STOECKEL - *CW cavity ring-down spectroscopy.* Chem. Phys. Lett., 264, 316-322 (1997).

[He1] Y. HE AND B. J. ORR - *Optical heterodyne signal generation and detection in cavity ring-down spectroscopy based on a rapidly swept cavity.* Chem. Phys. Lett., 335, 215-220 (2001).

[He2] Y. HE AND B. J. ORR - *Rapid measurement of cavity ring-down absorption spectra with a swept-frequency laser*. Appl. Phys. B, 79, 941-945 (2004).

Box 2 - New laser sources for absorption spectroscopy

Most lasers have a frequency tuning range which is restricted to a small fraction of the frequency gap between the quantum levels connected by the laser radiation. This rather limited wavelength tunability has restricted the potential use of the main lasers to only a few applications of spectroscopy. Indeed, in order to address the fundamental absorption lines of most molecular species, a laser source that provides wide tuning over the mid-infrared domain (2-10 μm) is needed. Among the potential laser sources, there are quantum cascade lasers and parametric devices. Here, our interest is mainly focused on parametric devices which are very promising for spectroscopy due to their very broad tunability.

Parametric devices are wavelength converters based on a second order nonlinear optical process. Basically, the frequency conversion is obtained by illuminating a nonlinear crystal with a laser beam at a given frequency (ω_p), see Figure B2-01. The crystal acts as a gain medium for the production of two waves called signal and idler, respectively at frequencies ω_s and ω_i such that $\omega_p = \omega_s + \omega_i$, this relationship expresses the conservation of the photon energy which is a specific property of any parametric process. Because the parametric conversion is not a resonant process, the possible values of the signal and idler frequencies do not depend on the discrete energy levels of the nonlinear medium, in opposition to a laser medium. Indeed, ω_s and ω_i are determined by the conservation of momentum or phase matching condition $k_p = k_s + k_i$ where k_j is the wave vector of the wave j. Given that each wave vector depends on the refractive index of the medium, the signal and idler frequencies can easily be tuned by changing the propagating conditions of the three waves through the nonlinear crystal yielding a frequency tuning range that is limited only by the optical dispersion of the index of refraction and the optical transmission of the nonlinear crystal.

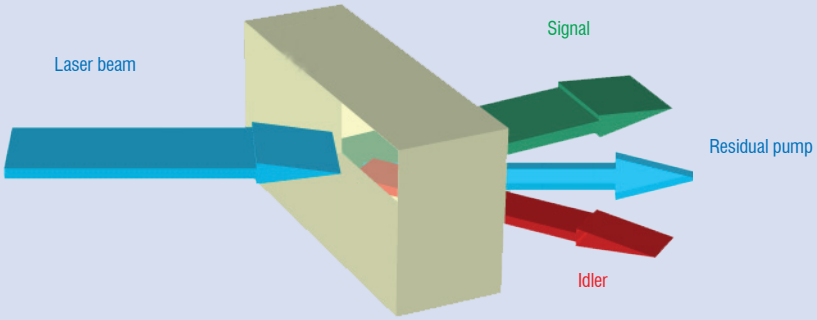

Figure B2 - 01 - Illustration of the parametric conversion process

Two main approaches for adjusting the output wavelengths are now well developed. The first one uses a birefringent crystalline medium where the phase matching condition and subsequently the ω_s and ω_i frequencies are obtained by selection of the waves' polarizations, crystal orientation and/or temperature adjustment. The second one uses a micro-structured nonlinear medium to compensate the optical dispersion of the material periodically. In which case, the momentum conservation is obtained in a quasi-phase matching approach where the optical wave vectors are related to the grating vector of the periodic structure (kG) by $k_p = k_s + k_i + k_G$, where $|k_G| = 2\pi / \Lambda$, Λ is the grating period. Most of commercial quasi-phase matched crystals are produced with ferroelectric materials (lithium niobate, lithium tantalite, ….) where the ferroelectric orientation has been periodically poled in opposite directions by using an electric-field poling technique, see Figure B2-02. Such a technique allows the nonlinear material to be engineered for the desired output wavelengths by choosing the poling period. The signal and idler frequencies can be tuned around the central wavelength, which is fixed by the poling period, by adjusting the crystal's temperature.

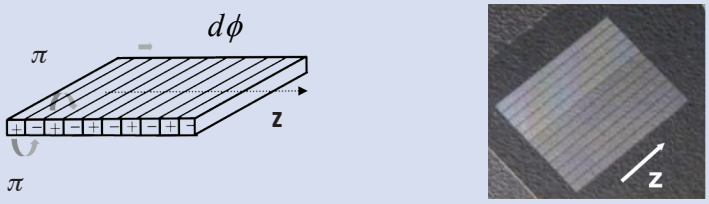

Figure B2 - 02 - Principle of the quasi-phase matching technique (left) and picture of a commercial periodically poled crystal comprising 12 parallel gratings

Parametric devices based on birefringent or quasi-phase matched crystals are able to convert a fixed pump frequency into a pair of widely tunable mid-infrared radiations that can be used for spectroscopic applications. Nonetheless, the simplest architecture based on a pump laser followed by a non linear crystal cannot provide the required specifications for most spectroscopic applications. Firstly, the parametric conversion efficiency is rather low and therefore, after only one pass through the non linear crystal, the available energy is usually too limited for high sensitive gas sensing. Secondly, the band width of the parametric gain curve is relatively broadband (10 cm^{-1} or more) leading to signal and idler line widths that are too broad for spectroscopic applications which require a line width of less than 0.01 cm^{-1}.

To overcome these two limitations, two approaches have been developed. The first one is based on difference frequency generation (DFG). Basically, DFG-systems use a mid-IR narrow band radiation which is obtained by mixing a pump laser beam and a tunable diode laser, usually working in the telecom band, through a nonlinear crystal. This approach has been mainly used in the continuous wave regime with a multipass cell in order to perform high sensitive DFG-spectrometers. The main advantage of DFG-spectrometers results from their simplicity, however the range of applications is limited by the availability of tunable diode lasers and the low output power level available after DFG. The second approach is based on optical parametric oscillators (OPOs). In this case, the nonlinear crystal is placed within an optical resonator, taking advantage of multiple round-trips through the parametric gain medium.
The simplest OPO scheme is based on an optical resonator which is resonant at only one wavelength (signal or idler, exclusively). Singly resonant OPO provides good conversion efficiency (> 10 %) and can deliver a narrow line width by inserting intra-cavity dispersive elements or by injection-seeding the optical resonator with an external laser source. However, the introduction of dispersive elements (diffraction grating, Fabry Perot etalon) increases the optical losses of the resonator and consequently the threshold of oscillation of the OPO whereas the injection seeding technique reduces the spectral range of the OPO to the seed source tunability. These two limitations can be circumvented by using an optical resonator where both the signal and idler radiations are resonant in two separate cavities, see Figure B2-03. As has been demonstrated at Onera, a dual-cavity doubly resonant OPO can oscillate on a single longitudinal mode with a low threshold of oscillation. For reasons of compactness, the dual-cavity doubly resonant OPO developed at Onera is based on two entangled cavities where four mirrors are placed symmetrically on each side of the non linear crystal, see Figure B2-03. The signal and idler waves oscillate between pairs of mirrors M1-M3 and M2-M4, respectively. The inner mirrors (M1, M4) are deposited onto the crystal faces whereas the external mirrors (M2, M3) are mounted on two PZT actuators for fine frequency tuning. The radii-of-curvature of external mirrors are chosen to optimize the mode overlapping between the two cavities and the pump beam.

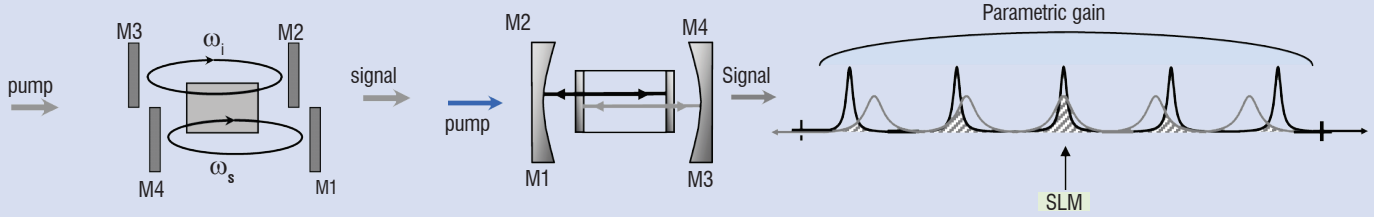

Figure B2 - 03 - Dual-cavity doubly resonant OPO (left); entangled cavities arrangement (right).

Figure B2 - 04 - Principle of the spectral filtering by Vernier effect.

In a dual-cavity doubly resonant OPO, the signal and idler fields experience two different cavities whose optical lengths can be separately adjusted to obtain different free spectral ranges. Doubly resonant oscillation can only take place at discrete spectral positions where there is a mode coincidence between the signal and idler cavities within the parametric gain curve. Thus, single longitudinal mode operation can be achieved if the two cavities lengths are adjusted to get just one mode coincidence. This situation is achieved by choosing slightly different optical lengths. Figure B2-04 illustrates the principle of mode selection that we call 'spectral filtering by Vernier effect'. Experimentally, stable single longitudinal mode operation is obtained if the two cavity lengths differ by 5 to 10 %. Once the doubly resonant oscillation has been achieved, the output frequency can be finely tuned by adjusting the two cavities' lengths simultaneously by means of two PZT actuators so as to maintain the mode coincidence during the frequency scanning procedure.

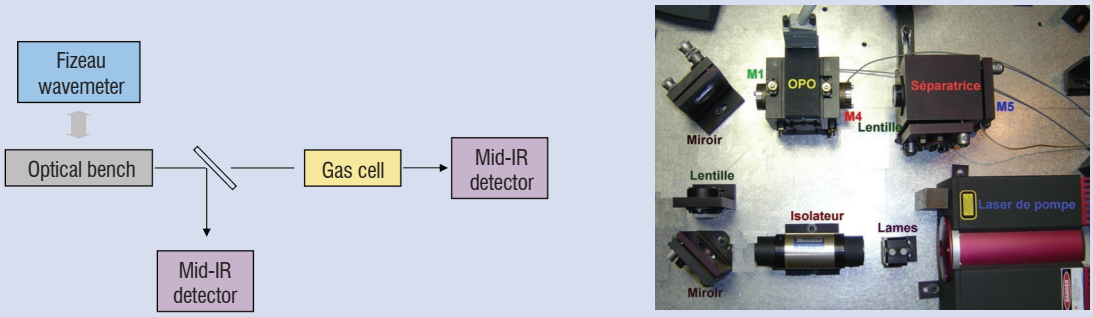

Figure B2-05 : Experimental set-up for absorption spectroscopy; general diagram (left) an optical bench (right)

The potentiality of the dual-cavity doubly resonant OPO for spectroscopic applications has been tested with the experimental set-up depicted in Figure B2 - 05. The pump radiation is produced by a compact passively Q-switched Nd: YAG laser. This commercial laser (Innolight, model Mephisto Q) delivers 20 μJ pulses at a 10 kHz repetition rate, the pulse duration is 8 ns. The non linear crystal is a 6 mm-long multi-grating periodically poled lithium niobate (PPLN) providing a tunable idler radiation between 3.8 to 4.2 μm. The output coupling of the idler field is obtained through M4, which has a partial reflectivity (70 %) around 3.9 μm.

In order to perform high resolution absorption spectroscopy, 50 % of the idler radiation goes through a 10-cm long absorption cell while 50 % is used for power normalization. We get absorption spectra by recording the ratio of the two signals versus the idler wavelength. A Fizeau wavemeter monitors the signal wavelength coming from the OPO.

An absorption spectrum of N_2O at a pressure of 10 hPa is shown in Figure B2-06 as well as the simulated spectrum obtained from the Hitran database. The results demonstrate that absorption spectra can be recorded in continuous, mode-hop-free scans over more than 10 nm. They also illustrate the narrow optical line width delivered by the dual-cavity doubly resonant OPO. This experiment is a preliminary step towards making highly sensitive gas sensors based on optical parametric oscillators.

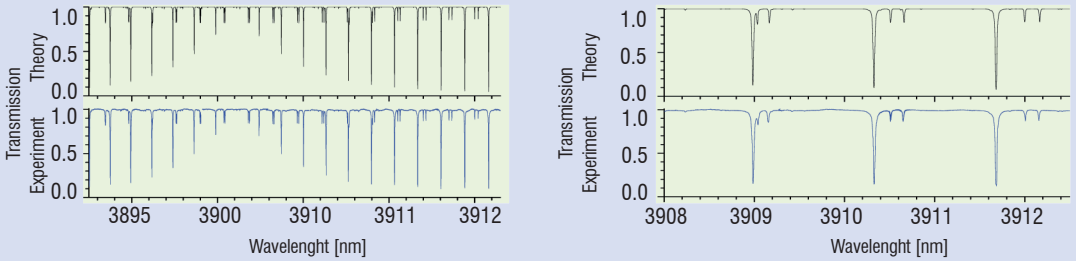

Figure B2 - 06 - N_2O absorption spectrum recorded at 10 hPa (in blue), the high resolution is illustrated by zooming the 3910 nm region (right side); the most-intense absorption lines are attributed to the $2\nu_1$ fundamental vibrational band, whereas the doublets of lines are related to the hot vibrational band $(2\nu_1 + \nu_2 \rightarrow \nu_2)$.

References

[1] J. C. HILL, G.P. MONTGOMERY - *Diode Lasers for Gas Analysis*. Applied Optics, vol.15,n° 3, p.748-755, 1976

[2] B. ROSIER, D. HENRY, A. COPALLE - *Carbon Monoxide Concentrations and Temperature Measurements in a Low Pressure CH4-O2-NH3 Flame*. Applied Optics, vol.27,n° 2, p.360-364, 1988

[3] M. P. ARROYO, S. LANGLOIS, R. K. HANSON - *Diode Laser Absorption Technique for Simultaneous Measurements of Multiple Gas Dynamic Parameters in High Speed Flows Containing Water Vapor*. Applied Optics, vol 33, nm15,20 May 1994

[4] A. K. MOHAMED, B. ROSIER, D. HENRY, Y. LOUVET, P. L. VARGHESE - *Tunable Diode Laser Measurements on Nitric Oxide in a Hypersonic Wind-Tunnel*", AIAA Paper 95-0428

[5] A. K. MOHAMED, B. ROSIER, P. SAGNIER, D. HENRY, Y. LOUVET, D. BIZE - *Application of Infrared Diode Laser Absorption Spectroscopy to the F4 High Enthalpy Wind Tunnel*. Aerospace Science and Technology, n°4,241-250, 1998

[6] A. MOHAMED, D. HENRY, J. P. FALÉNI, P. SAGNIER, A. MASSON,W.BECK - *Infrared Diode Laser Absorption Spectroscopy Measurements in the S4MA, F4 and HEG Hypersonic Flows*. International Symposium on Atmospheric Reentry Vehicles and Systems, Arcachon (France),16-18 March 1999

[7] W. H. BECK, O. TRINKS, M. WOLLENHAUPT, A. MOHAMED, C. NIEDERBAÜMER, P. ANDRESEN, T. KISHIMOTO, H. BITO - *Probing of the Reservoir, Free Stream and Shock Layers in HEG using Spectroscopic Techniques*. Paper 1350, 21st International symposium on Shock Waves, Great Keppel Island, Australia, July 20-25, 1997

[8] A. MOHAMED, J.L. VERANT, J. SOUTADÉ, P. VIGUIER, B. VAN OOTEGEM, P. TRAN - *Mid-Infrared Diode Laser Absorption Spectroscopy Measurements in CO-CO_2 Hypersonic Flows of F4 and SIMOUN*. 6th European Symposium on Aerothermodynamics for Space Vehicles, Versailles (France) 3-5 November 2000

[9] ANATOLIY A. KOSTEREV AND FRANK K. TITTEL - *Chemical Sensors Based on Quantum Cascade Lasers*. IEEE journal of quantum electronics, Vol. 38, no. 6, June 2002

[10] W. W. BEWLEY, C. L. CANEDY, C. KIM, M. KIM, J. A. NOLDE, D. C. LARRABEE, J. R. LINDLE, I. VURGAFTMAN, AND J. R. MEYER - *Mid-Infrared Interband Cascade Lasers Operating CW at Thermoelectric-Cooler Temperatures.* Conference on Lasers and Electro-Optics/Quantum Electronics and Laser Science Conference and Photonic Applications Systems Technologies, OSA Technical Digest (CD) (Optical Society of America, 2008), paper CTuZ3

[11] ABDELMAGID SALHI, DAVID BARAT, DANIELE ROMANINI, YVES ROUILLARD, AIMERIC OUVRARD, RALPH WERNER, JOCHEN SEUFERT, JOHANNES KOETH, AURORE VICET, AND ARNAUD GARNACHE. *Single-Frequency Sb-based Distributed-Feedback Lasers Emitting at 2.3 μm above Room Temperature for Application in Tunable Diode Laser Absorption Spectroscopy*. Appl. Opt. 45, 4957-4965 (2006)

[12] A. DESORMEAUX, M. LEFEBVRE, E. ROSENCHER, AND J.-P. HUIGNARD - *Mid-Infrared High-Resolution Absorption Spectroscopy by Use of a Semimonolithic Entangled-Cavity Optical Parametric Oscillator*. Opt. Lett. 29, 2887-2889 (2004)

[13] G.BERDEN, R.PEETERS, G.MEIJER - *Cavity Ring-Down Spectroscopy: Experimental Schemes and Applications*. International Reviews in Physical Chemistry, Vol. 19, No. 4., pp. 565-607, (2000)

[14] A. K. MOHAMED - *MSTP Phase 2 Progress Report. Infrared Diode Laser Absorption Spectroscopy in Wind Tunnels*. I-Experimental Setup, II-Data Reduction Procedures (ESA -HT-TN-E34-701&702&703-ONER), Onera Technical Report n° 8 and 9 /7301 PY, 1996.

[15] L. S ROTHMAN. et al. *The HITRAN 2008 molecular spectroscopic database*. Journal of Quantitative Spectroscopy and Radiative Transfer, Volume 110, Issues 9-10, Pages 533-572 1992, June-July 2009

[16] PH. SAGNIER, J. L. VÉRANT - *Flow characterization in the Onera F4 high_enthalpy wind tunnel*. AIAA J., Vol.36, N°4, pp.522-531, 1998

[17] PH. SAGNIER, J. L. VÉRANT - *On the Validation of High Enthalpy Wind Tunnel Simulations*. Aerospace Sciences and Technology, n°7, p. 425-437 , 1998

[18] MENELAS - *Project Final Report*. European Community Contract G4RD-CT-2002-00645, Onera RF 3/07279 DMPH - September 2006

[19] T. BEHRENDT, C. HASSA, A. MOHAMED, J.-P. FALÉNI - *In situ Measurement and Validation of Gaseous Species Concentrations of a Gas Turbine Model Combustor by Tunable Diode Laser Absorption Spectroscopy (TDLAS)*. Paper GT2008-51258, Proceedings of ASME Turbo Expo 2008,Berlin, Germany, June 9-13, 2008

[20] H.W. JENTINK, H.P.J. VEERMAN, A.K. MOHAMED AND P. GEISER - *Spectroscopic Measurements of Aircraft Exhaust Gas*, MENELAS Report D 12, National Aerospace Laboratory NLR Report NLR-CR-2006-100, 2006

Acronyms

DLAS (Diode Laser Absorption Spectrometer)
HWHM (Half-Width at Half Maximum)
OPO (Optical Parametric Oscillator)
MIDROPO (Mid-Infrared Doubly Resonant Optical Parametric Oscillator)
MIRPL (Mid-Infrared Pico-second LIDAR)
TDLAS (Tunable Diode Laser Absorption Spectroscopy)
CRDS (Cavity Ring Down Spectroscopy)

AUTHORS

Ajmal Khan Mohamed obtained his Ph.D. in Molecular Physics from the University of PARIS XI in 1991. He then joined the Physics Department of Onera to continue the development of several optical diagnostics (Infrared Diode Laser Absorption Spectroscopy, Electron Beam Fluorescence, Emission Spectroscopy) to probe high enthalpy hypersonic flows in arcjets and shock tubes. He has also been involved in solid state laser development for Laser Induced Fluorescence and in cavity enhanced spectroscopy for trace species detection. He managed several internal or European projects on these techniques for in-flight measurements as well as for environmental applications and is still active in this field of optical diagnostics.

Michel Lefebvre received his Ph.D Degree from the University of Lille I and the Habilitation Degree in Optics from the University of Paris XI. He is currently senior scientist at Onera where he leads the 'Laser Sources and Sensing Physics' research unit in Palaiseau. He conducted various studies in non linear optics and laser sources. He developed and applied the CARS technique to reactive flow and hypersonic wind tunnels. His current research covers parametric conversion processes and optical parametric laser sources.

M. Barthelemy, L. Hespel, N. Rivière,
(Onera)
B. Chatel
(Irsamc)
T. Dartigalongue
(Onera)

Email: thibault.dartigalongue@onera.fr

Pump Probe Experiment for Optical Diagnosis of Very Thick Scattering Media

Scattering media with very high optical density are present in a great variety of application: clouds, paints, spray and biological cells. New optical diagnosis tools developments are very important in order to get in situ characterization without disturbing the sample. The goal of this paper is to describe a new method for determining the Particle Size Distribution (PSD) of a very thick scattering medium. This method is based on Optical Density (OD) measurements for different wavelengths, and a numerical inversion algorithm. The experimental challenge is to operate a light source that is both bright enough and tuneable in order to carry out such measurements. In addition, the scattered light has to be filtered. We will demonstrate that femtosecond spectroscopy overcomes all of these difficulties. A numerical inversion algorithm has been implemented in order to determine the PSD from an OD spectrum.

Introduction

The Optical Density spectrum (*OD*) can be obtained using very basic measurements. The idea is to measure the transmission of a given sample for different wavelengths λ. Optical density is defined by:

$$OD(\lambda) = \log_{10}\left(\frac{I_0}{I_t}\right) \quad (1)$$

where I_0 denotes the incident flux, and I_t the transmitted flux after the sample. Many commercial spectrophotometers can be readily found, and almost every optical laboratory possesses one. *OD* measurements can give a huge variety of information regarding the sample of interest: optical, physical and chemical properties. The goal of this paper is to focus on the Particle Size Distribution *PSD* determination of very thick scattering media. The size of the different particles of a scattering medium is a key factor [14,15]. When studying the optical behaviour of a cloud, it is the size of water droplets that governs the behaviour of the cloud. The size of the particles in an exhaust pipe just at the outlet of a combustion chamber will give relevant information about the efficiency of combustion. The composition of paints can be optimized if the size of the particles of a paint spread and dried in a coat is known. The list of all possible applications of (*PSD*) determination is quite long. In this paper, we study the model case of a suspension of homogenous spherical particles in a solvent. We define r as the radius of the particle and m the ratio between the refractive index of the particle and the refractive index of the solvent. This index ratio can be a complex number if we consider absorption processes. At the interface between the particle and the solvent, the change of refractive index will create reflection or refraction of the light. As a result, the interaction between light and particles will change the direction of the incoming beam light. This is the so called scattering process. The extinction cross section σ_{ext}, *i.e.* the probability that a photon will be scattered by a particle (or be absorbed) is calculated by Lorenz-Mie theory [10], and strongly depends on m, r and the wavelength λ. For a suspension of particles with an uniform radius r, the Beer-Lambert law can be written as:

$$I_t = I_0 \exp\left[-NL\sigma_{ext}(m,r,\lambda)\right]$$

where N is the number of particles per m^3 and L is the path length of the sample. In this simple case, $OD=NL\sigma/ln(10)$. Under real conditions, a distribution of particles with different radii has to be considered. The optical density can be expressed as a function of the normalized particle size distribution *PSD* or $f(r)$ in the following way:

$$OD(\lambda) = \frac{NL}{\ln 10}\int f(r).\sigma_{ext}(m,r,\lambda)dr \quad (2)$$

Equation (2) simply expresses the fact that the optical density is a linear combination of the different optical densities that would be obtained with a single radius r. **Our goal is to invert equation (2), in other words to determine *f(r)* as a function of the experimental data points *OD(λ)* assuming that we know σ_{ext}.** For many interesting applications, a typical *OD* can be greater than 5. In other words, the transmitted flux will be at least 5 orders of magnitude smaller than the incident flux. A photon will undergo a large number of scattering events while it travels through the sample. As a result, the scattered flux will be stronger (5 orders of magnitude stronger) than the transmitted flux.

Under such conditions, a measurement of angular distribution [4,8] of scattered light $I(\theta)$ could be more efficient. Equation (2) can be transposed for angular distribution as:

$$I(\theta) \propto \int f(r).\sigma_{scat}(m,r,\lambda)dr \qquad (3)$$

where σ_{scat} is the intensity scattered for various angles θ. Note, however, that this equation is limited by the assumption of single scattering event [10]. For thick media, we have to consider multiple convolution integrals, where the order of convolution is equal to the number of scattering events that one photon has undergone on its way through the sample. As a result, for a typical *OD* greater than 0.5, $f(r)$ cannot be numerically determined from a measurement of $I(\theta)$. Angular methods based on equation 3 are consequently limited to dilute media[1]. On the contrary, *OD* is based on the measurement of transmitted light, *i.e.* non-scattered light. As a result, it is possible to carry out measurements even if the assumption of a single scattering event is not true, and to characterize very dense scattering media. However, the scattered light is still an issue as it might be collected by the detector, and as mentioned earlier, the scattered flux can be greater than the transmitted flux. To get a proper determination of the *PSD*, three major difficulties must be overcome. First the light source has to be bright enough and tuneable. Then, we have to be able to get rid of the scattered light in the collection angle of the detector. Finally, we have to carry out the inversion of equation (2). We will show how femtosecond laser technology can solve the first two points. We used a numerical code developed in our laboratory in order to carry out the numerical inversion.

Light source requirements

We will first briefly discuss here how bright and spectrally large the light source should be in order to makeover accurate measurements. We have represented (Figure1) the evolution of σ_{ext} as a function of the radius of the particle for a given m and λ. For small particles $(mr/\lambda<<1)$, $\sigma_{ext}(m,r,\lambda)$ follows the Rayleigh regime and equation 3 can be rewritten as:

$$\sigma(m,r,\lambda) \propto \frac{r^6}{\lambda^4} \quad , \quad OD(\lambda) \propto \frac{\int f(r)r^6 dr}{\lambda^4}$$

This exhibits a clear redundancy of the spectral measurement: a single measurement for a given wavelength determines $\int f(r)r^6 dr$ *i.e.* all of the information we can obtain about $f(r)$, and this is not enough to determine the full *PSD*. For big particles $(mr/\lambda>>1)$, the expression of $\sigma(m,r,\lambda)$ falls into the geometric regime: $\sigma(m,r,\lambda)=2\pi r^2$. We can draw analogous conclusions as there is no more dependence with λ.Therefore, if we want to determine $f(r)$ accurately, the wavelength range has to match the radius range so that mr/λ is in the intermediate regime, also called the *Mie* regime.

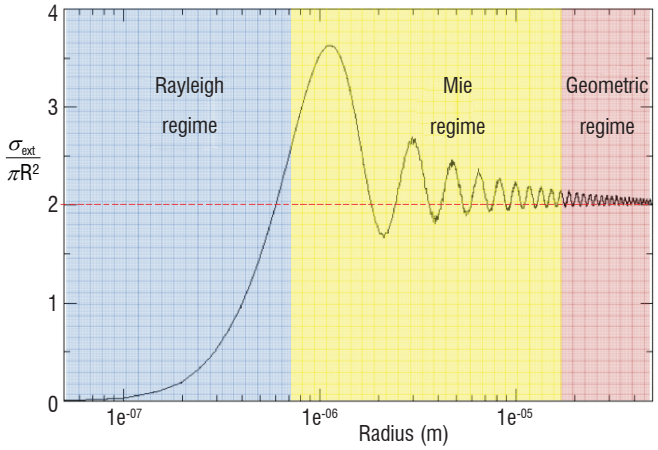

Figure 1 – Evolution of σ_{ext} with the radius of the particle. λ=400 *nm* and m=1.18. Note the different regimes: Rayleigh, Mie Geometric.

Note here that this condition not only depends on the ratio r/λ, but on the contrast of index: for a larger m, the limit between the Rayleigh regime and the Mie regime is shifted toward smaller radii. We used the inversion scheme [2] (described at the end of this article) to check the feasibility of the inversion for m=1.18 (particles of SiO_2 in water), and for a spectral measurement of 12 points between 400 nm and 700 nm. We were able to carry out an accurate inversion for *PSD* with a central radius between 100 nm and 5 μm (The *OD* spectra were calculated using the Mie theory). This shows that a huge spectral width is required, (400 nm - 700 nm typically), in order to carry out accurate inversion on a relevant radius range (100 nm - 5 μm). For larger or smaller radii, we have to consider broader light sources. Amplified femtosecond laser sources, coupled with Optical Parametric Amplifier technology (*OPA*) can deliver pulses from 200 nm up to 20 μm. Furthermore, the typical energy delivered per pulse is 100 μJ. With a detection limit of 30 photons, and a wavelength of 500 nm, such a system could measure an *OD* up to 13. For such level of *OD*, the amount of scattered light is huge so we have to implement a filtering device.

Filtering out the scattered light

We now have to study carefully the effect of the parasitic scattered light that might reach the detector. In order to accurately measure the *OD,* this light must be filtered.This is feasible by placing a lens after the scattering sample and a small pinhole at the focal point (Figure 2). The transmitted light maintains its initial propagation direction after the sample. As a result, it will go through the pinhole and reach the detector. Most of the scattered light will be stopped by the pinhole.

1 We mention here one possible way to carry out a *PSD* determination based on an angular method in the multiple scattering regime. A succession of scattering events will strongly affect the Degree Of Polarization (*DOP*) of the light. We could measure $I(\theta)$ and $DOP(\theta)$ simultaneously. However, the relationship between these two observables and the *PSD* is not direct as there is no simple analytic expression. A numerical optimization scheme is required. This method was implemented successfully in our laboratory and *PSD* with *OD* up to 5 were determined [18].

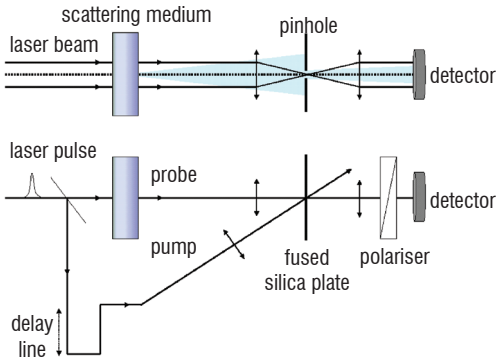

Figure 2 – Comparison of classical spatial filtering (top part), and femtosecond spatial filtering (bottom part). Most of the scattered light is stopped by the pinhole. The pump beam drills a virtual pinhole in the fused silica plate.

The principle of "femtosecond spatial filtering" is to use femtosecond laser pulses, and to generate optical Kerr gating in a fused silica plate [12]. Each laser pulse is split in two parts: the probe pulse and the pump pulse. Thanks to a delay line, we can fine-tune the time delay between the 2 pulses. The probe pulse goes through the sample in order to measure the *OD*, and then, both pump pulse and probe pulse are focused into the fused silica plate. The pump pulse instantaneously induces a birefringence in the plate (which will only last during the pump pulse), which in turn induces a rotation of the polarization of the probe beam. With a crossed polarizer placed in front of the detector, **the light can reach the detector only if the two beams perfectly overlap spatially and temporally.** Let's consider first the spatial overlap. This is strictly speaking the equivalent of a virtual pinhole: all of the probe light that is not overlapping the pump light will be stopped by the analyzer. The advantages of such of virtual pinhole compared to a classical one are huge. First, the size of such a pinhole can be fine tuned by changing the focus of the pump beam. Then, the overlap can be optimized at any space time by optimizing the Kerr effect signal. Let's now consider the temporal overlap. The ballistic light (transmitted light) will go straight through the sample, it will arrive first (Figure 3). The scattered light will undergo a more complex pathway, it will arrive later. As a result, when we fine tune the delay between the pump pulse and the probe pulse, the "temporal gate" will first sample the ballistic light, and then the scattered light. The experiment is repeated for several delays between the two pulses in order to obtain the temporal profile of the scattered light. Then we can integrate temporally the light around the ballistic "zero delay" and realize a temporal filtering of the scattered light.

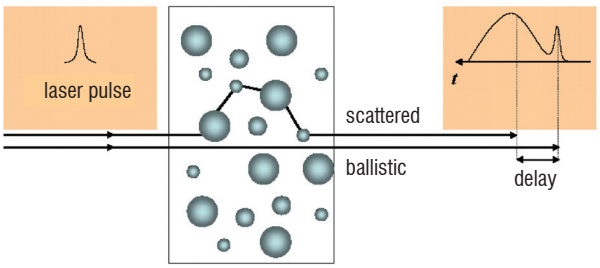

Figure 3 – Temporal filtering: different path way for the ballistic light and the scattered light.

In order to evaluate the relative efficiency of the temporal and spatial filtering **we developed a temporal Monte Carlo scheme [1,17]**. We sent particles of light (that we will call photons) randomly through the sample by computer simulation. Knowing the spatial size of the laser beam and the duration of the pulse, we randomly picked an initial position and an initial time for the photon. Then we calculated the different probability laws (distance between two scattering events, angle, time spent in the particle) in order to randomly build a pathway for the photon through the sample, toward the detector, keeping track of the time of flight of the photon. We carefully reproduced the geometry of figure 2, defining the position of the iris and the lens, in order to evaluate precisely the relative weight of the transmitted light and scattered light that goes through the iris and reaches the detector. We used a pinhole of 30 μm diameter and reasonable values for the other geometrical parameters. We considered that the spatial filtering was efficient if the scattered flux was smaller than or equal to the transmitted flux (error of 2 on I_t *i.e.* 0.3 on the *OD*). We observed that **the spatial filtering is efficient for a typical *OD* up to 7**. We also simulated the efficiency of the temporal filtering integrating the weight of the photon around the ballistic "zero delay" and outside of this temporal window. This additional **temporal filtering is efficient for a typical *OD* up to 11.** We observed that both spatial and temporal filtering are much more efficient for small particles than for big particles (typical values given earlier were estimated for 1 μm radius SiO_2 particle in water, L=1 cm, λ =500 nm). This is mainly due to the fact that big particles mainly scatter light in the forward direction. This will add almost no delay and almost no deviation to the photon.

Experimental illustration

We carried out a preliminary experiment using a 250 μJ, 1 kHz, 800 nm amplified laser source (Amplitude Technology, *LCAR/UPS*). The pump pulse was generated using a small part of the laser energy (10 μJ). The remainder was used to seed a Non collinear Optical Parametric Amplifier *(NOPA)* [3,6,11,13] tuneable from 490 nm to 700 nm. The spectral bandwidth of the *NOPA* output was carefully reduced and controlled for every wavelength. An additional measurement at 400 nm was obtained with the frequency doubled output of the laser. We carried out measurements on a calibrated suspension of SiO_2 particles in water. An average *OD* of 2 was small enough to be filtered spatially. Nevertheless, we carefully checked the temporal profile of the Kerr signal obtained after the sample and after a reference sample of water. No delayed scattered light was observed. In both cases, we measured a cross correlation of 200 fs. Typical results are shown (Figure 4). The black squares represent the *OD* obtained at different wavelengths. Experimental results are the averaging of ten measurements. The error bars are given by the root mean square of the distribution, mainly due to the laser instability. Error bars and average values were input into the inversion scheme outlined at the end of this article. The result of the inversion is represented (Figure 5) with red squares. The *PSD* result was then used to calculate an optimized *OD* spectrum using equation 2, plotted (Figure 4) in red. The match between the measured and optimized *OD* spectrum is excellent. The *PSD* result is compared with other results based on Polarization Induced Differential Scattering measurements (*PIDS* black circles (Figure 5)). As far as the radial average is concerned, both measurements are in good agreement with the specification of the SiO_2 particles we used to realize the experiment: 0.1 μm. The discrepancy regarding the distribution width is probably due to the fact that we are at the border of the Mie regime which is a problem for both methods (*OD* and *PIDS*). These are the first preliminary experimental results.

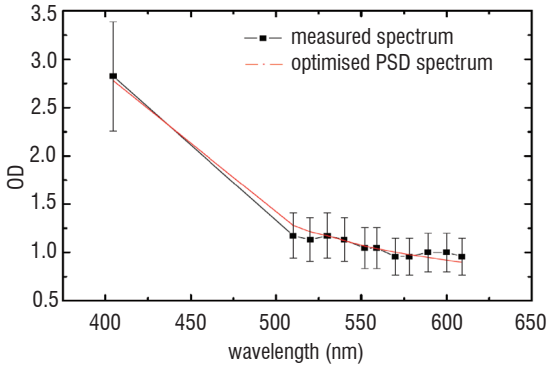

Figure 4 – *OD* spectra of a suspension of SiO_2 particles in water (0.1 μm central radius).

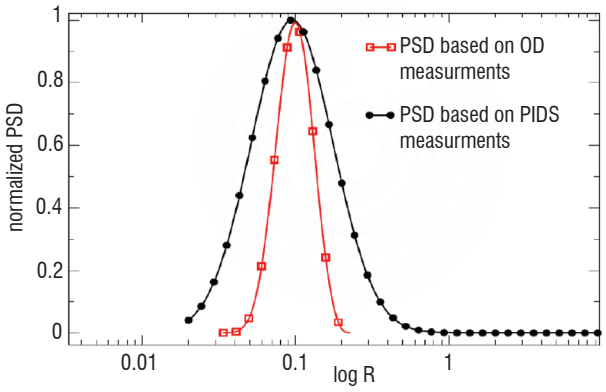

Figure 5 – Comparison of the inverted spectra with results based on a Polarisation Induced Differential Scattering measurement (*PIDS*). The two measurements were taken on the same sample.

Conclusion

We have demonstrated that femtosecond laser sources are very efficient for taking *OD* measurements of very dense scattering media. Such sources are bright and tuneable. Furthermore, an accurate filtering of scattered light can be implemented. We have carried out a preliminary experiment and have successfully retrieved the *PSD* of a model sample. Further experiments will be implemented using broader and brighter femtosecond laser sources and different samples ■

Box 1 - Instability of the Fredholm integral equation of the first kind. One possible resolution

Numerical instability

Equation (2) and equation (3) are called Fredholm integral equations of the first kind [9]:

$$g(y) = \int_{x_{\min}}^{x_{\max}} f(x).K(x,y)dx$$

Our goal is to invert this equation, in other words to determine $f(x)$ as a function of experimental data points $g(y)$ assuming that we know $K(x,y)$ (equation 2 and 3 are technically written with R_{min} and R_{max}, the physical limit for the determination of the particle size). This problem is ill conditioned. Let's draw some comparisons between this mathematical problem and the non linear differential equation. We assume that $x(t)$ is a solution of a non linear differential equation, with the initial condition $x(0)=x_0$ and $y(t)$ solution for $y(0)=y_0$.y_0 and x_0 can be very close and $x(t)$ and $y(t)$ can be very different. This is a very famous effect, known as the "butterfly effect". We will demonstrate here that a Fredholm equation leads to the same effect: a tiny little difference on the experimental data point g (initial condition) can have dramatic consequences on the solution f. This is due to the nature of the integral operator of the right hand side of this equation: given the Lesbegue theorem,

$$\forall y, \lim_{n\to\infty} \int_{x_{\min}}^{x_{\max}} \sin(nx).K(x,y)dx = 0$$

(as far as K is a continuous function, which is true for our application). As a result, $f(x)$ and $f(x)+A\sin(nx)$ will both be good solutions for the experimental data set $g(y)$ since the integration of the oscillating term can be arbitrarily small, as long as n is big enough. We have shown that there are two similar data sets, corresponding to two very distinct solutions. Fast oscillations of $f(x)$ will have very little impact on $g(y)$. **The only way to correctly solve this equation is to find a way to constrain the solution not to oscillate too fast.** Furthermore, some experimental data $g(y)$ may have no solution $f(x)$. We can differentiate the Fredholm equation with respect to y. The right hand side will be very regular as $K(x,y)$ is regular. As a result, $g(y)$ can have a solution only if it is regular. This might not be true as we consider experimental data with potential discontinuities and angular points. As a result, **we have to consider the experimental data *g(y)*, and a confidence interval** and assume that within this interval, we can find a regular curve $g(y)$ that will admit a solution. There is one more issue to consider: for our particular application, $f(x)$ is strictly positive (Particle size distribution $f(r)$). **The solution has to be constrained so that it always remains positive.** We have developed a numerical process in order to address all of these issues [5]. This method was initially developed to invert the data of angular single scattering experiments [4] (equation 3). The transposition to the spectral domain (equation 2) was straightforward [2]. This method is one inversion method among many others [16]. Let's describe briefly the general idea of our method.

One possible solution

The first step is to enter the result of the N measurements $g_i=g(y_i)$. For each y_i, $(i=1,N)$, the experiment has been done several times so we have a distribution of experimental values. For each parameter y_i, we enter the average value g_i and a confidence interval Δg_i. N measurements could in the ideal case lead to the determination of N independent parameters. We logically try to find a first solution $f_0(r)$ as a linear combination of N base functions $S_j(r)$:

$$f_0(x) = \sum_{j=1}^{N} C_j S_j(x)$$

S_j can be a step function, defined on knot points x_j: inside the interval $[x_j , x_{j+\mu}]$ S_j is equal to 1 and is 0 outside. In order to get a more accurate inversion, we use *cubic splines* for the base functions S_j as it will lead to a more regular solution, but the resolution is strictly equivalent to step functions. The choice of the grid x_j is critical as it directly governs how fast the solution can oscillate. In order to determine the first solution f_0, the decomposition is input in the Fredholm equation:

$$\forall i g_i = \sum_{j=1}^{N} K_{ij} C_j \quad \text{with} \quad K_{ij} = \int_{x_j}^{x_{j+1}} S_j(x) K(x,y) dx$$

This is a square linear system, the inversion is straightforward, and we determine the vector (C_j) and the solution f_0. This basic result is not accurate for three reasons. First, the grid (x_j) is not optimized. If it is too fine, the solution is allowed to oscillate too fast and the numerical system is not stable. Then, we have tried to extract N independent parameters (C_j) from N distinct measurements. This is not appropriate because the N measurements might be redundant (for example, if the *PSD* $f(r)$ is larger than the Mie regime). Finally, f_0 can be negative. To tackle these points, the second step of our method consists of a numerical regularization based on the Mellin transform formalism [9]. We are able to define a set of eigen functions of the operator $f \rightarrow \int fK$:

$$f_\omega(x) = \frac{\cos(\omega \ln(x))}{\sqrt{x}}$$

Using the Lesbegue theorem, these eigen values will decrease very strongly with ω. The idea is to decompose the coarse solution f_0 we obtained previously on the f_ω bases. Then, we only consider the lower frequencies ($\omega<\omega_{cut}$) to calculate the correspondent $g_i(\omega_{cut})$. When we realize:

$$\forall i, \left| g_i(\omega_\infty) - g_i(\omega_{cut}) \right| < \Delta g_i$$

we obtain the maximum frequency ω_{cut} to consider. In other words, if we allow the solution f to oscillate faster than ω_{cut}, this will correspond to a precision requirement on g_i greater than Δg_i. To avoid this situation, the step of the grid $ln(x_j)$-$ln(x_{j-1})$ will be equal to π/ω_{cut}. Decreasing ω_{cut} will increase the step of the grid. As x_{min} and x_{max} are fixed, this will in turn decrease the number of base functions S_j in the linear decomposition. The linear system is now a rectangular system and the algorithm will perform the inversion using a standard *Non Negative Least Squared Method* proposed by Lawson and Hanson [7]. This will constrain the solution to remain positive. Every time we find a solution, we calculate the corresponding g_i, and check that it is within the confidence interval. This method has been implemented, checked and used successfully to solve many different problems, in the angular situation (equation 3) [5], and in the spectral situation (equation 2) [2].

References

[1] M. BARTHELEMY - *Apport d'une source laser amplifiée pour la mesure de spectre d'exctinction d'un milieu diffusant optiquement épais.* Thèse de doctorat Onera/Université de Toulouse (2009).

[2] M. BARTHELEMY, N. RIVIÈRE, L. HESPEL AND T. DARTIGALONGUE - *Pump Probe Experiment for High Scattering Media Diagnostics.* SPIE Proc. (2008).

[3] G. CERULLO AND S. DE SILVESTRI - *Ultrafast Optical Parametric Amplifiers*. Review of Scientific Instruments 74(1). 1-18 (2003).

[4] L.HESPEL AND A.DELFOUR - *Mie Light-Scattering Granulometer with Adaptative Numerical Filtering: Experiments.* Appl. Opts. 40, 974-985 (2000).

[5] L.HESPEL AND A.DELFOUR - *Mie Light-Scattering Granulometer with Adaptative Numerical Filtering: Theory*. Appl. Opts. 39, 6897-6917 (2000).

[6] T. KOBAYASHI - *Sub-10-fs Tunable Pulses in Visible End NIR and Visible Sub-5-fs Pulses Generated by Non Collinear OPA.* Journal of Luminescence 87-89, 119-120 (2000).

[7] C. L. LAWSON and R. J. HANSON - *Solving Least Squares Problems*. Series on Automatic Computation Prentice-Hall Englewood Cliffs 1 (1974).

[8] H.S.LEE, S.K.CHAE and B.Y.H.LIU - *Size Characterization of Liquid Borne Particles by Light Scattering Counters.* Part.Part. Syt. Character 6, 93-99 (1989).

[9] J.G. MCWHIRTER and E.R. PIKE - *On the Numerical Inversion of the Laplace Transform and Similar Fredholm, Integral Equation of the First Kind*. J. Phys. A 11,1729-1745 (1978).

[10] G.MIE - *Beitrage zur Optik trüber Medien speziell kolloidaler Metallösungen.* Ann. Phys. (leipzig) 25, 377-445 (1908).
[11] A. MONMAYRANT, A. ARBOUET, B. GIRARD, B. CHATEL, B. J. WHITAKER, A. BARMAN, and D. KAPLAN - *Optimisation of NOPA Output Pulse Shaping Using an AOPDF with Dispersion Self-Correction*. Applied Physics B 81(2-3), 177 - 180 (2005).
[12] M. PACIARONI and M. LINNE - *Two-Dimensional Ballisitic Imaging through Scattering Media*. Applied Optics, 43, 26 (2004).
[13] E. RIEDLE - *Sub-20-fs Pulses Tunable Across the Visible from a Blue-Pumped Single Pass Noncollinear Parametric Converter*. Optics Letters 22, 1494-1496, (1997).
[14] H. SCHNABLEGGER and O.GLATTER - *Sizing of Colloidal Particles with Light Scattering: Correction for Beginning Multiple Scattering.* Appl. Opt. 34, 3489-3501 (1995).
[15] N.G. STANLEY-WOODS and R.W. LINES - *Particle Size Analysis*. Royal Society of chemistry (1992).
[16] S.TWOMEY - *Introduction to the Mathematics of Inversion in Remote Sensing and Indirect Measurement*. Elsevier New York, (1977).
[17] N. RIVIÈRE, M. BARTHELEMY, L. HESPEL and T. DARTIGALONGUE - *Modeling of Femtosecond Pulse Propagation Through Dense Scattering Media.* SPIE Proc. (2008).
[18] N. RIVIÈRE - *Apport de la polarimétrie à l'étude de milieux diffusants peu dense ou optiquement épais*. Thèse de doctorat Onera/université de Rouen (2006).

Acronyms
DOP (Degree Of Polarization)
NOPA (Non collinear Optical Parametric Amplifier)
OP (Optical Density)
OPA (Optical Parametric Amplifier)
PIDS (Polarization Induced Differential Scattering)
PSD (Particle size Distribution)

AUTHORS

Marie Barthelemy graduated in fundamental physics from the Université Paul Sabatier, Toulouse, France. She's particularly interested in laser matter interaction and potential applications on biological systems. For this reason, she chose to study for a Ph.D. at Onera on high scattering media using ultrafast optical diagnosis. She received her PhD degree on February 2009. She has joined the Femto team in the Laboratoire Collisions Agregats Réactivité to work for a year on UV ultrashort pulse shaping.

Laurent Hespel received his Ph.D. degree in physics from the Ecole Centrale de Paris, Châtenay-Malabry, France in 1999. The subject was "Theoretical and experimental studies of radiative transfer in scattering media. Experimental determination of radiative properties under high charge rate conditions". He studied for it in the group led by J. Greffet. He then joined the Onera (the French Aerospace Lab), first as a post doctoral fellow for a year and then as a research scientist. He is currently at the head of a research group named "Light interaction with Matter, Imaging and detection Laser Systems unit." His research group works on a large variety of areas of application: development of new laser imaging systems, Lidar, radiative transfer modelling, simulation of speckle, optical diagnosis of scattering media…

Nicolas Rivière received his engineering degree in Physics in 2002 from the University of Science Paul Sabatier, Toulouse, France. He obtained his Ph.D. degree in Physics in 2006. He is currently a Research Scientist with the Onera, the French aerospace lab. His main areas of interest are vector radiative transfer modelling and the Monte-Carlo method. He is involved in the development of direct codes and inverse techniques for the retrieval of optical properties from optically thick scattering media. His research activities currently concern time resolved scattering and modelling for imaging and ranging applications. He contributes to the development of new experimental setups for validating these concepts in the Light Interaction with Matter, Imaging and Detection Laser Systems Unit, Onera.

Béatrice Chatel received her Ph.D. degree in physics from Université Pierre et Marie Curie, Paris, France in 1996. The subject was "Measurement of the absolute frequencies 2S-8S/D in hydrogen and deuterium atoms. Determination of the Rydberg constant". She studied for it in the group led by F. Biraben in the Laboratoire Kastler Brossel. She then spent a year working on Characterization of ultrashort pulses in the Laboratoire d'Optique Appliquée with C. Dorrer and JP Chambaret. In 2000, she joined the Femto team in the Laboratoire Collisions Agregats Réactivité (Toulouse) as a CNRS researcher. She has published many works on pulse shaping techniques and coherent control experiments using shaped ultrashort pulses. She collaborates with academic institutions (Oxford, LPCNO-Toulouse, LAC-Orsay....) to further these areas of interest and with companies to extend the limits of pulse shaping techniques (Fastlite-Palaiseau)...

Thibault Dartigalongue graduated from Ecole Polytechnique in 2001. He received his Ph.D. degree in physics from Ecole Polytechnique Palaiseau, France in 2005. The subject was "Conformational dynamic of myoglobin followed by time resolved circular dichroism". He studied for it in the group led by F. Hache in Laboratoire d'Optique et Bioscience. He then joined Dwayne Miller's group at the University of Toronto as a post doctoral fellow for two years. He worked on ultrafast electron diffraction, studying the thermal dynamics of gold and silicon. He is currently a Research scientist at Onera (French aerospace lab). He is involved in the development of a femtosecond laser laboratory devoted to optical diagnosis of very thick scattering media.